Holographic Diffraction Imaging at the Nano-scale by Coherent Hard X-ray Synchrotron Radiation

---

Dissertation

zur

Erlangung der naturwissenschaftlichen Doktorwürde

(Dr. sc. nat.)

vorgelegt der

Mathematisch-naturwissenschaftlichen Fakultät

der

Universität Zürich

von

Mirna Toni Saliba

aus dem Libanon

Promotionskomitee

Prof. Dr. Jürg Osterwalder (Vorsitz)

Prof. Dr. Pierre Thibault

Prof. Dr. Christoph Rau

Prof. Dr. Ueli Straumann

Zürich, 2016

Abstract

In the interest to unveil structural information of matter at the nanometer scale and beyond, there is an endless quest to innovate new techniques that provide images and maps of a probed sample. From the first X-ray radiograph obtained by Wilhelm Röntgen in 1895 when he accidentally discovered X-rays, to the latest developments in microscopy, where we can *see* carbon atoms in a graphene layer, and in coherent diffractive imaging and protein crystallography, where structural information of proteins can be visualised on the atomic level, the field of imaging and microscopy is forever evolving. Today, it is the caliber of quantitative information about the structure, chemical composition, magnetic properties and much more in a static or dynamic setting that makes the field of imaging very competitive and gives rise to a vast variety of techniques.

Methods that rely on image-forming lenses are limited by the optical properties of the lenses and can only achieve a certain level of resolution before the intrinsic aberrations begin to distort the imaging process. Hence, diffraction-based lensless techniques emerge as an alternative. They rely on recording diffraction patterns of samples where the structural information is encoded into a Fourier spectrum. The detected intensity distribution is the Fourier transform of the squared modulus of the object wave-field. Detectors are only sensitive to intensity and do not record the phase or amplitude information, which are what relate to the physical properties and the atomic distribution of the sample. This issue is known as the phase problem.

A reliable solution to the phase problem is holography where the phase information is intrinsically preserved by virtue of a reference wave. Holography provides image reconstructions of the complex wave-field at the exit of the sample, but it is hindered by the formation of overlapping twin images. The twin images are the result of holography performing similarly to a lens system, giving a real image and virtual image. However, when one image is brought into focus at a plane z, the twin image is also reconstructed in the field but appears out-of-focus by a distance 2z. This issue has triggered the development of off-axis holography which effectively disentangles the twin images by offsetting the reference source.

Yet, coherent diffraction imaging techniques (CDI) using iterative algorithms also provide a solution to the phase problem and produce complex-valued images of a sample at diffraction-limited resolution. The reconstruction procedure is iterative and starts from assuming certain conditions about the values of the amplitude and phase of the sample, which in turn governs the uniqueness and disambiguity of the solution. In addition, scanning coherent diffractive imaging, also known as ptychography, provides high-resolution reconstructions of a probed sample by shifting the illumination area and solving a large system of equations by using the overlap information to converge to a unique solution.

X-ray radiation has the virtue of having high penetration depth which means it can provide depth information about thick samples, hence it is widely used in medical imaging as well as archeology, and paleontology, and the material sciences. Coherent imaging methods that use iterative algorithms generally rely on high computational power and require apriori information about the sample or the illumination area to achieve successful results. However, for applications to radiation-sensitive samples where one aims to obtain an image of a sample before it disintegrates, and for applications in ultrafast femtosecond processes on the atomic level, there rises a need for a single-shot imaging technique. With the new-generation x-ray synchrotrons that provide coherent x-rays with high brilliance, and with the rise of X-ray free-electron-lasers that produce intense pulses of light with orders of magnitude higher flux and femtosecond time-lapses, the development of single-shot imaging techniques becomes highly motivated.

We have developed a holographic diffraction imaging technique particularly tailored for hard X-rays but generally transferable to all coherent radiation. The main feature of our method is the use of a novel three-dimensional reference structure with phase-shifting properties that overcomes the limitations associated with absorbing substrates predominantly employed in soft X-ray holography using extended, customized and point-source references. The method directly and non-iteratively produces complex-valued reconstructions of an imaged specimen by single-shot exposure with high contrast and nanometre-scale resolution.

Owing to innovative nano-fabrication methods using atomic layer deposition, we also introduce an upgraded reference design that elevates the resolution and contrast of the imaging system beyond the fabrication capacity of electron/ion-beam milling. The method was successfully applied to absorbing samples, weak phase samples, as well as biological samples such as Deinococcus Radiodurans bacterial cells and marine microplankton coccolithophorids.

In addition, we implemented a flexible experimental design that involves decoupling the sample plane and the reference plane mitigating many of the technical constraints and allowing translation and rotation of the two planes independently. This leads to enhanced data refinement and background filtering, better statistics by sample shifting, accommodating a large set of samples, and facilitating tomographic measurements.

These advantages along with being a noise-robust, non-scanning and non-iterative imaging method, provide great potential for single-shot femtosecond tomographic imaging of biological samples and ultrafast processes using x-ray free-electron-lasers.

Zusammenfassung

Das Interesse strukturelle Informationen der Materie auf der Nanometerskala und darüber hinaus zu untersuchen, führt zu einer andauernden Entwicklung neuer Techniken zur Erstellung von Bildern der zu untersuchenden Proben. Seit der ersten Röntgenaufnahme von Wilhelm Röntgen im Jahr 1895, als er zufällig die Röntgenstrahlung entdeckte, bis hin zu den neuesten Entwicklungen der Mikroskopie, die Kohlenstoffatome in einer Graphenschicht sichtbar macht, der Bildgebung mittels kohärenter Röntgenbeugung und der Proteinkristallographie, die strukturelle Eigenschaften von Proteinen mit fast atomarer Auflösung sichtbar macht, hat sich das Gebiet der Mikroskopie ständig weiterentwickelt. Heutzutage ist es die Vielfältigkeit quantitativer Informationen über die Struktur, die chemische Zusammensetzung und die magnetischen Eigenschaften etc., die Mittels statischer und dynamischer Experimente gewonnen werden können, die das Gebiet der Bildgebung sehr kompetitive macht und zur Entwicklung einer Vielzahl unterschiedlicher Techniken geführt hat.

Bildgebende Verfahren, die auf Linsen beruhen, sind durch die optischen Eigenschaften der Linsen bestimmt und können daher nur ein begrenztes Mass an Auflösung erreichen, bevor die unvermeidlichen Aberrationen den Abbildungsprozess beeinflussen. Daher haben sich beugungsbasierte linsenfreie Techniken zu einer Alternativen entwickelt. Sie beruhen auf der Messung des Beugungsbildes der Probe, wobei die Strukturinformation in einem Fourier-Spektrum kodiert ist. Die gemessene Intensität ist die Fourier-Transformation des Betragsquadrates des Objektwellenfeldes. Detektoren können nur Intensitäten und nicht die Phasen messen. Beide Grössen werden jedoch benötigt, um Rückschlüsse auf die physikalischen

Eigenschaften und die atomare Verteilung innerhalb der Probe zu ziehen. Dieses Problem ist unter der Bezeichnung Phasenproblem bekannt.

Eine zuverlässige Lösung für das Phasenproblem ist die Holographie, wobei die Phaseninformation mit Hilfe einer Referenzwelle kodiert wird. Holographie liefert eine Bildrekonstruktionen des komplexen Wellenfeldes am Ausgang der Probe, das aber durch Überlappung von sogenannten Doppelbildern beeinflusst wird. Die Doppelbilder sind im Gebiet der Holographie das Analogon zu reellen und virtuellen Bildern bei abbildenden Linsensystemen. Wie auch immer, wenn man auf eines der Bilder fokussiert, wird auch das andere Bild rekonstruiert, allerding erscheint seine Bildebene um 2z verschoben. Dies hat zur Entwicklung der azentrischen Holographie gefuehrt, die die Doppelbilder räumlich voneinander trennt, indem die Referenzlichtquelle und das Objekt gegeneinander verschoben sind.

Darüberhinaus können Methoden, die auf kohärenter Roentgen beugung (CDI) beruhen und die iterative Algorithmen benutzen, das Phasenproblem ebenfalls lösen und komplexwertige Bilder, mit nahzu beugungsbegrenzter Auflösung, erzeugen. Der Rekonstruktionsprozess ist iterativ und macht einige Annahmen bezüglich der Amplituden und Phasenschiebung in der Probe, welche im Gegenzug die Eindeutigkeit der Lösung bedingen. Zusätzlich kann bei kohärenten Röntgenbeugungsexperimenten die Probe abgerastert werden, also das beleuchtete Gebiet über der Probe verschoben werden. Diese als Ptychographie bekannte Methode, erlaubt hochaufgelöste Rekonstruktionen, indem ein sehr umfangreiches Gleichungssystem gelöst wird. Die Konvergenz des iterativen Algorithmus wird durch Überlapp zwischen den beleuchteten Probenbereichen erzielt.

Röntgenstrahlung besitzt eine hohe Eindringtiefe, das heisst, sie kann Tiefeninformation über dicke Proben liefern. Daher wird sie auch vielfältig in der medizinischen Bildgebung, sowie Archäologie und Paläontologie und den Materialwissenschaften eingesetzt. Kohärenz basierte bildgebenden Verfahren, die iterative Algorithmen benutzen, benötigen im Allgemeinen eine hohe Rechenleistung und Apriori-Informationen über die Probe oder das Beleuchtungsfeld, um brauchbare Ergebnisse zu erzielen. Für Anwendungen bei strahlungsempfindlichen Proben hingegen, bei denen man versucht ein Bild zu erhalten, bevor die Probe zerstört wird

und bei Anwendungen im Zusammenhang mit ultraschnellen atomaren Prozessen im Femtosekundenbereich werden Einpulsmethoden benötigt. Mit der neuen Generation Synchrotron basierter Röntgenquellen, die kohärente Röntgenstrahlen mit hoher Brillanz generieren und mit dem Aufkommen Freier-Elektronen-Laser im Röntgenbereich, die intensive Lichtpulse mit um Grössenordnungen höheren Flüssen und Attosekunden-Zeitauflösung erzeugen, hat die Motivation für bildgebende Einzelpulsverfahren deutlich zugenommen.

Wir haben ein auf diffraktiver Bildgebung beruhendes holographisches Verfahren speziell für harte Röntgenstrahlung entwickelt, welches sich aber mit jeder Art von kohärenter Strahlung verwenden lässt. Das wesentliche Charakteristikum ist eine neuartige dreidimensionale phasenschiebende Referenzstruktur, die die Limitierungen der aus absorbierenden Substraten bestehenden ausgedehnten, speziell angepassten und punktartigen Referenzobjekte, wie sie vorwiegend bei der Röntgenholographie mittels weicher Röntgenstrahlung eingesetzt werden, überwindet. Das Verfahren erzeugt auf direktem Wege, ohne Iterationen, mit einer einzigen Belichtung komplexwertige Rekonstruktionen von abzubildenden Proben mit hohem Kontrast und einer Auflösung im Bereich von Nanometern.

Aufgrund neuartiger Nanostrukturmethoden, die Atomlagenabscheidung verwendet, können wir ein verbessertes Konzept für die Referenzobjekte realisieren, das die Auflösung und den Kontrast des abbildenden Systems über die Fabrikationsmöglichkeiten von Elektron-/Ionenstrahlfräsen steigert. Die Methode wurde an absorbierenden und schwach Phase schiebenden Proben, sowie an biologischen Proben wie Deinococcus Radiodurans Bakterienzellen und marinen Mikroplankton Coccolithophoriden erfolgreich angewendet.

Darüberhinausgehend realisieren wir einen flexiblen experimentellen Aufbau, der die Objekt- und Referenzebene voneinander entkoppelt und damit das unabhängige Verschieben und Rotieren der beiden Ebenen ermöglicht und folglich viele technische Begrenzungen überwindet. Dies ermöglicht eine bessere Auswertung der Daten durch das Herausfiltern des Hintergrundes und eine verbesserte Statistik durch das Translatieren der Proben, sowie die Untersuchung grosser Proben, was tomographische Messungen vereinfacht.

Diese Vorteile in Verbindung mit der Störunempfindlichkeit des Bildgebungsverfahrens und der Möglichkeit auf ein Abrastern der Probe und auf iterative Rekonstruktion zu verzichten, haben unter Zuhilfenahme Freier Elektronenlaser ein grosses Potential für Femtosekunden-Tomographie im Einzelpulsverfahren an biologischen Proben und von ultraschnellen Prozessen .

Dedicated to my father and mother, Toni and Norma
My strength. My weakness. My rock.

Acknowledgements

I would like to thank all the people who contributed or helped in any way, scientific, technical or otherwise, to achieve this work. If I forget any names, please forgive me and know that to you I am grateful.

First, I would like to express my gratitude to Prof. Ueli Straumann, the director of the Physics Institute at UZH and the dean of studies at the MNF Faculty. I came to him during a difficult time and he helped me and supported me with no prejudice and nothing but graciousness. He believed in me and gave me the opportunity to do this research and form a collaboration with Diamond Light Source, where I met wonderful people, broadened my scientific horizons, and understood my true capabilities. For this I say Thank You Ueli. I would like to thank the University of Zurich who provided the financial support during my PhD studies. To Prof. Juerg Osterwalder, I am deeply grateful who followed my work as my thesis advisor. He supported my project and travelled to Diamond Light Source in England to make sure everything was on track and his input was always given with honesty, integrity, and high knowledgeability.

I hold great gratitude to Prof. Monica Zwicky who mediated to accomplish my research transition, and was a person who believed in justice and incessantly, selflessly, and righteously fought for justice to get me to where I am today. I thank the administration staff at UZH, especially Ruth Halter, Monika Roellin, and Carmelina Genovese who were always ready to help, and who showed me what true kindness means.

I am grateful to the staff at DLS, the Director of Physical Sciences Trevor

Rayment for approving our collaboration and giving us the opportunity to undertake the experimental work at DLS. I am thankful to Andrew Richards for facilitating my stay at DLS making sure all the legal aspects of our collaboration were met.

To Pierre Thibault I would like to say a big thank you. I came to Pierre with an idea and a broken wing, and he accepted me. I had the pleasure to work with such a brilliant mind and admired his modesty, kindness, and patience. He supervised my work at DLS and always came in to help during the beamtime experiments at DLS. It was sure that Pierre would always provide witty insight into the work and provide quick and easy ways to make things simpler. Even with his busy schedule, he made time for discussions and managed to resolve a dozen issues within a 15 minute meeting.

I would like to thank Christoph Rau who was my supervisor at DLS. Christoph welcomed me at DLS and never hesitated to make sure that I had all I needed to make my experience as smooth as possible. He approved my scientific project and provided the I13 beamline to carry out my research. More than that, I think I can say that Christoph was a friend too. The fun and witty conversations we shared are something I will never forget. Christoph was a true support; he guided me, and helped me understand my priorities. He was there during the sad times and during the good times and pushed me to believe in myself when I almost didn't. Thank you Christoph.

I would like to say a heart-felt thank you to my late colleague and dear friend Jeroen Bosgra. I worked closely with Jeroen on planning the experiments and he prepared the lithography samples for me at PSI. He joined during the beamtime and generously stayed till the late hours to support the experiment. He was the true definition of selfless giving, always with a smile on his face, and ready for a laugh. We were such a good team together, and long days and nights of experimental work passed like a few hours with him. I was deeply saddened and shocked to hear that he passed away. I will forever be grateful to him and will always miss him. May he rest in peace.

I would like to thank Aaron and Ulrich whom I closely worked with during

the experiments and were always ready to make sure the experiment runs as planned. They taught me the physical and technical important aspects of running a beamline experiment with a passion for science. They were colleagues and dear friends, as we enjoyed many funny conversations and mindless banter as well as deep conversations about life. Special thanks goes to Ulrich for translating my abstract to German. I am also grateful to Joan Vila Comamala who was the go-to-guy on all things "zoneplates" and was always ready to give a helpful hand. To Andy Bodey, I say thanks for all the laughs. To Stefanos, Charan, Simone, and Marie, my colleagues in the UCL ptychography group, I say cheers and I wish you the best of luck with your theses, I am sure you will do great.
I am grateful to Manuel Guizar whose thesis was my scientific bible and my motivation. I met him and had a few discussions with him, and I admire his passion for science and his generous giving nature when it comes to joining minds to better science. His input has been much appreciated and very valuable. I would also like to thank Bjoern Enders for quickly answering emails and providing input regarding the holographic theories. I also thank Lil Read for providing the plankton samples and helping with the characterisation of the plankton.

Finally, I express my eternal gratitude to my parents Toni and Norma who are my strength. To my mother, who always worried about me, whose hugs are a ray of sunshine, and whose home-cooked Lebanese food brings me back to life, I say thank you. To my father, who always understands what I'm going through, always listens, never judges me, who has always believed in me since I was a little girl writing fictional stories and poetry until I graduated with a Physics diploma, received a Masters scholarship, and finished my PhD thesis, with a heart full of love, I say thank you. To my sister Daniella, my roommate, my buddy, my team player, with the kindest softest heart, I say thank you my heart. Finally, my nephews and Godsons Robin and Julian, you bring me joy like no one has given me. I can't wait to watch you grow up and teach you Physics!

Last but not least, I would like to thank God, my lord and saviour, for giving me strength and perseverance, for keeping me, guarding me, guiding me, and giving me all these blessings.

Contents

1 Introduction

In scientific fields such as solid-state physics, semiconductors and electronics, life sciences, such as oncology, micro- and molecular biology, neuroscience, genetics, as well as archeology and paleontology, among others, probing a specimen of interest under coherent illumination to obtain an image is a vital method to uncover physical, chemical, and material properties in a static or dynamic setting.

When imaging with x-rays, microscopical methods (that utilise lenses to form the image) are often limited by the quality of the lenses used. For example, Fresnel zone plates (FZP) are used in transmission x-ray microscopy (TXM) and scanning transmission x-ray microscopy (STXM) [1, 2] to serve as the image-forming x-ray optics. FZPs are designed in such a way to serve as an approximate lens or mimic the behaviour of a glass lens with visible light but with x-ray wavelengths. The properties of a zone plate, i.e the size of the focal spot, the depth of focus and the efficiency, depend on the x-ray energy used [3, 4]. At higher x-ray energies (hard X-rays), the requirements for fabricating a high-efficiency zoneplate become more stringent [5]. In general, ideal diffraction-limited optics are difficult to manufacture and the attainable resolution and image quality ultimately depends on the quality of fabrication of the zoneplate.

Similary, when imaging with electrons, the image obtained in a transmission electron microscope (TEM) with a probe size of 0.1 nm is ideally wavelength-limited, but it is first limited by the electron lenses used in the system. A well-documented

resolution-limiting problem with TEM imaging is lens aberrations, which triggered the development of high-end and costly TEMs [6] with built-in spherical aberration correctors and the SuperSTEM.

On the other hand, coherent lensless imaging techniques [7, 8, 9], applicable with x-rays, visible light, electrons of high and low energy, as well as ultraviolet radiation [10], enable the user to obtain an image of the inspected sample without the use of a lens. In CDI, the transmissivity of the sample is retrieved by measuring the far-field diffraction pattern and numerically inverting the recorded intensity. Only the intensity is recorded, the phase information is lost; this is known as the phase problem [11]. Phase retrieval in CDI is performed by iterative algorithms [12, 13] that require adequate sampling of the intensity distribution (oversampling) by surrounding the sample by a padding area of zeros (zeropadding). The phase is input into the iterative engine at the first iterative run as a phase guess or an estimate based on apriori information about the sample. In general, the method risks stagnation or ambiguity, and the convergence of the reconstruction is computationally expensive.

Ptychography, however, has emerged as an alternative coherent diffractive lensless imaging method that alleviates many of the inconveniences associated with CDI. In far-field ptychography [14, 15, 16], the sample is scanned by a well-defined "probe" or illumination field, a far-field diffraction pattern of each subregion of the sample is recorded as the probe scans across the sample with sufficient spatial overlap for better convergence. Virtually, a large system of equations that describe regions of the sample is solved by utilising the overlap regions. Phase retrieval is efficiently performed owing to the scanning method. The reconstruction procedure is fairly vast and computationally demanding. However, recent developments in ptychographic reconstruction algorithms have allowed for a standardised algorithm to be made available for users world-wide, which has helped to break the barrier between the scientist who seeks the application and the scientist who develops the method.

Apart from resolution, robustness to noise and decoherence, and computational effort, a main concern regarding lensless coherent imaging methods is their

applicability as non-destructive methods and their capability to unveil dynamic processes on the molecular level in a femto-second timeframe. To record the far-field scattering signal of a bio-molecule just before it bursts due to radiation damage is a notion known as "diffract and destroy", a term coined by John Spence [17]. With the emergence of high brilliance free-electron lasers (FEL) [18] that provide orders of magnitude more flux than second generation synchrotrons, the question arises: which coherent diffractive imaging technique is most suitable for imaging of ultrafast [19, 20] and/or biological samples [21] with FELs or high brilliance x-ray sources? Ideally, one would aim to obtain a single femto-second exposure snapshot of the sample before it is destroyed, and attempt to reconstruct the far-field diffraction data [22, 23]. CDI is applicable for such an aim, but the sample area must be particularly isolated, which is difficult for a water burst of molecules at certain energies. In addition, the computational expense to iteratively process millions of datasets would span years and employ tens of computer clusters and mind power.

While ptychography is computationally robust and immune to unideal coherence, it faces the disadvantage of being a scanning method, which renders it inapplicable for single-shot or "diffract and destroy" imaging, unless single atto- or zepto-second pulses could be sustainably generated to keep the cumulative exposure of multiple scans below the decay time.

Holography, on the other hand, proves to be advantageous as a lensless coherent imaging method [24] that preserves the phase information, eliminating the need for iterative engines, phase guessing or scanning the probe. The amplitude and phase reconstruction of the sample is adequately achieved by processing the holographic pattern recorded in a single exposure shot. As a single shot imaging method, it proves suitable for "diffract and destroy" imaging and measurement of ultrafast dynamic processes using femtosecond FEL pulses.

In classic Gabor holography (inline holography) [25, 26], a sample contained in a highly transmissive support is illuminated by a coherent spherical wave emerging from a point source, a hologram is recorded at a distance. The point source (or reference) and the sample center are co-axial, i.e. both aligned on the optical axis

hence the term "inline". The inline hologram is magnified by the ratio of distances to the detector and to the object respectively from the point source and it portrays the shape of the object with surrounding modulating fringes. By Huygens-Fresnel principle, the sample can be reconstructed by back-propagation to the object plane. Holography requires coherent illumination over the object area and (in case of offset references) sufficient transverse coherence to cover the transverse separation between the object and reference. It is resolution-limited by the size of the point source and the numerical aperture. Due to the interference between the illuminating reference wave and the scattered object wave, the phase is preserved within the interference term. Therefore, holography overcomes the phase problem and image reconstruction from holographic data is direct and non-iterative.

In the inline scheme, the reconstructed image at –z overlaps with the twin image, a complex-conjugate mirror-flipped version of the image at +z; this is known as the twin image problem [27]. Off-axis holography solves the twin image problem by laterally offsetting the reference beam from the optical axis. Upon reconstruction, the twin image is then located symmetrically from the reconstructed image with respect to the optical axis with an offset corresponding to the lateral separation of the point source. In holography, three dimensional imaging is made possible by virtue of the Huygens-Fresnel propagation. One can reconstruct different cross-sections of the sample that correspond to different object planes to obtain the three-dimensional information using the Fresnel propagator.

So far, holography has been described as Fresnel-type, where the conditions existing between the object plane and the recording plane are in the Fresnel regime. Holography in the Fraunhofer regime is accomplished when the hologram resides in a plane that yields the Fourier transform of the object amplitude transmissivity. The transformation between object plane and detector plane then falls within the Fraunhofer diffraction equation. In lensless Fourier Transform Holography [28, 29], the object is illuminated by a coherent uniform planar wave creating a scattered object wave that propagates to the detector plane as in Fraunhofer diffraction. A point-scatterer or point-source positioned in the vicinity of the object (classically in the object's optical plane) generates a diverging spherical reference wave which

interferes with the object wave. With no lenses past the object, the interference is recorded in the far-field as an intensity pattern consisting of a sinusoidal fringe distribution with a spatial frequency specific to the object function, bound by the Fourier transform.

Therefore to compare Fresnel and Fraunhofer holography, the Fresnel-hologram encodes each object point into a portion of the fringe, forming a pattern of a range of spatial frequencies as in Huygen's principle of secondary wavelets. In contrast, the Fourier transform hologram encodes the object into sinusoidal fringes of constant frequency, which allows more efficient use of the space-bandwidth product (or the extent of encoded information).

In Fourier transform holography, the presence of a point source in the object plane results in the capability of direct image reconstruction by a single Fourier transform. This is due to the fact that the sample's transmission function is comprised of the sum of the object function and the reference function (when they are sufficiently separately from one another). The inverse Fourier transform of the recorded intensity gives the autocorrelation of the transmission function at the sample plane. The autocorrelation is that of the sum of the object and reference function. When the reference is a point-source, it is mathematically approximated to a delta-like function. Owing to its sifting property, the cross-correlation of a delta function with another function, such as the object function, yields the object function itself at the coordinates of the delta function. Therefore, the inverse Fourier transform of a far-field intensity distribution produced by a scattered object wave interfering with an offset reference wave results in a direct reconstruction of the amplitude and phase of the object at the position of the reference point [30]. Due to the cross-correlation of the object function with the reference function, resolution in Fourier transform holography is ultimately limited by the size of the point source which generates the reference wave.

The point reference is typically fabricated as a small pinhole using a Focused Ion Beam (FIB) or electron beam lithography in an absorbing sample substrate. With applications to hard x-rays, it becomes particularly difficult to mill a nanometre-scale pinhole through an absorbing mask since the mask must be very

thick to absorb x-rays of such high energy. Even using electron beam lithography to mill a 1000/1 aspect-ratio pinhole is a difficult task. In addition, the total flux transmitted through the small pinhole would be very low compared to the object signal which results in deteriorated signal-to-noise ratio (SNR). Hence, a trade-off between resolution and contrast must be considered.

One way to increase the SNR with the pinhole reference scenario, is to introduce multiple point references [31, 32, 33] to produce a sum of multiple reconstructions that are stitched together, with the squared error E^2 inversely proportional to the number of reconstructions. Yet, this method results in enlarging the reconstructed field of view. For better statistics, one includes as many reference points as possible while maintaining the separation conditions between consecutive reference points and between the reference point and the object.

Fourier transform holography has also been accomplished with prepared point-scatterers [34, 35] such as gold dots or sharp scatterers that lie within or around the object. This method ideally requires apriori knowledge about the point-scatterers to obtain their approximate transmission function, since the reconstruction is performed by deconvolution to yield better quality reconstructions. It does not suffer from the constraints related to FIB fabrication yet still lies within the resolution-contrast trade-off regime.

Holography with extended references [36, 37] exploits the use of a wide variety of reference sources of different shapes, sizes, and transmission properties. It offers more flexibility regarding substrate fabrication and ensures better SNR without majorly compromising on resolution; it even proves to be noise-robust in certain cases, while conserving the ease of a fast and direct reconstruction method. The method is based on using a reference structure that comprises of sharp features whose transmission function can be mathematically reduced to a delta-like function using differential or integral operators [38]. For example, a slit milled through an absorbing substrate is reduced to two point sources (delta- like functions) at the ends of the slit by applying a directional derivative to its transmission function. Similarly, a square is differentially reduced to 4 delta-like functions, and so on.

The flux and noise expectations of the imaging system are a key issue to consider when deciding the shape of the reference, i.e. pinhole, slit, rectangle, corner etc. As we will determine in Chapter 2, the SNR analysis of different references is very well dependent on the geometry of the reference. The thickness and material that constitutes the reference structure compared to the surrounding substrate is an important parameter that determines the strength of transmitted reference signal and affects the contrast and visibility of the reconstructions.

When imaging at x-ray wavelengths, we consider the two terms that result of the interaction with matter: transmission and phase. X-rays passing through a thickness of material will be attenuated and phase-shifted according to the β and δ of the material respectively, with energy and elemental dependence. Transmission is inversely proportional to β, where β is proportional to the electron density. The phase shift is proportional to δ, the material thickness, and the x-ray energy. The phase shift being in units of π radians means that the amount of material required to create a considerable phase shift from 0 to π is much less than that required to create a surge in absorption from 0% to 100%. This aspect becomes particularly attractive when considering the choice of reference material for hard x-ray holography.

In regards to hard x-ray holography with extended references, manufacturing the exemplary transmitting (or absorbing) reference structure with a high and sufficiently sharp transmission transition between the reference and substrate is a nontrivial task, if not impossible. It is thence of particular interest to use phase-shifting reference structures [39, 40] where much less material is required to create a π phase shift thus simplifying the fabrication requirements considerably. After deriving the total transmissivity of the sample (reference + object) on a transmitting substrate, we arrive to the conclusion that a π phase-shifting reference amplifies the magnitude reference signal by 4 times and the object amplitude signal strength by 2 times and results in higher contrast compared to a transmitting/absorbing reference.

In this thesis, we will first give a mathematical and theoretical overview of the physical phenomenon of diffraction imaging starting from the Maxwell equations and the wave propagation of light, discussing the phase problem, and introducing diffraction-based methods in Fresnel and Fraunhofer regime which solve this problem. We will introduce holography and elaborate on the theoretical background of Fourier transform holography. We will discuss the effect of different types of reference structures and highlight the value of phase-shifting references for applications with hard x-rays.

In Chapter 3, we will discuss the experimental setup of measurements performed at I13 DLS to lead to successful complex-valued image reconstructions of a variety of samples: strongly scattering and weakly scattering absorption and phase test samples, as well as biological samples such as marine microplankton and bacterial cells. Numerical methods will be discussed and we will show how with the sample plane and reference plane being geometrically unconfined, we achieve new degrees of freedom and flexibility and we enhance the reconstructions by means of background correction.

We will introduce a novel compound holographic reference fabricated by high-resolution atomic layer deposition and we will show the advantage and superior performance of such references for holographic diffraction imaging of samples at nanoscale resolution. The results will be compared between the two types of references and we will finally show reconstructions of bacterial cells and other samples with edge-enhancement and differential contrast owing to the novel reference. In Chapter 5, we will extend the holographic imaging method with hard x-rays to high-resolution high-efficiency Fresnel zone-plates which provide intense reference waves with a fine focal spot. We will showcase the results obtained using zoneplate-based Fourier transform holography and we will finally end with a conclusion and outlook for further advancements in the domain.

2 Theory

In this chapter, we will introduce the mathematical tools that help to understand the theoretical basis of holographic and diffraction imaging. Starting from the Maxwell equations, we will develop the wave equation and discuss the solutions to the wave equation. This will give the foundation of understanding wave propagation and wave scattering leading to Fresnel diffraction and Fraunhofer diffraction. Consequently, we will introduce the infamous "phase problem" [11] and introduce the two imaging methods that solve this problem: Coherent Diffraction Imaging, which involves iterative numerical algorithms to estimate the phase and converge to a unique solution, and Holography which involves using a reference wave to encode the phase information. Holographic methods will be reviewed starting with Gabor holography and ending with the hybrid method of Fourier Transform Holography which involves interference between the scattered wave-field of a sample and a holographic reference wave in the far-field limit. A theoretical overview of holography using extended references and its effective benefits will be discussed with illustrative simulations. We will compare types of extended references: the absorbing reference structure on a transmissive substrate and the transmissive reference structure on an absorbing substrate. We will present the importance of coherent imaging at hard x-ray wavelengths and its applications. With that motivation, we demonstrate the advantage of using a phase-shifting reference structure instead of a transmissive/absorbing reference, and we will highlight the superior performance of such references regarding SNR, contrast, resolution,

fabrication flexibility, and experimental applicability. In summary, this chapter provides the mathematical and theoretical backbone of the experimental results discussed in the next chapters, and introduces the technical conditions required for the successful experimental implementation.

2.1 Mathematical Tools

Convolution

The convolution of two functions f and g is the integral of the point-wise multiplication of f and g as a function of the translation between the two functions:

$$(f * g)(x) = \int_{-\infty}^{+\infty} f(x')\, g(x - x')dx'. \tag{2.1}$$

Cross-Correlation

Similar to the convolution, the cross-correlation takes the integral of the pointwise multiplication of f and the complex conjugate of g:

$$(f \otimes g)(x) = \int_{-\infty}^{+\infty} f(x')\, g^*(x - x')dx'. \tag{2.2}$$

The autocorrelation is the cross-correlation of the function f with itself:

$$(f \otimes f)(x) = \int_{-\infty}^{+\infty} f(x')\, f^*(x - x')dx'. \tag{2.3}$$

The Fourier Transform

The Fourier transform is the expression that decomposes a function f into the frequencies that constitute it. The definition of the Fourier transform $\tilde{f}(q)$ of an integrable function $f(x)$ is given by:

$$\mathcal{F}[f(x)] = \frac{1}{\sqrt{2\pi}} \int_{-\infty}^{+\infty} f(x) \exp[-iqx]\, dx = \tilde{f}(q). \tag{2.4}$$

The inverse Fourier transform is:

$$\mathcal{F}^{-1}[\tilde{f}(q)] = \frac{1}{\sqrt{2\pi}} \int_{-\infty}^{+\infty} \tilde{f}(q) \exp[+iqx]\, dq = f(x). \tag{2.5}$$

The two-dimensional Fourier transform and inverse Fourier transform are:

$$\mathcal{F}[f(x,y)] = \frac{1}{2\pi} \iint_{-\infty}^{+\infty} f(x,y) \exp[-i(qx+py)]\, dxdy = \tilde{f}(q,p), \tag{2.6}$$

$$\mathcal{F}^{-1}[\tilde{f}(q,p)] = \frac{1}{2\pi} \iint_{-\infty}^{+\infty} f(p,q) \exp[+i(qx+py)]\, dqdp = f(x,y). \tag{2.7}$$

The properties of the Fourier transform are particularly useful for signal processing, which is a core principle in diffraction imaging. Parseval's theorem states that the sum of a squared function is equal to the sum of its squared Fourier transform:

$$\int_{-\infty}^{+\infty} |\tilde{f}(q)|^2 dq = \int_{-\infty}^{+\infty} |f(x)|^2 dx. \tag{2.8}$$

The shift theorem states that a translation in real space is equivalent to multiplying by a linear phase factor (or a plane wave) in reciprocal space or a phase ramp:

$$\mathcal{F}(f(x-x_0)) = \frac{1}{\sqrt{2\pi}} \int_{-\infty}^{+\infty} f(x-x_0) \exp[-iqx] dx \tag{2.9}$$

$$= \exp[-iqx_0] \frac{1}{\sqrt{2\pi}} \int_{-\infty}^{+\infty} f(x) \exp[-iqx] dx \tag{2.10}$$

$$= \exp[-iqx_0] \mathcal{F}(f(x)). \tag{2.11}$$

The Fourier transform of the convolution of two real-space n-dimensional functions is equivalent to a multiplication of the two functions in Fourier space:

$$\mathcal{F}(f * g) = (\sqrt{2\pi})^n (\mathcal{F}f \cdot \mathcal{F}g). \tag{2.12}$$

The Fourier transform of the cross-correlation of two real-space functions is equivalent to a multiplication of one function with the complex-conjugate of the second in Fourier space:

$$\mathcal{F}(f \otimes g) = (\sqrt{2\pi})^n (\mathcal{F}f \cdot (\mathcal{F}g)^*). \tag{2.13}$$

The Fourier transform of the autocorrelation of a two-dimensional function is proportional to the squared amplitude of the function in Fourier space.

$$\mathcal{F}(f \otimes f) \; = 2\pi \left[(\mathcal{F}f) \cdot (\mathcal{F}f)^*\right] \; = \; 2\pi \left[|\mathcal{F}f|^2\right]. \tag{2.14}$$

This relation, also known as the Wiener-Khinchin theorem, has a fundamental implication on diffraction imaging, in that the Fourier transform of the autocorrelation of the sample function equals to the power spectrum of the sample.

Differentiation in real space is equivalent to multiplication by a linear function in Fourier space:

$$\begin{aligned} \frac{\partial}{\partial x}\{\mathcal{F}(f(x))\} \; &= \frac{\partial}{\partial x}\left\{\frac{1}{\sqrt{2\pi}}\int_{-\infty}^{+\infty} f(x)\exp[-iqx]dx\right\} \\ &= \frac{1}{\sqrt{2\pi}}\int_{-\infty}^{+\infty}(-iq)f(x)\exp[-iqx]dx \\ &= \mathcal{F}\{(-iq)\cdot f(x)\}, \end{aligned} \tag{2.15}$$

$$\frac{\partial}{\partial x}\{\mathcal{F}^{-1}(\tilde{f}(q))\} \; = \mathcal{F}^{-1}\{(+iq)\cdot \tilde{f}(q)\}. \tag{2.16}$$

For a two-dimensional function:

$$\frac{\partial}{\partial x \partial y}\{\mathcal{F}(f(x,y))\} \; = \mathcal{F}\{(-iq)(-ip)\cdot f(x,y)\}, \tag{2.17}$$

$$\frac{\partial}{\partial x \partial y}\{\mathcal{F}^{-1}(\tilde{f}(q,p))\} \; = \mathcal{F}^{-1}\{(+iq)(+ip)\cdot \tilde{f}(q,p)\}. \tag{2.18}$$

The Delta Function

The Dirac Delta function $\delta(x)$ is a continuous distribution function that is zero everywhere expect at $x = 0$ where it reaches infinity.

$$\delta(x) = \begin{cases} \infty, & \text{for } x = 0 \\ 0, & \text{for } x \neq 0 \end{cases} \tag{2.19}$$

It is infinitesimal in width i.e lim $\delta(x_{0-}) - \delta(x_{0+}) \to 0$ and it is infinitely tall. The integral of the delta function equals exactly 1:

$$\int_{-\infty}^{+\infty} \delta dx = 1. \tag{2.20}$$

The Dirac delta function is also considered as the derivative with respect to x of the Heaviside unit step function:

$$\frac{\partial}{\partial x} H(x) = \delta(x), \tag{2.21}$$

$$\text{where } H(x) = \begin{cases} 1, & \text{for } x \geq 0 \\ 0, & \text{for } x < 0. \end{cases} \tag{2.22}$$

The Dirac delta function is applied to continuous functions and returns a continuous scaled impulse function. The Kronecker delta function differs to the Dirac delta function in that the amplitude is equals unity whereas the integral does not. It is similarly infinitesimally thin but it applies a discrete impulse function to a continuous function and returns the amplitude of the signal.
The scaling property of the delta function:

$$\begin{aligned} \int_{-\infty}^{+\infty} \delta(ax) dx &= \frac{1}{|a|}, \\ \Leftrightarrow \ \delta(ax) &= \frac{\delta(x)}{a}, \end{aligned} \tag{2.23}$$

which means $\delta(x)$ is an even and homogeneous distribution of degree -1 with:

$$\delta(-x) = \delta(x). \tag{2.24}$$

The delta function could be defined as a Lebesgue measure where:

$$\int_{-\infty}^{+\infty} f(x)\delta(dx) = f(0). \tag{2.25}$$

The translation property of the delta function is:

$$\int_{-\infty}^{+\infty} f(x)\delta(x - x_a)dx = f(x_a). \tag{2.26}$$

The Fourier transform of the delta function can be calculated from the Fourier transform of the Heaviside step function with a final derivative along x, and is given by:

$$\mathcal{F}(\delta(x)) = \frac{1}{\sqrt{2\pi}}. \tag{2.27}$$

Convolution of the delta function with a function f:

$$(f * \delta)(x) = f(x) \quad \text{and} \quad (\delta * f)(x) = f(x). \tag{2.28}$$

Cross-correlation of the delta function with a function f:

$$(f \otimes \delta)(x) = f(x) \quad \text{and} \quad (\delta \otimes f)(x) = f^*(-x). \tag{2.29}$$

The translation property combined in the cross-correlation leads to:

$$f(x) \otimes \delta(x - x_0) = f(x + x_0), \tag{2.30}$$

$$\delta(x - x_0) \otimes f(x) = f^*(-x + x_0). \tag{2.31}$$

These properties of the delta function along with the Wiener-Khinchine theorem will provide the fundamentals of Fourier transform holography described later on this chapter.

The Discrete Fourier Transform

Consider the continuous form of the Fourier transform:

$$\mathcal{F}[f(x)] = \frac{1}{\sqrt{2\pi}} \int_{-\infty}^{+\infty} f(x) \exp[-iqx]\, dx = \tilde{f}(q). \tag{2.32}$$

The Fourier transform of a continuous function $f(x)$ can be discretised by sampling the x-space with a fine grid of N samples with Δx intervals such that $f(x) = f(m\Delta x)$ in one dimension. The integration is performed over a limited real-space sample area S_x such that $S_x = N \times \Delta x$. Hence, the Fourier spectrum is also sampled such that $\tilde{f}(q) = \tilde{f}(n\Delta q)$. Similarly the reciprocal-space area S_q equals $N \times \Delta q$. The discretisation of the real space and reciprocal space grid is thus:

$$x = m\Delta x, \quad \text{where } m = 1, 2, 3, \ldots, N; \tag{2.33}$$

$$q = n\Delta q, \qquad \text{where } n = 1, 2, 3, \ldots, N. \tag{2.34}$$

By plugging Eq. 2.33 and Eq. 2.34 in Eq. 2.32, discretising the continuous integral into a digital sum, and performing a change of variable, we obtain the one-dimensional discrete Fourier transform (DFT) of the function f:

$$\tilde{f}(n\Delta q) = \sum_{m=1}^{N} f(m\Delta x) \exp[-i\ m\Delta x\ n\Delta q]. \tag{2.35}$$

The Fast Fourier Transform (FFT) is given by:

$$\tilde{f}(n) = \frac{1}{\sqrt{N}} \sum_{m=1}^{N} f(m) \exp\Big[- i\frac{2\pi}{N}\ m\ n\Big]. \tag{2.36}$$

By comparing Eq. 2.35 and Eq. 2.36, we arrive at the relation:

$$\Delta x \Delta q = \frac{2\pi}{N}. \tag{2.37}$$

The highest frequency of the DFT of f sampled with an interval Δx is:

$$q_N = N\frac{\Delta q}{2}. \tag{2.38}$$

Plugging Eq. 2.37 into Eq. 2.38, we get:

$$q_N = \frac{\pi}{\Delta x}. \tag{2.39}$$

The term q_N is known as the Nyquist frequency defined as the minimum frequency at which the signal $\tilde{f}(q)$ can be sufficiently sampled without introducing errors. Sampling the signal with a frequency of at least twice the Nyquist frequency q_N is known as oversampling. Sampling the signal in Fourier space by twice the Nyquist frequency is equivalent to surrounding the real-space function f by a region of zeros amounting to twice the size of the original array $2 \times N$. This is particularly relevant to coherent diffraction imaging as zero-padding the object function in real space is equivalent to oversampling the Fourier spectrum in reciprocal space, which leads to the correct inversion of the diffraction pattern to the sample image, given initial values of magnitude and phase.

2.2 The Wave Equation

Maxwell Equations

The phenomenon of diffraction of light is a result of the wave nature of light. By definition, light is electromagnetic radiation governed by the Maxwell equations:

$$\nabla \cdot D = \rho \tag{2.40}$$

$$\nabla \cdot B = 0 \tag{2.41}$$

$$\nabla \times H = \frac{\partial D}{\partial t} + J \tag{2.42}$$

$$\nabla \times E = -\frac{\partial B}{\partial t}\ , \tag{2.43}$$

where E is the electric field vector (V/m), H is the magnetic field vector (A/m), J is the current density (A/m^2), ρ is the space charge density (C/m^3), D is the electric displacement field (or flux in C/m^2), and B is the magnetic density field (T) such that:

$$D = \epsilon E, \tag{2.44}$$

$$B = \mu H, \tag{2.45}$$

where ϵ and μ are the electric permittivity and magnetic permeability of the medium respectively, whose values in vacuum are

$$\epsilon_0 = 8.854 \cdot 10^{-12} F/m, \tag{2.46}$$

$$\mu_0 = 4\pi \cdot 10^{-7} N/A^2 \approx 1.256 \cdot 10^{-6} H/m, \tag{2.47}$$

such that the speed of light in vacuum is

$$c = \frac{1}{\sqrt{\epsilon_0 \mu_0}}. \tag{2.48}$$

The divergence of a vector A is given by the Laplacian $\nabla \cdot A$ and the curl is given by $\nabla \times A$ with Cartesian coordinates

$$\nabla \cdot A = \frac{\partial A_x}{\partial x} + \frac{\partial A_y}{\partial y} + \frac{\partial A_z}{\partial z}, \tag{2.49}$$

$$\nabla \times A = \begin{vmatrix} \mathbf{u}_x & \mathbf{u}_y & \mathbf{u}_z \\ \frac{\partial}{\partial x} & \frac{\partial}{\partial y} & \frac{\partial}{\partial z} \\ A_x & A_y & A_z \end{vmatrix}, \tag{2.50}$$

where $\mathbf{u}_x$, $\mathbf{u}_y$, $\mathbf{u}_z$ are the x,y,z unit vectors, and Eq. 2.50 expands as

$$\nabla \times A = \left(\frac{\partial A_z}{\partial y} - \frac{\partial A_y}{\partial z}\right)\mathbf{u}_x + \left(\frac{\partial A_x}{\partial z} - \frac{\partial A_z}{\partial x}\right)\mathbf{u}_y + \left(\frac{\partial A_y}{\partial x} - \frac{\partial A_x}{\partial y}\right)\mathbf{u}_z. \tag{2.51}$$

Considering the diffraction medium to be a uniform, isotropic dielectric medium in which the charge ρ and current density J are zero, the Maxwell equations are reduced to:

$$\nabla \cdot (\epsilon E) = 0 \tag{2.52}$$

$$\nabla \cdot (\mu H) = 0 \tag{2.53}$$

$$\nabla \times H = \epsilon \frac{\partial E}{\partial t} \tag{2.54}$$

$$\nabla \times E = -\mu \frac{\partial H}{\partial t}. \tag{2.55}$$

Solutions to the Wave Equation

Taking the curl of both sides of Eq. 2.54 and Eq. 2.55 and given the identity

$$\nabla \times \nabla \times H = \nabla(\nabla \cdot H) - \nabla^2 H. \tag{2.56}$$

We arrive at the wave equations of the magnetic and electric field

$$\nabla^2 H - \epsilon\mu \frac{\partial^2 H}{\partial t^2} = 0, \tag{2.57}$$

$$\nabla^2 E - \epsilon\mu \frac{\partial^2 E}{\partial t^2} = 0. \tag{2.58}$$

With the electric and magnetic fields sinusoidally oscillating with time-varying dependence, we consider the phasor representation taking into account the frequency-dependent and space-dependent electric permittivity $\epsilon(r)$ [41]. The phasor representation reduces the differentiation $\partial/\partial t$ in the Maxwell equations to a multiplication by jw. The propagating frequency-dependent electric and magnetic fields satisfying

the differential equations Eq. 2.57 and Eq. 2.58 in phasor representation are

$$E(r,t) = \text{Real}|\tilde{E}(r)\exp(jwt)|, \tag{2.59}$$
$$H(r,t) = \text{Real}|\tilde{H}(r)\exp(jwt)|. \tag{2.60}$$

Hence the Maxwell equations in terms of the phasors $\tilde{E}(r)$ and $\tilde{H}(r)$ become

$$\nabla \cdot [\epsilon(r)\tilde{E}(r)] = 0 \tag{2.61}$$
$$\nabla \cdot \tilde{H}(r) = 0 \tag{2.62}$$
$$\nabla \times \tilde{H}(r) = jw\epsilon(r)\tilde{E}(r) \tag{2.63}$$
$$\nabla \times \tilde{E}(r) = -jw\mu\tilde{H}(r). \tag{2.64}$$

The phasor representation reduces the wave equations Eq. 2.57 and Eq. 2.58 to

$$\nabla^2\tilde{H} + \epsilon\mu w^2\tilde{H} = 0, \tag{2.65}$$
$$\nabla^2\tilde{E} + \epsilon\mu w^2\tilde{E} = 0. \tag{2.66}$$

With n being the refractive index of the medium such that,

$$n = \sqrt{\frac{\epsilon}{\epsilon_0}} = c\sqrt{\epsilon\mu}, \tag{2.67}$$

and k being the wave-vector given by

$$k = \frac{nw}{c} = \frac{2\pi}{\lambda}, \tag{2.68}$$

we finally obtain the scalar time-independent wave equation, where Ψ is either the magnetic or electric scalar component of the electromagnetic wave, otherwise known as the *Helmholtz* equation:

$$\nabla^2\Psi + k^2n^2\Psi = 0. \tag{2.69}$$

A solution to the Helmholtz equation is the planar wave

$$\Psi(\vec{r}) = A\exp(i\vec{k}\vec{r}), \tag{2.70}$$

where the wave propagates in a direction parallel to $\vec{k}$ and $\vec{k}\vec{r} = C$ defines the planar wavefront which is orthogonal to $\vec{k}$. A is the complex amplitude and the argument of $\vec{k}\vec{r}$ is the phase.
Another solution to the Helmholtz wave equation is the cylindrical wave where $\vec{k}\vec{r} = k\rho = k\sqrt{x^2 + y^2} = C$ and is given by

$$\Psi(\vec{r}) = A\frac{\exp(i\vec{k}|\vec{r}|)}{\sqrt{|\vec{r}|}}. \tag{2.71}$$

The spherical wave is another solution to the Helmholtz equation where the wave-vector $\vec{k}$ is parallel to the displacement vector $\vec{r}$ which results in a spherical wavefront such that $\vec{k}\vec{r} = kr = k\sqrt{x^2 + y^2 + z^2} = C$ and

$$\Psi(\vec{r}) = A\frac{\exp(i\vec{k}|\vec{r}|)}{|\vec{r}|}. \tag{2.72}$$

From this we can calculate the modulation of an incident planar or spherical wave by a thin film and understand the phase shift and transmission properties as a result, which is discussed in detail in [42, 43]. Consider a time-dependent plane wave of initial amplitude E_0

$$E(\vec{r}, t) = E_0 \exp(-iwt - \vec{k}\vec{r}). \tag{2.73}$$

In x-ray physics, the index of refraction n is expressed as a complex-valued term equal to

$$n = 1 + \delta n = 1 - \delta + i\beta \quad \text{and} \quad k = nw/c, \tag{2.74}$$

where δn corresponds to the change introduced by the specimen or thin film and is non-zero only within the finite region of the specimen, and for all x outside the specimen $\delta n = 0$ [43]. After propagating through a material, the contribution of the non-zero δn arises and we obtain

$$E(\vec{r}, t) = E_0 \ \exp[-iw(t - r/c)] \ \exp[-i(2\pi\delta/\lambda)r] \ \exp[-(2\pi\beta/\lambda)r]. \tag{2.75}$$

The two latter exponential terms are the contributions of the phase shift and the decay respectively. Hence the squared modulus or transmission intensity I and the

decay length l_{abs} are:

$$I = I_0 \exp(-4\pi\beta/\lambda)\Delta r \quad \text{and} \quad l_{abs} = \frac{\lambda}{4\pi\beta}. \tag{2.76}$$

Furthermore, the phase shift introduced by the thin film of thickness Δr, defined as the change in phase of the incident wave as a result of the refraction of the propagating wave by the atoms of the medium, is given by:

$$\Delta\phi = \left(\frac{2\pi\delta}{\lambda}\right)\Delta r. \tag{2.77}$$

Helmholtz Equation in Fourier Space

When studying the wave-field propagation in free-space, it is useful to develop the Helmholtz equation in Fourier space to understand the changes in the near-field and in the far-field and to easily simplify approximations. We recall Eq 2.69:

$$\nabla^2\Psi \; + \; k^2 n^2 \Psi \; = \; 0.$$

With the wave propagating in free space, we find that $\delta n = 0$ and $n = 1$, which leads to the free-space Helmholtz equation:

$$\nabla^2\Psi \; + \; k^2\Psi \; = \; 0. \tag{2.78}$$

By taking the Fourier transform, we obtain:

$$\mathcal{F}[\nabla^2\Psi] + \mathcal{F}[k^2\Psi] = 0 \tag{2.79}$$

$$(2\pi iq)^2\tilde{\Psi} + k^2\tilde{\Psi} = 0 \tag{2.80}$$

$$(k^2 - 4\pi^2 q^2)\tilde{\Psi} = 0, \tag{2.81}$$

where $\tilde{\Psi}$ is the Fourier transform of Ψ. By taking the 2π as part of the reciprocal coordinate q, we can rewrite Eq. 2.81 as

$$(k^2 - q^2)\tilde{\Psi} = 0, \tag{2.82}$$

which gives rise to the notion of the *Ewald sphere*. It has a solution of $\tilde{\Psi} = 0$ except when $|q| = k$. If we separate the components into a transverse component and a parallel component, we find that the wave-field $\tilde{\Psi}$ in reciprocal space occupies a sphere governed by $|q| = k$ where $|q|$ is the modulus of the transverse and parallel components.

Wave Propagation and Small-Angle Scattering

If we separate the coordinates into z, the parallel coordinate, and $r_\perp$, the transverse coordinate [44], we obtain the parallel component of the wave-field Ψ_z and the transverse component of the wave-field $\Psi(q_\perp)$, which represents the scattering. In diffraction imaging, we are interested in observing the scattering of the wave-field, i.e the wave-field component in the transverse plane $\Psi(q_\perp)$. Hence if we perform the Fourier transform of the free-space Helmholtz equation Eq. 2.78 in the transverse plane with r separated into $r_\perp$ and z, we get

$$\begin{aligned} \nabla^2\Psi(r_\perp, z) + k^2\Psi(r_\perp, z) &= 0 \\ \frac{\partial^2}{\partial r_\perp^2}\Psi(r_\perp, z) + \frac{\partial^2}{\partial z^2}\Psi(r_\perp, z) + k^2\Psi(r_\perp, z) &= 0, \end{aligned} \tag{2.83}$$

$$\mathcal{F}_{q_\perp}\left[\frac{\partial^2}{\partial r_\perp^2}\Psi(r_\perp, z)\right] + \mathcal{F}_{q_\perp}\left[\frac{\partial^2}{\partial z^2}\Psi(r_\perp, z)\right] + \mathcal{F}_{q_\perp}[k^2\Psi(r_\perp, z)] = 0 \tag{2.84}$$

$$\begin{aligned} (iq_\perp^2)\tilde{\Psi}(q_\perp, z) + \frac{\partial^2}{\partial z^2}\tilde{\Psi}(q_\perp, z) + k^2\tilde{\Psi}(q_\perp, z) &= 0 \\ -q_\perp^2\,\tilde{\Psi}(q_\perp, z) + \frac{\partial^2}{\partial z^2}\tilde{\Psi}(q_\perp, z) + k^2\tilde{\Psi}(q_\perp, z) &= 0 \\ \left[-q_\perp^2 + \partial_z^2 + k^2\right]\tilde{\Psi}(q_\perp, z) &= 0. \end{aligned} \tag{2.85}$$

The solution of Eq. 2.85 is

$$\tilde{\Psi}(q_\perp, z) = \tilde{\Psi^-}(q_\perp)\exp(-i\kappa z) + \tilde{\Psi^+}(q_\perp)\exp(+i\kappa z), \tag{2.86}$$

where κ is the scattering wave vector such that $\kappa = \sqrt{k^2 - q_\perp^2}$, and $\tilde{\Psi}^-$ and $\tilde{\Psi}^+$ represent the backward and forward scattering terms respectively. The back-scattering term can be neglected as in diffraction experiments we are generally

interested in the wave-field past the sample. Hence we can retrieve the wave-field at the sample plane to understand the behaviour in the near-field and far-field regime by first performing the inverse Fourier transform of Eq. 2.86 without the back-scattering term:

$$\tilde{\Psi}(q_\perp, z) = \tilde{\Psi^+}(q_\perp) \exp(+i\kappa z), \tag{2.87}$$

$$\mathcal{F}^{-1}[\tilde{\Psi}(q_\perp, z)] = \mathcal{F}^{-1}[\tilde{\Psi^+}(q_\perp) \exp(+i\kappa z)], \tag{2.88}$$

$$\Psi(r_\perp, z)] = \mathcal{F}^{-1}[\tilde{\Psi^+}(q_\perp) \exp(+i\kappa z)]. \tag{2.89}$$

By considering the small angle (paraxial) approximation which states that $|q_\perp| \ll k$, we factorise the argument of Eq. 2.89 by k and recall the first-order Taylor expansion series where $\sqrt{(1-a^2)} \to (1-a^2)$ as a tends to 0, and we get

$$\Psi(r_\perp, z) = \mathcal{F}^{-1}[\tilde{\Psi}(q_\perp)] \ \exp[\ iz\sqrt{k^2 - q_\perp^2}\ ] \tag{2.90}$$

$$= \mathcal{F}^{-1}[\tilde{\Psi}(q_\perp)] \ \exp[\ izk\sqrt{1 - q_\perp^2/k^2}\ ] \tag{2.91}$$

$$= \mathcal{F}^{-1}[\tilde{\Psi}(q_\perp)] \ \exp[\ izk(1 - q_\perp^2/k^2)\ ]. \tag{2.92}$$

Eq. 2.92 is the equation of the scattered wave-field in the *paraxial approximation.* By recalling the convolution theorem in real and Fourier space where

$$f * g = \int f(x')\ g(x - x')dx', \tag{2.93}$$

$$\mathcal{F}^{-1}(f \times g) = \mathcal{F}^{-1} f * \mathcal{F}^{-1} g. \tag{2.94}$$

Eq. 2.92 becomes:

$$\Psi(r_\perp, z) = \mathcal{F}^{-1}\{\tilde{\Psi}(q_\perp)\}_{r_\perp} \ * \ \mathcal{F}^{-1} \exp\Big[\ izk\Big(1 - \frac{q_\perp^2}{k^2}\Big)\Big]_{r_\perp} \tag{2.95}$$

$$\Psi(r_\perp, z) = \Psi(r_\perp) \ * \ -\frac{ik}{z} \exp\Big[\ ikz\Big(1 + \frac{r_\perp^2}{2z^2}\Big)\Big]. \tag{2.96}$$

The second part of the convolution in Eq 2.96 is the *Fresnel propagator* $P(r_\perp, z)$,

$$P(r_\perp, z) = -\frac{ik}{z} \exp\Big[\ ikz\Big(1 + \frac{r_\perp^2}{2z^2}\Big)\Big]. \tag{2.97}$$

The convolution of the wavefield with the Fresnel propagator results in the equation of the near-field diffraction, whereby applying the real-space convolution theorem in Eq. 2.94 to Eq. 2.96 we finally get the Fresnel integral

$$\Psi(r_\perp, z) = \frac{-ik}{2\pi z}\exp(ikz)\iint_{-\infty}^{+\infty} d^2r'_\perp\,\Psi(r'_\perp)\exp\Big[\frac{ik}{2z}(r_\perp - r'_\perp)^2\Big]. \tag{2.98}$$

To distinguish between the near-field limit and the far-field limit, it is useful to take the integral in Eq. 2.98 as a Fourier transform in terms of the unit vector $\mathbf{u}= r_\perp/z$ that describes the propagation direction. Hence by replacing $r_\perp/z$ by $\mathbf{u}$, and taking the Fourier transform in terms of $q = k\mathbf{u}$ in Eq. 2.98, we obtain

$$\Psi(z\mathbf{u}, z) = \frac{-ik}{2\pi z}\exp\Big[ikz\Big(1+\frac{\mathbf{u}^2}{2}\Big)\Big]\iint_{-\infty}^{+\infty} d^2r'_\perp\,\Psi(r'_\perp)\exp\Big[\frac{ikr'^2_\perp}{2z} - ik\mathbf{u}\cdot r'_\perp\Big], \tag{2.99}$$

$$\Psi(z\mathbf{u}, z) = \frac{-ik}{z}\exp\Big[ikz\Big(1+\frac{\mathbf{u}^2}{2}\Big)\Big]\mathcal{F}\Big\{\Psi(r'_\perp)\exp\Big(\frac{ikr'^2_\perp}{2z}\Big)\Big\}_{q_\perp}. \tag{2.100}$$

In the far-field limit, at large propagation distances where $z \gg \frac{kr'^2_\perp}{2}$, the term $\exp(kr'^2_\perp/2)$ inside the integral in Eq. 2.99 is reduced to 1. After reducing the terms, Eq. 2.99 then respresents the Fraunhofer integral and the Fourier transform in Eq. 2.100 is reduced to purely that of $\Psi(r'_\perp)$ without the additional phase term. Therefore, the scattering intensity becomes proportional to the squared modulus of the Fourier transform $\tilde{\Psi}(q_\perp)$ in the transverse plane of the wavefield $\Psi(r_\perp)$ at the exit of the specimen. This is the principle of Fraunhofer diffraction according to the paraxial approximation. Satisfying Parseval's theorem in Eq. 2.8, the scattering intensity is given by

$$I(u) \;=\; \Big|\Psi(r_\perp)\Big|^2_{z\to\infty} \;\propto\; \Big|\mathcal{F}\{\Psi(r'_\perp)\}\Big|^2 = \Big|\tilde{\Psi}(q_\perp)\Big|^2. \tag{2.101}$$

As a simplification, we define the Fresnel number as a dimensionless unit which allows us to identify whether we are in the near-field or in the far-field

$$F = \frac{D^2}{\lambda z}. \tag{2.102}$$

Fraunhofer diffraction occurs when $F \ll 1$; and Fresnel diffraction occurs when $F \sim 1$, where D is the characteristic width of the diffracting aperture.

Returning to Eq. 2.74 and Eq. 2.75, we consider the modulation of the wave-field by a thin film with $\delta n \neq 0$. We can use the Helmholtz equation within the small angle approximation and separate the coordinates into $r_\perp$ and z, to find the solution of the wave equation for a limited refractive medium of thickness Δz with $\delta n \neq 0$, such that

$$\frac{\Psi(r, z + \Delta z)}{\Psi_0(r, z)} = \exp\,(ik_0 \delta n_\perp), \tag{2.103}$$

where $\Psi(r)$ is the solution to the wave equation and it is proportional to a function $A(r_\perp)$ that defines the incident wave in the transverse plane and an exponential function of δn that encodes the phase shift and decay induced by the thin film,

$$\Psi(r) = A(r_\perp)\ \exp(\ ik\delta n_\perp\ ), \tag{2.104}$$

where the refractive index along the propagation distance Δz is given by,

$$\delta n_\perp(r_\perp) = \int_{\Delta z} \delta n(r_\perp, z)\ dz. \tag{2.105}$$

We are able to evaluate the optical thickness, which is a measure of the attenuation of the transmitted power through a material at specific x-ray wavelengths, by calculating the value of $|k\delta n_\perp|$. For $|k\delta n_\perp| \ll 1$, the film is considered to be optically thin; and for higher values of $|k\delta n_\perp|$, the film is optically thick.

2.3 Diffraction Imaging

The Phase Problem

As we have shown in the previous section, we are able to calculate the complex wave-field exiting a sample using analytical methods that involve the Fresnel propagator or the Fourier transform for near-field and far-field diffraction respectively, while taking into account a set of approximations. The calculation can be rendered computationally inexpensive by digitising the continuous Fourier transform into

the Discrete Fourier Transform (DFT) and rapidly processed through the Fast Fourier Transform (FFT). Therefore, theoretically we could recover the object wave from the complex-valued scattered wave-field at a distance z using a simple FFT. However, in practice, experimental diffraction imaging methods use detectors to record the intensity distribution of the projected diffraction patterns. As Eq. 2.101 shows, the intensity is the squared modulus of the wave-field. While detectors can only record the intensity and not the complex-valued scattered wave-field, the phase information is lost. Hence the wave-field at the exit of the object can not be directly reconstructed by a Fourier transform. This notion is known as the *phase problem* [11]. Nevertheless, the Wiener-Khinchin theorem [45] shown in Eq. 2.14 states that the Fourier transform of the autocorrelation of the sample equals the power spectrum of the sample. In other words, by applying an inverse Fourier transform to the recorded intensity distribution (or power spectrum), we obtain the autocorrelation of the sample 4

$$\mathcal{F}^{-1}\{I\} = \mathcal{F}^{-1}\{\tilde{\Psi} \cdot \tilde{\Psi}^*\} = \Psi \otimes \Psi. \tag{2.106}$$

One way to circumvent the phase problem is using iterative numerical methods that involve providing an initial guess of the phase and limiting the amplitude of the object by means of a mask. The iterations go from real-space to reciprocal space by performing a Fourier transform and an inverse Fourier transform back and forth while applying regularisation filters until the phase and amplitude converge to the correct values thus reconstructing the sample complex wave-field. This method requires oversampling and zero-padding [13, 46], as well as imposing tight constraints onto the amplitude information of the sample. These factors affect the uniqueness and unambiguity of solution and the iterative process could be computationally expensive.

Another method to overcome the phase problem that does not involve iterative numerical methods is holography, whose virtue lies in the fact that the object wave interferes with a reference wave that encodes the phase information. However, by taking advantage of the Wiener-Khinchin theorem, Fourier transform Holography rises as an alternative method that allows direct retrieval of the complex wave-field of the sample.

Holography

Holography was introduced by Dennis Gabor [25] in 1948 as a novel method for lensless imaging. The method originally called "wavefront reconstruction" was an alternative to imaging a sample without the use of lenses hence relieving the limit of the optical element. Holography is based on interference of coherent light and is achieved by adding a spherical or planar wavefront of known amplitude and phase (the reference) to the unknown wavefront corresponding to the scattering of the illuminated sample. This is illustrated in Figure 2.1 and can be demonstrated as follows. Consider the scattered object wave U(x,y) expressed in Cartesian coordinates as

$$U(x,y) = |U(x,y)| \exp[i\phi(x,y)], \tag{2.107}$$

and a reference wave R(x,y) expressed as

$$R(x,y) = |R(x,y)| \exp[i\phi'(x,y)]. \tag{2.108}$$

The interference of the reference wave and object wave is recorded as an intensity distribution $I(x,y)$ resulting from the sum of the two waves such that

$$I(x,y) = |U(x,y)|^2 + |R(x,y)|^2 + 2|U(x,y)||R(x,y)| \cos[\phi'(x,y) - \phi(x,y)]. \tag{2.109}$$

The first two terms in Eq. 2.109 depend on the intensities of the object wave and reference wave whereas the third term includes $cos(\phi' - \phi)$ which gives the relative phase of the two waves. Compared to diffraction imaging techniques, this essentially demonstrates how holography encodes the object phase information in the recorded intensity distribution as a result of the interference (summation) of the object wave and reference wave. When holography was invented, photographic film plates were (and still are sometimes) used to record the interference patten. The amplitude transmittance $t(x,y)$ at the photographic plate depends on a factor β related to the response curve of the film and the type of transparency. Assuming that the intensity of the reference wave $|R|^2$ is constant throughout the film material, we can assume that the transmittance of the recorded plate is

$$t(x,y) = t_b + \beta'[|U(x,y)|^2 + R(x,y)^* U(x,y) + R(x,y)U(x,y)^*], \tag{2.110}$$

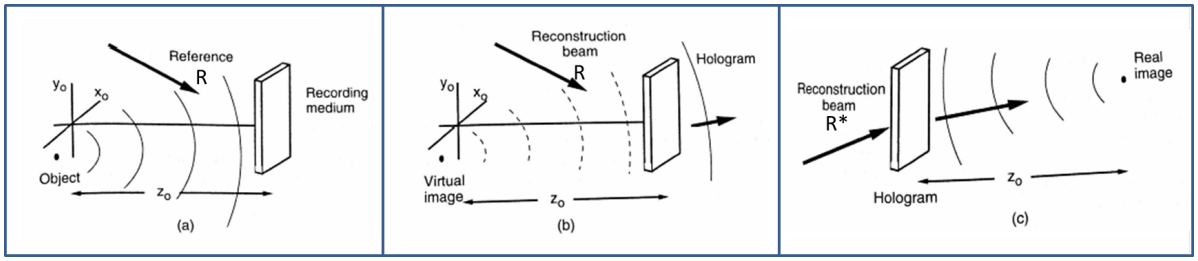

Figure 2.1: Illustrating schematic of holography and and the reconstruction procedure (schematic taken from Ref [42]).

where t_b is the bias transmittance due to the exposure of the constant reference wave. Using photographic films, the reconstruction is performed by coherently illuminating the recording medium with a reconstruction wave $R'(x, y)$ after the object wave information has been recorded. Hence we obtain

$$\begin{aligned} R'(x,y)t(x,y) &= t_b R' + \beta'|U|^2 R' + \beta' R^* R' U + \beta' R R' U^* \\ R'(x,y)t(x,y) &= A_1 + A_2 + A_3 + A_4. \end{aligned} \tag{2.111}$$

If R'(x,y) is identical to R(x,y) as shown in Figure 2.1(b), we get

$$A_3 = \beta'|R|^2 U(x,y). \tag{2.112}$$

If R'(x,y) is equal to the complex conjugate of R(x,y) (Figure 2.1(c)), we get

$$A_4 = \beta'|R|^2 U^*(x,y). \tag{2.113}$$

Thus we find that the terms of interest A_3 and A_4 are equal to the object wavefront U(x,y) with a multiplicative constant due to the the constant intensity of the reference wave. Furthermore, this leads us to the statement that holography is an image-forming method (Figure 2.2). This can be illustrated by considering the object wave to be a spherical wave emerging from the object coordinates (x_0, y_0, z_0) and replacing the expression of U(x,y) in the terms A_3 and A_4 such that

$$U(x,y) = U_0 \ \exp\left[jk\sqrt{((x-x_0)^2 + (y-y_0)^2 + z_0^2)}\right]. \tag{2.114}$$

When the reconstruction wave R'(x,y) is taken to be identical to the reference wave R(x,y), the term A_3 is proportional to the object wave that is seen to originate from

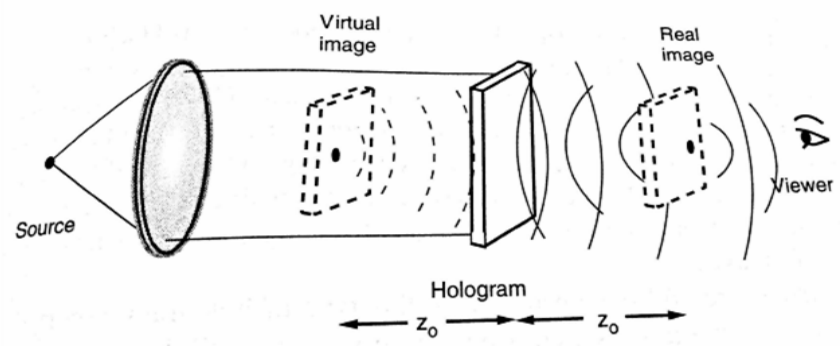

Figure 2.2: Formation of twin images by inline holography (photo from Ref [42]).

a virtual image of the object at the original position z_0 of the object. Similarly, when R'(x,y) = R*(x,y), the term A_4 forms a real image of the object at a position z_0 on the opposite side of the recording medium according to the expression

$$\begin{aligned} A_4(x,y) &\propto |R|^2 U^*(x,y) \\ A_4(x,y) &\propto |R|^2 U_0^* \ \exp\left[jk\sqrt{((x-x_0)^2+(y-y_0)^2+z_0^2)}\right]. \end{aligned} \tag{2.115}$$

Nowadays, we utilise detectors to record the holographic intensity distributions and employ computers to perform the reconstructions. Analogous to the post-illumination of the photographic film by a reference wave, we multiply the recorded array by a quadratic phase factor or apply a near-field propagation back to the plane of the virtual image and forth to the plane of the real image.

In Gabor holography, the reference wave represents the directly transmitted light through a highly transmissive object. The transmitted planar wave and the scattered object wave interfere to produce an intensity distribution that encodes both the phase and amplitude of the scattered object wave as in Eq. 2.109. Hence the "source" of the reference wave and the source of the object are aligned on the same optical axis. Therefore, Gabor or inline holography generates simultaneous real and virtual images of the object transmittance both aligned on the optical axis and separated by a distance $2z_0$. When the real image is brought into focus, it overlaps the out-of-focus virtual image. This is known as the twin image problem. Experimental methods are available to disentangle the twin images, which can also be achieved computationally using specialised algorithms.

A number of experimental methods emerged to solve the twin image problem, mainly circling the notion of *off-axis holography*. *Leith-Upatnieks holography* uses a prism to deflect the reference source from the optical axis thus misaligning the object and the reference and breaking the inline geometry. Holographic methods that involve using a reference source that is laterally offset from the optical axis are broadly named off-axis holography. As such, the twin images are formed away from the optical axis, and the reconstruction wave set at a specific angle separates the two. Hence, this procedure overcomes the overlap of the two twin images. Furthermore, Leith and Upatnieks extended the method to achieve three-dimensional imaging. By splitting the reference beam using a mirror, the different angles of the object can be visualised by changing the viewing angle, thus demonstrating that hologram retains the three-dimensional information of the object, which can be retrieved by varying the propagation direction of the reconstruction wave.

Limitations and Comparison

In general there are practical limitations to standard inline and off-axis holography techniques. For example, inline Gabor holography requires that the sample transmissivity be high enough to allow the direct reference beam to penetrate through and to satisfy the assumption that the A_2 term is negligable with respect to the reconstruction terms A_3 and A_4. Many of the classical holographic techniques use optical components (mirrors, lenses, prisms) that define or deflect the reference beam, or that are even used to form the real holographic image. The optical elements introduce aberrations (spherical, chromatic, astigmatism, distortion, coma) and thus distort the reference beam and affect the image quality. In addition, being an interferometric technique, it is necessary that all path-length differences of the interfering waves are shorter than the coherence length and are kept stable during exposure to ensure best visibility of the interference fringes.

Furthermore, it is important to understand how the object information is encoded compared to Fraunhofer diffraction imaging. For example, in the case where the reference is a diverging spherical wave or a planar wave interfering with the object wave in an inline or off-axis scheme, and the detector plane lies within the Fresnel region (as in Gabor or Lieth-Upatnieks holography), we obtain a Fresnel

hologram. In this case, the amplitude and phase information of each point in the object plane is encoded into the Fresnel hologram. In such a setup, the resolution is limited by the numerical aperture (NA) of the signal detected at the highest angle with respect to the optical axis, which is related to the opening angle of the diverging spherical reference wave. The phase and amplitude information of each point in the object plane is encoded into the Fresnel hologram in the form of frequency-chirped sinusoidal fringes, analogous to the function of a sinusoidal zone-plate composed of an entire range of spatial frequency components.

In CDI however, the object is illuminated by a monochromatic uniform planar wave and the scattered object wave is recorded in the far-field as a Fraunhofer diffraction pattern where the relation between the object plane and the detector plane is a Fourier transform within the paraxial approximation. In contrast to the Fresnel hologram, the information of each object point is encoded into the diffraction pattern in the form of sinusoidal fringes of constant spatial frequency that is unique to that object point. Neglecting the phase problem and computational constraints, in lensless diffraction imaging the resolution is ideally diffraction-limited, i.e it is limited by the maximum scattering angle of the sample which determines the maximum observable momentum transfer wave number q_{max}.

We are interested in achieving a method that makes most efficient use of the space-bandwidth product of the imaging system. This could be accomplished by combining three attributes of the aforementioned methods into one imaging system:
a) Diffraction-limited performance: diffraction imaging of an illuminated sample to maintain the Fourier transform relation between the object plane and the detector plane, within the paraxial approximation, and capturing the maximum scattering angle of the sample;
b) Overcoming the phase problem: achieving non-iterative direct retrieval of the amplitude and phase of the object function by means of a holographic setup;
c) Lensless imaging: using no image-forming lenses (no lenses past the sample) hence avoiding lens-related aberrations that limit the reconstructions.

These attributes are combined through a hybrid method based on Fourier Transform Holography which is discussed in the following section.

2.4 Fourier Transform Holography

Fourier Transform Holography (FTH) emerges as a method that combines the advantages of CDI and holography, where diffraction patterns of a sample that consists of an object and an off-axis holographic reference are recorded in the far-field [28, 29, 30]. The method takes advantage of the Wiener-Khinchin theorem [45] that states that the Fourier transform of the autocorrelation of the sample equals the power spectrum of the sample. The reconstruction procedure is direct and non-iterative and involves a single inverse Fourier transform.

General Formulation

The basic principle of FTH is to include a pinhole or point-scatterer in the vicinity of the object to provide an off-axis reference wave that will result in holographic interference. We consider a sharp pinhole whose transmission function $r(x, y)$ is approximated to the delta function. The one-dimensional expression of the complex wave-function at the exit of the sample plane z is hence

$$\Psi(x) = r(x - x_0) + o(x), \tag{2.116}$$

where $o(x, y)$ is the function of the sample, $r(x - x_{,}y - y_0)$ is the function of the reference placed at x_0, y_0 with respect to the sample, and the summation of the two wave-functions represents the superposition or interference of the two waves. By approximating the reference function to a delta function we get

$$\Psi(x) = \delta(x - x_0) + o(x). \tag{2.117}$$

When the sample plane is illuminated by a monochromatic, uniform, parallel wave, the intensity distribution of the far-field diffraction pattern $I(x, y)$ is equal to the squared modulus of the Fourier transform of the sample wave-function Ψ:

$$I(q) \;=\; \Big|\mathcal{F}\{\Psi(x)\}\Big|^2 = \Big|\tilde{\Psi}(q)\Big|^2. \tag{2.118}$$

The Fourier transform of the autocorrelation is given by

$$\mathcal{F}(\Psi \otimes \Psi) \;\propto\; [\mathcal{F}\{\Psi(x)\} \cdot \mathcal{F}\{\Psi(x)\}^*], \tag{2.119}$$

where the proportionality is a multiplicative factor $\sqrt{2\pi}^n$ where n is the dimension number. Using Eq. 2.118, we find that the intensity distribution is equal to the Fourier transform of the autocorrelation of the sample wave-function:

$$I(q) \propto \mathcal{F}\{\Psi(x) \otimes \Psi(x)\}. \tag{2.120}$$

Thus we retrieve the autocorrelation function of the original real-space wave-field of the sample by applying a IFFT to the recorded intensity distribution as

$$\mathcal{F}^{-1}\{I(q)\} \propto \Big(\Psi(x) \otimes \Psi(x)\Big). \tag{2.121}$$

The implications of Eq. 2.121 form the basis of FTH. When Ψ is tailored such that it is composed of the sum of a delta-like reference function and an object function, Eq. 2.121 results in the direct retrieval of the original complex-valued function of the sample o(x,y). This is due to the sifting property of the delta function. By taking the autocorrelation of Eq. 2.117, and taking $\delta(x - x_0) = \delta_{x_0}$, and $o(x) = o_x$, denoting the reference offset from the center by $x - x_0$, we get

$$\begin{aligned} \Psi \otimes \Psi &= (\delta_{x_0} + o_x) \otimes (\delta_{x_0} + o_x) && (2.122)\\ &= \delta_{x_0} \otimes \delta_{x_0} + o_x \otimes o_x + o_x \otimes \delta_{x_0} + \delta_{x_0} \otimes o_x && (2.123)\\ &= A_1 + A_2 + A_3 + A_4. \end{aligned}$$

The third and fourth terms in Eq. 2.123 are the important part of the result as the cross-correlation of the delta function with another function returns that same function but at shifted coordinates such that

$$A_3 = o(x) \otimes \delta(x - x_0) = o(x + x_0) \tag{2.124}$$

$$A_4 = \delta(x - x_0) \otimes o(x) = o^*(x - x_0). \tag{2.125}$$

Therefore Eq. 2.123 becomes

$$\Psi \otimes \Psi = \mathcal{F}^{-1}\{I(q)\} = (\delta \otimes \delta)(x) + (o \otimes o)(x) + o(x + x_0) + o^*(x - x_0), \tag{2.126}$$

where the terms $o(x + x_0)$ and $o^*(x - x_0)$ represent the reconstruction of the object wave-field (or the separated holographic twin images) located centro-symmetrically with respect to each other at a distance $\pm x_0$ from the center. In the classical

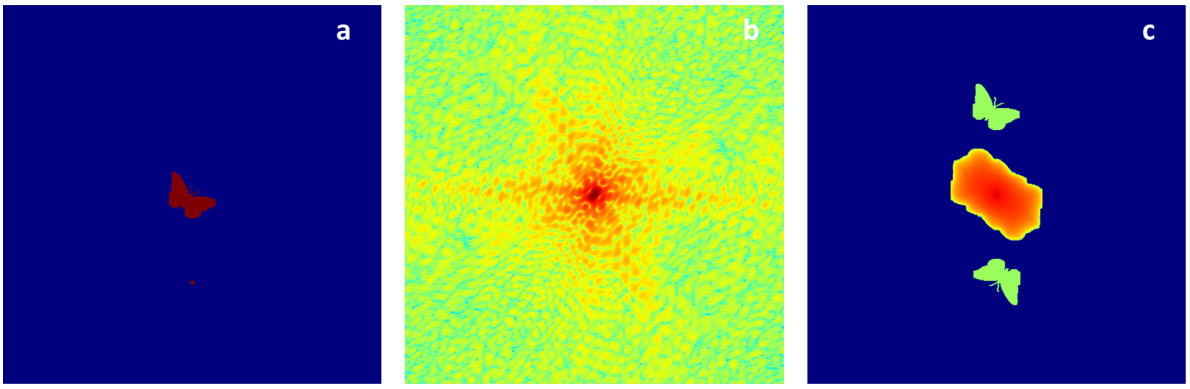

Figure 2.3: Simulation of FTH with a single pinhole reference. (a) FOV in the object plane showing the butterfly sample and an offset pinhole, (b) simulated Fraunhofer diffraction pattern, (c) reconstructed FOV obtained by taking IFFT of (b) showing the reconstructed twin images of the sample.

holographic cases discussed in the previous section, the twin images appear at different planes $\pm z$ due to the reference source and the object being separated in z. In comparison, in the FTH case, the twin images are both reconstructed in the same plane due to the fact that reference and object are coplanar.

This result is the basis of FTH and practically means that if the sample is surrounded by a sharp point-scatterer or pinhole that mathematically approximates to a delta function, one can directly and non-iteratively reconstruct the complex-valued function of the sample by applying an inverse Fourier transform (IFFT) to the recorded intensity distribution. It is important to note that the approximation of the reference function to a delta peak is an ideal limit and can not be practically achieved. For this reason, we must assume that the realistic representation of the physical parameters of the reference is expressed as the function d which when convoluted with the delta-function results in a sharp peak serving as the reference function. The parameters that define the function d are the width of the reference point, the transmission amplitude representing the height of the peak, and the area of the reference which dictates the transmitted flux of the reference. Since the convolution and the cross-correlation are interrelated through the complex-conjugate, the contribution of the convoluted reference function $r = \delta * d$ to the

autocorrelation $\psi(= r + o) \otimes \psi$ leads to the same object reconstruction terms as previously shown in Eq. 2.126 but with a realistic representation.

We simulated a binary test object shaped like a butterfly with a single-pixel wide reference "pinhole" placed above it. The simulation, shown in Figure 2.3 takes a surrounding area of zero transmission and both the object and pinhole of unity transmission. This is analogous to an experimental case where the object and pinhole represent apertures that are milled through a fully absorbing substrate. This is to simulate an ideal and simple binary example where we will see later on how deviations from this scenario affect the results. The simulated intensity distribution resulting from the the binary butterfly and the single-pixel reference is shown in Figure 2.3(b) where the photon energy was taken as 9 keV, the pixel size as 55 μm, and the propagation distance as $14.5m$ which fulfills the Fraunhofer limit. The reconstructed field of view in Figure 2.4(c) is 33 μm and is obtained by taking the IFFT of the intensity distribution. The reconstruction represents the autocorrelation of the sample that consists of the object and reference. As expected, we find a structure in the center twice the size of the object that represents the autocorrelation of the object (the A_2 term), overlapping with a faint peak which represents the autocorrelation of the reference. At a distance $(x \pm x_0, x \pm y_0)$ from the center, we find two mirror-flipped complex-conjugate images of the object. The images are well separated from the contributions of $o \otimes o$ and $\delta \otimes \delta$ due to the sufficient offset of the reference position with respect to the object position in the original sample plane. In order to avoid overlap between the four contributions, a set of separation conditions is established and will be discussed in the next section.

Resolution and SNR

Since the reconstruction of the object is a result of the cross-correlation of its wave-function with that of the reference, the image resolution is thus limited by how close the reference function approximates to a delta function. When the reference point is infinitely sharp, it resembles a delta function, and generates the highest resolution. Therefore, the image resolution is directly proportional to the width of the reference point. On the other hand, the image contrast is proportional

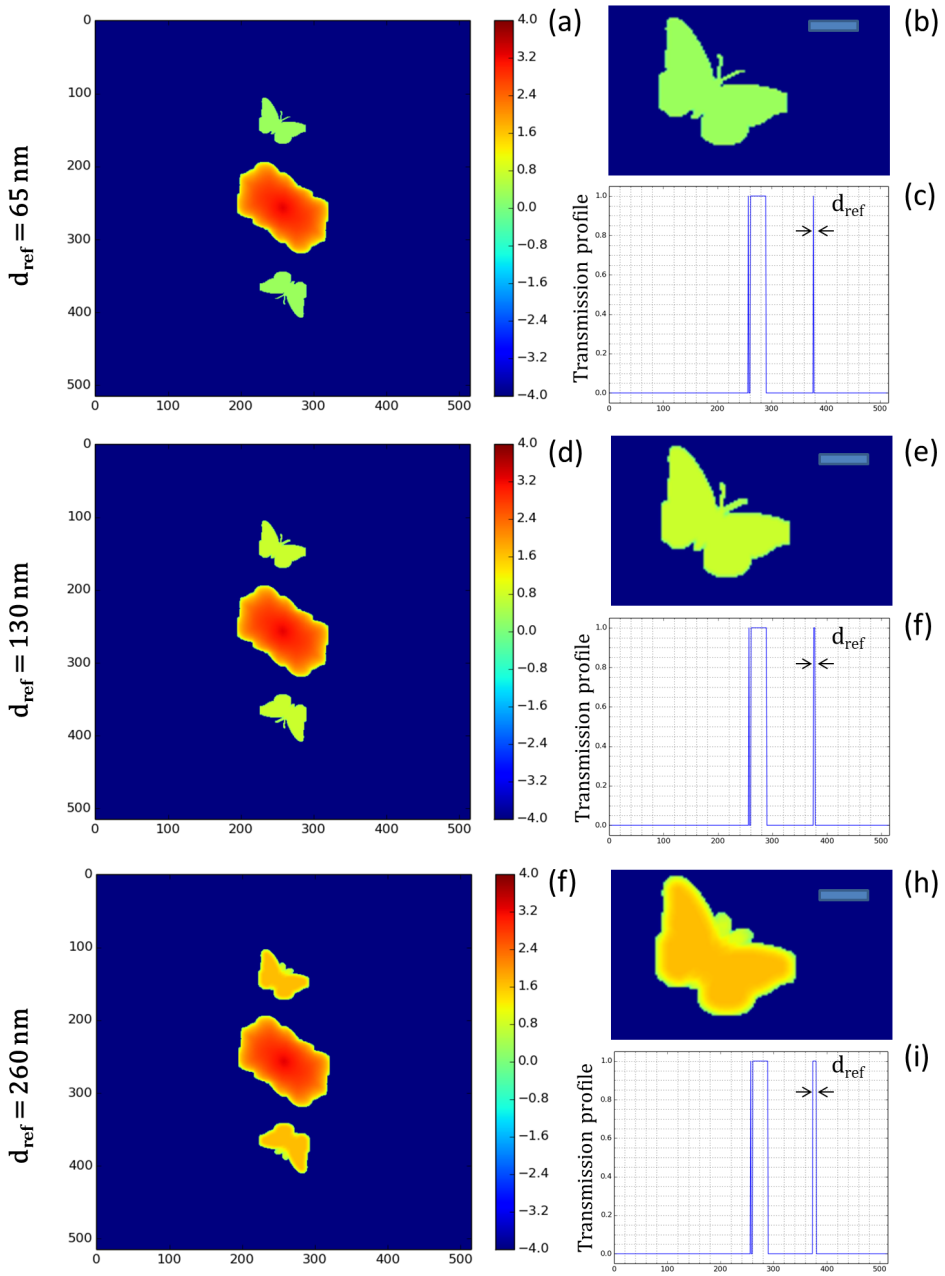

Figure 2.4: The effect of increasing reference diameter on resolution and contrast. (a,d,f) reconstructed FOV obtained with increasing reference size with diameter: 65 nm (1 px), 130nm (2 px), and 260nm (4 px) respectively; (b,e,h) magnified inset of reconstructions in (a,e,h); (c,f,i) profile plot of transmission profile in the object plane cutting through the sample edge and across the pinhole, illustrating the change from delta-like function to a narrow top-hat function.

to the total transmitted flux through the reference area. The amplitude strength of the reference wave increases with higher surface area of the reference. Inversely, the signal strength of the reference wave decreases with smaller reference sizes, which affects the noise statistics of the reconstructed image. This implies that the signal-to-noise ratio (SNR) is thus inversely proportional to the square of the pinhole diameter. Therefore, we conclude that the resolution and SNR are inversely coupled together in relation to the reference diameter. The smaller the reference diameter is, the higher the resolution but the lower the SNR and contrast. In other words, FTH using a single pinhole reference suffers a trade-off between resolution and SNR/contrast which is illustrated in Figure 2.4.

The simulation compares the resulting object reconstruction with an increasing reference diameter $\mathrm{d_{ref}}$. We compare three cases: $\mathrm{d_{ref}} = 65nm$, roughly 1 pixel wide, $\mathrm{d_{ref}} = 130nm$, and $\mathrm{d_{ref}} = 260nm$. The transmission profile across the reference and object in the original sample plane is plotted for the three cases in Figure 2.4(c,f,i) where we observe $\mathrm{d_{ref}}$ increasing until it resembles more of a narrow top-hat function than a peak. Note that a realistic case involves a Gaussian profile of the reference transmission function, but for simplicity we neglect this in the simulation and assume an ideal case. The reconstructed field of view corresponding to the autocorrelation $\psi \otimes \psi$ of the three cases is shown in Figure 2.4(a,d,f) and the respective magnified crop-out of the $o \otimes r$ twin image in Figure 2.4(b,e,h). The reconstruction in Figure 2.4(b) corresponds to the finest-width reference and exhibits the highest resolution compared to the other two cases. As $\mathrm{d_{ref}}$ increases, we observe the resolution beginning to deteriorate as the antennas and the sharp edges of the butterfly become blurred out. In addition, we observe the intensity of the reconstructed object to be the lowest for the smallest $\mathrm{d_{ref}}$ which illustrates lower contrast. In these simulations, we do not include poisson noise, hence it is difficult to see the effect of $\mathrm{d_{ref}}$ on the SNR but we can demonstrate it as follows.

Guizar fully develops the signal-to-noise analysis of FTH as well as holography using extended references in his thesis [47] and compares the normalised squared error for different types of references, which will prove to be useful to our further work with extended references in the next chapter. In the case of the

point-reference FTH, the normalised squared error of the reconstruction is

$$E^2 \approx \frac{MN}{\phi\pi^2\rho_x^2\rho_y^2},, \tag{2.127}$$

where (M,N) are the dimensions of the reconstructed array, ϕ is the sample flux or the number of detected photons transmitted through the sample area, and $\pi^2\rho_x^2\rho_y^2$ is the area of the point-reference of width ρ_x and ρ_y. Note that E^2 only accounts for the statistical noise and does not include the effect of loss in resolution. E^2 is the inverse of the signal-to-noise ratio of the reconstructed image. As expected, it is apparent that the error is inversely proportional to the flux. In addition, E^2 is inversely proportional to the reference area, which validates our discussion that the decrease in reference size leads to an increased error and hence a lower SNR.

Reconstructed Area and Oversampling

The positions and sizes of the components in the object plane as well as the experimental parameters $(\lambda, N, \Delta_s, z)$ all take part in defining the reconstructed field of view (FOV) in FTH. The pixel size in the object plane is given by:

$$p_{obj} = \frac{z\lambda}{N\Delta_s}, \tag{2.128}$$

where Δ_s is the detector pixel size, N is the number of pixels, z is the propagation distance from the sample to the detector, and λ is the wavelength. The size of the detector array (or the screen) in one dimension is given by

$$S_q = N \times \Delta_s. \tag{2.129}$$

The size of the reconstructed area S_o in the object plane (or the field of view in microscopy terms) which is sampled by N pixels in one dimension is given by:

$$S_o = N \times p_{obj} = \frac{z\lambda}{\Delta_s}. \tag{2.130}$$

The implication of this for a successful implementation of FTH is that the sizes and separation distances of the object and reference should be such that their corresponding autocorrelation and cross-correlation images are fitting within the

reconstructed FOV S_o. The oversampled object area which is the maximum area sampled with the Nyquist frequency at the given set of parameters is hence:

$$S_{Ny} = S_o/2. \tag{2.131}$$

What this means in practicality is that the sample area consisting of the object and reference, or the separation distance between the object and the single reference, must be within the oversampling limit S_{Ny}.

Figure 2.5 shows the variation of the reconstructed field of view as a function of the energy and the propagation distance z (applicable to x-ray energies and z-distances available at the X-ray Coherent Imaging Beamline *I13-1* at Diamond Light Source, UK). As we shall see in the following chapter discussing experimental results, the optimal photon energy used is between 8 keV and 9.7 keV and the propagation distance was taken as the maximum distance in the hutch $z = 14.5$ m, i.e the blue curve, which results in a maximised reconstructed FOV between 30 μm and 40 μm for the given energies.

Separation Conditions

The geometrical conditions of the object and reference in the sample plane for a successful FTH reconstruction (for a single point-reference) such that all the cross-correlation and autocorrelation contributions in the reconstructed area are separated are as follows:

a) $(4 \times L_o) \leq S_o$ along one direction; where L_o is the length of the object. That is to say that we need to fit the object autocorrelation of size $2 \times L_o$ plus two twin images of size L_o each in the area S_o;

b) $(x_o - x_r) \geq 3L_o/2$, where x_o and x_r are the positions of the object and reference respectively. This essentially means that the lateral separation distance between the object and the reference must be large enough in order that the central autocorrelation of the object does not overlap with the cross-correlation twin images in one direction;

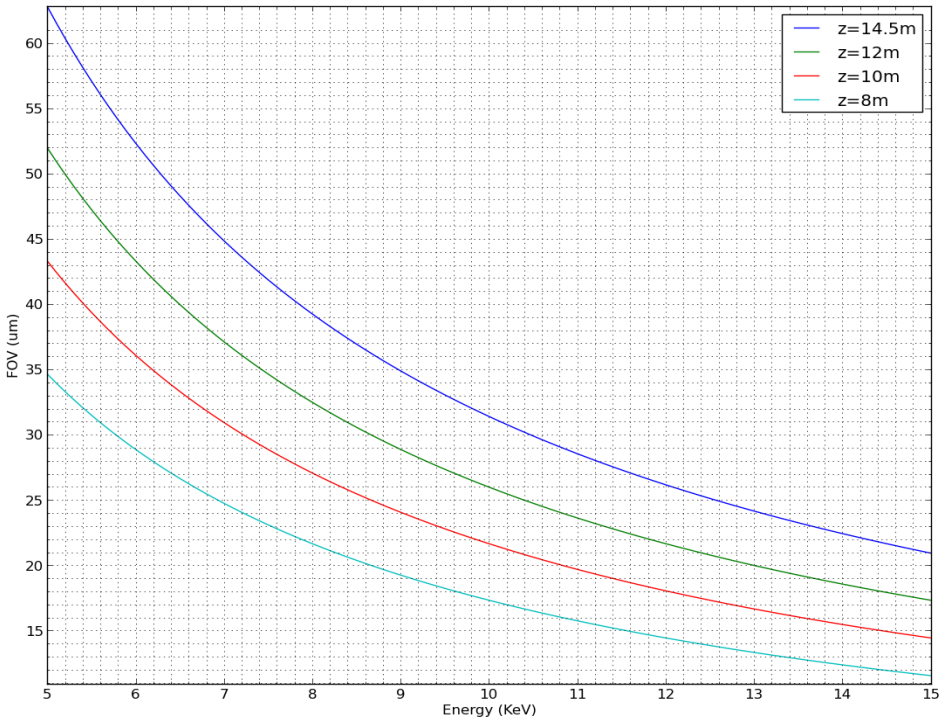

Figure 2.5: Reconstructed object area S_o as a function of energy for a fixed detector pixel size of 55 μm plotted for different propagation distances.

c) $(x_{r_1} - x_{r_2}) \geq L_o$ in the case of more than one reference point, or an extended reference, the distance between two consecutive reference points (or corner edges) $(x_{r1} - x_{r_2})$ must be at least the size of the object L_o to avoid overlap between the consecutive cross-correlation reconstructions.

Three more conditions must be maintained that are irrelevant to the separation conditions of the cross-corrlations and autocorrelations but have more to do with the experimental conditions:

d) $L_c \geq (x_o - x_r)$, meaning that the lateral coherence L_c must be larger than the combined size of the object and reference, or the separation between them (and extends automatically for more references at larger separation distances). This is to ensure coherent interference between the signals;

e) $S_{Ny} \geq (x_o - x_r)$, which means that the separation distance, or the size of the object-reference area must not be larger than the required oversampled area.

This is to ensure sufficient sampling of the interference signal;

f) the illumination profile of the incident beam must be flat, uniform, homogeneous, and sufficiently intense within a diameter of at least $x_o - x_r$.

Note that in some cases the separation condition (b) can be neglected. It is important to estimate the amplitude strength of the term $o \otimes r$ with respect to $o \otimes o$. In a case where the signal strength of the reference is much higher than that of the object, the intensity of $o \otimes o$ appears to be very faint with respect to the holographic twin images resulting from $o \otimes r$ and $r \otimes o$. Therefore, in such a case, condition (b) that states (that the reference must be sufficiently separated from the object in order not to overlap the central autocorrelation with the cross-correlations) can be neglected. An example of such a scenario is shown experimentally in Chapter 5 where the source of the reference was a high-efficiency zoneplate.

2.5 Extended-Reference Holography

The Linear Differential Operator (LDO) simplifies the reconstruction procedure and allows to generalise the application of FTH to a wide variety of reference shapes. The concept was demonstrated in the work of Guizar [36, 47] and Podorov and Enders [40, 48]. Guizar coined the term HERALDO which means holography with extended references by autocorrelation linear differential operations and proved that the method can be furthered by using extended references such as a slit, corner, parallelogram, or virtually any shape that contains sharp corners. For each type of reference, there exists a LDO which results in complex-valued reconstructions of the object similar to the case of point-reference FTH. The boundary waves generated by the edges of the extended structure serve as the reference wave. By applying a directional derivative along a direction specific to the edges, the edge functions are reduced to delta-like peaks, and hence we remain within the working principle of FTH. HERALDO can be considered as an extension of FTH with a point-reference, or inversely the latter can be considered as a special case of the former. The purpose of applying such a method lies within the resolution/SNR trade-off inherent to the single-point FTH technique [30]. To overcome the loss of SNR with

increased resolution, some methods involved using multiple point-references [31, 20] and averaging the total reconstructions. Other methods [32, 33] involve using a Uniformly Redundant Array (URA) [49] as the source of the reference wave, which is an array of pinholes that leads to a higher total signal strength of the reference wave. However, these methods are challenged by experimental constraints, since the FOV is effectively much larger, which means much higher coherence length is needed and the oversampling condition then requires much finer sampling due to the large object area. In turn, if these conditions are satisfied, they transform into constraints on the sample, which means that for the aforementioned conditions to be met, a much smaller and isolated sample can only be used. It affects the choice of sample and hence hinders the diverse applicability of the method. In addition, applications are mostly restricted to optical lasers and soft x-ray radiation where it is relatively easy to fabricate such structures. Although the URA method provides reconstructions with higher SNR, the fabrication requirements are more stringent, and apriori knowledge about the URA matrix is required.

However, with the development of HERALDO, we benefit from high reference flux due to the extended area of the reference thus increasing the SNR substaintially as well as maintaining high-resolution as it becomes governed by the edge sharpness, which is more easily fabricated than a sharp milled pinhole. Hence, this method opens a door to applications with high energy x-rays and other radiation wavelengths since the reference structure and properties can be customised to one's experimental needs. In addition, the method relaxes some of the separation conditions as for example, in the case of a large area reference such as a square or extended polygon. With such a reference, the object may lie within the reference area, and successful reconstructions are still obtained without worrying about the separation conditions. If the transmissivities of the object and reference are appropriate to comply with such a scenario, the fact that they are no longer required to be separated relaxes the constraints on the coherence length, oversampling area, and permits smaller illumination areas. These, among many other benefits that will be revealed throughout the thesis, create a new ground for imaging at various wavelengths and open the door to further developments and applications in the field of holographic imaging.

The Linear Differential Operator

Let us consider a reference structure of function $r(x, y)$, which for now remains as an arbitrary shape consisting of at least one sharp feature at a distance from the object $o(x, y)$. Let $\mathcal{L}^{(n)}\{\}$ be a linear differential operator given by

$$\mathcal{L}^{(n)} \equiv \sum_{k=0}^{n} a_k \frac{\partial^n}{\partial x^{n-k}\, \partial y^k}, \tag{2.132}$$

where n is the differential order and a_k is a constant coefficient, such that when $\mathcal{L}^{(n)}$ is applied to $r(x, y)$, we obtain the resulting delta functions as

$$\mathcal{L}^{(n)}\{r(x, y)\} = A\delta(x - x_0)\delta(y - y_0) + g(x, y). \tag{2.133}$$

The function g(x,y) represents additional delta functions associated with multiple corner edges of the reference in addition to contributions of imperfections, and A is an arbitrary complex-valued constant. To retrieve the object reconstructions, we apply $\mathcal{L}^{(n)}$ to the autocorrelation $(\Psi \otimes \Psi)$ where $\Psi = o + r$ and we get

$$\mathcal{L}^{(n)}\{\Psi \otimes \Psi\} = \mathcal{L}^{(n)}\{r \otimes r\} + \mathcal{L}^{(n)}\{o \otimes o\} + (-1)^n o \otimes \mathcal{L}^{(n)}\{r\} + \mathcal{L}^{(n)}\{r\} \otimes o. \tag{2.134}$$

The third and fourth terms of the Eq. 2.134 contain the application of the LDO to r(x,y), which using Eq. 2.133 and the sifting property of $\delta(x, y)$ becomes

$$\begin{aligned} \mathcal{L}^{(n)}\{\Psi \otimes \Psi\} &= \mathcal{L}^{(n)}\{r \otimes r\} + \mathcal{L}^{(n)}\{o \otimes o\} \\ &+ (-1)^n o \otimes \{A\ \delta(x - x_0)\delta(y - y_0) + g(x, y)\} \\ &+ \{A\ \delta(x - x_0)\delta(y - y_0) + g(x, y)\} \otimes o \end{aligned} \tag{2.135}$$

$$\begin{aligned} \mathcal{L}^{(n)}\{\Psi \otimes \Psi\} &= \mathcal{L}^{(n)}\{r \otimes r\} + \mathcal{L}^{(n)}\{o \otimes o\} \\ &+ (-1)^n A^* o(x + x_0, y + y_0) + A o^*(x - x_0, y - y_0) \\ &+ (-1)^n o \otimes g + g \otimes o. \end{aligned} \tag{2.136}$$

The third and fourth terms resemble those of the twin images as in FTH Eq. 2.126. The terms $g \otimes o$ and $o \otimes g$ account for reconstructions from additional reference points. In the single point-reference case, $g(x, y) = 0$ and $n = 0$ then

$$r(x, y) \propto \delta(x - x_0)\delta(y - y_0), \tag{2.137}$$

which means the reference function is reduced to a single delta peak as with a pinhole reference due to the LDO being equal to the identity operator $\mathbf{I}$ as

$$\mathcal{L}^0\{\} = \mathbf{I}; \qquad \Rightarrow \mathcal{L}^0\{r(x,y)\} = r(x,y). \tag{2.138}$$

Application of the Linear Differential Operator to Extended References

First, let us explain what constitutes an extended reference. An extended reference describes a structure that is an extension of a single point, a structure whose geometry constitutes sharp corners or edges so that the transmission function of say an aperture of such geometry contains a sharp transition in amplitude or phase at the edges or corners. Mathematically, the derivative in x of a Heaviside function H(x) results in a delta peak at the edge interface. Similarly, the derivative of a top-hat function rect(x) results in a positive and negative peak at each edge. A one-dimensional top-hat function could be representative of the transmission function of a slit aperture, where Δy is the infinitely thin width and Δx is the length of the slit. On the other hand, the transmission function through a square-shaped aperture, (albeit a parallelogram or a single corner), resembles a two-dimensional top-hat function. Hence, a double directional derivative applied in x and y to the two-dimensional top-hat function rect(x,y) results in four delta peaks, each at a position of a square corner. The double derivative is required since the reference structure is not only extended in one direction x (like the slit) but in two directions, and consists of a width Δx and a length Δy. From this we can understand how the LDO operates on the extended reference and we can deduce that with a slit reference, the LDO is a first order differential, and with a square/parallelogram/corner reference, the LDO is a second order differential. Thus we obtain the expressions of the LDO for the slit reference (one-dimenional extension):

$$\mathcal{L}^1\{\} = \cos\alpha\frac{\partial}{\partial x} + \sin\alpha\frac{\partial}{\partial y} = \alpha\cdot\nabla \qquad \text{and} \quad \mathcal{L}^1\{\} = \frac{\partial}{\partial x} \quad \text{for} \quad \alpha = 0, \tag{2.139}$$

where α is the angle formed between the slit and the x-axis, and $\alpha = 0$ denotes a horizontally aligned slit. Similarly, for the parallelogram reference whose sides make an angle of α and β with the x-axis, we obtain

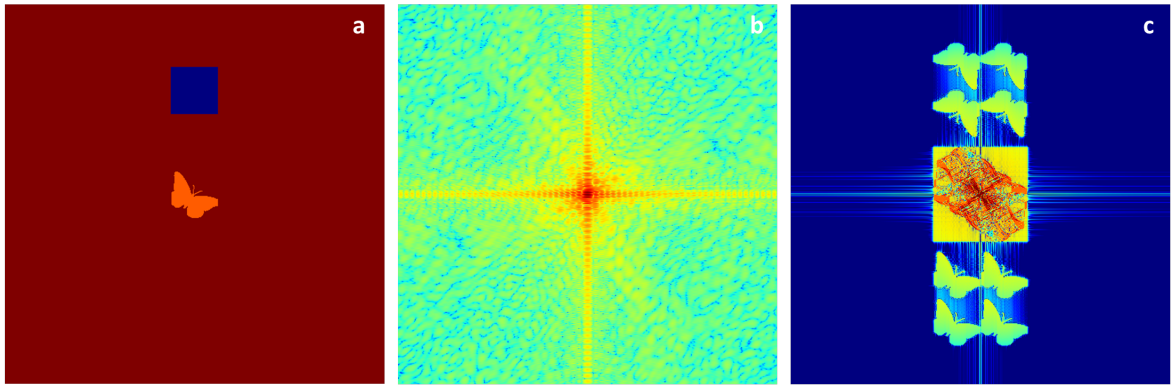

Figure 2.6: Simulation of square-shaped reference with a test-object. (a) object-plane wavefield; (b) simulated Fraunhofer diffraction pattern; (c) reconstructed FOV obtained by the LDO.

$$\mathcal{L}^2\{\} = \frac{1}{|\sin(\beta-\alpha)|}\,[\alpha\cdot\nabla]\,[\beta\cdot\nabla] \quad \text{and} \quad \mathcal{L}^2\{\} = \frac{\partial^2}{\partial x \partial y} \quad \text{for} \quad |\beta-\alpha| = \pi/2, \tag{2.140}$$

where the right side of Eq. 2.140 represents a square reference aligned with (x,y). The operators $\mathcal{L}^1\{\}$ and $\mathcal{L}^2\{\}$ reduce the reference function to a set of positive and negative delta peaks. Furthermore, we are able to do the same by applying the LDO in Fourier space. Using Eq. 2.16 and Eq. 2.18 which show that the first order differential of a function in real space is equal to the Fourier transform of the function multiplied by a linear function in reciprocal space, we obtain the Fourier version of the LDO. As the reconstruction is performed by applying a IFFT to the intensity distribution, we obtain the reconstructed field $\mathcal{L}^n(\Psi \otimes \Psi)$ as

$$\mathcal{L}^1\{\Psi\otimes\Psi\} = \frac{\partial}{\partial x}\Big\{\ \mathcal{F}^{-1}[I(p,q)]\Big\} = \mathcal{F}^{-1}\Big\{2\pi i q\cdot I(q,p)\Big\}, \tag{2.141}$$

for the case of the first-order extended reference such as a reference slit, neglecting the angle α. And for the case of a square reference, we get

$$\mathcal{L}^2\{\Psi\otimes\Psi\} = \frac{\partial^2}{\partial x \partial y}\Big\{\ \mathcal{F}^{-1}[I(p,q)]\Big\} = \mathcal{F}^{-1}\Big\{(2\pi i)^2\ q\cdot p\cdot I(q,p)\Big\}, \tag{2.142}$$

where the expression could be easily extendable for the case $\alpha, \beta \neq 0$. This simplifies the reconstruction procedure, where processing the LDO in the Fourier domain involves multiplying the detected intensity distribution array by a grid array in terms of (q, p) where $q = x\Delta_s/\lambda z$ and $p = y\Delta_s/\lambda z$ whose center is aligned to that of the zero order peak of the diffraction pattern. This process can be also considered as a linear Fourier filter, often used in signal processing. Being a linear multiplicative factor means that the high-frequency oscillations associated with noise in the recorded diffraction pattern are also amplified. Hence, it is advised that the linear Fourier filter is multiplied by a Gaussian function in order to trim the noisy edges. Nevertheless, the numerical reconstruction procedure in its basic form is efficient enough to provide quality reconstructions. Additional steps, such as a Gaussian filter, high-pass/low-pass filtering, deconvolution, and using an iterative hybrid input-output algorithm, can all contribute to the refinement and beautification of the image, but we would like to illustrate the adequacy of the method in its basic form.

Figure 2.6 shows a simulated example of a square aperture used as reference positioned near a butterfly object with transmission properties of 340 nm gold, simulated at 9 keV photon energy, with a 55 μm detector pixel size, and a propagation distance of $14.5m$. The intensity distribution of the diffraction pattern in Figure 2.6(b) shows the intense modulations of the sinc function resulting from the square aperture superposed with the speckle pattern of the object. The reconstructed field of view in Figure 2.6(c) is obtained by applying the differential filter in reciprocal space as in Eq. 2.142. The central region is composed of the autocorrelation of the butterfly sample and the autocorrelation of the square reference, that is four repeating copies of the square forming a total square area of twice the size. Above and below the central region, four images of the butterfly object and their twin images are found, where each image occurs at the position of the virtual corner of the square reference, i.e where the δ function appears due to the LDO.

With extended references, additional separation conditions must be taken into account, namely that the distance between two consecutive corners must be larger or equal to the size of the object in order to avoid overlap between the corner

reconstructions. In addition, the area required to be oversampled now includes the square reference area plus the object area and the distance between them. The same goes for the lateral coherence length. Now that there is a total of 8 reconstructions due to the 4 reference corners, it is advisable to maintain that the reconstructed field of view S_o fits all the reconstructions, so that $S_o \geq 6 \times L_o$. Satisfying these conditions is rather straightforward, as the appropriate sizes and positions of the reference and object can be calculated beforehand to create optimal experimental conditions. However, if the latter condition $S_o \geq 6 \times L_o$ is not completely satisfied, it does not have a detrimental effect on the results, as long as at least one of the corner reconstructions fits into the area S_o and not necessarily all eight.

Resolution and SNR

The resolution of the imaging system using extended references is defined by the sharpness of the edge of the reference structure. Specifically, it is defined by the width or narrowness of the transition in transmissivity across the edge. In the case of the pinhole reference, it was defined by the size of the pinhole. In the case of a slit reference, it is defined by the width of the slit. In the case of a two-dimensional extended reference such as a square aperture or a three-dimensional structure such as a square pillar, it is defined by the sharpness or the slope of the edge. For a square aperture in an absorbing mask, it is the width of the peak in transmission from the substrate material to the aperture. For an absorbing square pillar on a transmissive substrate, it is the width of the dip in transmission between the pillar material and the substrate material. For a phase-shifting square pillar on a substrate, it is defined by the width or the sharpness of the phase jump. With all that in mind, we must note that it is more technically straightforward using lithographic methods to refine or sharpen edges of a large area than creating a sharp and isolated one-dimensional structure such as a slit or a pinhole. Hence, larger area references such as the parallelogram/square/corner (or any polygon) prove to offer more flexibility while maintaining high-resolution.
Furthermore, calculations of the normalised square error E^2 ($\propto 1/SNR$) of the reconstructed object area show that the square/parallelogram reference gives superior performance compared to the other reference types. As Guizar demonstrated

[47], the expression of E^2 for the slit reference of width ρ_y is given by

$$E^2 = \frac{4\ln(2)MN}{\pi\phi\rho_y^2} \frac{\sum_{q,p}^{M,N}\left(\left|\mathcal{L}^2\{\tilde{o}(q,p)\}\right|^2\right)}{\sum_{q,p}^{M,N}\left(|\tilde{o}(q,p)|^2\right)}, \tag{2.143}$$

where ϕ is the flux, (M,N) is the pixel dimension of the reconstructed array, $\tilde{o}$ and $\tilde{r}$ are the object function and reference function in reciprocal space. As expected, the error decreases with increasing flux and increasing slit width, which validates the resolution-SNR trade-off statement. E^2 is similar to that of the pinhole in Eq. 2.127, apart for the terms inside the sum, which show dependence on the ratio of the squared sum of the object derivative to the squared sum of the object. The error of the reconstructions with the square reference is given by

$$E^2 = \frac{MN}{\phi} \frac{\sum_{q,p}^{M,N}\left(\left|\mathcal{L}^2\{\tilde{o}(q,p)\}\right|^2 + 4\left|\{\tilde{r}(q,p)\}\right|^2\right)}{MN\sum_{p,q}^{M,N}\left(|\tilde{r}(p,q)\tilde{o}^*(q,p)|^2\right)}, \tag{2.144}$$

where E^2 is independent of the square length or sharpness and increases with lower flux. In the limit of an infinitesimally sharp corner, Eq. 2.144 is reduced to

$$E^2 = \frac{MN}{\phi} \frac{\sum_{q,p}^{M,N}\left(\left|\mathcal{L}^2\{\tilde{o}(q,p)\}\right|^2\right) + 4}{\sum_{p,q}^{M,N}\left(|\tilde{o}(q,p)|^2\right)}, \tag{2.145}$$

where the factor 4 comes from the contribution of the four corners, the object transmissivity contributes to the signal, and the derivative of the object transmissivity contributes to the error. Unlike the error for the slit Eq. 2.143 and the pinhole reference 2.127, when we consider the limit of the corner widths $(\rho_x, \rho_y) = 0$, the value of E^2 reaches to a finite non-zero value, whereas with the slit or pinhole reference E^2 will keep decreasing quasi-exponentially as $\rho \to 0$. The reason is that the square reference is an open area aperture and the transmitted light will not decay to zero for an infinitely sharp corner since in fact, the boundary wave will always be generated by the aperture no matter how sharp its corners.

Differential Wireframe Extended Reference

Another type of extended reference, different than the full-area square/parallelogram reference, is the wireframe or cross-wire reference. The function of the wireframe can be considered as the differential $\partial_x \partial_y$ of the full-area square reference. This essentially means that when applying the operator $\mathcal{L}^2$, the corners do not result in single positive and negative delta functions as in the square reference case. Instead, we obtain the derivative of the delta functions, meaning a double peak of positive and negative polarity at a single corner position. In addition, applying the second order LDO to the reconstructed area results in an outline reconstruction of the sample with high intensity. Another way to approach this is to consider that the reconstruction procedure should include an integral operator LIO instead of a differential operator LDO. The purpose of the LIO would be to reduce the corners back to their respective delta functions. Numerical methods for applying the LIO are discussed in [38, 47].

Figure 2.7 shows a simulation of a wireframe reference with a butterfly test object. The amplitude profile plot vertically through the center of the sample array is shown in Figure 2.7(b). The diffraction pattern shows the rectangular sinc modulations superposing with the speckle pattern of the reference. The amplitude reconstructed area is shown in Figure 2.7(d) where the linear Fourier filter was applied (reciprocally equivalent to the operator $\mathcal{L}^2$). We observe the outline of the butterfly sample repeating four times (and their twin images) similar to the full-area square reference case. In addition, the reference autocorrelation shows the square outline with zero signal in the inner area. This effect could be advantageous for imaging a weakly scattering sample, or a thin sample, where we prefer $r \otimes r$ not to overpower the object signal. Or, for example, if we decrease the lateral offset between the sample and the reference, the overlap of the reconstructions with the wireframe autocorrelation would not be detrimental and the sample structure would still be distinguishable. Such a method falls within the category of differential-contrast imaging or edge enhancement and could be relevant for imaging applications where we are interested in the boundaries of a sample more than the bulk information.

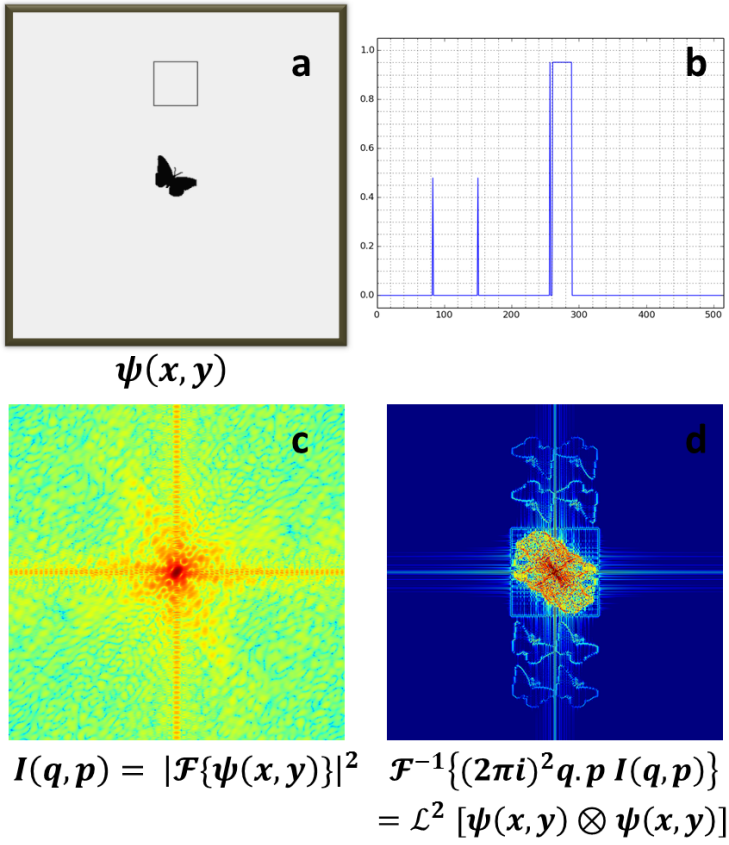

Figure 2.7: Simulation of reconstructions using differential wireframe reference. (a) object-plane wavefield; (b) transmission profile plot cutting through the center of the sample plane vertically across the wireframe reference; (c) simulated Fraunhofer diffraction pattern; (d) reconstructed FOV showing 4 images of the sample and their twin images centro-symmetrically.

2.5.1 Phase-Shifting Vs. Absorbing References

In holographic imaging with extended references with soft x-rays, optical laser light, and EUV radiation, most of the prominent results were achieved by using a reference structure that consists of a milled aperture in an absorbing mask or an obstructing (absorbing) structure on a transmissive substrate. However, since the reference wave is a result the boundary waves generated by the edges of the extended structure, we deduce that the choice of reference structure can be broadened to include not only transmissive/absorbing apertures but also phase-shifting structures. This notion is valuable for applications with hard x-ray imaging where a much higher thickness of

material is required to contribute to the absorption. Due to the high penetration of hard x-rays, it is much more difficult to fabricate a transmissive reference aperture on an absorbing mask while maintaing sharp edges.

Fabrication Requirements

Focussed Ion Beam devices (FIB) and e-beam lithography are standardised milling techniques that provide high milling resolution of thin membranes. With silicon nitride as an example, 0.4 mm of material thickness is required for 100% absorption of x-rays at 9 keV. With soft x-rays, coherent imaging experiments are performed in the energy range of 400-700 eV, where the transmission curve is nonlinear. 200 nm of silicon nitride produces an absorption of 80% at 410 eV, and in general a thickness of under 1 μm would be sufficient to produce considerable absorption (as long as x-ray transmission edges of the element are kept in mind). It is very straightforward to mill an aperture using the FIB in a membrane of silicon nitride with a thickness of 1 μm or less. In fact, the latest models of FIBs can produce a milling resolution of less than 30 nm. Yet, it is virtually impossible to mill an aperture in a 0.4 mm film of silicon nitride with sharp edges of that caliber.

Another example is gold, which has a high sputtering rate and is suitable to serve as the absorbing mask in which the reference aperture is milled. 500 nm of gold is sufficient to produce an absorption of 90-100% for soft X-rays below 3 keV (excluding the gold peak at around 2 keV where absorption is 60%). However, at 9 keV, 15 μm of gold is required for 100% absorption. FIBs require a thin membrane of less than 1 μm for effective milling. Due to the high sputter yield and surface interaction with high-energy galium ions, FIB milling of even a 500 nm gold film still does not produce high resolution edge profiles and is often accompanied by surface damage such as redeposition, amorphisation, swelling, melting, and distorted edges. Therefore, much thinner films are required for serving the purpose. For 15 μm gold films, FIB lithography does not apply and e-beam lithography can serve as an alternative, but preparing features of less than 100 nm size with high aspect-ratio also becomes virtually impossible. The most that has been accomplished with e-beam lithography was in the vicinity of a 1:10 aspect-ratio with 100 nm holes in a 1 μm film where still the stability of the structures is fragile.

The implication is that fabrication requirements of holographic references are very stringent for experiments with hard x-rays. Yet, the benefits and applications of imaging with high energy x-rays are vast. Due to their large penetration depth and low diffuse scattering, we can probe the internal structure of thick samples with high phase sensitivity, which is very attractive for medical applications such as imaging of biological tissue, the imaging of fossils, as well as diagnostics for material science. Therefore, a solution to the fabrication constraints is critical for holographic hard x-ray imaging with extended references. The solution is found in discarding the premise of having an extended reference mask with edges that produce a transition in absorption, and adopting the phase-shifting extended reference.

Characteristics of a Phase-Shifting Structure and the Reference Wave

In the case of a transmissive aperture in an absorbing substrate (or the opposite), the sharp transition in the amplitude transmissivity across the edge of the reference structure produces a boundary wave that serves as the reference wave. In contrast, in the case of a phase-shifting extended structure, the boundary reference wave is produced as a result of the sharp transition in phase across the edge of the reference structure. This fact greatly relaxes the fabrication requirements since at high x-ray energies, the thickness of a material requires to produce a phase shift $\Delta\phi = \pi$ is much less than that required to produce an absorption of 100%. In addition, it is not necessarily required that the π phase shift is produced by the reference structure itself but by the phase difference between the structure and the substrate. This makes the mask preparation requirements much more flexible and simplifies the fabrication procedure.

For these reasons, we find that a good candidate for a phase-shifting extended reference mask would be a silicon-based material. Nanofabrication techniques, often used for fabrication of Fresnel zoneplates for x-ray microscopy, have the capability of producing high-resolution structures with high aspect-ratio based on etching techniques of light material such as HSQ, silicon dioxide, and silicon. For example, taking the crystal structure of silicon, it is possible to nanopattern a silicon wafer of around 20 μm thickness into structures with edge sharpness of less than 100 nm by aligning the etching direction with the crystal planes. Therefore, high-

resolution nanolithography is highly reliable and reproducable with crystalline light materials. At 9 keV, a thickness of 7.8 μm silicon produces $\Delta\phi = \pi$. Hence, a mask constituting of a silicon pillar in the 10 μm order of thickness placed on a transparent substrate with $\Delta\phi = 0$ could serve as the required reference structure. In general, any phase-shifting reference mask of thickness Δx_r could serve the purpose as long as the change in phase is considerable (or close to π) between the edge of a reference structure and a substrate of any given thickness Δx_s.

If we were concerned with the absorption at 8-10 keV of such structures on a transparent substrate, we would be find that the transmission is around 97%. Without considering the phase-shift contribution, one would expect the reference signal to be weak hence causing the reconstructions to have low SNR and low contrast. The contrast in holographic imaging with extended references is determined by the extent (height) of the transition in complex transmissivity across the reference edge. With that in mind, the phase of such a structure exibits a high transition from zero to π, while the transmission in absorption is negligable. It is the large phase jump that translates into high contrast reconstructions. Furthermore, the resolution is determined by the sharpness of the edges, i.e the slope of the edge transition. With the ultra-sharp edges fabricated by nanolithography, the application of the differential operator to the reference function will result in ultra-sharp delta peaks and hence we expect image reconstructions with high resolution. We conclude that there is no compromise when it comes to switching from an absorbing frame to a phase-shifting frame. In fact, the phase-shifting frame proves to be more advantageous as it involves flexible fabrication requirements, it maintains high image contrast, and potentially provides higher resolution than expected with an absorbing frame.

Figure 2.8 and Figure 2.9 show a simulated example of a square-shaped reference of 8 μm thick silicon, with $\Delta\phi = \pi$ and $T = 95\%$. The reference is placed above the butterfly test object with the properties of 350 nm gold material. The object and reference are simulated to be surrounded by a fully transmissive substrate with zero phase shift. The plots vertically through the centre of the amplitude and phase of the sample frame are shown in Figure 2.8(c) and (d) respectively.

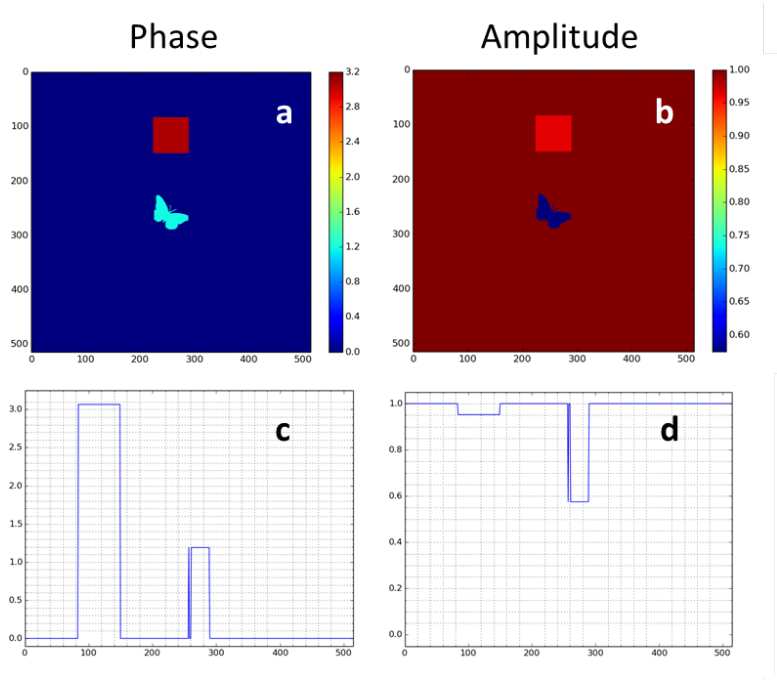

Figure 2.8: Simulated sample plane $\Psi(x, y)$ consisting of phase-shifting extended reference made of 8 μm thick silicon with $\phi = \pi$ and $T = 95\%$ and butterfly test object of 340 nm gold.

The reconstructed area is obtained by applying the linear Fourier filter Eq. 2.142 to the intensity distribution of the diffraction pattern in Figure 2.9(a,b). Figure 2.9(c) and (d) show the phase and amplitude of the reconstructed area applying by the real-space double directional derivative Eq. 2.136 to the IFFT of the intensity distribution. As we can see in the plot of the amplitude transmission profile, the absorption of the reference structure is almost negligable. Yet, the reconstructions show four reconstructed images of the butterfly gold object with high contrast, which is the result of the phase-shift of the reference structure. Compared to an absorbing mask, the phase-shifting reference produces reconstructions with much higher phase contrast. In fact, employing a phase-shifting reference has the potential of amplifying the reference signal strength and reconstructed object contrast due to the π phase shift. This effect is explained in the following by developing the expressions of the resulting complex transmissivities.

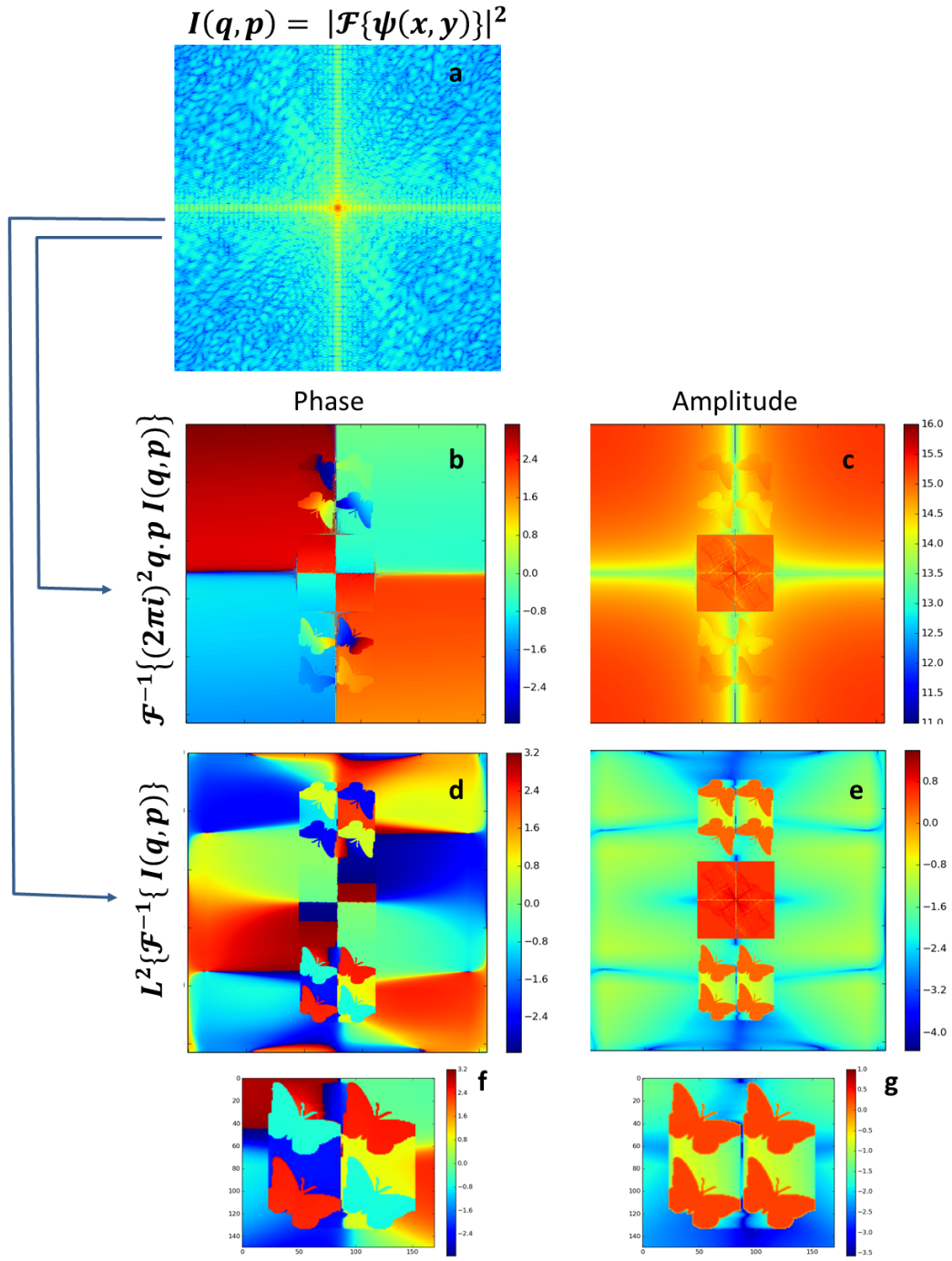

Figure 2.9: Simulation of phase-shifting extended reference made of 8 μm thick silicon with $\phi = \pi$ and $T = 95\%$.

Signal Amplification by a Phase-Shifting Reference

Let us consider the transmissivity function of the reference frame to be

$$r(x, y) = \tau_s + (\tau_r - \tau_s)H(x, y) \tag{2.146}$$

where τ_r and τ_s are the complex-valued transmissivities of the reference and the substrate surrounding the reference respectively, and H(x,y) is the spatial extent of the reference structure, i.e in case of a square reference, H(x,y) is a two-dimensional heaviside function. Notice that the reference transmissivity function is proportional to the term $(\tau_r - \tau_s)$. This means that highest signal strength of the reference is attained when the phase shift between the reference and the substrate is π. Neglecting absorption, $|\tau_r - \tau_s|$ is equal to $|e^{i\pi} - e^{i0}| = 2$. Taking the reference signal intensity, or the magnitude, the amplification is thus proportional to $|\tau_r - \tau_s|^2 = 4$, which means the reference signal amplification is four times higher than the case of the absorbing/transmissive reference mask [39, 40].
Consider also that an object of transmissivity τ_o is on the substrate of transmissivity τ_s and lies outside the reference area H(x,y), such that

$$o(x, y) = \tau_s(\tau_o(x, y) - 1), \tag{2.147}$$

within the object area, and is zero otherwise. A more detailed explanation about how these expressions are derived is found in [39, 47, 48]. With these two expressions, we can find the autocorrelation and cross-correlation terms. First, we calculate the result of applying the LDO to the autocorrelation of the square reference r(x,y)

$$\mathcal{L}^2\{r(x, y) \otimes r(x, y)\} = \mathcal{L}^2\{r(x, y)\} \otimes r(x, y) \tag{2.148}$$

Given that the differential operator $\mathcal{L}^= \frac{\partial^2}{\partial x \partial y}$ applied to the two dimensional heaviside function results in four delta functions (using the property of differentiation of a cross-correlation), Eq. 2.148 becomes

$$\mathcal{L}^2\{r \otimes r\} = \sum_j C_j r^*(x_j - x, y_j - y) \tag{2.149}$$

such that (x_j, y_j) are the coordinates of the corners of the reference, C_j is a complex-valued arbitrary constant, and the fact that it is a sum denotes that there is a total of 4 reconstructions, where j is the index of the corner which in the square case is $j = 1, 2, 3, 4$. We notice that the LDO of the autocorrelation of $r(x, y)$ returns the function $r^*(x, y)$ repeated j times and shifted according to (x_j, y_j). This is due to the sifting property of the delta function as it returns a shifted conjugated copy of the square function when cross-correlated with it. By replacing Eq. 2.146 in Eq. 2.149, and using the symmetry property of the heaviside function, we obtain

$$\mathcal{L}^2\{r \otimes r\} = |\tau_r - \tau_s|^2 \sum_j c_j H(x - x_j, y - y_j). \tag{2.150}$$

Similarly, $\mathcal{L}^2$ applied to $o \otimes r$, $r \otimes o$ gives us the reconstruction terms

$$\mathcal{L}^2\{o \otimes r\} \propto \tau_s(\tau_o - 1)^*|(\tau_r - \tau_s)| \tag{2.151}$$

$$\mathcal{L}^2\{r \otimes o\} \propto \tau_s(\tau_o - 1)\ |(\tau_r - \tau_s)|^* \tag{2.152}$$

which for a phase shift of π between the reference and substrate, and assuming a fully transmissive substrate, and invoking the Babinet's principle, gives an amplification of the object reconstruction signal strength by a factor of 2

$$\left|\mathcal{L}^2\{o \otimes r\}\right| \propto 2\ |\tau_o^*| \tag{2.153}$$

$$\left|\mathcal{L}^2\{r \otimes o\}\right| \propto 2\ |\tau_o| \tag{2.154}$$

The main two implications that a) the intensity of the reference signal is potentially amplified by a factor of four, and b) the signal of the object reconstructions is amplified by a factor of two, for the case of a π phase shift, stand as a great advantage over using an absorbing/transmissive reference for holographic imaging using extended references. In addition, this will prove to yield positive results when applied with hard x-ray imaging of both weakly scattering and strongly scattering thin and thick samples as we will see in the following chapter.

3 Experimental Setup: HDXI using Phase-Shifting References

In this chapter, we will discuss the experimental setup of Holographic Diffraction X-ray Imaging (HDXI) using phase-shifting extended references with hard x-ray synchotron radiation [39, 50, 51, 52]. The experiments were performed at the *coherence* branch of I13 at Diamond Light Source, UK [53, 54, 55]. We will describe the preparation techniques involved in the lithographic fabrication of the reference structure and characterise it experimentally. We have implemented the method with various samples: thin gold test samples (absorbing samples), thin silicon dioxide test samples (phase samples), as well as biological samples such as marine microplankton and bacteria cells of the Deinococcus Radiodurans strain. We will describe the preparation techniques involved with the biological samples and show optical micrographs as well as SEM images to give an overview of the sample properties. We will then describe the experimental setup for x-ray imaging, and discuss the technical procedure required for achieving optimal experimental conditions such as beam characterisation, the detector setup, alignment, and data acquisition. In addition, we will highlight the novel aspect of deconfining the sample plane and the reference plane in a holographic setup and demonstrate the benefits and applications.

3.1 Extended References

The structure and material of the extended references is chosen such that the fabrication process produces sharp corners and edges of a structure with a thickness creating a π phase shift on a substrate of high transmissivity (or alternatively a substrate with $0 \pm 2\pi$ phase shift) at x-ray energies between 8 keV and 9.7 keV.

3.1.1 Structure and Fabrication

Materials such as silicon, silicon nitride, poly(methyl methacrylate) (PMMA), and Hydrogen silsesquioxane (HSQ) have low electron densities and are characteristically grown, chemically etched, or lithographically fabricated into high-resolution fine layers or structures. Heavy materials such as gold, platinum, palladium etc... can be lithographically etched as well to produce pillars with sharp corners. At 8 - 9.7 keV, the thickness of gold required to produce a π phase shift would be around 1-2 μm. On the other hand, the thickness of silicon required to do the same would be in the order of 10 μm. Yet, the etching quality of silicon crystal is highly superior compared to amorphous gold. When considering e-beam lithography, FIB, or wet etching, if the etching direction is aligned with the crystallographic orientation, the produced edge is potentially atomically sharp. Although high Z materials benefit from a high milling rate, due to the large interaction volume with an electron beam, the probability of producing an ultra-sharp edge is lower than with low-Z crystalline materials, not to mention risking other artefacts in the structure such as swelling, surface damage, or fissures depending on the milling technique used.

High-resolution nano-lithography techniques [5, 56] have rapidly developed in recent years to provide a large range of nano-devices to serve for x-ray optical systems, electron microscopes, electronics, etc... Fine structures reaching up to 5 nm resolution with high aspect-ratio can be fabricated with selective materials using atomic layer deposition (ALD). We have collaborated with Dr. Jeroen Bosgra of the Laboratory for Micro- and Nanotechnology lead by Christian David at the Paul Scherrer Institute in Switzerland to prepare high-resolution phase-shifting pillars by silicon nano-lithography. Figure 3.1 shows a plot of the transmission ratio

and phase shift in units of π radians for varying material thickness and various light materials at 8 keV photon energy, where we find that $10\mu m$ of silicon produces a π phase shift compared to 6 μm of HSQ, and that the transmission of around 10 μm thick light material at 8 keV is above 90%.

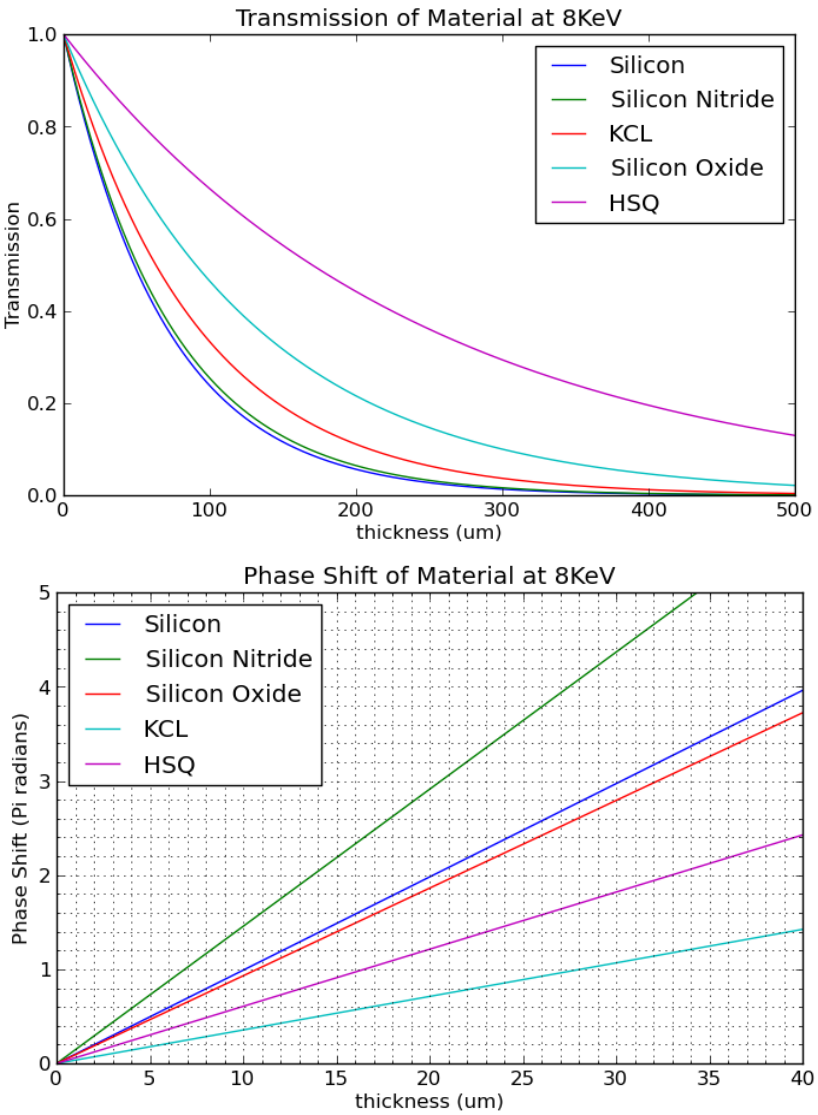

Figure 3.1: Calculated transmission and phase shift of low Z materials as a function of material thickness at 8 keV.

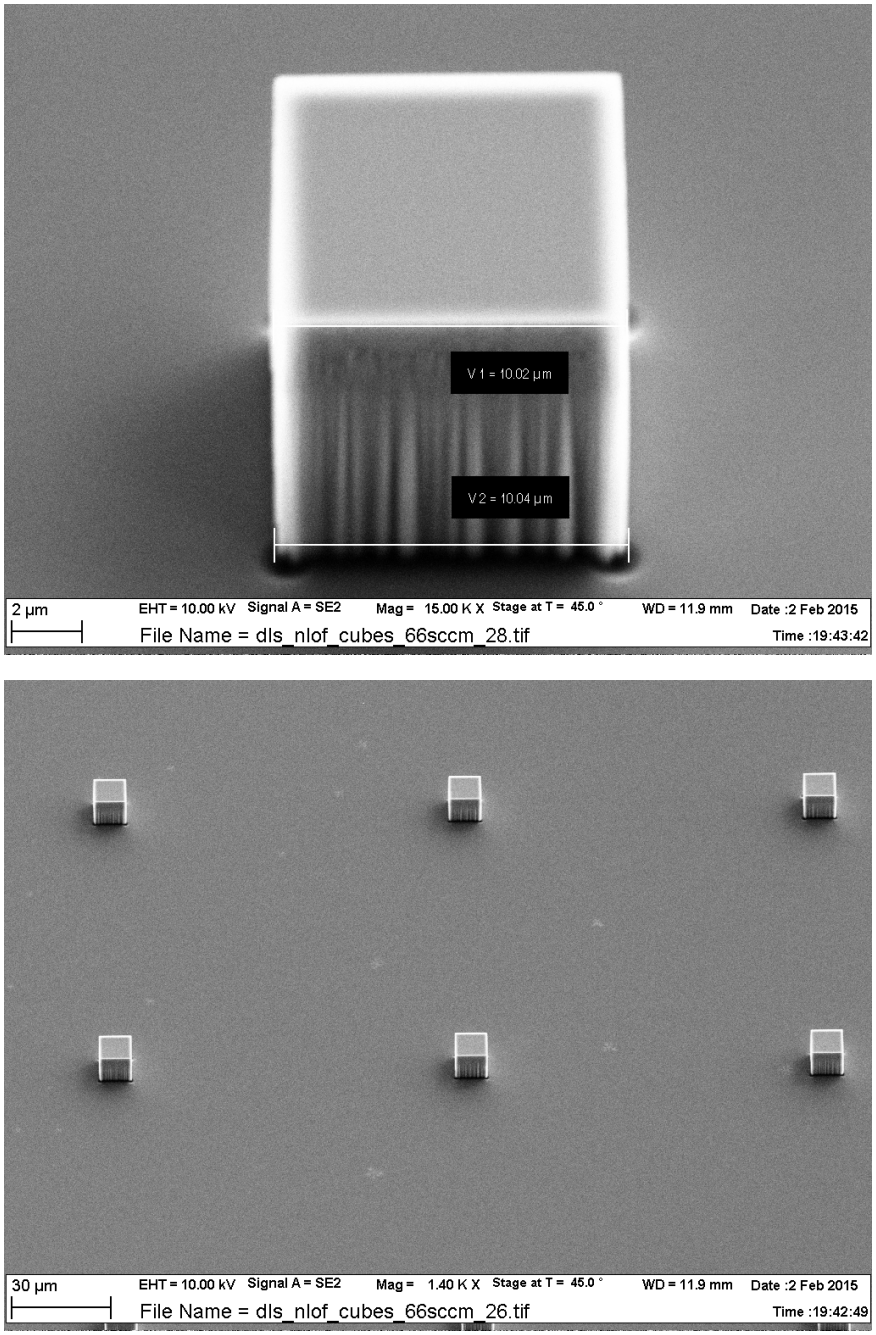

Figure 3.2: SEM images of nano-fabricated $9\mu m$-thick silicon pillars. [57]

Square Silicon Pillars

The silicon pillars were fabricated using e-beam nanolithography and were set to have a height of 9 μm with face dimensions varying from 4 μm to 20 μm in order to comply with various sample sizes. The lithographic fabrication process generated ultra-sharp square corners which will serve as the high-resolution reference point-source. The silicon pillars lie on a silicon wafer of 20 μm thickness, such that the phase shift between the pillar and the substrate is considerable in the energy range 8 - 9.7 keV is between 2.5 radians and π radians. During the experiment, the lateral dimension of the pillar is chosen based on the size of the object we wish to image. The pillars are arranged in a square matrix such that the separation between two consecutive pillars is at least 100 μm, which allows sufficient isolation of a single reference structure within the beam diameter. Figure 3.2 shows two SEM images of the square silicon pillars of 10 μm width arranged in a matrix.

ALD Iridium Wire-frame

Since the resolution of the imaging system is limited by the corner and edge sharpness, an iridium-coated silicon pillar reference sample was prepared. The iridium coating is done by atomic layer deposition (ALD) which ultimately means that the reference structure will represent an extremely sharp iridium wireframe on top of a silicon pillar. ALD allows to deposit single-atom layers of material onto a surface in a manner which produces ultra-smooth fine nanometre-thin layer of material. A 3.9 μm-thick silicon pillar is prepared as mentioned above. After that, a few nanometres of Iridium are deposited by ALD. With an ultra-sharp silicon edge, the iridium atoms will stack up one upon the other along the sides of the pillars where the result is a silicon pillar that is uniformly, homogeneously, and finely coated by a nanometre-layer of Iridium. When the face of the pillar is perpendicular to the incoming x-ray beam, the x-rays will *see* a silicon square structure, that attenuates the photons by less than 1% and shifts the phase by a fraction of π, and a nanometre-thin wireframe of iridium that is 3.9μm in depth outlining the silicon square face. Due to iridium being a heavy element, 3.9μm of iridium contributes significant absorption as well as a phase shift around π at 8 - 9.7 keV. The compound wireframe reference structure therefore constitutes a

π-phase shifting Iridium wireframe of nanometre lateral thickness which refines the resolution of the imaging system and provides edge enhancement and an underlying silicon pillar which contributes to the bulk image contrast. Figure 3.3(top) shows a schematic of the fabrication technique with HSQ of $2\mu m$ thickness. Figure 3.3(bottom) shows an SEM image of a $5\mu m$ compound ALD reference where we observe the ultra-fine coating of iridium on the silicon face, the sharper edges, and the clear and sharp corners compared to the silicon pillar in Figure 3.2.

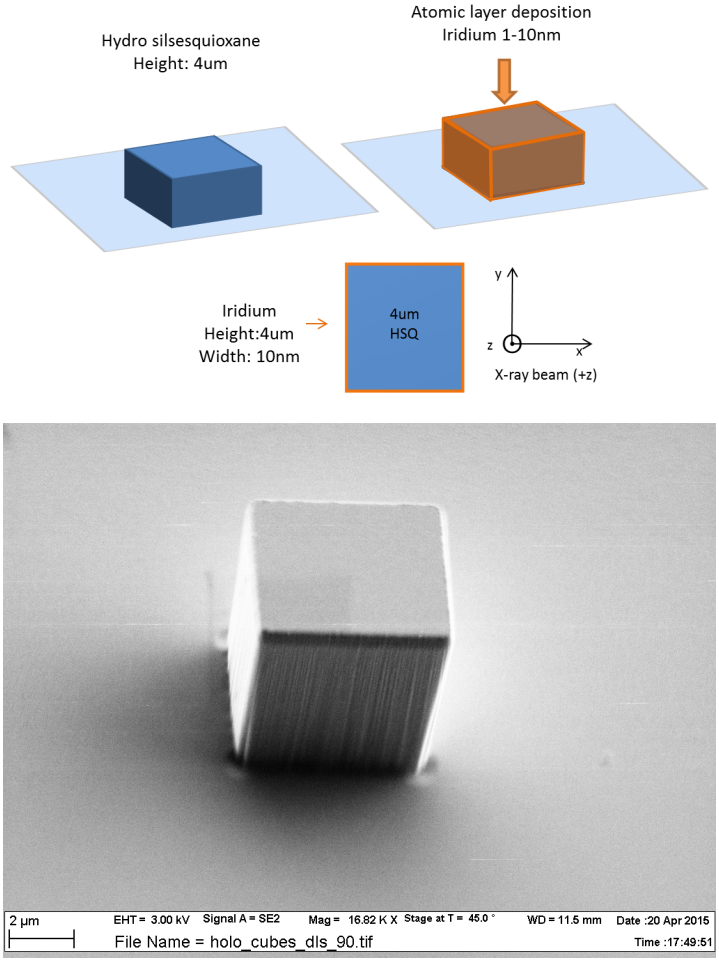

Figure 3.3: (top) Schematic illustration of fabrication steps of ALD iridium-coated pillar. (bottom) SEM image of SiO_2/HSQ pillar with 10 nm iridium by ALD. [57]

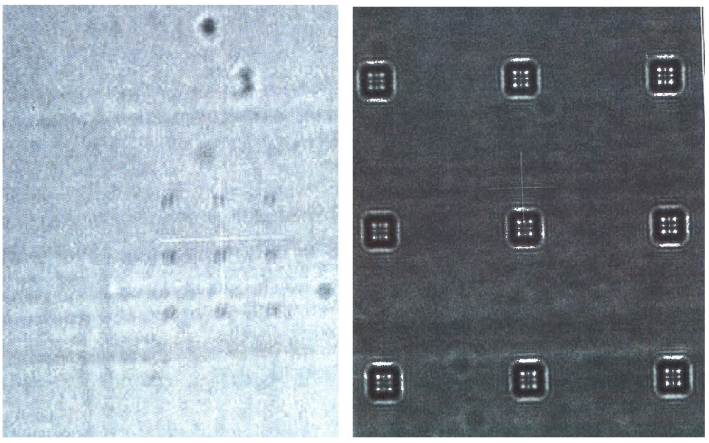

Figure 3.4: Alignment procedure showing array of silicon pillars viewed in near-field projections at 8 keV.

3.1.2 Reference Characterisation

The reference membrane is mounted on a piezo-stage and exposed to the incoming parallel beam of coherent x-rays at 8 keV. The reference stage undergoes an angular test to qualitatively and quantitatively find the optimal angle that renders the face of the cube perpendicular to the direction of the incoming beam and therefore rendering the pillar edges most parallel to the beam. This is qualitatively studied by comparing the width of the near-field diffraction fringes of the projections (Figure 3.4) on a scintillator detector placed in the near field.

Using the far-field photon-counting detector, the diffraction pattern resulting from the square pillars is studied as the pitch angle changes such that the square face is rocking with respect to the incident beam. The x-rays *see* a square aperture when the edges are aligned, and *see* two overlapping apertures when the pillar is at an angle and the top side of the pillar appears shifted and overlapping with the bottom side of the pillar. We find the angle corresponding to the smallest fringe separation and the most symmetric beams to correspond to the aligned setting. In addition, we rule out large misalignment by rocking the sample to large angles (30° or more). The less aligned the cubes are, the more the diffraction pattern tends towards that of a Young's double slit portraying beat modulations. At the

negative extremum and at the positive extremum of the pitch angle we observe the beat modulations, we hence align the zero position to the mid-angle between the two extrema, and roughly assume that the midpoint is the angle where the face of the cube is perpendicular to the beam. Figure 3.5 shows the recorded diffraction patterns at the maximum rocking angles from the negative extremum to the positive extremum in both directions where the diffraction fringes become diminished along one axis corresponding to the direction of the rocking axis. The four datasets correspond to the limits, the midpoint of which gives roughly the aligned angle. Figure 3.6 shows the recorded diffraction pattern and the profile plots along the horizontal and vertical fringes corresponding to the case of an aligned reference pillar with symmetric beams and minimal fringe width.

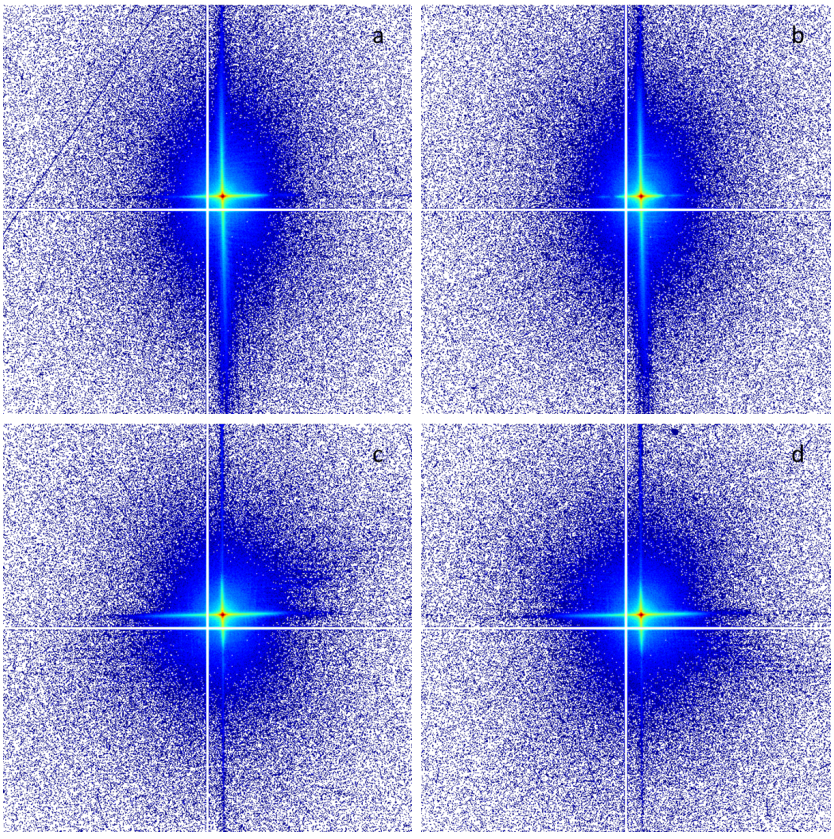

Figure 3.5: Diffraction patterns of silicon pillar with rocking alignment angle from negative to positive extrema in two directions.

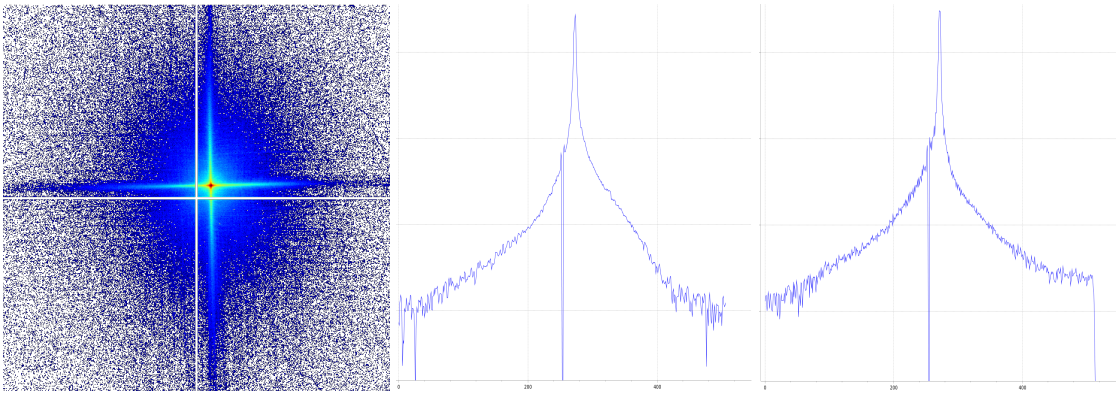

Figure 3.6: (left) recorded diffraction pattern of silicon pillar with edges aligned to x-ray direction. (middle, right) profile plot through horizontal and vertical fringe modulations.

3.2 Sample Preparation

3.2.1 Test samples

The test sample with which the holographic measurements commenced consisted of a *cartoon*-shaped fish of 4 μm length and 2.7 μm width created by electron beam lithography with a 340 nm thickness of gold on a 150 nm Si_3N_4 substrate within a 200 μm Si frame. The eye of the fish was fabricated as a 400 nm gold dot, to generate a circular speckle pattern and the fins as two horizontal gold bars of 150 nm in width and 700 nm in length with a sub-50 nm separation between the two bars to generate slit-type diffraction. The tail contained sub-100 nm detail and the outline was 150 nm throughout. The SEM image of the test pattern is shown in 3.7(top).

Similarly, other test patterns were fabricated with the same absorption properties but with some varying dimensions such as a cartoon *fish in a bowl* (Figure 3.7(middle)). To extend the testing to weakly scattering samples made of light material that do not contribute much in absorption, we also prepared a test pattern of a cartoon *fish bone* made of 590 nm - thick silicon dioxide and coated with 10 nm of iridium for better detectability and contrast (Figure 3.7(bottom)). The silicon dioxide bone fish contains slit-like structures (the bones) with ultra-fine features of varying width, which serves as a good resolution-testing sample.

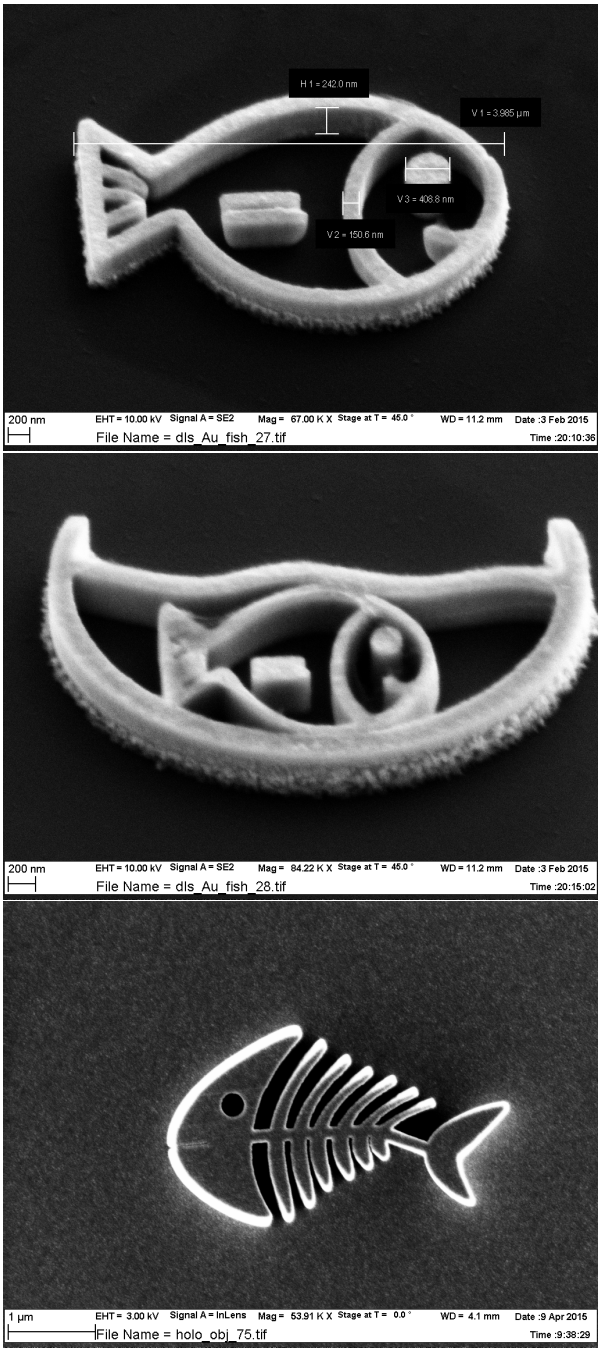

Figure 3.7: SEM images [57] of (top) 340nm thick gold fish cartoon pattern, (middle) 340nm gold fish in a bowl, (bottom) 590nm silicon dioxide coated with an iridium nanolayer, deposited on a silicon nitride membrane of 150nm thickness. Scalebar: 200nm

3.2.2 Biological samples

Marine Micro-Plankton

X-ray imaging of marine micro-plankton [58] is of particular interest to study the distribution and concentration of trace elements deposited in plankton such as in calcified shells[59]. The study of remineralisation, calcification and iodine deposits in plankton helps to trace paleoceanographic conditions and gain insight into global climate changes that date back to millions of years. Energy dispersive x-ray analysis (EDX), particle-induced x-ray emission, and x-ray fluorescence analysis [59] are complementary analytical techniques providing chemical sensitivity, quantitative analysis, and detection of elemental isotopes, in addition to lateral resolution. X-ray phase contrast imaging and x-ray micro-beam tomography also provide information about the mineral deposits distribution in microplankta and the trace element content. Hard x-ray holographic diffraction imaging also holds potential to recover structural information of microplankta since it provides a direct reconstruction of both the phase and the amplitude of the sample.

A few milligrams of a sample of marine microplankton (coccolithophores, calcium carbonate) in powder form was supplied to us by Elisabeth Read, Cambridge University. We then prepared the sample preparation at the chemistry labs of DLS. The powder was crushed using a pestle and mortar to reduce the particle size. The grinding results in the plankta to break apart into *plates* known as *coccolithophorids* [60, 61]. Some of the coccolithophorids may also break into smaller fragments. The crushed powder is then diluted in ultra-purified water of which a micro-droplet is deposited on the flat surface of a silicon nitride membrane and let to dry at room temperature. Upon inspection under the optical microscope, we find a low concentration of coccolithophorids residing on the membrane with sizes ranging from 5 μm to 25 μm, which is ideal for application with the holographic references and to satisfy the sample isolation condition. The low concentration of plankta on the membrane provides good conditions for our holographic imaging system, such that each plankton is sufficiently surrounded by a region of empty space so as to not provide diffraction artefacts from the neighbouring organisms.

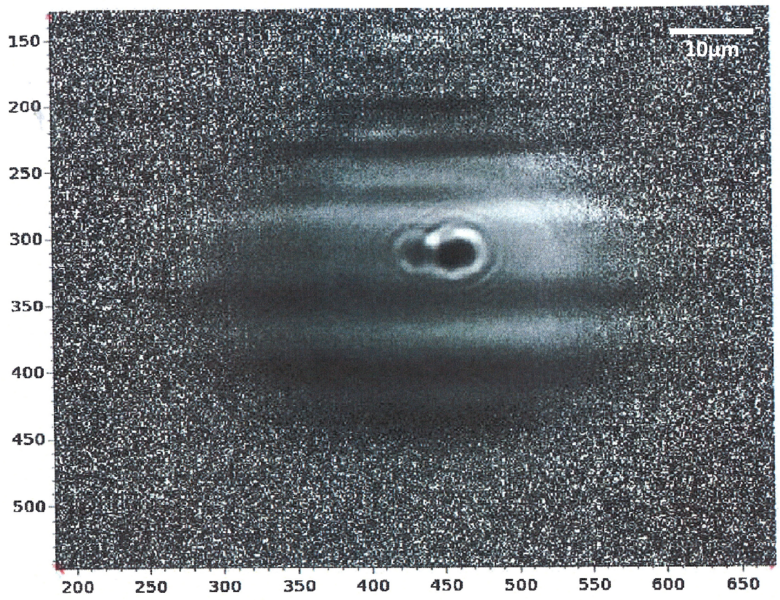

Figure 3.8: Near-field Fresnel projection of 2 coccolithophorids at 8keV x-ray energy.

Deinococcus Radiodurans Bacteria

Famously known as *Conan the Bacterium* [62, 63], the *Deinococcus Radiodurans* is an extremophyllic bacteria; in other words, it is known to be a survivor of extreme conditions. It survives cold, vacuum, dehydration, and acid, and it is one of the most radiation-resistant [64] organisms known to man. It is highly resistant to ultraviolet light, desiccation [65], and oxidizing and electrophilic agents. D. radiodurans is documented to be a large spherical bacterium with sizes ranging from 1 μm to 3.5 μm. It typically grows in a tetrad, as four bacterial cells normally stick together forming a tetrad bacterial unit.

Scientists seek to understand the history, genetics, and dynamics of the D. radiodurans in the fields of genetic engineering, aerospace engineering, medicine etc... Due to its hard radiation-resistance, understanding the properties of these bacteria helps to develop bioremeditation to clean radioactive supersites that remain from nuclear wars. After having completed the genetic sequencing of the D. radiodurans genome, scientists say that D. radiodurans can be involved in enhancing the survivability of man in extraterrestrial environments. They can be genetically manipulated to provide drugs to treat humans when ill, to recycle waste into oxygen and water, and even produce food supplements. By being immune to radiation-induced DNA damage, an oxidizing type of damage that is often implicated with cancer and genetic mutation, D. radiodurans have adapted to millions of years of harsh survival conditions. The study of D. radiodurans could provide vast possibilities to enhance life on Earth as well as open new beginnings of life on Mars.

Cells of the Deinococcus Radiodurans bacteria wild-type strain were ordered from DSMZ [66] as a freeze-dried culture in a powder palette. We prepared a sample of bacteria the freeze-dried palette without cultivation using the following method. A milligram of the freeze-dried palette was diluted with 100 μL of ultra-purified water and let to stir for a few minutes. 5 μL of the stirred bacteria solution was then deposited on the flat surface of a 1 mm silicon nitride membrane and let to dry at 30° under ambient pressure. When inspected under the optical microscope, we observe a low concentration of D. radiodurans tetrads as shown in Figures 3.9 and

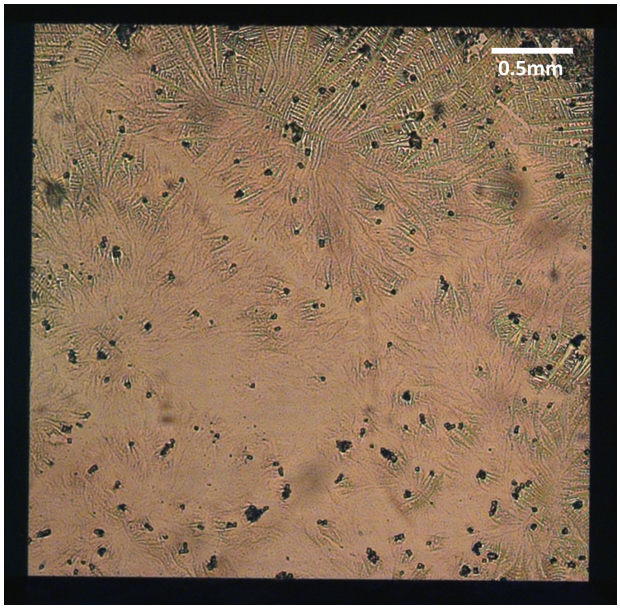

Figure 3.9: Overview image obtained with the optical microscope at 5X magnification showing the prepared sample membrane covered with bacteria.

3.10. The concentration is ideal for our sample isolation conditions. As seen in the optical micrograph in Figure 3.9, the bacteria is well-dispersed across the membrane where many clusters are isolated within at least 80 μm diameter. Figure 3.10(top) shows a tetrad isolated within a 100 μm diameter with a neighbouring cluster of 2 tetrads; this is visible in the 40X-magnified image in Figure 3.10(bottom).
Note that although the strain was not cultivated but only extracted from a freeze-dried palette and hydrated, we find the bacterial tetrad structure intact as in Figure 3.10(bottom). Since there is no nutrient medium for the bacteria to cultivate, they will merely be inactive. We select bacterial clusters with sizes under 10 μm to be imaged in the setup in order to comply with the size of the oversampling conditions and with the holographic separation conditions for selected reference pillars. In addition to the aforementioned home-made hydrated sample, an active culture of the bacterial cells was ordered from DSMZ where the freeze-dried culture is let to cultivate in a nutrient medium over silicon nitride membranes and Kapton foils in an Agar plate. The cultures were produced in three different concentrations for optimal sample isolation. The active cultures were prepared by Dr. Rüdiger Pukall from DSMZ. Figure 3.11 shows a near-field fresnel projection of one of

the bacterial cells align in the x-ray beam at 9.15 keV photon energy. Recording projections at the scintillator detector in the near field helps to align the sample for the holographic setup.

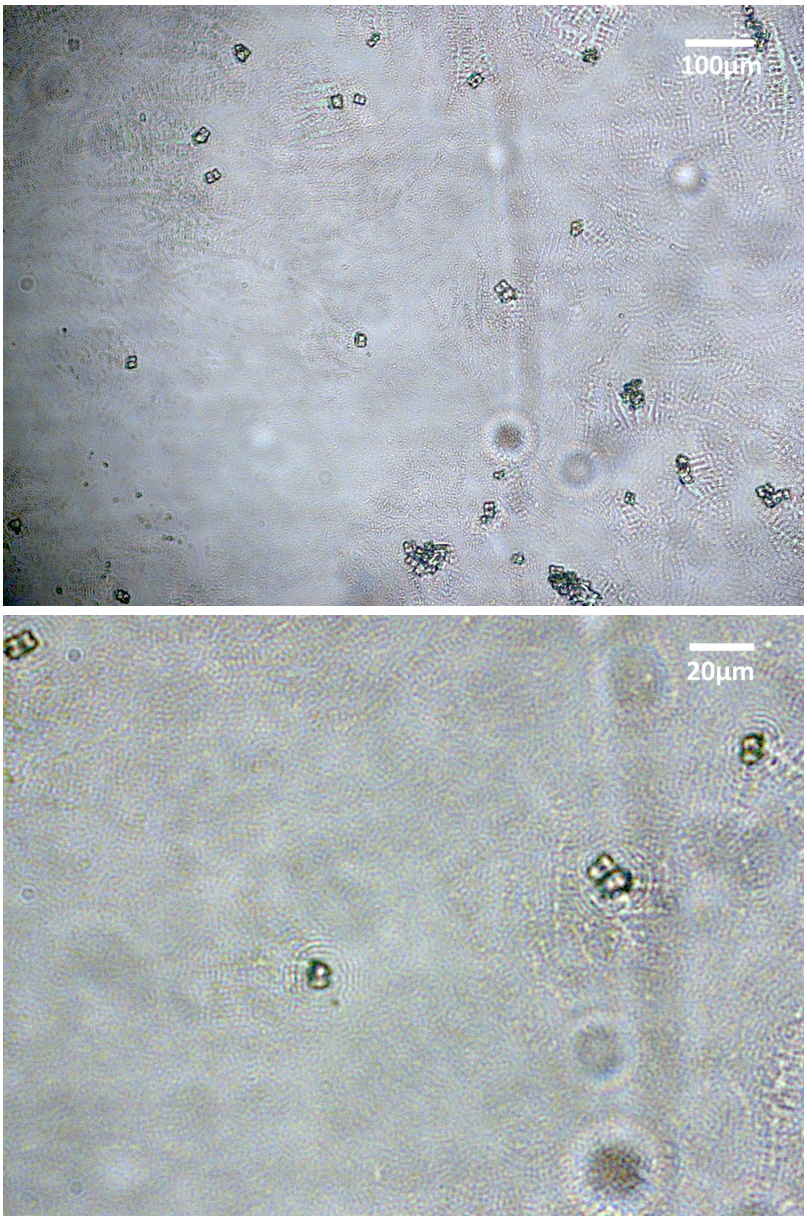

Figure 3.10: (top) Optical microscope image at 20X magnification showing regions with a single bacteria and regions with clusters of two, four or more bacteria. (bottom) 40X magnification image showing the 4 quadrants of the bacterial cells.

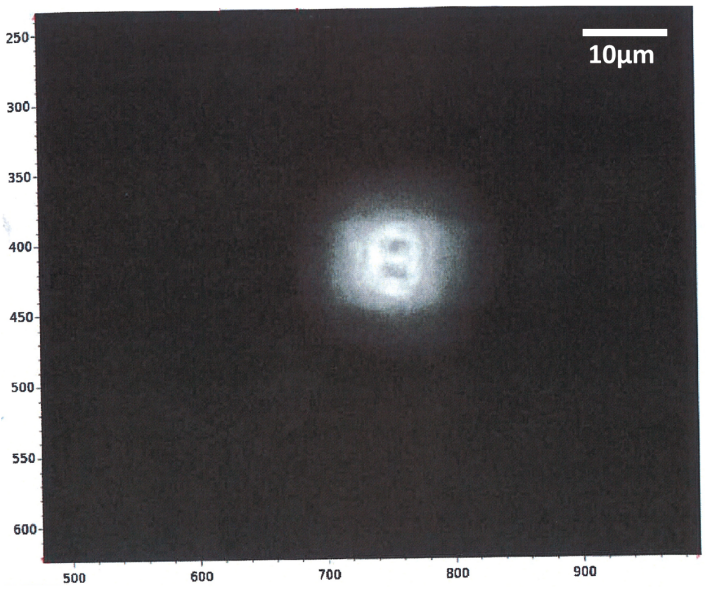

Figure 3.11: Near field Fresnel projection of bacterium illuminated with a parallel coherent x-ray beam at 9.15 keV.

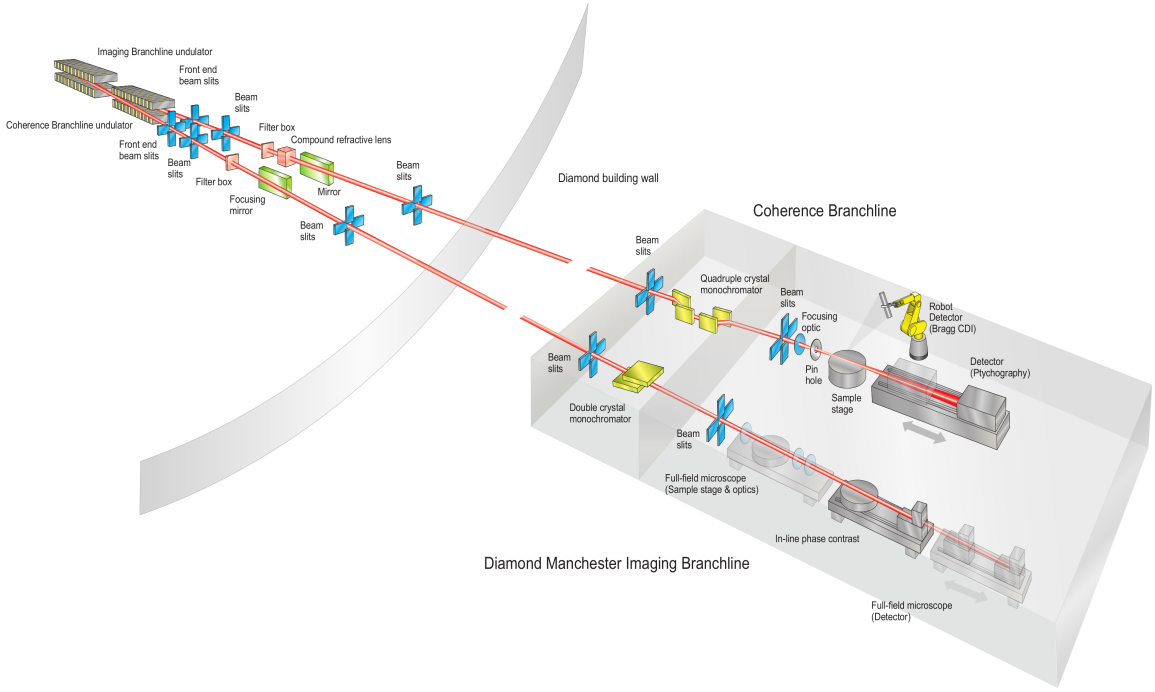

Figure 3.12: Schematic of the two experimental branches at I13 Diamond Light Source. (Figure provided by Ulrich Wagner.)

3.3 Experimental Setup

The Holographic Diffraction X-ray Imaging (HDXI) experiment was set up at the Coherence Branch of the I13 beamline at Diamond Light Source (DLS). The experimental hutch is located at 250 metres from the storage ring to provide high coherence in the order of 300 μm vertically and 150 μm horizontally. We used a monochromatic beam of hard x-rays at energies ranging between 8 keV and 9.7 keV, which was then meticulously trimmed and cleaned using upstream slits to form a flat, uniform and homogeneous beam with high flux. The reference plate is mounted on a x-y-z-θ-ψ piezo stage, behind which the sample plate is mounted on a x-y-z piezo. The reference and sample are hence physically decoupled allowing the translation and rotation of each element independently from the other. This novel aspect, compared to the mainstream work in FTH and extended holography experiment, plays a crucial role in optimising the imaging conditions, improving the reconstruction procedure, as well as allowing 3-dimensional imaging. In this

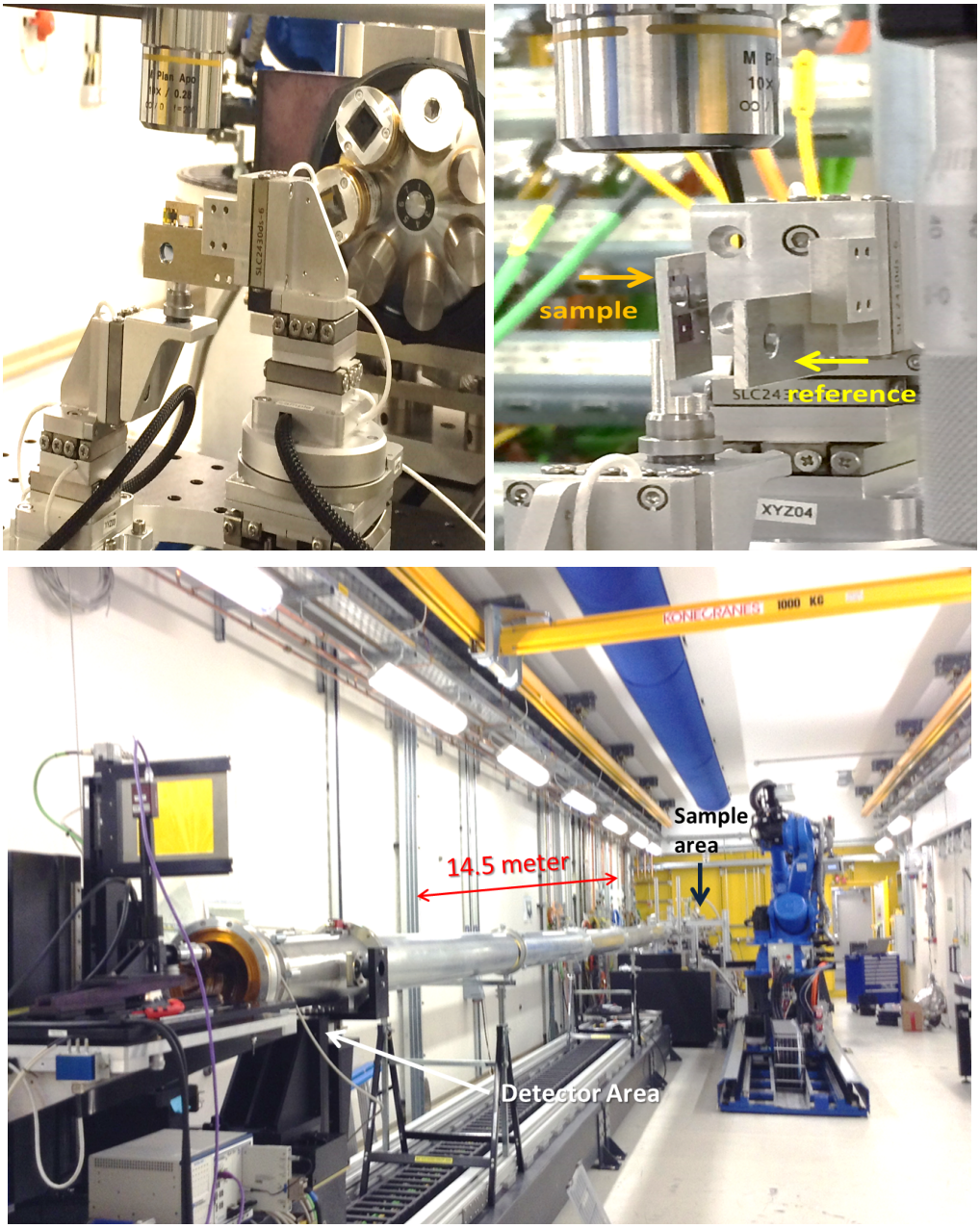

Figure 3.13: (top) Photos of sample plate and reference plate mounted on piezo stages and brought closely together, with the alignment microscope aligned on the top and the scintillation screen in the back. (bottom) The 14.5m hutch distance viewed from the detector side up the flight tubes to sample area.

experiment, the reference plane and sample plane are brought into the beam and roughly aligned using the scintillator detector and then moved by small z-steps until

the separation distance between them is around 100 μm. The centre of rotation and eucentric point are aligned using a nearby PCO4000 CCD camera connected to a scintillation screen. The z-piezos are then locked to avoid the reference and sample crashing. Far-field holographic diffraction patterns are recorded at a *Merlin* [67] quad-chip photon-counting detector located 14.7 m downstream. The monochromator is parked to avoid drift, the CRLs are installed at the specific energy for increased flux, and the flight tubes are pumped down to atmospheric pressure to avoid air scattering. The sample and reference planes are then aligned at the micron scale to commence the measurement. Behind the sample, there are no elements except a 14.7 m flight tube leading to the photon-counting detector at the end of the hutch.

3.3.1 Beam Profile

The x-ray beam incoming from the synchrotron source encounters slits, filters, CRLs, and a double crystal monochromator before it reaches the sample area at 250 m from the storage ring. Five pairs of vertical and horizontal slits are distributed along the beamline: at the front-end (S1), through the optical and experimental hutch (S3,S4), and a few meters from the sample stage (S6,S7). Using the beam-forming slits, the x-ray beam is clipped, trimmed and cleaned to form a flat-field uniform and homogeneous beam profile.

The front-end slits (which are located close to the storage ring) and the S2 slits, as seen in Figure 3.12 are kept wide open to ensure maximum flux. The S3 slits are used to apodise the beam. The further sets of downstream slits S4, S6 and S7 are then used to clip and clean the flares and modulations. The process is done iteratively from S3 to S7 until a flat, uniform, homogeneous beam is created with at least a 50 μm diameter required for flood-illuminating the sample of interest without illuminating unwanted neighbouring objects. After forming the required beam profile, the slits, windows, and stages are then finally readjusted to obtain the diffraction pattern that portrays the optimal coherence, sharpest, furthermost and most symmetric diffraction fringes, lacks flares due to the upstream slits or irrelevant diffraction effects due to dust on the windows, specks on the edges of

the slits, or other artefacts due to mid-stream components. The beam profile is measured to have high coherence [68] as seen in Figure 3.14, with a total flux of 240 G photons/s/mm^2 according to the ID goniometer, and a total detected number of photons at the detector plane of $3 \cdot 10^6$ - $7 \cdot 10^9$ photons depending on the sample arrangement.

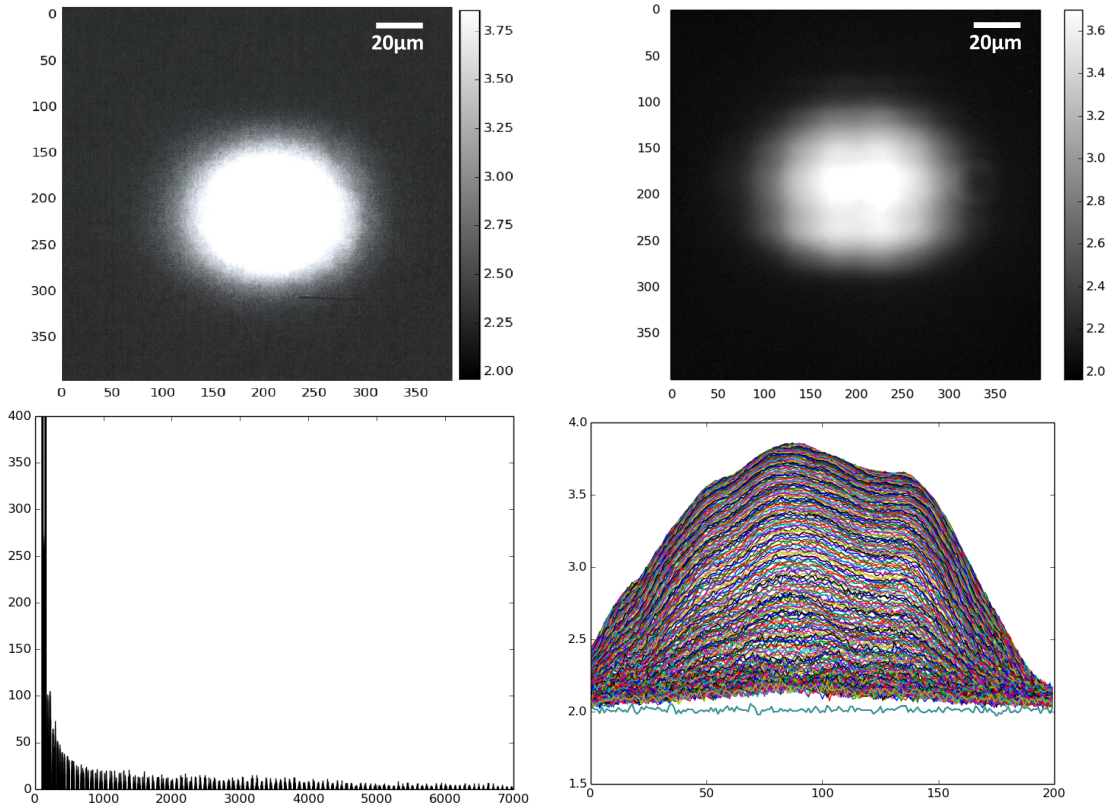

Figure 3.14: (top left) beam profile as recorded on scintillator screen, (top right) beam profile with the sample in the beam, (bottom left) histogram showing a distribution attributed to high coherence, (bottom right) surface plot of the beam profile (in top left).

3.3.2 Detector

The detector used to record the far-field diffraction data in this experiment was the Medipix3, a photon-counting solid state pixel detector with a 300 μm thick silicon sensor. It has a 256 $\times$ 256 array of 55 μm pitch pixels and a configurable counter depth, most commonly used in 12 or 24 bit modes. The Medipix chip is controlled by the Merlin readout system (developed at Diamond). There are 4 pixel arrays of 256 $\times$ 256 pixels^2 each, with a pixel size of 55 $\times$ 55 μm^2, creating a sensor area of 28 $\times$ 28 mm^2. The minimum exposure time is 1 μs with no practical maximum. As HDXI is represented as a single-shot non-iterative imaging method, it is quite beneficial to use photon-counting detectors since they only account for Poisson noise. Since it is not a scanning method and does not use iterative reconstruction routines, it is important that the data is recorded with low-noise detectors with a narrow point-spread function. In the case of the Medipix3, and most photon-counting detectors, the point-spread function is one pixel wide. This means that below a certain threshold count (in a linear acquisition mode), every incident photon results in one photon count which only generates statistical noise and no background noise as compared to scintillation detectors. This attribute is hence highly beneficial for single-shot recording of diffraction data and direct image reconstruction methods such as HDXI.

During data acquisition, the gap between the four sensor chips appears as a horizontal and vertical zero-intensity line of 3 pixels and 5 pixels wide respectively. By shifting the detector by 5 pixels in x and y and patching-up the 4 recorded arrays we obtain one array that corrects for the gaps. Figure 3.15 shows the four shifted detector arrays and the resulting patched-up array by numerical processing in Figure 3.15(e) where the horizontal and vertical gaps as well as the dead pixels have been filled.

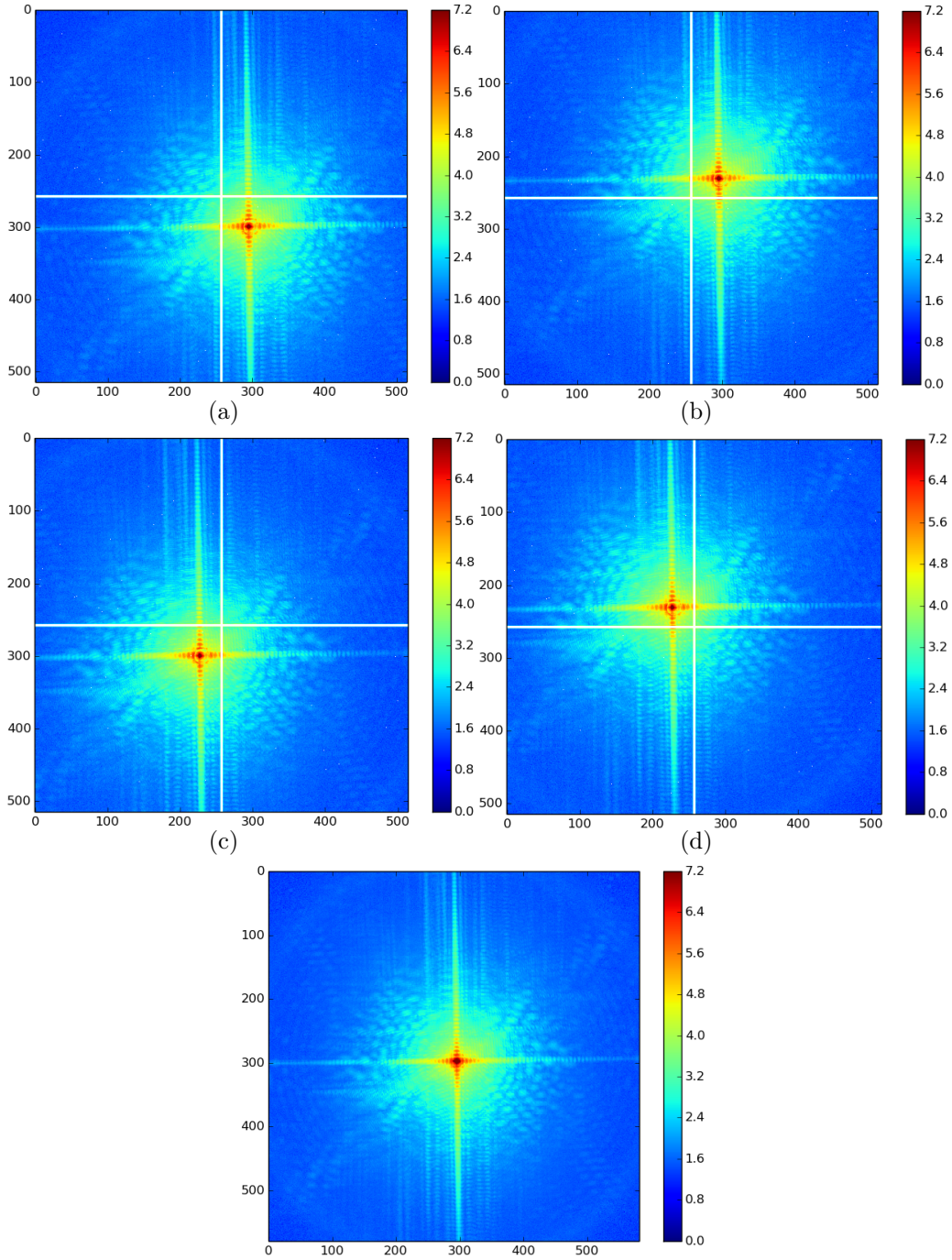

Figure 3.15: (a) to (d) The four shifted recorded detector arrays with showing the gaps. (e) final array corrected by patching up the arrays (a) to (d).

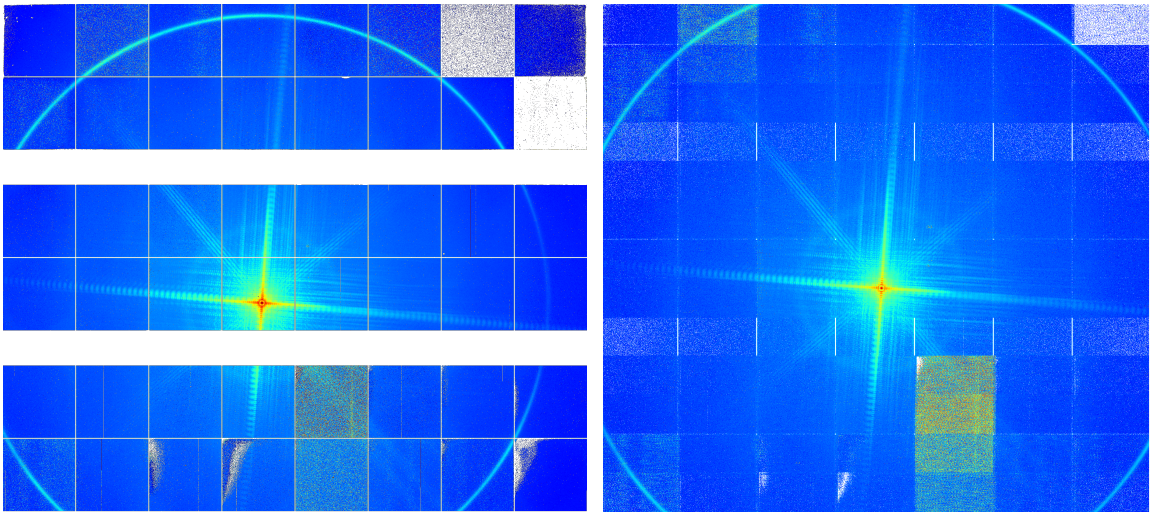

(a) (b)

Figure 3.16: (a) Diffraction pattern recorded with the large-area detector Excalibur showing a full sensor area of 8×6 14 mm chips with two 6 mm gaps. (b) Correcting (a) for the gaps by shifting the detector.

Large Area Photon-Counting Detector

The Excalibur detector is composed of three 8×2 modules, 14×14 mm^2 each, amounting to a detector array of 2096×1796 pixels^2 and a sensor area of 114×99 mm^2 with 2×6 mm gap. Similar to the Merlin, the Excalibur is a photon-counting detector developed at Diamond. During this experiment we used the first version of the Excalibur which contained a few dead areas. This makes the correction more difficult than with the current Merlin array. Figure 3.16 shows the recorded diffraction pattern using the Excalibur. The array in Figure 3.16(b) corrects for the horizontal gaps by shifting the detector. We note that the procedure has not been optimal to correct for all the defective chips in addition to the vertical gaps between the chips. To perform such a correction, we would require to shift the detector by a distance in $\pm x$ and $\pm y$ that amounts to the size of one chip (14 mm). This would require a long wait time for the heavy stages to move by 14 mm which is not ideal from a single-shot point of view since the sample is likely to change during the long wait time. Nevertheless, the large area of the Excalibur allows

us to record high resolution diffraction patterns up to the diffraction limit for the case of HDXI using phase-shifting extended objects. The new Excalibur detector, released in Fall 2015, promises to deliver all fully-functional modules free of defects and dead areas by using the Medipix3 chip as with the Merlin. Using the new Excalibur [69, 70] for HDXI experiments will be highly beneficial in many ways, the most prominent of which are two: 1. The large sensor area will allow to push the resolution limit of HDXI reconstructions by recording higher scattering angles, and 2. a larger number of detector pixels will reduce the effective object-area pixel size. This means that nano-sharp reference objects may well be used to yield nano-scale image resolution.

Beamstop

Although necessary to protect the detector from the intense central beam, the beamstop plays an important role in obtaining the optimal reconstruction from the diffraction data. Depending on the size and material, the beamstop can cause artefacts when reconstructing the object space. For example, a relatively large beamstop with a sharp transmission profile creates background low-frequency circular fringes which may overpower the signal of the reconstructed object. Therefore the shape and profile of the beamstop should be carefully selected. Ideally, it is preferable to characterize the beamstop transmission profile in order to correct for it in the HDXI data.

We used a 25 μm thick Nb beamstop of 1 mm diameter to block the central beam. To facilitate post-processing corrections due to the beamstop artefacts, we find the transmission profile of the beamstop by recording and dividing two arrays: 1. the illumination of the beamstop in an empty beam (Figure 3.17(a)), and 2. the empty beam at the same slit arrangement (Figure 3.17(b)), energy, and detector position. This enables us to calculate the attenuation profile of the beamstop (Figure 3.17(e)) and apply the corresponding scaling factor at different beam energies. Hence we use the calculated profile to correct for the beamstop in the recorded HDXI data. Note that this procedure is not necessarily needed but might come in handy in case the beamstop edges are inducing strong artefacts.

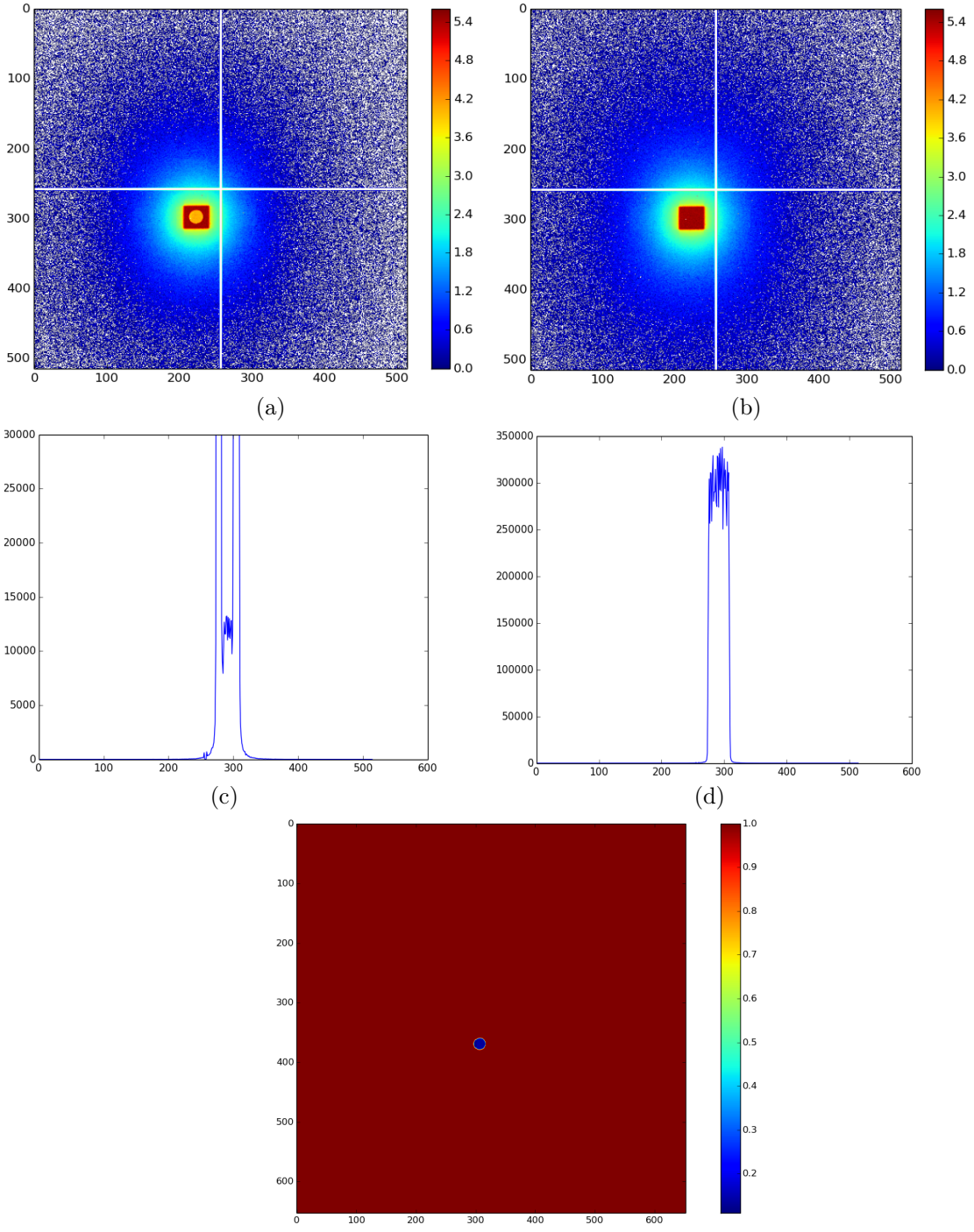

Figure 3.17: (a) illumination of the beamstop in the empty beam at 8 keV. (b) empty beam without beamstop at exact parameters as (a). (c) line profile of (a). (d) line profile of (c). (e) transmission profile of the beamstop calculated at 8 keV by dividing (a) by (b).

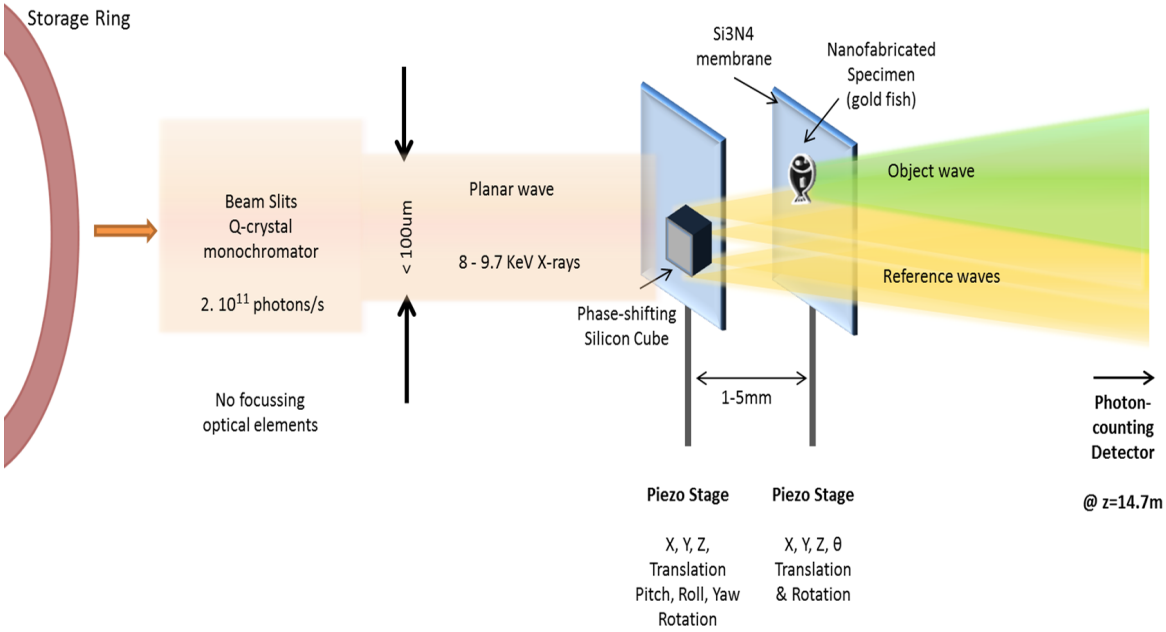

Figure 3.18: Schematic of the setup HDXI using phase-shifting references where the sample plane and reference plane are decoupled and separately mounted on piezo stages. The sample is laterally offset with respect to the reference as needed.

3.3.3 Measurement

As in the schematic of Figure 3.18, the membrane containing the phase-shifting pillars is positioned before the sample plane such that the two planes are separated by 0.1 - 0.3 mm (Figure 3.19(b)). The reference substrate is a clean silicon wafer which is transmissive enough to allow the direct beam to penetrate to the sample plane. The two different test-samples and the two biological samples are attached all on one sample plate mounted on a magnetic stub to facilitate the process of imaging many samples without dismounting (see Figure 3.19(a)). We align the centered positions of the test-sample structure and the reference structure with respect to the beam using a near-field scintillator detector (Figure 3.20(a), (b), (c)).

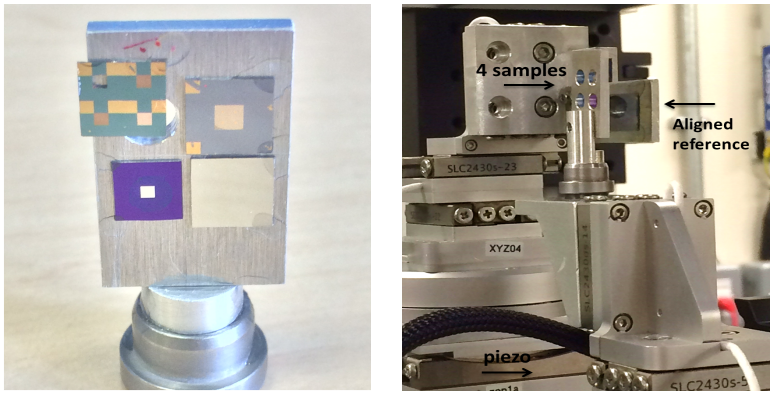

(a) (b)

Figure 3.19: (a) 4 samples mounted on a magnetic stub. (b) overview onto the sample stage where the sample plate is placed behind the reference plate and the microscope lens is positioned above the sample plate for precision alignment.

Sample-Reference Alignment

The test-sample is kept at the centre of the beam (or at the x-y position with the highest photon counts near the centre) and the reference pillar is laterally offset by a distance ρ from the sample. According to the separation conditions mentioned in Chapter 2, the reference pillar was offset from the centre by 7 - 8 μm in the y-direction and by 1 - 2 μm in the x-direction. The greater offset was set in y due to the fact that the vertical coherence in this setup is higher than the horizontal coherence. Figure 3.20(a) shows the test-sample Fresnel pattern at 9.15 keV of the 4 μm gold fish centered in the beam with the 10 μm silicon pillar offset to the right. Figure 3.20(b) shows the 10 μm silicon pillar centered in the beam with the test-sample behind it at the centered position as well. The circular fringes from neighbouring sample objects appear around the fringes of the silicon pillar. Figure 3.20(c) shows the 10 μm silicon pillar offset in x and y with respect to a sample of hydrothermal-vent sea creatures recorded at 8 keV. This demonstrates the alignment procedure where each of the elements are individually centered in the beam and then one is offset by a distance ρ in 1 μm steps using the piezo stage movement. This alignment procedure has proven to be an effective method within ± 0.5 μm as we have seen in the reconstructions. After computing the reconstructed object space we find that the alignment and offsetting executed by

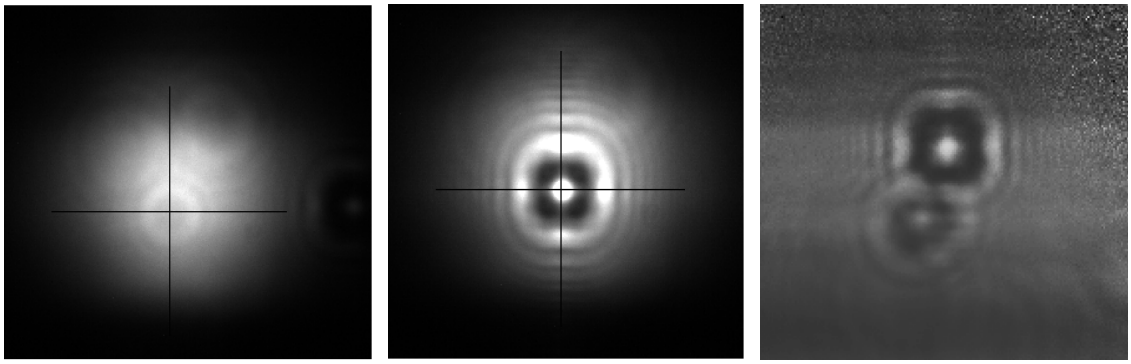

(a) (b) (c)

Figure 3.20: (a) Near-field projection of the test-sample (gold fish) showing circular Fresnel fringes, (b) projection of the aligned reference pillar with the offset test-sample, (c) near-field projection of aligned reference pillar with a hydrothermal vent sea creatures sample.

piezo steps using the method above satisfies the separation conditions and results in the cross-correlation reconstructions appearing at the exact positions $\pm 0.5\ \mu m$ as estimated per the alignment procedure. For better statistics, we record additional datasets where the reference and sample positions are shifted by $\pm 1\ \mu m$ in the x- and y-direction.

Oversampling

At 9.15 keV photon energy, with a detector pixel size of 55 μm, and $z = 14.5$ m, the reconstructed object area $S_o = N \times p_{obj} = z\lambda/ds$ is 34 μm which means the oversampled area S_{Ny} is 17 μm. The autocorrelation and reconstruction images that result of Fourier-transforming the recorded holographic diffraction pattern to object-space must all be oversampled within the area $S_{Ny} = 17\ \mu m$. Thus the positions (x_o, y_o and x_r, y_r) and sizes (L_o and L_r) of the sample and the reference within the illumination area must be chosen compliantly with this condition. In this experiment, we maintain that a) the lateral coherence ℓ is greater than 17 μm, b) the illumination is uniform and intense within the 17 μm area, and c) L_o, L_r, and ρ are each less than S_{Ny}.

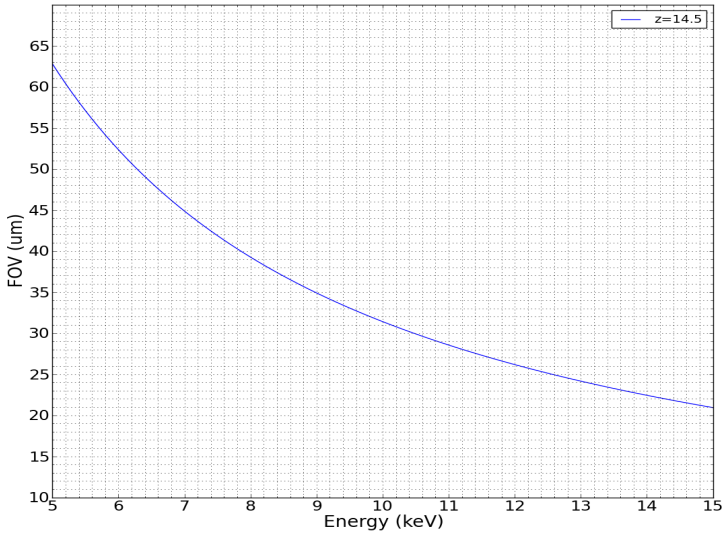

Figure 3.21: Plot of the reconstructed object area as a function of X-ray energy at a propagation distance of $14.5m$.

Data Acquisition

With the reference pillar offset with respect to the sample (as described above) and both planes separated by around 100 μm in z, both structures are illuminated by the uniform parallel beam at 9.15 keV. Data is recorded at the Merlin detector set $14.5m$ downstream from the sample stage. Every data set comprises recording the diffraction pattern at the 4 shifted detector positions with the beam stop in place. The ion chamber at the entrance of the upstream slits detects 242 $\cdot 10^9$ photons/s/mm^2. At the detector, the diffraction pattern resulting from the scattering off the sample and reference plane propagated by $14.5m$ ranges between $3 \cdot 10^6$ photons and $7 \cdot 10^9$ photons depending on the type of sample. The ID gap is tuned or detuned to increase or decrease the total flux incident on the detector and to maintain the linear counting mode of the detector. Depending on the required flux, the exposure time ranges from 60 s to 800 s with a typical value of 200 s. The cumulative exposure time for a sample at a single position is around 800 s. The above-mentioned beam parameters provided the competent setting to yield good reconstructions and sufficient signal-to-noise ratio for the specific samples used. In the next section, we will show the effect of the flux and exposure time on the SNR statistics, contrast, and visibility of the reconstructions.

4 Experimental Results: HDXI using Phase-Shifting References

In this chapter, we will elaborate the data processing procedure that leads to a successful reconstruction of a specimen by HDXI. We will show successful sample reconstructions obtained using the phase-shifting references in a holographic diffraction setup by numerical processing of the recorded data using the real-space and Fourier-space linear differential operator. The results will be compared with varying flux, object scattering signal strength, and the resolution limit of the system will be derived. Reconstructions of coccolithophorids of marine microplankton samples will be shown and characterised. Furthermore, we will compare the results using a full-area phase-shifting silicon pillar reference with the results using a wireframe reference fabricated with high edge resolution by atomic layer deposition. We will highlight the compound reference type that constitutes a silicon pillar (light material square reference) overlapping with a nano-layer of iridium (heavy material wireframe reference). The results of using such a compound reference will show differential phase and amplitude contrast as well as edge enhancement and will provide a much higher resolution than the previous reference type where the resolution reaches the detector limit. The experimental reconstructions will be compared to simulations to properly characterise the physical phenomenon and mathematical reasoning behind the holographic behaviour of the compound wireframe reference. Furthermore, the imaging method is extended to bacterial samples to demonstrate the applicability of this method to weakly-scattering biological samples composed of mainly hydrocarbons which contribute a minuscule absorption and phase shift.

This will extend holographic diffraction imaging using phase-shifting references to a wide variety of specimens and will prove that it efficiently produces sample images with amplified contrast and nanoscale resolution by single-shot exposure and non-iterative numerical reconstruction. In addition, a quantitative analysis of the measured amplitude and phase of the sample reconstructions will be shown to demonstrate that the method not only provides spatial images of the sample but also quantitative, chemical, and depth information. Finally, we will show a comparison of the reconstructions using phase-shifting references, discuss image averaging and additional prospective refinement methods, as well as a comparison to ptychography, and conclude the chapter.

4.1 Sample Reconstruction

The recorded diffraction patterns at the 4 shifted positions of the detector are shifted, padded, and combined to form a single corrected diffraction patten where the detector gaps are filled. When needed, artefacts introduced by sharp beamstop edges are also corrected for by dividing the recorded array by the beamstop illumination profile. We correct for additional dead pixels in the detector array by setting the value to an average of neighbouring values. The final data array is then run into the numerical algorithm to obtain the reconstruction of the object.

The main computational tools involved are the inverse Fourier transform and the directional filter. Hence the reconstruction is obtainable by two different procedures: a) applying two directional derivatives to the inverse Fourier transform of the diffraction pattern (the autocorrelation) i.e real-space filtering, or b) applying a linear differential operator to the diffraction pattern followed by an inverse Fourier transform i.e Fourier-space filtering as explained in Chapter 2. The reconstruction procedure illustrating the two methods is shown in Figure 4.1. The purpose of the directional derivative and the differential operator is to reduce the extended reference to a set of point-source delta-like functions. The directional derivative is set according to the directions of the two sides of the square reference pillar. Similarly, the direction of the linear differential operator is set by inspecting the direction of modulations due to the extended reference in the recorded diffraction pattern without needing prior information about the shape of the reference. We will refer to the reconstruction obtained by the double gradient in x and y as Gxy and that obtained by the linear differential Fourier filter as DF-filter.

After differentiation, we apply a near-field propagator by a distance that corresponds to the z-separation between the object plane and the reference plane. If the sample and reference structure lie on the same substrate such that they are coplanar, there is no need for the final propagation step. Hence, we obtain the final in-focus sample reconstruction at the position corresponding to the X-Y offset distance of the sample with respect to the reference.

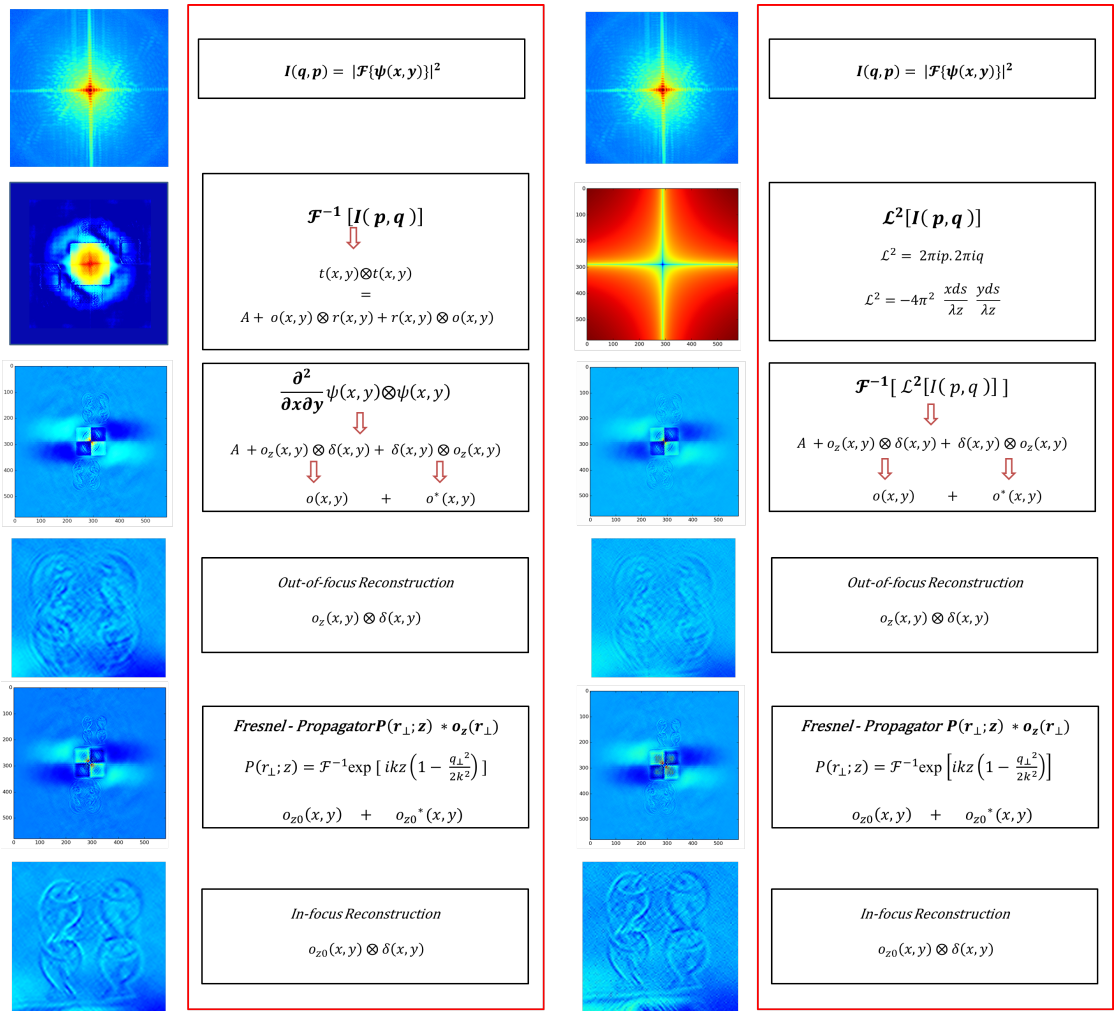

Figure 4.1: Summary of numerical procedure leading to the sample reconstruction using the Gxy method (left) and the DF-filter method (right).

To remove parasitic background artefacts, the object reconstruction is further refined by background subtraction in real space. This is done by recording three separate diffraction patterns for every data set with a) none of the reference or sample structures in the beam path, b) only the reference pillar positioned in the beam, and c) only the sample in the beam. Hence, we obtain three separate autocorrelations each of the sample and the reference structure individually, as well as that of the beam through the substrates. The effect of real-space filtering is studied by subtracting the sample, reference, and background autocorrelations from the final reconstruction to remove the background artefacts.

Holographic diffraction imaging has been successfully implemented using two different types of phase-shifting extended references described in Section 3.1: a) square-faced silicon pillars, and b) iridium nanolayer-coated square-faced silicon pillars by ALD; representing a compound wire-frame structure. In Section 4.1.1, we will discuss the results obtained with type-(a) silicon reference structures. Type-(b) ALD reference results will be discussed in Section 4.1.2.

The samples imaged using the aforementioned reference types were:
a) gold *fish* test-sample, b) gold *fish in a bowl* test-sample, both with $\rho = 19.32$ g/cm^3, 4 μm length and 340 nm thickness contributing to a 90% transmission and 0.18π phase shift (Section 3.2.1). The gold fish test-sample contains resolution-testing features: a 400 nm gold dot as the eye of the fish, 2 straight gold bars with 700 nm length, 150 nm width, and sub-50 nm separation as the fins, a 150 nm outline of the fish, and sub-100 nm diagonal lines as the inner detail of the tail. ;
c) weakly scattering silicon dioxide *fish-bone* test-sample with $\rho = 2.2$ g/cm^3, 4 μm length and 590 nm thickness contributing to a 99.7% transmission, and a 0.05π phase shift, coated by atomic layer deposition with 10 nm iridium of $\rho = 22.42$ g/cm^3, with the iridium edge (extended along the 590 nm SiO_2 edge) contributing in the forward direction to 83% transmission and 0.36π phase shift;
d) marine micro-plankton coccolithophorids (or platelets) composed of calcium carbonate with $\rho = 2.7$ - 2.85 g/cm^3 and sizes ranging from 3 μm to 6 μm (see Section 3.2.2).
d) Deinococcus Radioduran bacteria with sizes ranging from 5 μm cells to 20 μ tetrads with an approximate density of $\rho = 1.35$ g/cm^3 considering the cells are mainly constituted of a protein of empirical formula H50C30N9O10S1 (See Section 3.2.2). With the given parameters we estimate a transmission of 99.8% and a 0.1π phase shift.

Table 4.1: Sample properties at 9 keV x-ray photon energy

Sample	gold fish	fish bowl	SiO2/Ir fish bone	Plankton	Bacteria
thickness	340 nm	340 nm	590 nm	2 μm	500 nm
length	4 μm	4 μm	4 μm (SiO_2) 30 nm (Ir)	4 - 6 μm	4 - 10 μm
electron density ρ (g/cm^3)	19.32	19.32	2.2 (SiO_2) 22.42 (Ir)	2.7 - 2.85	1.35

Table 4.2: Sample transmission and phase shift at 8 keV - 9keV x-ray photon energy

Sample	gold fish	fish bowl	SiO2/Ir fish bone	Plankton (2μm - 5μm)	Bacteria
T (9 keV)	90.7%	90.7%	99.7%(SiO_2) 83.5% (Ir)	97% - 92%	99.8%
Φ (9 keV)	0.18π	0.18π	0.048π (SiO_2) 0.37π (Ir)	0.2π - 0.5π	$\leq 0.1\pi$
T (8 keV)	87.2%	87.2%	99.6%(SiO_2) 77.6% (Ir)	96% - 90%	99.7%
Φ (8 keV)	0.21π	0.21π	0.05π (SiO_2) 0.425π (Ir)	0.23π - 0.59π	$\leq 0.12\pi$

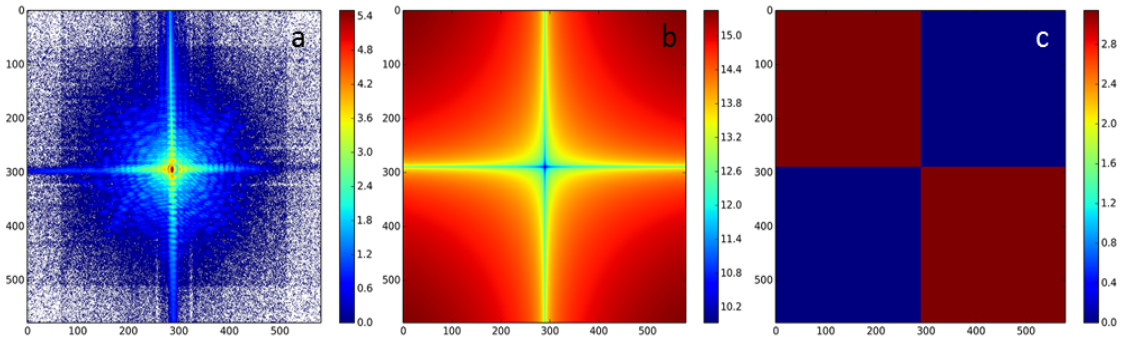

Figure 4.2: (a) Recorded intensity distribution of far-field diffraction pattern with the reference and sample coherently illuminated at 9.096 keV. (b) DF-filter amplitude array (c) DF-filter phase array to be multiplied by (a).

4.1.1 Results: Silicon Pillar Extended Reference

Reference silicon pillars with lateral sizes ranging from 4 μm to 20 μm with a fixed height of 9 μm were tested in this experiment. With a 38.7 μm reconstructed field of view and the larger dimension of the test-sample being 4 μm, we find that the most successful results were obtained with the 4 μm and 6 μm reference square sides due to the high flux density and beam uniformity close to the center of the beam in addition to the sufficient oversampling of the object-reference transmissivity.

Figure 4.2 shows the diffraction pattern recorded using a photon counting detector with N = 515 × 515 px^2 and 55 μm pixel size, measured at 9.096 keV photon energy with 50 sec exposure time and z = 14.5 m using a reference silicon pillar of 4x4x9 μm^3 that is vertically offset from the centered gold fish sample by y = 6 μm. The total number of detected photons is 3.3 $\times 10^7$ counts at 50 sec exposure time. The recorded diffraction pattern in Figure 4.2(a) is the result of patching up four shifted detector arrays. This procedure increases the total number of pixels of the corrected array to N = 579 x 579 px^2 resulting in a smaller pixel size in object-space.

The corrected diffraction pattern is processed through the Gxy and DF-filter method (as described in Figure 4.1). The amplitude and phase of the DF-filter array by which the recorded array is multiplied is displayed in Figure 4.2(b) and (c)

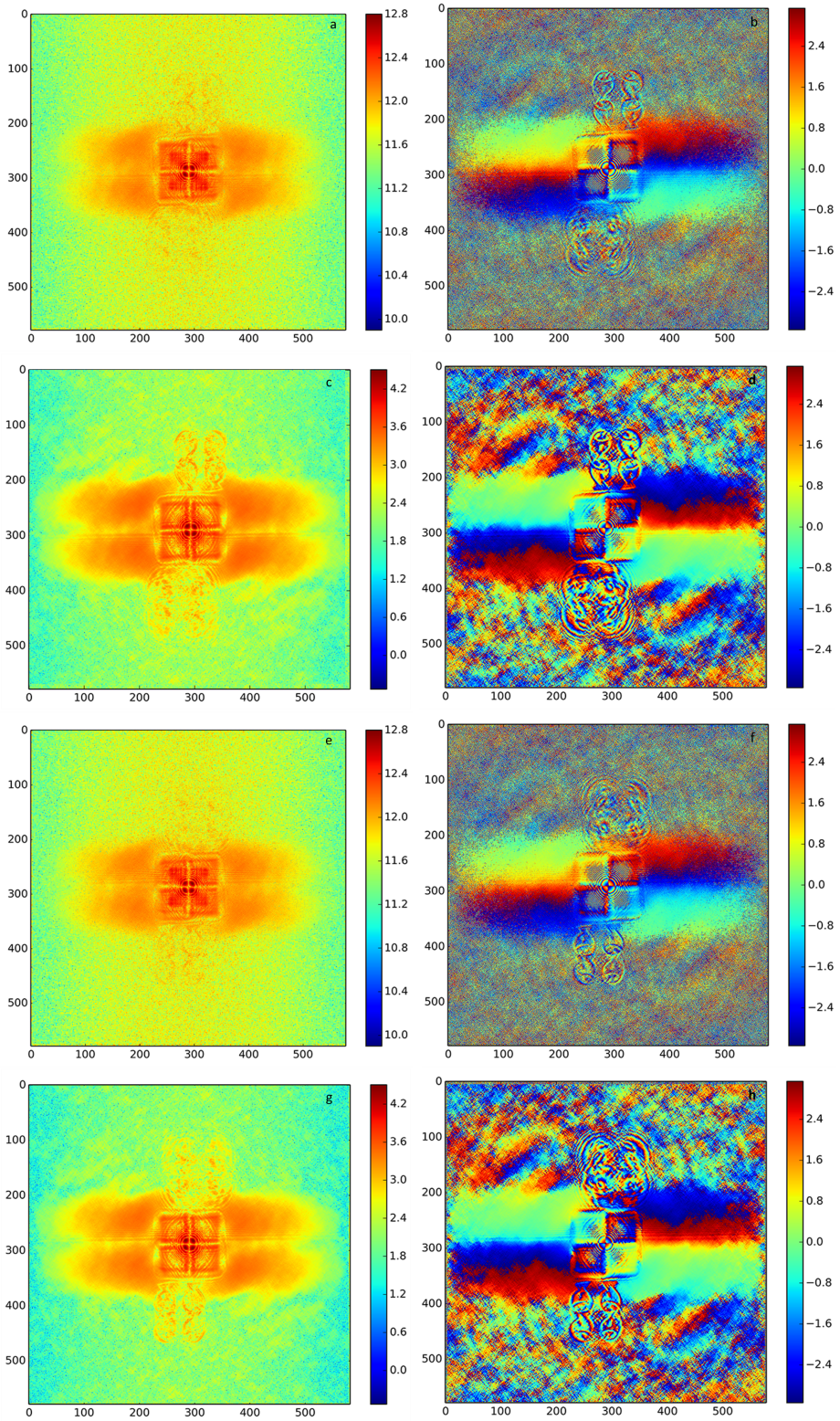

Figure 4.3: Raw amplitude and phase reconstructed FOV using (a,b) DF-filter propagated to +3.5mm; (c,d) propagated to -3.5mm; using Gxy method (e,f) propagated to +3.5mm; (g,h) propagated to -3.5mm. FOV = 38.7 μm.

respectively. The result of applying the two methods and performing a near-field backward propagation by ± 3.5 mm is shown in Figure 4.3 as the amplitude and phase of the final reconstructions.

At the center of the reconstruction FOV lies the autocorrelation of the 4 μm reference square silicon pillar which appears as 4 complex-conjugate copies of the square amounting to an area of 8 x 8 μm^2. Overlapping with the reference autocorrelation lies the autocorrelation of the gold fish sample structure with a faint intensity with respect to the reference autocorrelation. After back-propagating to z=-3.5 mm, the differentiated cross-correlation of the reference and sample is located at +7 μm vertically from the center representing 4 in-focus reconstructions of the sample at each of the 4 virtual corners of the reference square. The twin image is located at -7 μm vertically from the center representing 4 out-of-focus reconstructions, which would come into focus when propagating to z=+3.5 mm.

Varying the lateral distance between the center of the reference and the sample would allow the separation or overlap between the autocorrelation components and the sample reconstruction. With a sufficiently sized reference structure, varying the lateral distance between the reference and sample proves to be advantageous compared to methods where the sample and reference lie on one substrate. This allows to collect multiple datasets of various samples by either running through different sample substrates or scanning through many samples on a single substrate while maintaining the incident beam profile, constant experimental conditions, and keeping the reference fixed.

The reconstructions of the sample shown in Figure 4.3 appear to have low intensity with respect to the background signal. The intense blob in the center surrounding the reference autocorrelation appears to overpower the signal of the cross-correlations. This is due to the high intensity central zero-order peak. The horizontal ellipticity of it is due to the fact that the beam-stop positioned at the detector is slightly offset from the central peak resulting in a vertically elliptical zero-order peak. The DF-filter reconstructions in Figure 4.3 (a,b) contain a high-frequency noisy signal in the background due to the fact that the filter is a multiplicative linear operator. In addition, imperfections and fluctuations in

the background signal arise from artefacts at the sample region: surroundings of the sample, nearby structures and edges, the silicon substrate; as well as artefacts that the beam encounters before it reaches the sample such as: the shape of the beam formed by upstream slits, dust and scratches on the silicon windows, imperfections on the edges of the beam-forming slits. The phase of the Gxy reconstruction (in Figure 4.3 (d)) shows a fast rippling phase ramp and that of the DF-filter reconstruction shows a random high-frequency phase fluctuation. All these artefacts result in a deteriorated quality of the sample reconstruction.

Data Correction by Background Subtraction

Fortunately, our experimental setup has been uniquely implemented in such a way to be advantageous over standard co-planar FTH experiments in so far as the reference and sample planes are physically decoupled. We are able to record background projections and subtract that from the signal to enhance the final reconstructions. To that end, for every experimental setup (given that parameters remain constant and drift and vibrations are none), we record the projection of the beam passing through the sample substrate and the reference substrate with none of the sample or silicon pillar structures in view. We also record the projection with the reference pillar but without the sample structure in view. The reference pillar would be placed at the same position at which the holography dataset was recorded. Similarly, we record the diffraction pattern with the sample structure in the beam without the reference pillar in view. Therefore, for a set of data, we have three separate diffraction patterns of the beam alone, the reference alone, and the sample alone, as shown in Figure 4.4(a), (b), and (c) respectively.

This method proves to substantially enhance the quality of the final reconstructions. However, we will see that recording only one additional projection of the beam alone or the reference alone sufficiently demonstrates the desired result to obtain efficient background correction without the need for additional sample exposure. In other words, furthering the exposure dosage on the sample by recording an additional shot of the sample is completely avoidable, which is an important aspect regarding the "diffract and destroy" method applied with FELs. For example, in the case where a sample disintegrates during a single shot, it would

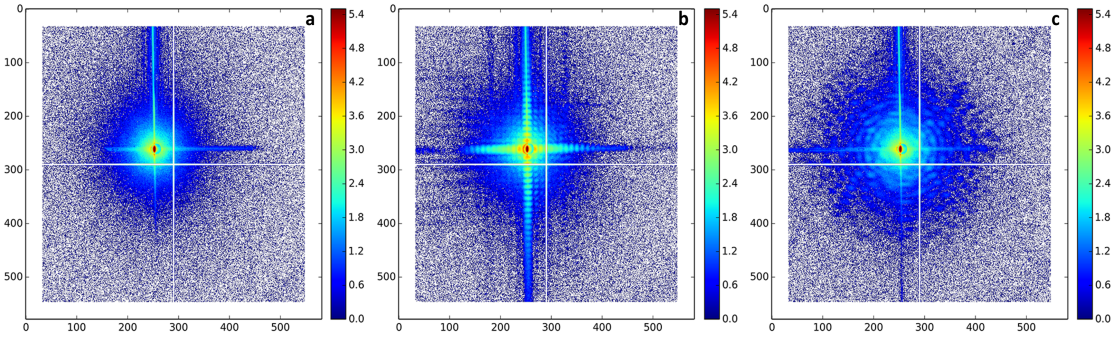

Figure 4.4: Separate recorded datasets of the beam only passing through (a) the substrates, (b) the reference, (c) the sample.

not be possible to take another shot of the exact same sample to subtract from the data, since it has already disintegrated. But it would indeed be possible to obtain a shot of the beam alone or reference alone without having to expose the sample.

In addition, this proves beneficial in the case of a radiation-sensitive sample where it's necessary to maintain a low dosage exposure. This demonstrates the value, advantage, and compatibility of this holographic imaging method with single shot imaging of biological samples with free-electron lasers. The computed reconstruction constitutes a sum of three main components: the autocorrelation of the reference, the autocorrelation of the sample, and the cross-correlation of both. In principle, when subtracting the reconstruction of the reference shot, we expect to remove the autocorrelation of the reference from the final reconstruction. Similarly when subtracting that of the sample alone, we expect to remove the autocorrelation of the sample. The cross-correlations resulting in images of the sample will remain unaffected. In addition, when subtracting the reconstruction of the empty beam, we expect to remove its autocorrelation hence correcting the central peak artefact as well as all contributions of the substrate and the beam-forming components.

Figure 4.5 (left)(a,b,c) show the result of computing the reconstruction by the DF-filter method from the beam alone, reference alone, and sample alone respectively, without propagating by 3.5 mm, whose diffraction patterns are shown in Figure 4.4. Figure 4.5 (right)(a,b,c) show the result of dividing the normalised

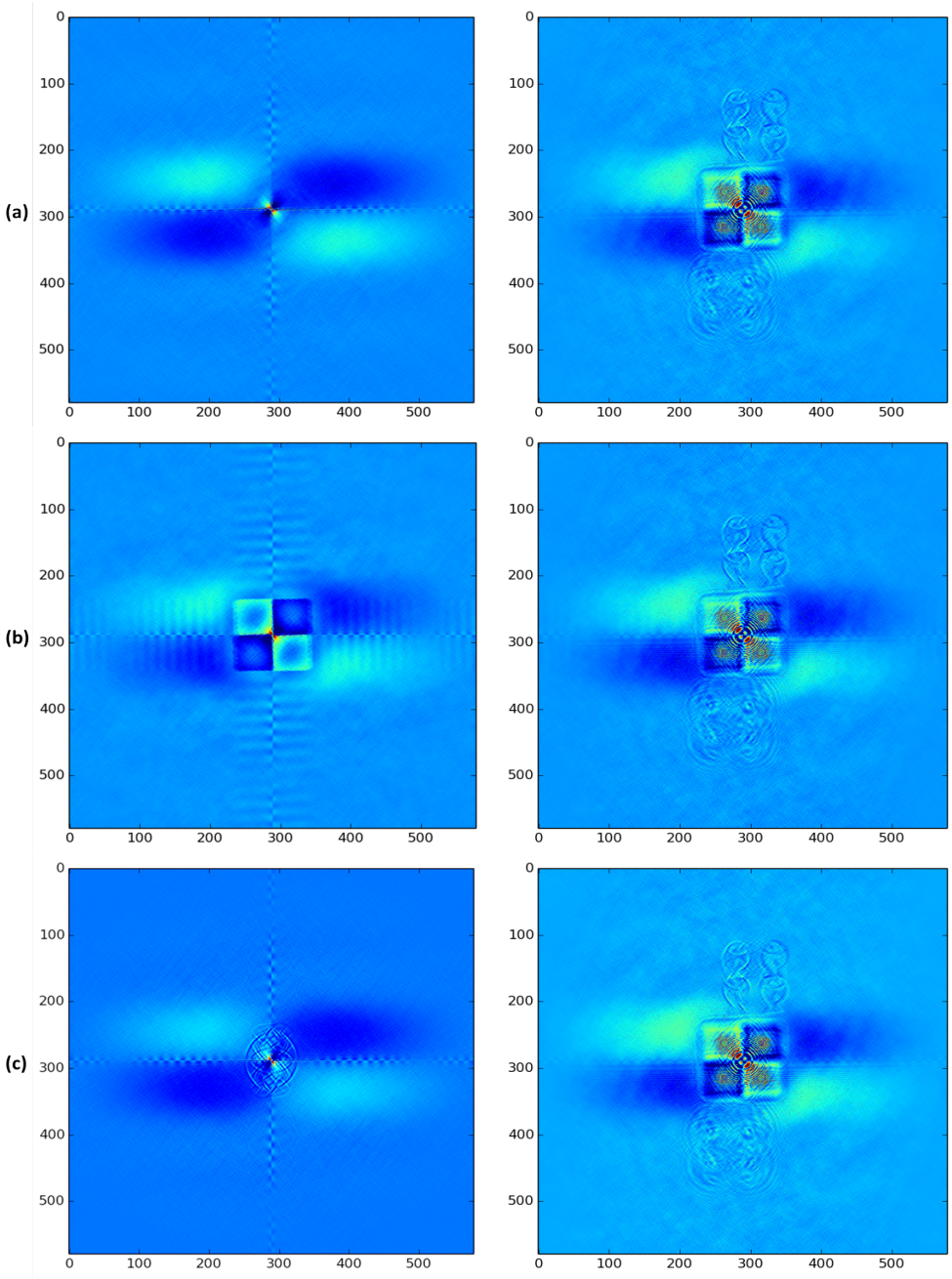

Figure 4.5: (left) Normalised reconstructions using DF-filter (a) beam only, (b) reference only, (c) sample only diffraction patterns. (right) Normalised holographic reconstruction (including reference and object in a single frame) divided by (a),(b), and (c) respectively. FOV = 38.7 μm

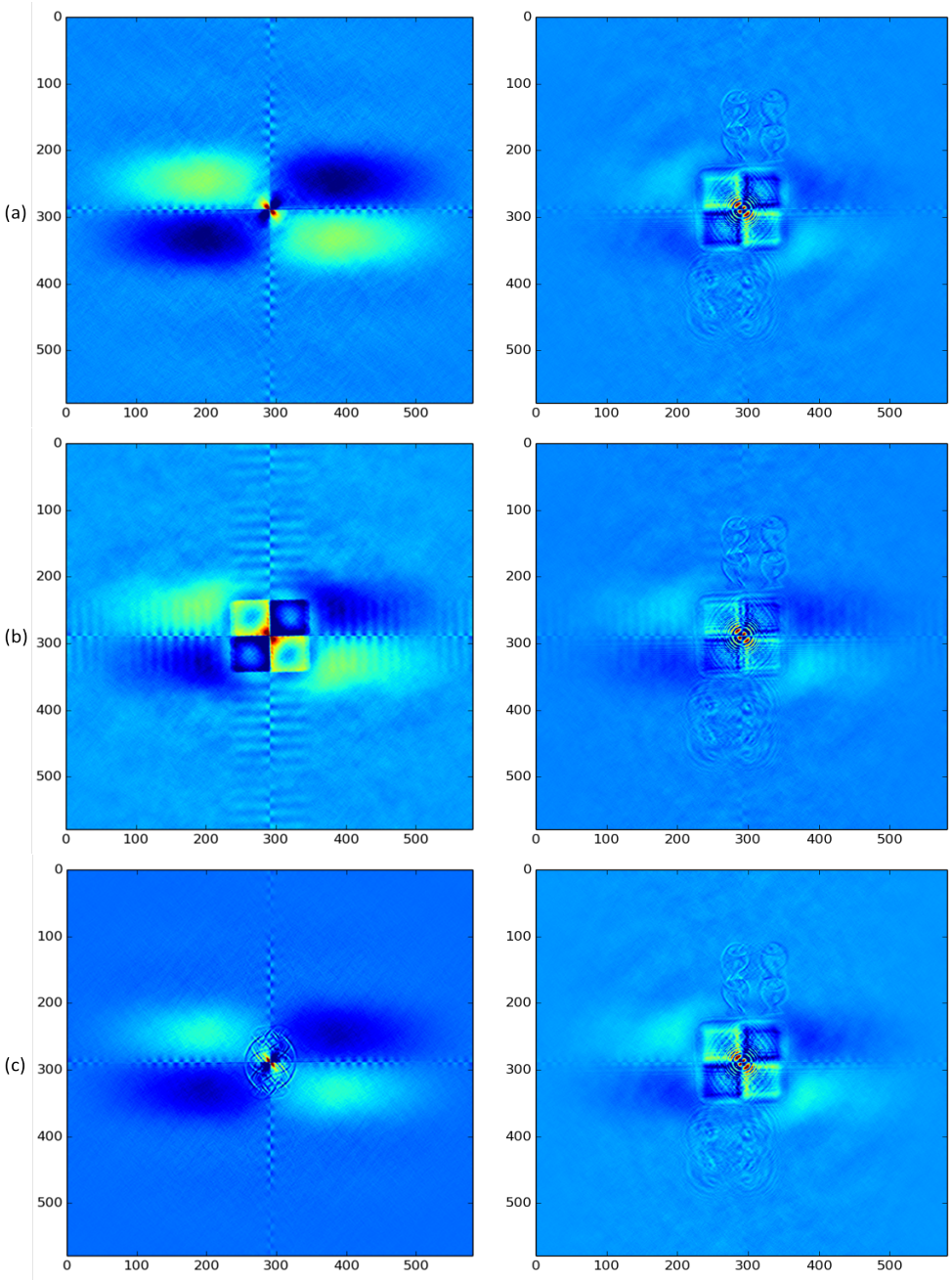

Figure 4.6: (left) Normalised reconstructions using Gxy (a) beam only, (b) reference only, (c) sample only diffraction patterns. (right) Normalised holographic reconstruction (including reference and object in a single frame) divided by (a),(b), and (c) respectively. FOV = 38.7 μm

reconstructions of the data with all the components (o+r) exposed (as in Figure 4.3) by the normalised reconstructions of the individual components (by Figure 4.5 (left)(a,b,c)). Figure 4.6 shows the same procedure but obtained with the Gxy reconstruction method. In both cases the holographic data (right columns of Figure 4.5 and 4.6) are propagated by 3.5 mm to bring the upper four fish reconstructions into focus. By comparing the corrected reconstructions in Figure 4.5 and 4.6 (right column) to the raw reconstructions shown in Figure 4.3, we find a clear uniform background signal that is diminished with respect to the object reconstructions. We also find that the large intense central blob is now reduced substantially. The gold fish sample reconstructions appear to be more distinguishable and have higher signal. As we move on to discuss the results obtained with different samples, references, and exposure time, the enhanced quality of the reconstructions due to this procedure will be more clearly distinguishable. The low-frequency intensity fluctuations are removed, and the fast rippling phase changes are also removed.

It is important to note that the procedure has been effective even though we have only recorded a shot of the background diffraction patterns at a single detector position and not at four shifted positions as was done with the holography data to correct for the detector gaps. This means the effective exposure, the resolution, and the photon statistics are not the same as in the patched up holographic data array shown in Figure 4.2 (a). This is why dividing by the reference pillar reconstruction does not entirely remove the reference autocorrelation. The corrected reconstruction shown in Figure 4.5(right)(b) shows the autocorrelation of the reference square but with a faint intensity compared to the raw reconstruction in Figure 4.3. Nevertheless, the background-correction procedure generates sufficiently improved results. Furthermore, beam stability, mechanical stability, and drift play an important role to maintain optimal data correction. For that reason, it is necessary to record the background shots with the same experimental conditions as the holographic datasets and to minimise the time lapse between the two recordings.

Figure 4.7 shows the cropped reconstruction of the sample and its twin image, respectively, obtained by background correction using the Gxy method (a,b) and the DF-filter method (c,d) compared to the SEM image (e). The experimental

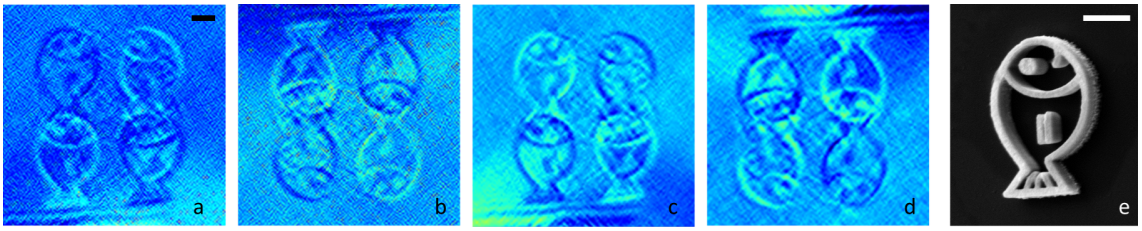

Figure 4.7: Reconstructions and twin images by background correction using (a,b) Gxy method, (c,d) DF-filter method. (e) SEM image of sample [57]. Scale: $1\mu m$.

resolution calculated from the maximum angle of the fringes in the diffraction pattern is estimated to be 102 nm in the x-direction and 88 nm in the y-direction. The lateral coherence of the x-ray source is higher in the vertical than in the horizontal which allows a higher detectability of fringes in the vertical. The image resolution calculated from the reconstructions of the gold fish using the background correction procedure is estimated to have an upper limit of 130 nm and a lower limit of 195 nm while the width of the gold fish outline is 150 nm. We calculate the spatial resolution by performing a 90% - 10% profile plot of the outline of the fish structure as shown in Figure 4.9.

Another test sample with finer features was also imaged as shown in Figure 4.8. The SEM image of the cartoon *fish in a bowl* test sample is shown in Figure 4.8(d) where the longer dimension of the structure is 4 μm, the width of *bowl* outline is 150 nm, similar to the previous sample, but the outline of the inner *fish* is 100 nm and the diameter of the eye is 220 nm compared to 400 nm in the sample in Figure 4.7. The structure in the tail of the fish has gaps of 40 nm, and the gap between the head of the fish and the *water level* starts at 35 nm and increases to 200 nm near the tail. The sample was imaged with the 4 μm reference silicon pillar with 3.2 $\times 10^7$ photon counts and the same exposure time and experimental settings as previously discussed. Figure 4.8(a,b) show the resolved outline of the bowl as well as the finer 100 nm outline of the inner fish. The fine structure of the tail is almost distinguishable, where the limitation here lies in the object-space pixel size. Reducing the pixel size would allow to better resolve fine structures on the nano-scale. The resolution according to the 90%-10% knife-edge criterium is calculated to have an upper limit of 130 nm.

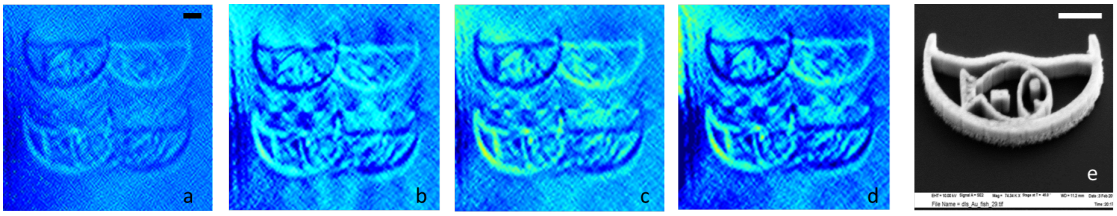

Figure 4.8: Reconstructions and twin images by background correction using (a,b) Gxy method, (c,d) DF-filter method. (e) SEM image of sample [57]. Scale: $1\mu m$.

We find a difference in resolution and SNR between the 4 corner reconstructions due to the fact that the structural quality of the four corners from fabrication is not exactly identical and therefore contribute individual holographic reference properties. Hence, we note the advantage of using an extended reference with multiple corners compared to a single point reference since it would give us a better statistic for obtaining at least one successful reconstruction from a single shot. In addition, the 4 corner reconstructions appear to have alternately positive and negative intensities. This is the result of the edge-transition in phase and absorption between the material of the reference pillar and the substrate. In other words, the differentiated transmission profile would show a positive delta-peak at the edge transition from substrate to reference structure, and a negative delta-peak (or dip) at the transition from reference structure to substrate. Therefore, the 4 alternating positive and negative delta-like functions lead to alternating positive and negative intensity reconstructions in the amplitude, and zero to π alternating phase reconstructions.

Note that the reconstructions from the bottom reference corners are of lower quality and fairly noisy in Figure 4.8. The same was observed with other samples and with some other reference pillars. This is due to the structure of the reference pillar, as we will see later on in the section. In some cases, one or more of the sides of the reference pillar contains small sharp bumps which act as a point source themselves. Hence, when performing the Fourier transform, we obtain a fainter reconstruction of the sample at the position of the sharp bump. When applying the differential operator, we obtain a faint edge reconstruction of that. The reconstructions resulting from the bumps do not have a dominant signal due to the nature of the pinhole / point-source reference with this holographic imaging technique and the

fact that the extended reference provides reconstructions with higher contrast and SNR compared to single point references as discussed in Chapter 2.

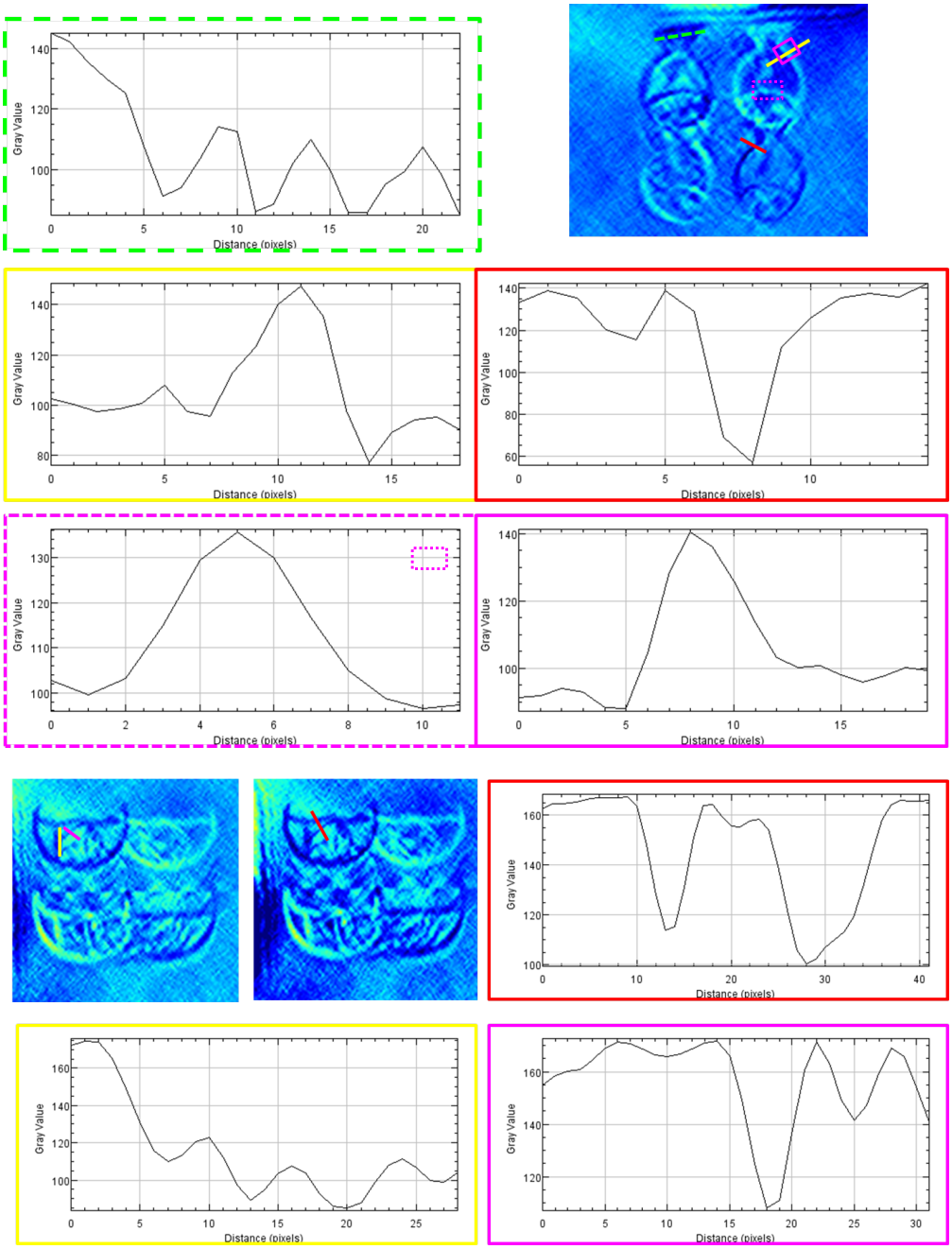

Figure 4.9: Profile plots color-coded by lines in inset showing 90-10% resolution test where 1 pixel is 65nm.

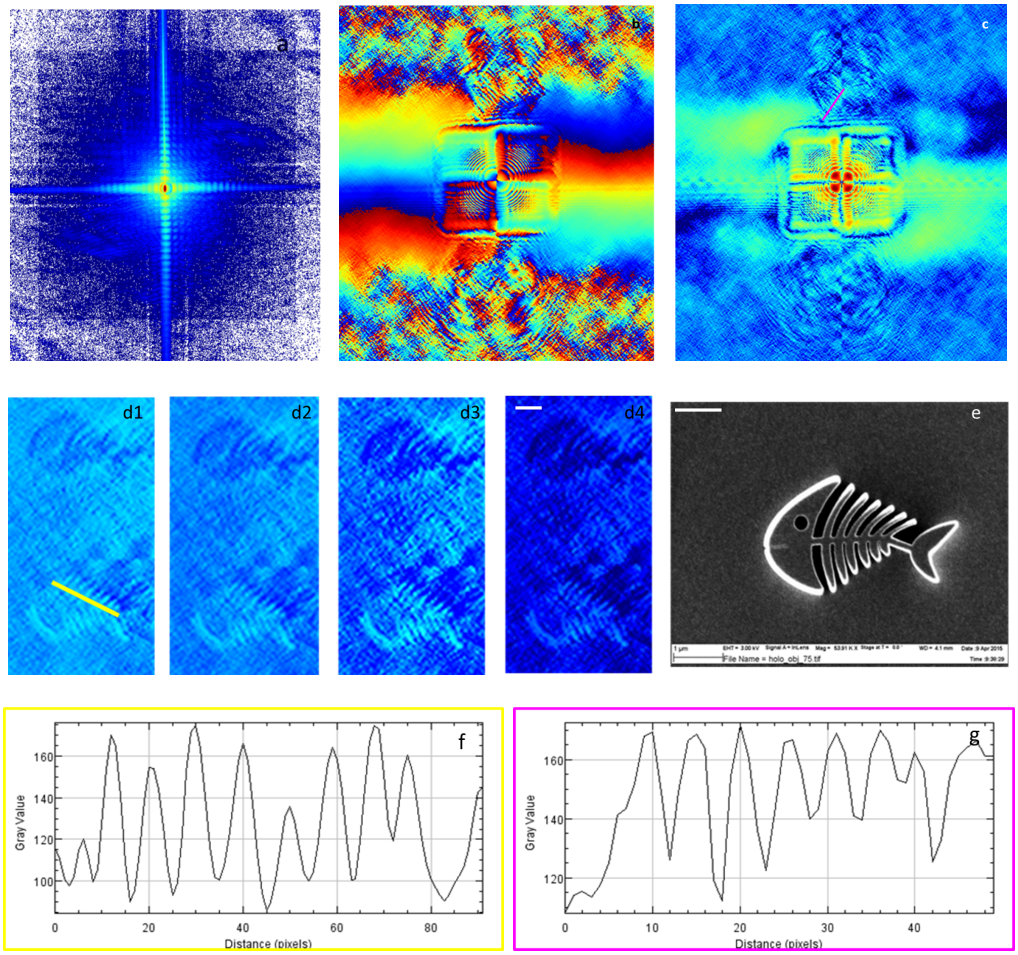

Figure 4.10: (a) Recorded diffraction pattern, (b) raw phase reconstructed area, FOV=38.7 μm, (c) background-corrected reconstruction of silicon dioxide fish bone sample, (d) crop-out magnified reconstructions (Scale: $1\mu m$), (e) SEM image [57], (f) profile plot of line through (d1), (g) profile plot of line in (c). 1 pixel = 65nm.

Reconstruction of Low-Absorption / Weak Phase Samples

The samples last discussed were composed of 340 nm gold deposited on a transparent silicon substrate. The properties of these samples at our specific photon energies are 90% transmission and 0.18π. Hence they contribute a fairly strong scattering signal compared to weakly-scattering samples or biological samples. To examine the potential of the imaging system with rather weakly-scattering samples, we used a fabricated test-sample that constitutes of 590 nm thick silicon dioxide

nano-structured in the shape of a *fish-bone* coated with 30 nm of Iridium by ALD as described in Section 4, Table 4.1 and 4.2. The underlying silicon dioxide contributes to absorption and phase shift of almost null at 8 keV, whereas the 30 nm Iridium coating contributes 77% transmission and 0.42π phase shift only along the longitudinal direction parallel to the x-ray beam. Note that due to the sample being prepared by atomic layer deposition the resulting structure is *seen* by the x-ray beam to have an ultra-sharp 30 nm outline of a dense material (Iridium) surrounding a highly transparent *fish-bone* structure of light material (silicon dioxide).

Figure 4.10 shows the reconstructions of the weakly-scattering iridium-coated sample using the same procedure as previously described with a total photon count of 3×10^7 at 50 sec exposure time. The reconstructed field of view obtained after background correction is shown in Figure 4.10(c) compared to the uncorrected phase reconstruction in Figure 4.10(b). The contrast and SNR is fairly low compared to the gold test-samples due to the low absorption and phase properties of the sample. The 30 nm iridium edge is finer than the object-space pixel size of 65 nm; thus we expect not to resolve the iridium edge. The largest gap between the *bones* of the fish is 190 nm and decreases to the finest gap of 60 nm. Despite the low SNR, we are able to identify the structure of the bones and the tail in the cropped reconstructions with a resolution of 105 nm (according to the plot in Figure 4.10) and with sufficient contrast to differentiate the sample structure from the substrate. Therefore, we conclude that the single-shot non-iterative holographic method that we have discussed has proven so far to be a robust imaging technique where we are able to obtain reconstructions with sufficient contrast and resolution of weakly-scattering samples measurements despite a fairly low photon flux.

To that end, in the next sections we will highlight the acquired increase in resolution and the amplified contrast of sample reconstructions obtained by increasing the photon flux, improving the illumination beam profile as well as utilising a high-resolution extended reference structure fabricated by atomic layer deposition.

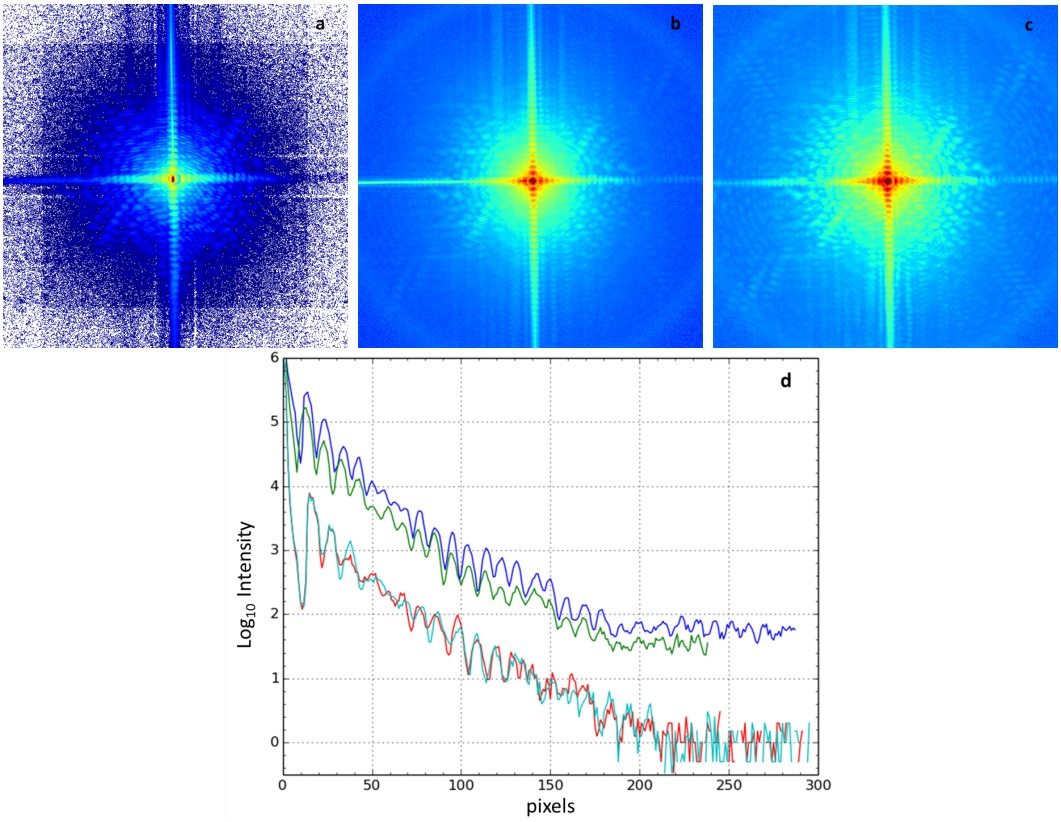

Figure 4.11: Diffraction patterns recorded at 3 exposure times: (a) 50 sec, (b) 100 sec, (c) 200 sec. (d) Plot of intensity modulations for increasing exposure time: (cyan,red) 50 sec; (green) 100 sec; (blue) 200 sec.

Effect of Increasing Photon Flux and Exposure

The photon flux was further increased to improve the noise statistics and record the outermost diffraction fringes enhancing the resolution of the reconstructions. Figure 4.11 shows three holographic diffractions patterns of the same test-sample and the 4 μm reference pillar at 50 sec, 100 sec, and 200 sec exposure time corresponding to n = 3.3 $\times 10^7$, 1.17 $\times 10^9$, and 2.87 $\times 10^9$ photon counts at the detector. The two latter datasets were obtained after the beam was cleaned up with the beam-forming slits and with complex refractive lenses (CRL) inserted.

The plot in Figure 4.11 shows the distribution of fringes of the log-scale diffraction pattern from the zero-order peak horizontally to the edge of the detector. The maximum of the 100 sec and 200 sec exposure fringe modulations in the diffraction

patterns start at log10=6 which corresponds to 10^6 counts and reach a value of 65 counts near the edge of the detector. The 50 sec exposure shows a maximum at the zero-order peak of 10^6 counts and the maxima decrease more rapidly to 2.5 counts at the edge of the detector at which point is at noise level. The outermost detected fringes above noise level have a value of 8 counts. The visibility of the fringes, however, is calculated to be 79.5% with the 50 sec exposure data (plots in red and cyan) which is higher compared to that of the 100 sec and 200 sec exposure data (plots in green and blue) with a visibility of 73.3%. On the other hand, the outermost detected fringes in the x-direction are highest with the 200 sec data at N = 275 pixels corresponding to 65 nm resolution whereas that of the 100 sec and 50 sec data correspond to 75 nm and 102 nm respectively.

Figure 4.12 shows the corrected reconstructions resulting from the diffraction pattern with 100 sec exposure time and N = 1.17 $\times 10^9$ photons displayed in Figure 4.11 (b) computed using the Gxy method. As expected from the plot in Figure 4.11, we find that the image resolution of the gold fish sample is higher than that of the 50 sec exposure data. The outline structure appears sharper and the 150 nm circular gold dot representing the eye of the fish is now resolvable compared to the 50 sec reconstructions shown in Figure 4.7 where the eye was not fully resolved. The 90% - 10% resolution test performed on the outline of the fish structure (shown in Figure 4.12 (b) and(c)) is calculated to have an upper limit of 90 nm.

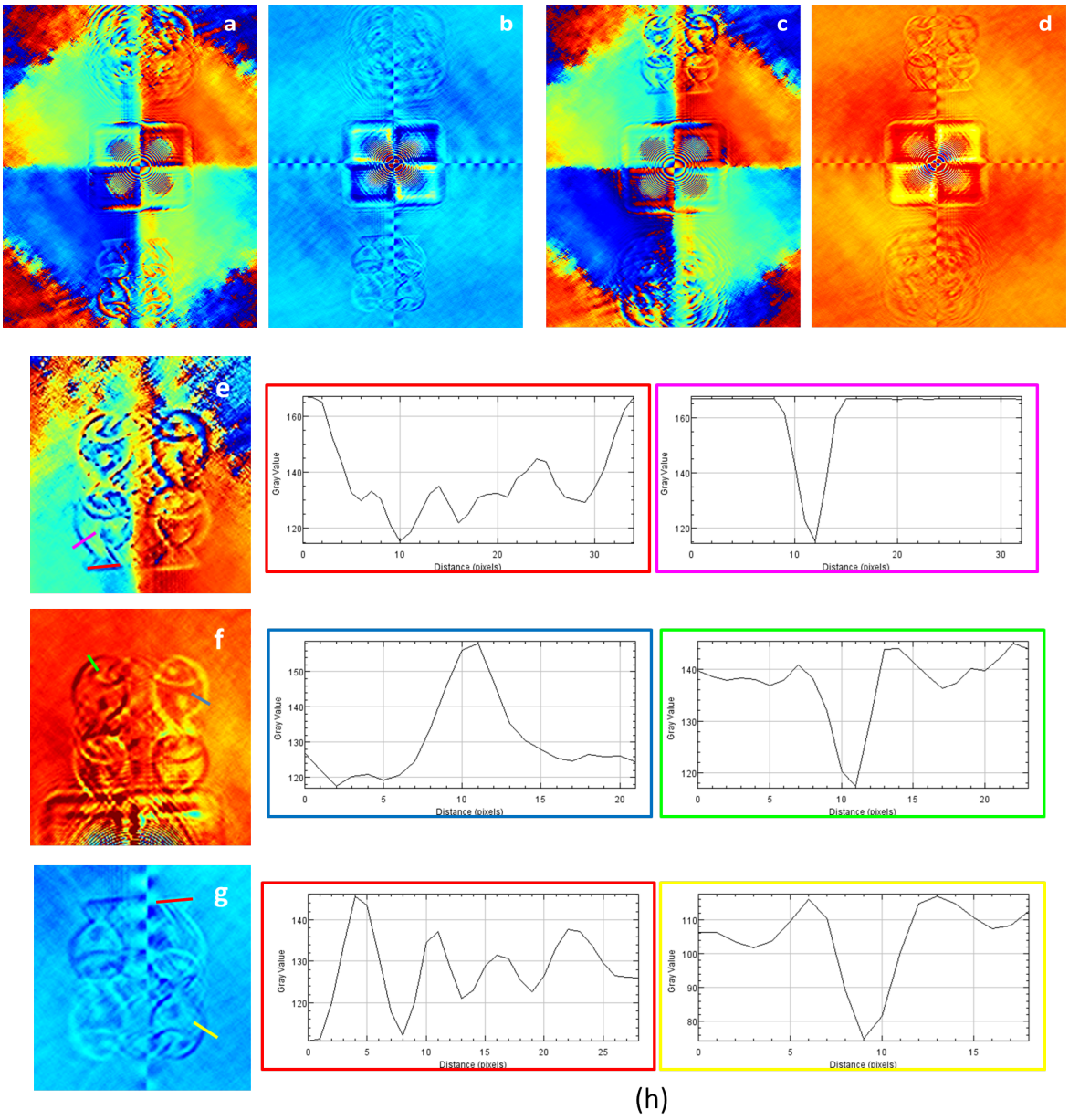

Figure 4.12: (a) Raw phase reconstructed area, (b) background-corrected, (c) same as a but back-propagated to focus the twin images, (d) background-corrected, (e,f,g) magnified crop-out of (a,d,b) respectively; (h) profile plots of color-coded line cuts. 1 pixel=61nm.

4.1.2 Results: Compound Ir/Si Nano-Wireframe Reference

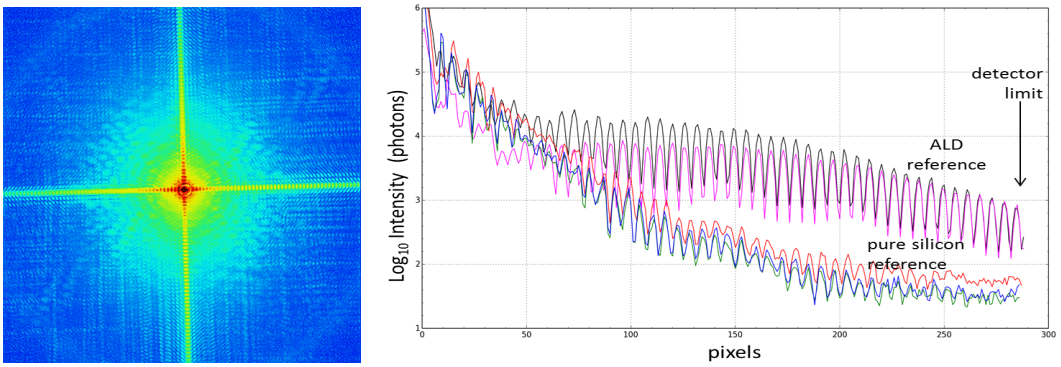

Figure 4.13: (left) Recorded diffraction pattern using the wireframe extended reference. (right) Plot comparing intensity modulations at exposure time of: 200 sec (magenta); 300 sec (black), for the Ir/Si wireframe reference; and 200 sec (red), 100 sec (blue & green) for the Si pillar reference.

As we have seen in the previous section, within the pixel size limit, increasing the photon flux and performing background correction can improve the resolution and contrast to a certain extent, but we are ultimately limited but the sharpness of the reference edges. Therefore, we have implemented an innovative fabrication technique to produce reference structures with high-resolution edges. The fabrication involves coating a silicon pillar with a nano-layer of Iridium by atomic layer deposition (ALD) as described in Section 3.1. ALD allows the deposition of one Iridium atom upon the other in a very structured manner such that the process results in a silicon pillar with a sharp 10 nm iridium edge. The sharpness of the Iridium edge will contribute to high resolution sample reconstructions compared to the bare silicon edge previously discussed.

Figure 4.13(a) shows a holographic diffraction pattern of a 6 μm ALD Iridium reference and a gold fish test-sample recorded at 200sec exposure time. Figure 4.13(b) shows the intensity distribution of fringes, from the center to the edge of the detector in the x-direction, of two wireframe datasets recorded at 200sec and 500sec, overplotted with the fringe distribution of data obtained with the bare silicon pillar references at 50 sec, 100 sec, and 200 sec exposure time. There is a clear

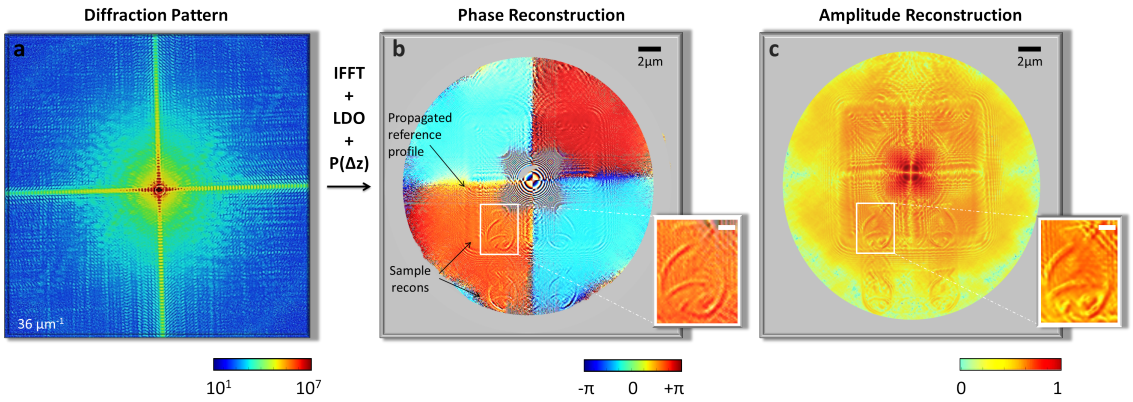

Figure 4.14: (a) Corrected diffraction patterns, (b) Phase and (c) Amplitude reconstruction of gold fish sample using Ir/Si wireframe reference at 200 sec exposure time.

increase in visibility of fringes as well as an evident increase in resolution. With the well-resolved outermost fringes reaching the edge of the detector, the experimental resolution reaches its maximum at 1 pixel size, i.e 61 nm at 9 keV.

Figure 4.14 shows reconstructions of the gold fish test-sample using the Iridium wireframe reference with side length of 6 μm. As in the setup configuration in Section 4.1.1, the sample and reference were laterally offset from one another by around 8 μm and separated in the z-direction by 3.5 mm while mounted on nano-precision piezo-electric stages. The measurements were taken at 9 keV photon energy, with an exposure time of 200 sec and 300 sec respectively using a flat and uniform monochromatic beam illumination that was shaped using beam-forming slits passing through a double-crystal monochromator and complex refractive lenses. The data was recorded using a photon counting detector with a 55 μm pixel size and pixel count of 515×515. The total number of photons reaching the detector was 2.45×10^9 counts per shot.

From a first glance onto Figure 4.14, we find that the sample reconstructions are sharper and high-resolution features are apparent. Furthermore, the resulting reconstructions appear to have sufficient contrast despite the small total area of iridium (being a nanowire extended to a square perimeter). The fact that the wireframe is made of a dense material means that it is strongly scattering to

introduce an intense reference signal. As apparent in Figure 4.15, sharp horizontal and vertical fringes surround the reference autocorrelation and begin to overlap with the sample reconstructions. These fringes are due to near-field propagation of the reference autocorrelation that constitutes the nano-thin wire of iridium with high phase shift and a substantial absorption through the edge. By sufficiently offsetting the sample from the reference we can avoid major overlap onto the sample reconstructions. The lower corner reconstructions of the fish sample overlap with the reference autocorrelation area.
Contrary to the reconstructions obtained with the bare silicon pillar, we find that while the sample reconstructions might overlap with the reference autocorrelation, the intensity of the sample image is not overpowered by the intensity of the reference autocorrelation but is in fact sufficiently intense to be distinguished in the overlap area. This is due to the fact that the reference area is that of weakly-scattering $3.9\mu m$-thick silicon which contributes to absorption close to null and to a phase-shift of less than $\pi/4$. This proves that the high contrast of the sample reconstructions is a product of the iridium reference edge whereas the underlying silicon structure contributes minimal signal.

Reconstructions from background-filtered data acquired at a higher exposure time of 500 sec is shown in Figure 4.15 with a total of 9.73×10^9 photons per shot at the detector and 3.89×10^{10} photons accumulated by patching up the four shifted arrays. We find in Figure 4.15(d) that the finest features of the sample are now resolvable i.e the two fins of the fish as well as the sub-50 nm gap in between them. By inspecting the 90%-10% knife edge plots of the sample features, we conclude that the holographic imaging system using the ALD iridium wireframe reference has reached the pixel-size resolution limit of 61 nm, i.e the maximum attainable image resolution with the given photon energy and detector pixel size.

To further push the resolution limit, one could increase the photon energy or utilise a larger detector array to effectively decrease the object-space pixel size. The virtue of reference structures prepared by atomic layer deposition is that the resolution could reach even higher values by preparing an ultra-sharp layer of a few nanometre thickness or even sub-nanometre. The electron-dense Iridium atoms

deposited one upon the other surrounding a few-micron thick silicon pillar would have considerable absorption in addition to a strong phase-shift which creates a strong reference signal. Despite the fine width of the nano-wire frame, the fact that it is laterally extended to a perimeter of a 6 μm square, or any perimeter customizable to the experimental needs, allows a sufficient total flux of the reference signal and maintains a good signal-to-noise ratio.

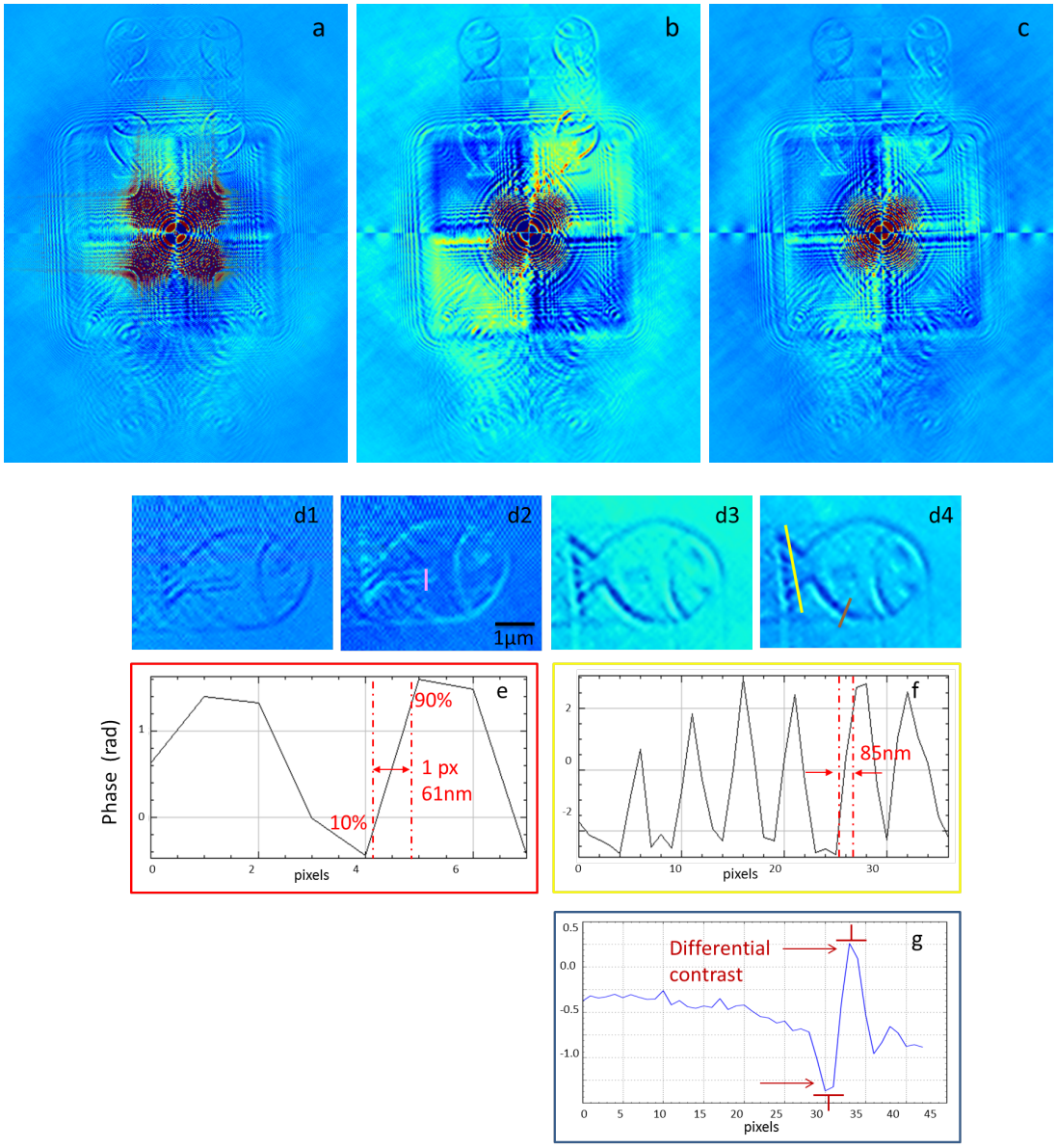

Figure 4.15: (a,b,c) collection of reconstructed areas at 500 sec exposure showing the wireframe autocorrelation and the upper-corner fish images in focus; (d) magnified crop-out of best images; line profiles across: (e) gap between the two fins (pink line d2); (f) tail structure (yellow line d4); (g) edge of the body outline (brown line d4). 1 pixel = 61 nm

4.2 Analysis

4.2.1 Reference Characterisation and Structural Aberrations

We are able to inspect the reference autocorrelation to characterise structural attributes of the reference. Figure 4.16 (a) and (b) show the amplitude and normalised phase of the autocorrelation of the ALD Iridium-coated reference pillar respectively. Due to the square structure of the reference, the autocorrelation represents four adjacent complex-conjugate copies of the reference structure. From these images we are able to visualise the structure of the reference and we identify the nanolayer of Iridium and the underlying silicon structure.

The profile plots (Figure 4.16 (d) and (g)) of the amplitude image in Figure 4.16(a) show a sharp dip in transmission compared to the almost fully transmissive inner area which demonstrates the iridium nanolayer being a thin absorbing edge that contributes high contrast reconstructions. Figure 4.16(a) perfectly depicts how the dense iridium nano-layer envelopes the light silicon structure resulting in what appears as a wireframe structure, hence the name of the method. Figure 4.16(c) shows a magnified inset where we distinguish the sharp, straight, and intense Iridium nanolayer around the reference edges overlying and adjacent to a visibly rough corrugated edge of the silicon structure. The average size of the bumps at the silicon edge compared to the sharp iridium edge is visualised in the plot in Figure 4.16(e). Characterising the reference structure helps us to understand some of the anomalies that appear in the sample reconstructions that cannot be attributed to computational reasons.

We notice a common artefact in the sample reconstruction results using both the bare silicon reference and the wireframe reference in the holographic experiment, that is: low-intensity repeating and overlapping copies of the sample occurring between two consecutive corner reconstructions. This can be clearly seen in Figure 4.15 (b) and (c) for the wireframe reference method and in Figure 4.9 and 4.12 for the full square reference. We conclude that this phenomenon arises due to the sharp corrugations of the silicon edge that act as individual delta-like point sources.

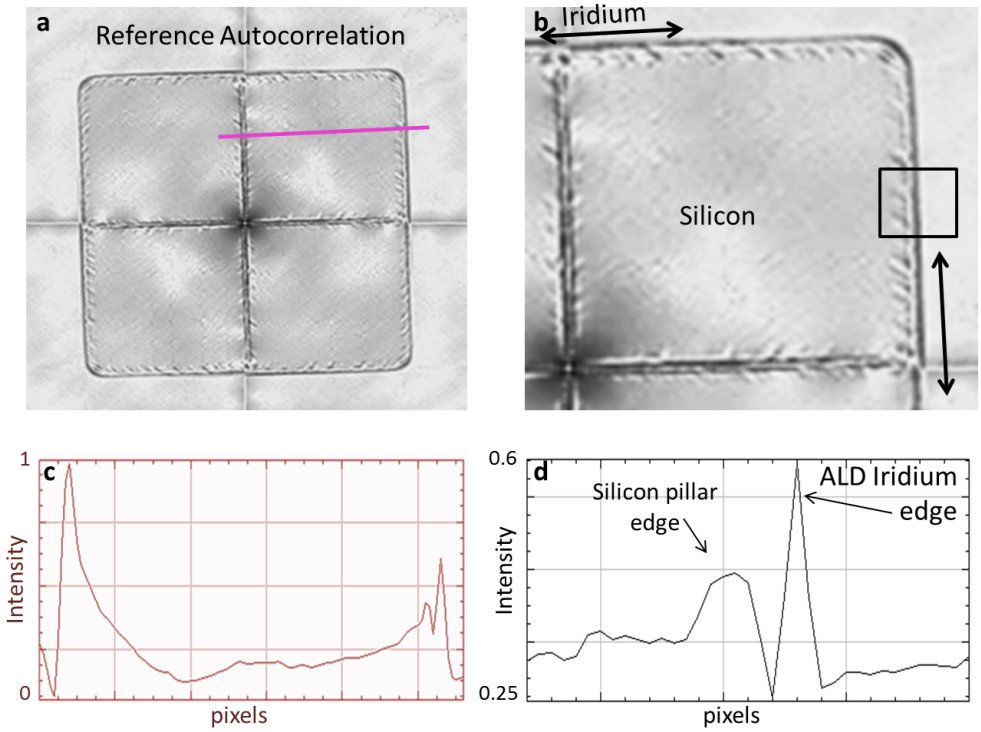

Figure 4.16: (a) amplitude autocorrelation reconstruction of reference; (b) magnified crop-out of (a); profile plot along (c) line in (a), and (d) box average area in (b) showing sharp iridium edge peak compared to rough silicon edge.

This justifies that it does not arise from the computational procedure due to the fact that the repeating overlapping copies do not equally appear with difference reference specimens and are not uniformly occurring around all the virtual edges i.e they are not equally spaced or equally intense and do not occur on every side of the virtual square reference. They are generally fainter than the corner reconstructions which justifies them being a product of corrugations in the silicon edge and not the iridium edge since we would expect high contrast from the iridium reference. Note that before performing atomic layer deposition, the underlying silicon pillar is fabricated by the same process as the bare silicon references discussed in the Section 4.1.1. The fact that this artefact similarly appears in the reconstructions produced with the bare silicon reference gives further proof that it is a result of the structural aberrations of the fabricated silicon structure. Therefore, if the occurrence of such artefacts is found to significantly inhibit the quality of the reconstructions (which is

not the case with our results) this may be corrected by fabricating smoother edges using a variety of nano-fabrication and lithographic techniques, not to mention the possibility of numerically disentangling the repeating copies by deconvolution.

4.2.2 Differential Contrast

The fact that the reference structure is a wireframe implies that the holographic mechanism is not equal to that of the bare silicon structure. Differentiating a square area twice along the two side directions results in four delta-peaks at the square corners, but differentiating twice a square wireframe structure along the side directions results in the derivative of four delta-peaks at the corners. Yet, by applying a double derivative, the image reconstruction shows attributes of differential contrast. In our setup, we still obtain the desired reconstruction of the samples but with a differential contrast and a higher resolution. Note that the structure of the reference is in fact of two components: a 3.85 μm thick silicon pillar and a 10 nm wireframe of Iridium. This means that the underlying silicon pillar serves as an extended reference in itself but with less of a phase shift and absorption compared to the previous setup with the 9 μm silicon pillar of a 0.83π phase shift. With the wireframe reference, the underlying 3.85 μm-thick silicon pillar contributes a sample image of weak contrast. The iridium edge contributes higher image contrast, due to the phase-shift created by 3.9 μm of iridium, and higher resolution, due to the thickness and sharpness of the nano-layer.

The nature of the wire-frame structure translates into a differential contrast image when applying the double directional derivative to reconstruct the object. This is observed in Figure 4.17 as edge contrast enhancement of the samples where the edge contrast in the amplitude reconstruction is proportional to the ratio of the iridium absorption to the silicon absorption. Similarly, the (differential) phase contrast is a function of the phase difference between the iridium edge and the silicon structure. For example, in the lower right corner fish in Figure 4.17(b), the signal at the lower right outline goes from dark (outer outline) to bright (inner outline); and diagonally across to the upper left side of the fish, the signal at the outline goes from bright (outer outline) to dark (inner outline). In other words, the phase of the fish outline shifts from high to low (or positive to negative)and

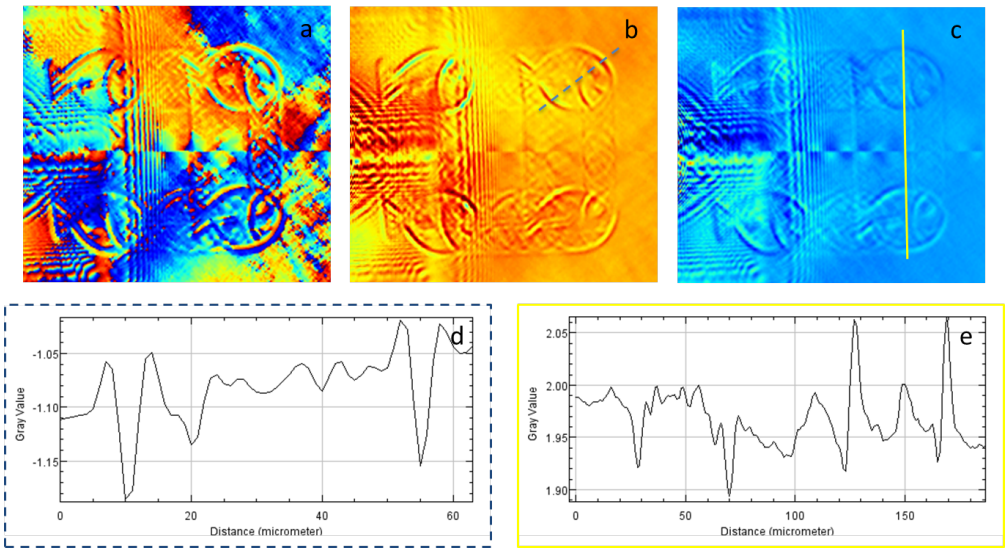

Figure 4.17: (a,b,c) Selection of reconstructions showing attributes of differential contrast, (d) line profile of (b) through dashed blue line; (e) line profile of (c) through dashed orange line.

vice versa creating an effect of enhanced edge contrast. The direction of differential phase contrast alternates diagonally in the consecutive corner reconstructions. This aspect is better illustrated in the simulations in the following.

Figure 4.18 shows a simulation that compares a full-area square reference to a wireframe square reference and the resulting reconstructions in Figure 4.20. The simulation attempts to mimic the references used in our experiment with the same experimental parameters. We simulate three different scenarios where we use: 1. a full-area square reference, 2. a 1-pixel wireframe reference, and 3. a full-area square reference coated with a nano-layer wireframe, with an offset object placed on a transmissive substrate, analogous to our experiment. The full-area reference was simulated to have the index of refraction of 9μm-thick silicon at 9 keV photon energy, with $\Delta\phi$ = - 0.83π and T = 91.5%, where $\Delta\phi$ and T are the phase shift and transmission respectively, and a lateral dimension of 6 μm, as in the experiments performed in Section 4.1.1. Similarly, the wireframe reference was simulated to have the index of refraction of iridium at 9 keV with a thickness that produces $\Delta\phi$ = - π and T = 23%. In the third case, the same wireframe as the second case is simulated but with an underlying silicon pillar with $\Delta\phi$ = - 0.6π and T = 95.5%.

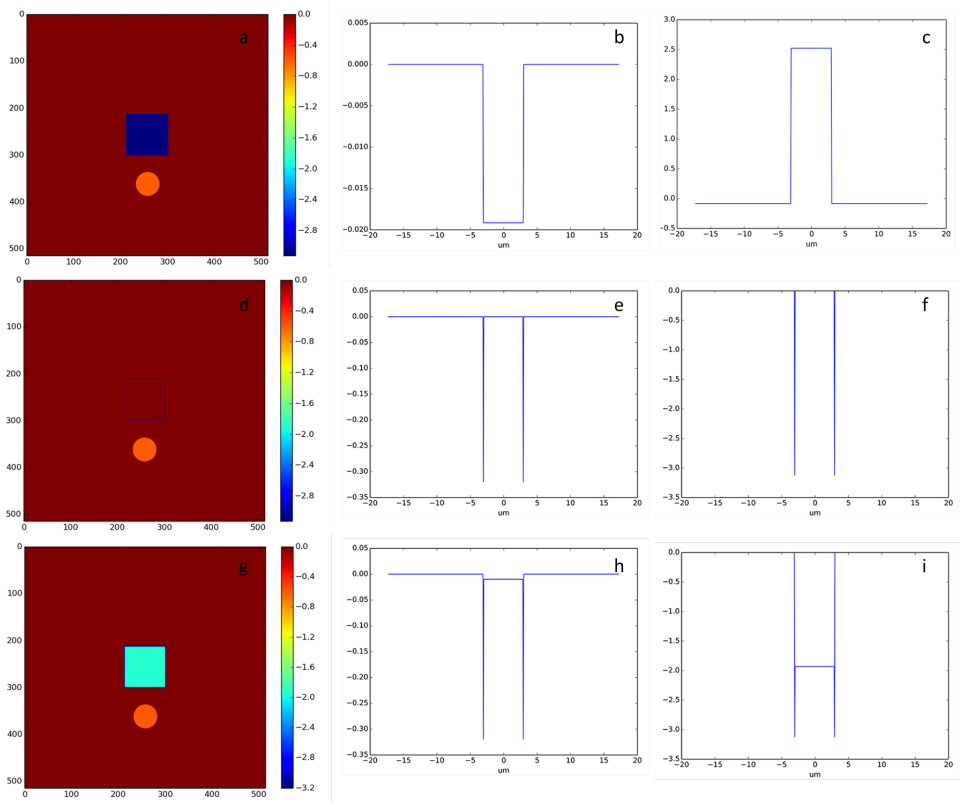

Figure 4.18: Simulation comparison of (a) full-area Si square reference, (d) pure Ir wireframe, and (g) compound Ir/Si wireframe reference, where (a,d,g) are the phase in the original sample plane, (b,e,h) are the Log amplitude profiles and (c,f,i) are the phase profiles through the respective references.

Analogous to the gold-fish test sample, the simulated object is a 3.5 μm-wide gold disc of 340 nm thickness (i.e a thin sample) with $\Delta\phi$ = - 0.596 radians and T = 90%. The object is vertically offset by 7 μm from the center of the reference such that there is no overlap between the autocorrelation and the cross-correlations. The object and reference structures are set on a fully transmissive substrate. A phase image of the sample area, the line profile of the log-scale transmission coefficient and the phase plot of the three reference structures are shown in Figure 4.18.

To establish a good reasoning of the phase and amplitude reconstructions shown in Figure 4.20 resulting from the three comparative simulations, it is important to understand the consequences of applying two directional gradients to a hologram using a wireframe reference, a full square reference, or a reference of multiple

structures. Therefore, we need to break down the mathematical analysis of the gradients and delta functions.

We consider the complex transmissivity of the three different structures shown in Fig.4.18 and apply a step-by-step numerical procedure that includes a directional derivative in x and a directional derivative in y that leads to the reconstruction result. Fig.4.19 shows the real part and the phase of the complex reference function throughout these steps. For example, Fig.4.19(a) and (b) show the real part and phase of the bare-silicon square pillar reference respectively, after applying the x-directional gradient (a1,b1), the y-directional gradient (a2,b2), and the two-directional gradients (a3,b3), with a final profile plot of the peaks resulting from the two directional gradients applied to the reference function. The peaks then represent point source reference functions which will be cross-correlated with the object function to obtain the object reconstructions.

The mathematical derivation for the case of the full-area reference (Fig.4.19(a) results in 4 individual dirac-delta functions of equal phase (Fig.4.19(a,b)), with two positive and two negative magnitudes of the four corner deltas where the change in sign is due to the complex-conjugation. This means that each corner point produces a single peak, and all corner peaks are equal and alike. This is similar to the standard Fourier transform holography formulation.

As for the wireframe reference (Fig.4.18(b)) with $\Delta\phi = -\pi$ and $t = 0.478$ (where t is the transmission coefficient t=$\sqrt{T}$), the result of the derivation at a single corner point is 2 adjacent (almost concurring) and opposite delta functions (Fig.4.19(c3,c4)), which is analogous to the derivative of a single delta peak. The real part of the derivation at a single corner shows a positive peak at +0.36 and negative peak at -0.36, separated by a sub-pixel distance, while the phase shows a single delta peak at -3.14 rad corresponding to the phase-shift of the wireframe material with respect to the substrate. In other words, a single corner results in a double point-source reference function of dual polarity with a sub-pixel separation that depends on the width of the wireframe and the object-space pixel size.

Thirdly, in the case of the iridium wireframe reference with an underlying silicon structure (Fig.4.18(c)), t and $\Delta\phi$ of the iridium edge and of the silicon

structure are (0.478 and -π rad) and (0.976 and -1.95 rad) respectively. Due to the contribution of the two materials, both the phase and magnitude at the corner points would consist of double peaks of opposite polarity. At a single corner, the real part constitutes of a positive peak at +0.04, and a negative peak at -0.36, less than 1 pixel apart; at the next corner, a peak at -0.04 and another at +0.36, and it continues symmetrically for the rest of the corners (Fig.4.19(e4)). On the other hand, the phase at a single corner constitutes of two almost coincident negative peaks, one at -1.423 rad and one at -π rad with sub-pixel separation; at the next corner, only a single positive peak at +1.718 rad (equal to $\pi - 1.423$), and continues symmetrically for the other two corners (Fig.4.19(f4)).

The cross-correlation of the derivated delta peak with the object results in amplitude reconstructions with an intensity gradient and phase reconstructions with differential phase contrast. The differential contrast depends on the range of maximum to minimum (or positive to negative) at a specific corner point. For example, in the pure wireframe case (Figure 4.19(c,d)), the differential contrast is largest among the three simulations due to the fact that at a single corner point we have two coincident negative and positive delta peaks of equal magnitude, hence twice the contrast of a single peak.

In the case of the wireframe with an underlying silicon, the differential contrast is lower than the pure wireframe case due to the fact that the range of the double peak at a single corner point is lower (seen Figure 4.19(c4,d4) compared to (e4,f4). Specifically, the range of the real part of the wireframe/silicon peaks is (0.36 - (-0.04)) which is less than the range (0.36 - (-0.36)) for the pure wireframe case; and for the phase, the range ($|\pi$ - 1.423|) is less than | 0 - $\pi|$. This predicts the extent of differential contrast as a function of the material properties and the reference structure.

As for the expected amplitude spatial information, the derivated delta peak produced by the pure wireframe reference should lead to mere outline amplitude reconstruction, due to the fact that the equal and opposite peaks cross-correlating with the object function result in the cancellation of the bulk object information. In comparison, the single peaks resulting from the bare silicon square reference

cross-correlate with the object function to return the object function itself with the bulk information without edge enhancement or intensity/phase gradients. On the other hand, the cross-correlation of the double peaks at a single corner point of the wireframe/silicon reference (Figure 4.19(f,e)), though they have positive and negative magnitudes, they do not have equal magnitudes and hence the information of the bulk of the object area does not cancel out. Therefore in such a reference setup we expect to find edge contrast contribution (outline information) and phase/intensity gradients as well as bulk information about the sample in the reconstructions, i.e a combination of the two methods.

Now we will verify the premise by examining the simulated reconstructions in Figure 4.20 produced by the sample areas shown in Figure 4.18. Using the extracted parameters from the previous section, we can make reason out of the amplitude and phase of the resultant reconstructions. The reconstruction procedure applied to the sample complex transmissivity in Figure 4.18 (left) involves taking the inverse Fourier transform of the simulated diffraction pattern and applying a double directional gradient along x and y. The method that uses a linear differential operator in Fourier space was also tested in the simulation but is not displayed in the figures for brevity. The amplitude and phase of the reconstructed field that results of the three reference structures is shown in Figure 4.20.

By comparing the reconstructions and their respective profile plots, the result of the pure iridium wireframe reference is an amplitude outline reconstruction of the edge of the gold disc without any contribution to the bulk material. This appears as a high-resolution absorption circular outline compared to the bare silicon reference in case 1 where the sample image has no edge contrast. The absorption edge is amplified according to the density ratio of the reference material and the substrate material. As expected from the analysis of the delta peaks using the iridium wireframe reference, in the phase reconstruction we find that the edge of the gold disc shows a clear phase gradient from negative to positive in a diagonal direction across the gold disc, whereas that of the silicon reference shows no phase gradient across the disc at all.

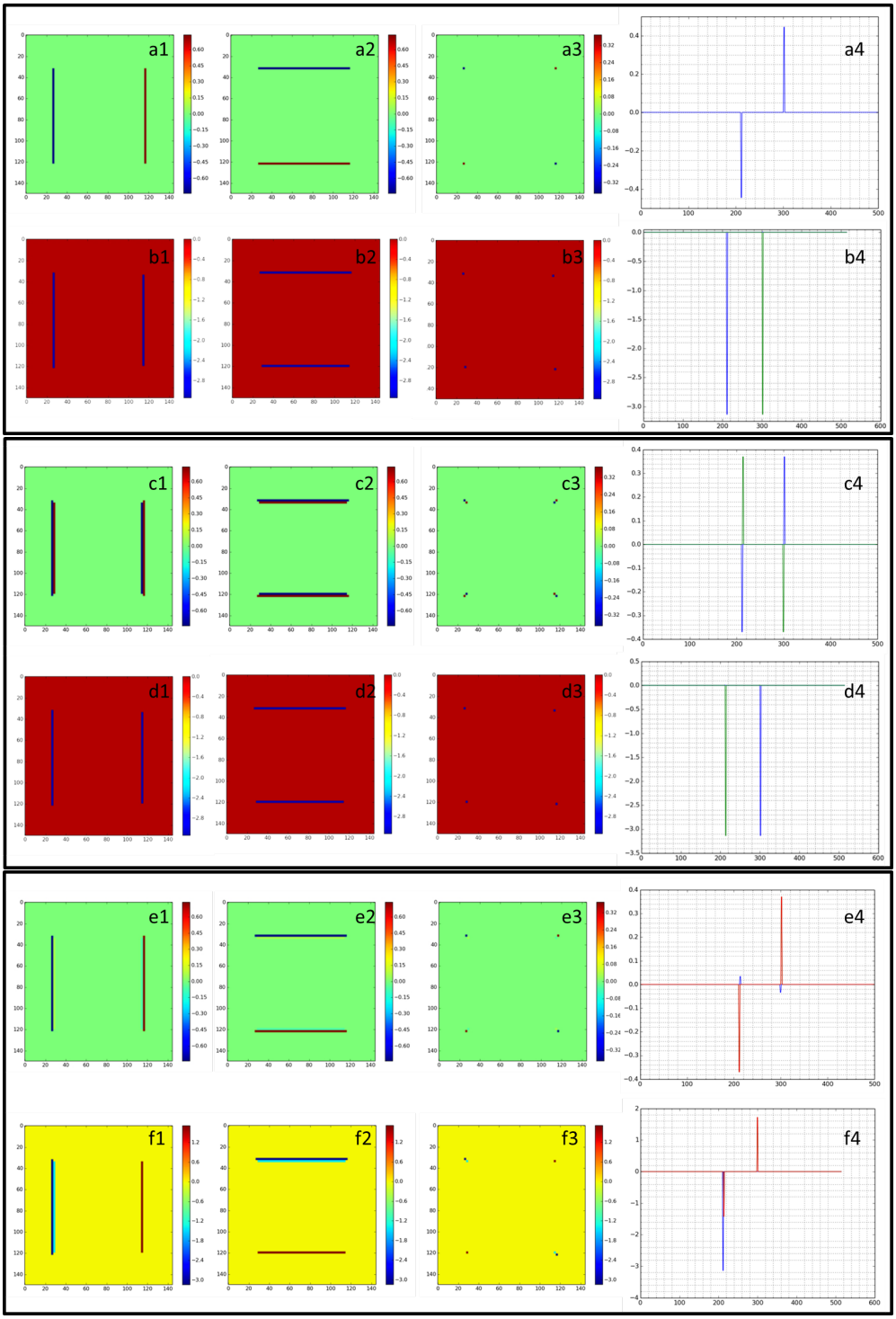

Figure 4.19: (a,b) log amplitude and phase (respectively) of: 1) ∂_x, 2) ∂_y, 3) $\partial_x\partial_y$ of full-area Si pillar reference, 4) profile plot through upper two corners.(c,d) same as (a,b) but for pure Ir wireframe reference, (e,f) same but for compound Ir/Si wireframe reference.

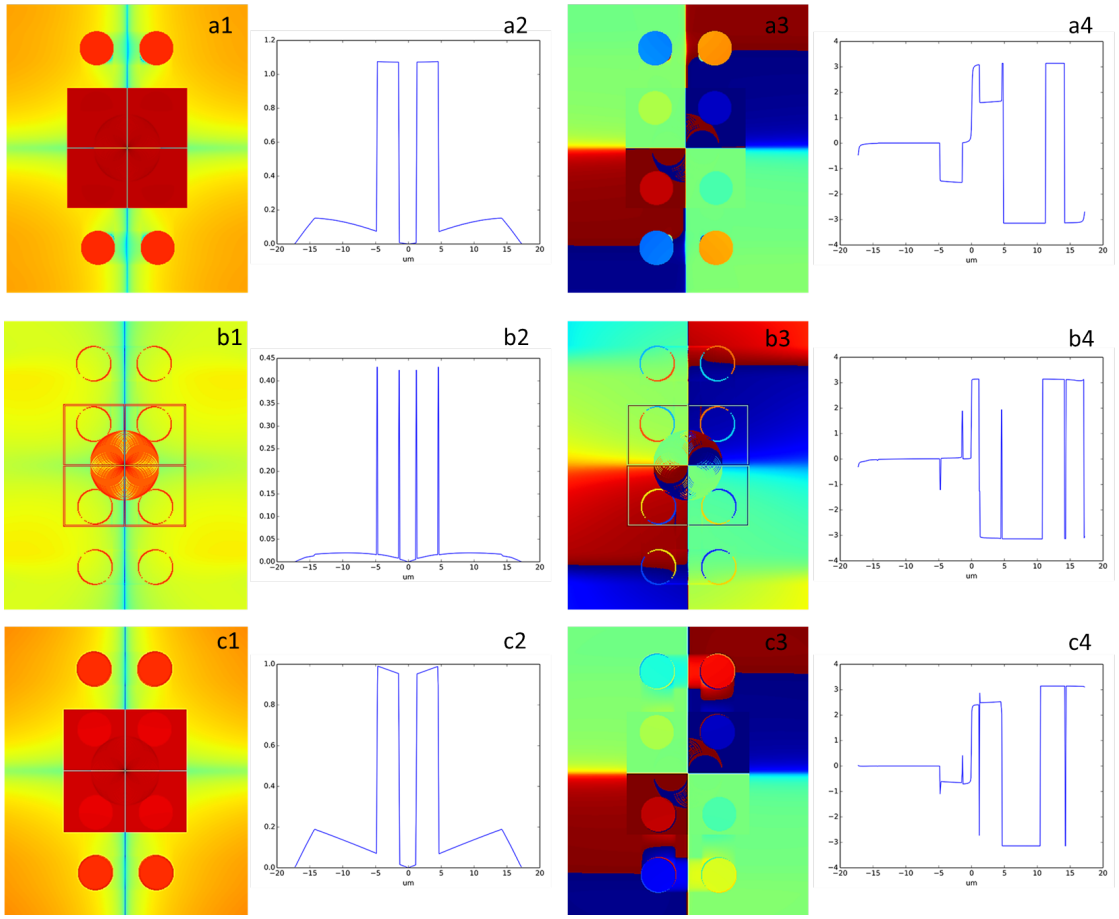

Figure 4.20: sample thickness = 0.34 μm. (a1) amplitude reconstruction by silicon reference. (a3) phase reconstruction. (a2)(a4) profile plot through the two upper reconstructions of (a1) and (a3); (b1-b4) same as (a1-a4) with iridium wireframe reference; (c1-c4) same as (a1-a4) with compound Ir/Si wireframe reference.

We also find that there is no phase contribution to the bulk of the sample as only the outline appears. This statement holds for a sufficiently thin sample, but changes when dealing with thicker samples. Since the real part of the derivated reference in Figure 4.19(c4) shows 2 delta peaks that are coincident, opposite, and equal in magnitude at each corner point, the amplitude reconstruction will always provide outline-only reconstructions even for thicker samples because the opposite and equal peaks cancel out the bulk information. While this is true for the amplitude, it is not necessarily the case for the phase, since the phase of the derivated reference shows single equal peaks of the same polarity for all corner points (Figure 4.19(d4)). Therefore, the cancellation of the bulk information does not apply in the phase; and for a sufficiently thick (or phase-shifting) sample, the bulk information appears in the phase reconstructions. This is clearly illustrated in Figure 4.21 where a thick sample is simulated and the amplitude reconstructions show outline-only images while the phase shows both outline and bulk information. To extend the comparison, the same three scenarios are simulated with the gold sample of 2 μm thickness, where a higher edge enhancement is observed and the Ir-wireframe/silicon reference gives superior reconstructions compared to the pure wireframe reference in edge and bulk contrast in amplitude and phase.

The reconstructions displayed Figure 4.20(c) using the Ir-wireframe/silicon reference illustrate our experimental case with almost identical parameters (i.e. the reference and sample characteristics), neglecting substrate contribution and assuming a homogeneous parallel incident beam. In this case, we find a reconstructed full-area image of the gold disc as well as enhanced outline contrast and a phase gradient. The amplitude plot (Figure 4.20(c2)) of the object reconstruction shows higher contrast of the bulk as well as an increase in intensity towards the edges compared to the pure wireframe case (Figure 4.20(b2)). On the other hand, the phase reconstruction (Figure 4.20(c3)) show high-resolution phase jumps at the edges of the disc alternating from negative to positive and vice versa, with sufficient phase contrast of the bulk but lower edge contrast compared to (Figure 4.20(b3)). The phase plot of the two upper gold discs (Figure 4.20(a4,b4,c4)) allows us to compare the values of the edges and bulk with the three references.

In summary, this signifies that such a holographic setup, as performed in our experiment, results in differential phase contrast as well as edge enhancement while maintaining sufficient contrast for the bulk information and enhanced edges in the absorption images. The reasoning behind this is explained in the previous sections; but in conclusion, this is the outcome of having the holographic point-source reference represented by two sub-pixel separated delta-like functions of inverse polarity.

The simulated reconstructions compare well to the experimental reconstructions in relation to the differential phase contrast, the direction of the phase gradient and the phase contrast of the edges of the sample. This is illustrated in the edge profile plot of Figure 4.15 as well as the line plots in Figure 4.17 through the center of the fish reconstructions where it is visible that the phase across the edges alternates from high to low values, specifically from $+\Delta\phi$ to $-\Delta\phi$ and where the gradient is most prominent in the diagonal direction and alternates its polarity for the consecutive corner reconstructions.

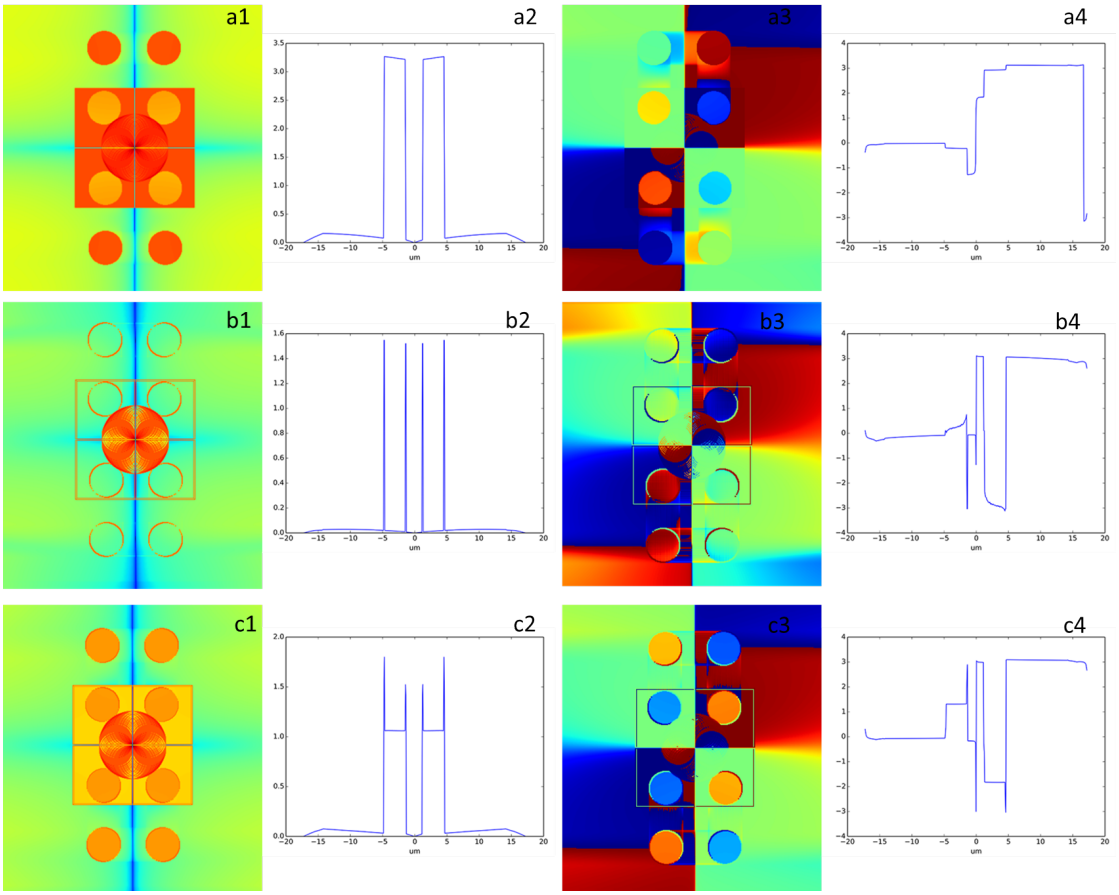

Figure 4.21: sample thickness = 2 μm. (a1) amplitude reconstruction using silicon reference. (a3) phase reconstruction. (a2)(a4) profile plot through the two upper reconstructions of (a1) and (a3); (b1-b4) same as (a1-a4) with iridium wireframe reference; (c1-c4) same as (a1-a4) with compound Ir/Si wireframe reference.

4.2.3 Quantitative analysis of absorption and phase

In the following, we will provide a quantitative analysis of the phase of the reconstructions to retrieve the phase value of the sample, which allows us to calculate the index of refraction and the electron density of the sample material. Here we recall the simulated reconstructions shown in Figure 4.20(c) and the analysis of the delta peaks in Figure 4.19(e,f). The phase of the inner area of the left reconstruction of the gold disc (shown in the profile plot in Figure 4.20(c4)) is at -0.625 rad, and at $+2.51 = \pi$ - 0.625 rad for the following complex-conjugate reconstruction on the right. With the flat level at -0.023 rad, the phase difference between the object and the substrate is $\Delta\phi = (-0.625) - (-0.023) = -0.602$ rad which is well-compared to the theoretical value of 340nm-thick gold of $\Delta\phi = -0.596$ rad at 9 keV within a 1% error. This is for a case where the reconstruction lies on a fully transmissive substrate with no phase contribution, whereas in a real experimental scenario we have to take the substrate contribution into account and the measured phase difference would be equal to difference between the phase of the sample and the substrate. Furthermore, the differential phase shift of the edges does not relate to the actual sample phase is a straightforward manner but it is a function of the phase difference between the iridium and the silicon structure that depends on the distribution and magnitude of the reference double peaks which we calculate using the following example.
Looking at the first negative edge at -1.152 rad in the plot of the simulated reconstructions of Figure 4.20 (bottom right), the phase shift is:

$$\Delta\phi = (-1.152) - (-0.023) = -1.129 \text{ rad};$$

At the consecutive positive edge of the same object, around 4 μm away from the first edge, the phase shift is:

$$\Delta\phi = (0.437) - (-0.70) = 1.137 \text{ rad}.$$

These are the values of the differential phase that stem from the contribution of both iridium and silicon structures to the reference signal. To understand the relation of these values to the actual phase information of the sample, we

cross-validate by inspecting the phase and amplitude values of the simulated delta peaks in Figure 4.19(e,f) and by considering that the theoretical phase of the gold object of 340 nm thickness is $\phi_{Au} = -0.596$ rad. Recall that the phase of the two coincident negative delta peaks in Figure 4.19(f4) was $\phi_0 = -3.141$ rad and $\phi_1 = -1.423$ rad, and that of the single positive peak was $\phi_2 = +1.718$ rad, where $\phi_1 + \phi_2 = \pi$. Given all these parameters, the phase shift at the 4 edges of the 2 complex-conjugate object reconstructions shown and plotted in Figure 4.20(c) is expected to be $\Delta\phi = \pm|\phi_2| \pm |\phi_{Au}|$ and $\Delta\phi = \pm|\pi - \phi_1| \pm |\phi_{Au}|$. Therefore, the expected edge phase shifts of the first object calculated using the delta peak values and the theoretical phase shift of 340nm-thick gold at 9 keV are:

$$\Delta\phi = |\pi - \phi_1| - |\phi_{Au}| = +1.121 \text{ rad}$$
$$\Delta\phi = \phi_2 - \phi_{Au} = -1.121 \text{ rad}$$

The calculation applies for the rest of the reconstructions and their complex conjugates that are located outside of the reference autocorrelation area. The expected values $\Delta\phi = \pm 1.121$ rad compare well to the phase shift of the object edges obtained in the simulated reconstructions: $\Delta\phi = -1.129$ and $\Delta\phi = -1.137$ within a 1.4% error.

This means that by performing this calculation, one can retrieve the phase shift of the sample material isolated from the contribution of the reference but must have a full understanding of the characteristics of the reference structure. Of course this can only be done if the illumination beam is assumed to be flat and homogeneous, and one must take into account contributions from the sample substrate or any windows or elements that disrupt the beam. If we have full knowledge of the contributing elements, inserting their expected phase shifts in the calculations may prove sufficient but also may result in a whole new bundle of complications. Therefore, in some cases we might find that extracting the isolated phase information of the sample could be a not-so-straightforward procedure that requires full apriori knowledge about all the elements of the experiment.
For example, in our experimental case we have 3.9μm-thick iridium wireframe of 10nm wire width, overlying a silicon pillar of 3.85 μm height, lying on a silicon substrate of 20 μm thickness, while the gold test sample is 340nm-thick lying on

a silicon nitride substrate of 200 nm thickness. There are no absorbing optical elements prior to the sample stage and the beam is assumed to be flat and homogeneous. A simulation of such a setup including all the substrate contributions leads to a different distribution and magnitude of delta peaks than the aforementioned example. In this case that best represents the experimental scenario we find 2 sets of double peaks for the phase, the first consisting a positive peak at +0.402 rad and a negative peak at -1.65 rad, and the second consisting of a positive peak at +2.68 rad and a negative peak at -2.73 rad, where $\phi_{3.85Si} = -1.6$, $\phi_{3.9Ir} = -1.65$, $\phi_{20Si} = -2.08$, $\phi_{200nm} = -0.08$, and $\phi_{obj} = -0.596$. The range of the double delta peaks is compared to the range of differential contrast in the reconstructed simulations to understand the relationship between the two and we find that the measured differential edge contrast is equal to the difference between the highest peak and the lowest minimum within a single corner located plus the phase of the sample. Since all the corner peaks are not alike, we find a variation of differential contrast from one reconstruction to the next virtual corner location.

To that end, we have performed calculation of the phase shift and the transmission from the data extracted from sample reconstructions using the two types of references: bare silicon 9 μm reference, and 3.85 μm silicon reference with a 3.9 μm wireframe. The phase shifts were measured as the difference between the cross-correlation reconstruction and the background phase right before or after the cross-correlation. The different corresponds to a phase difference between the sample phase and the substrate phase (as well as the reference phase for cases where the reconstruction lies within the reference autocorrelation area).
As for the the phase shift at the sample edges with differential contrast (as in the wireframe Ir/Si case), we measure the difference between the edge peak and the dip that follows or precedes it. The measured phase difference is then correlated to the real sample phase using the previously discussed method which entails theoretically calculating or simulating the expected distribution of double delta peaks. Since the calculation of phases with the wireframe method is not straightforward, we have used the simulated data to validate the measured values. On the other hand, phase measurements using the bare silicon reference are rather straightforward and it is not necessary to cross-validate with simulations.

It is important to note that in this case the measured calculations from both the experimental and simulated reconstructions take into account the contribution of the substrates of the reference chip and the sample chip. Hence the measured phase shift of the reconstruction using the bare silicon reference is given by:

$$\Delta\phi = \pm\phi_{obj} \pm (\phi_{s1} + \phi_{s2}), \text{ and } \Delta\phi = \pm(\phi_{obj} - \phi_{ref}) \pm (\phi_{s1} + \phi_{s2});$$

for reconstructions outside and inside the reference autocorrelation area respectively, where ϕ_{obj} is the actual phase of the sample material, ϕ_{s1} is the phase of the first substrate, ϕ_{s2} is the phase of the second substrate, and ϕ_{ref} is the phase of the reference.
The measured phase shift of the bulk area of reconstructions using the compound wireframe reference with an underlying pillar is given by:

$$\Delta\phi = \pm\phi_{obj} \pm (\phi_{s1} + \phi_{s2}), \Delta\phi = \pm(\phi_{obj} - \phi_{r1}) \pm (\phi_{s1} + \phi_{s2});$$

for reconstructions outside and inside the reference autocorrelation area respectively, where ϕ_{r1} is the phase of the silicon structure underneath the wireframe.
As for the measured differential phase at the edges of the reconstructions, i.e the extent of phase jump between maximum and minimum, the measurement depends on the location of the corner and thus its respective distribution of double peaks. The measured phase shift is equal to the difference between the maximum of the positive peak and the minimum of the negative peak (within a double peak) added to the phase of the sample. If the delta peak distribution is more complicated then we refer to the simulations for validation. It is fairly straightforward to calculate the theoretically expected delta peak distribution without having prior knowledge about the sample, it is sufficient to know the material thickness and index of refraction of the references and the substrate.
On the other hand, the absorption measurement is performed by taking $(max - min)/(max + min)$ of the squared amplitude of the reconstructed normalised complex transmissivity. The minimum value is taken as the average of the minimum plateau surrounding the cross-correlation area. Since the minimum value signifies the absorption contribution of the substrates and other components, by taking the $max - min$, we directly calculate the squared amplitude transmission of the sample.

Using the aforementioned methods, the calculated phase and transmission of the sample extracted from the reconstructions are listed in Table 4.3, obtained using the 9 μm silicon pillar reference at 8 keV and 9 keV, as well as the edge and bulk values using the 3.9 μm iridium Ir-wireframe/silicon reference. The measured values of the object phase and amplitude compare well with the theoretical values with a 15% margin. The discrepancy could be attributed to beam inhomogeneities, additional absorbing or phase-shifting components in the beam path, cross-correlation of the reference with additional imperfections, but mostly to the fact that the density or index of refraction of the materials that is used to calculate the theoretical values may well not be in accordance with the parameters used in fabrication. Nevertheless, it is notable to find that the extracted values are within realistic limits and hence the experimental holographic method does indeed provide direct quantitative information about the material properties.

340 nm Au at 9 keV Si Reference	$\Delta\phi_{cc}$	$\Delta\phi_{ob}$	T_{ob}
Experimental	+1.639	-0.510	ND
Theoretical	+1.553	-0.596	0.902

2 μm Au at 8 keV Si Reference	$\Delta\phi_{cc}$	$\Delta\phi_{ob}$	T_{ob}
Experimental	+2.575	+2.317	0.452
Theoretical	+ 2.514	+2.256	0.432

340 nm Au at 8 keV Si Reference	$\Delta\phi_{cc}$	$\Delta\phi_{ob}$	T_{ob}
Experimental	-0.440	-0.698	0.836
Theoretical	-0.426	-0.684	0.867

340 nm Au at 9 keV sample bulk Ir/Si Reference	$\Delta\phi_{cc}$	$\Delta\phi_{ob}$	T_{ob}
Experimental	-2.12	-0.626	0.891
Theoretical	-2.09	-0.596	0.902
Experimental	2.70	-0.676	0.885
Theoretical	2.62	-0.568	0.902

340 nm Au at 9 keV sample edge Ir/Si Reference	$\Delta\phi_{cc}$	$\Delta\phi_{ob}$	T_{ob}
Experimental	5.97	-0.627	ND
Theoretical	5.99	-0.550	ND

Table 4.3: Measured sample transmission and phase shift compared to theoretical values at 8 keV - 9 keV x-ray photon energy for two reference types.

4.3 Application to Biological Samples

So far, the experimental results of the holographic technique have involved especially fabricated test samples made of 340nm-thick gold or 590nm-thick silicon coated with a nanolayer of iridium. To prove that the technique is a good candidate for single-shot imaging of biological samples, which is a desired application for XFELs, we have performed some holographic experiments using three types of biological samples: a) marine micro-plankton platelets, (b) Deinococcus radiodurans bactera, and (c) microscopic sea-creatures found in hydrothermal vents. For a description of the samples and the preparation methods involved, we refer the reader to Section 3.2.

Marine Micro-Plankton

A specimen of micro/nano marine plankta was provided by Elisabeth Read from Cambridge University in powder form. We prepared a sample of the provided material at the I13 laboratory where a few milligrams of the powder was crushed using a mortar and hydrated in 100 μL of purified water and the solution was then stirred to ensure the separation of particles. A micro-droplet was deposited onto a silicon nitride membrane and air-dried. The sample was then mounted in the holographic setup maintaining all experimental parameters as the test-sample experiments. We scanned through the substrate to locate specimens of interest by using the alignment microscope located near the sample that produces near-field magnified projections of the sample. This allows us to have a clearer identification of samples before switching to far-field detector and operating in the Fraunhofer regime. We obtained holographic diffraction measurements of the plankta specimen at 8 keV and 9 keV photon energy and 50-200 sec exposure time using the 4 μm, 6 μm, and 8 μm bare silicon pillar reference where the maximum total detected photons reached 1.27 $\times 10^9$ counts per shot. Following the data-correction method discussed in Section 4.1.1, we obtain background-subtracted normalised images of plankton samples as shown in Figure 4.22.

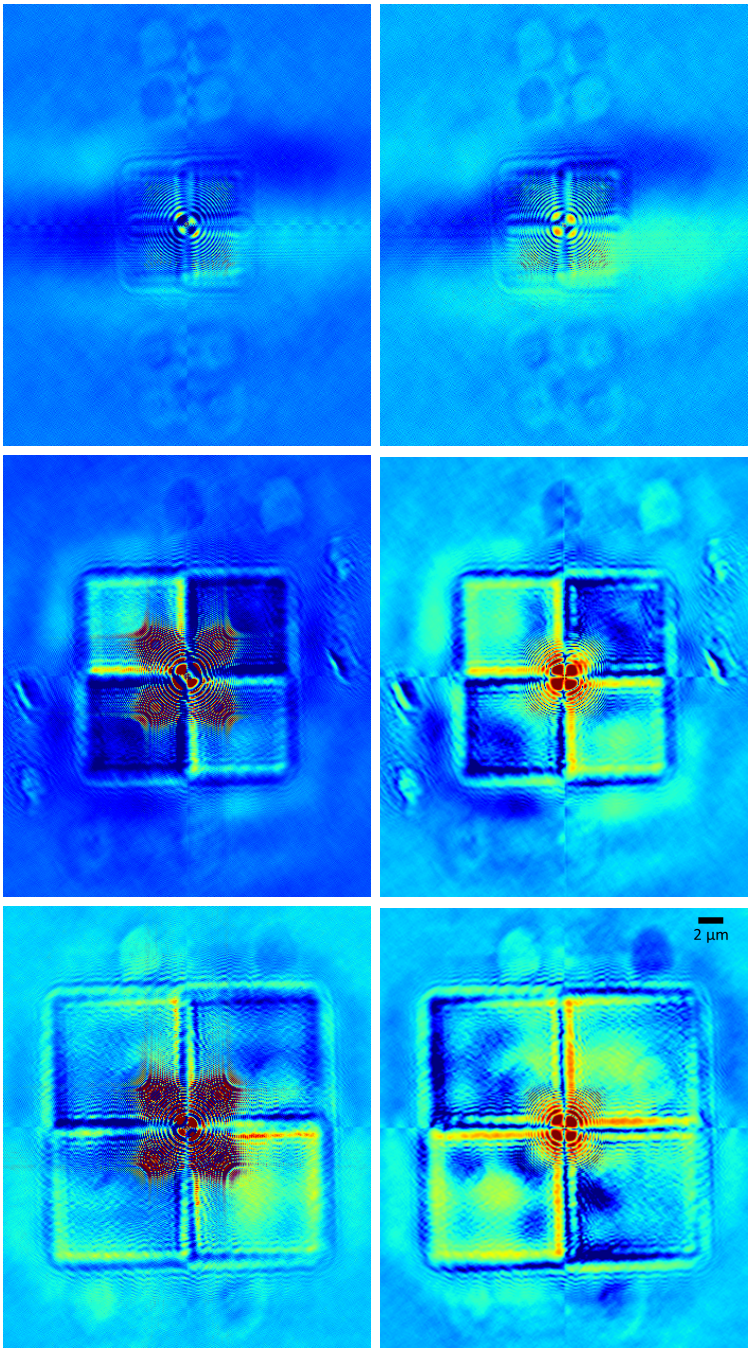

Figure 4.22: Selection of background-corrected phase reconstructions of coccolithophorids using a 4 μm reference pillar at 50 sec exposure (top), a 6 μm reference pillar at 200 sec exposure (middle) and a 8 μm reference pillar at 200 sec exposure (bottom). The upper reconstruction images are in-focus and the lower twin images are out-of-focus.

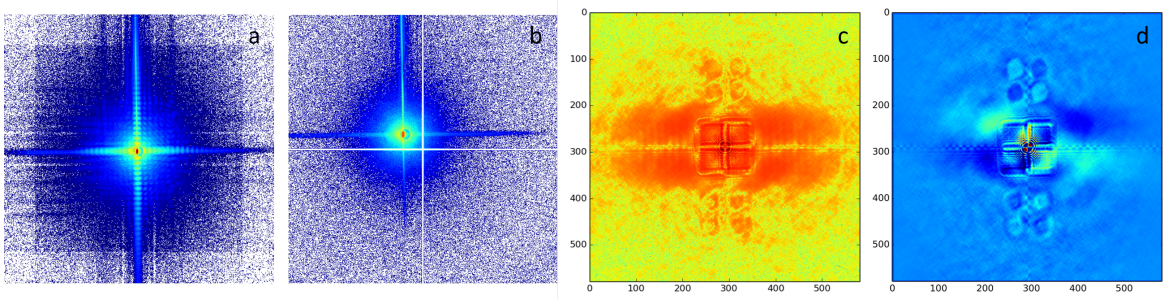

Figure 4.23: (a) Diffraction pattern of plankton coccolithophorid and 4 μm silicon pillar reference, (b) diffraction pattern of plankton alone, (c) amplitude reconstruction where the upper-side images are in-focus, (d) normalised scaled phase reconstruction with background correction. FOV = 38.7 μm.

We notice that the reconstructed area obtained with the 6 μm reference in Figure 4.22(middle) contains additional out of focus demagnified sample reconstructions which arise due to a neighbouring 4 μm reference structure that is partially illuminated by the beam. The reconstruction resulting from the 8 μm reference shown in Figure 4.22(bottom) shows two images of the plankton sample located close to the reference autocorrelation edge and two bottom images overlapping with the reference area. Note that the reference stage and the sample stage were separated by around 3.5 mm. By propagating the differentiated hologram in real-space by -3.5 mm, the sample reconstructions arising from the upper four virtual corners are brought into focus, and the lower four are out-of focus.

Figure 4.23(a) shows the recorded holographic diffraction pattern of the plankton specimen with an offset 4 μm silicon pillar measured at 8 keV and a total 3.3 $\times 10^7$ detected photons per shot. The speckle pattern resulting from only the plankton sample in the beam without exposing the reference is shown in Figure 4.23(b) where horizontal and vertical flares appear due to the beam-forming slits. It is apparent with such an exposure time and incident flux that the scattering signal of the sample is rather weak, covering a maximum of half the detector area. One would assume that this method, producing a direct unfiltered reconstruction from a single shot exposure, should not provide a well-resolved image with sufficient SNR of such a weakly scattering sample and would require a high incident flux and a lot of averaging. The background-subtracted reconstructions of the sample

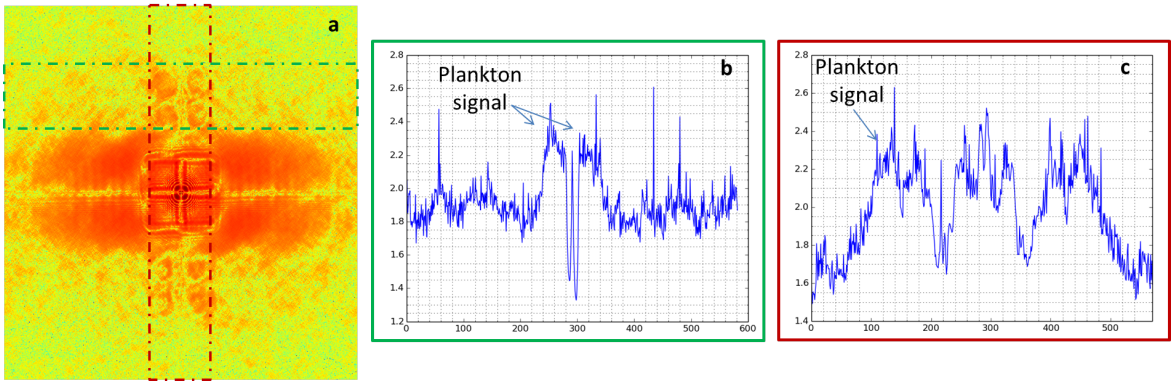

Figure 4.24: (a) amplitude reconstruction showing absorption signal of plankton coccolithophorids, plot profile of (b) summed vertical area in orange showing the amplitude signal level compared to the background, and (c) summed horizontal area in green showing the amplitude signal level compared to the reference autocorrelation. FOV=38.7 μm.

absorption and phase in Figure 4.23(c-d) show four images of the plankton specimen appearing as a round object with a pointy end. Contrary to humble expectations, the plankton signal at its highest level has a visibility of 75% with respect to the background level in the amplitude reconstruction and with a spatial resolution that allows us to distinguish details such as a skewed sharp pointy corner. This example represents the lowest level of capability of our holographic setup since it is at low flux, exposure time, messy incident beam, and using a rough-edged pillar reference. Nevertheless, the produced reconstructions are still of fairly impressive quality despite the imperfect settings. Figure 4.24(a-d) shows the background-subtracted amplitude reconstruction. The plots compare the signal intensity of the reconstructed area, with a 10% mean error and a maximum level of 200 units, to the background of average 63 units (log10 = 1.8) and to the reference autocorrelation signal (Figure 4.25). The absorption amplitude of the sample reconstructions is comparable to the reference autocorrelation signal, which makes it safe to conclude that the sample probably has similar absorption properties as the reference, i.e being a light material similar to silicon of low electron density.

The plots in Figure 4.25(b-c) show the phase of two opposite reconstructions in Figure 4.25(a) with the corresponding phase shift alternating from $\Delta\phi_1 = \phi_{obj} + (\phi_{s1} + \phi_{s2})$ to $\Delta\phi_2 = \phi_{obj} - (\phi_{s1} + \phi_{s2})$ with a sharp transition to 0 (or π) at the surrounding area, where ϕ_{obj} is the actual phase of the sample, ϕ_{s1} and ϕ_{s2} are

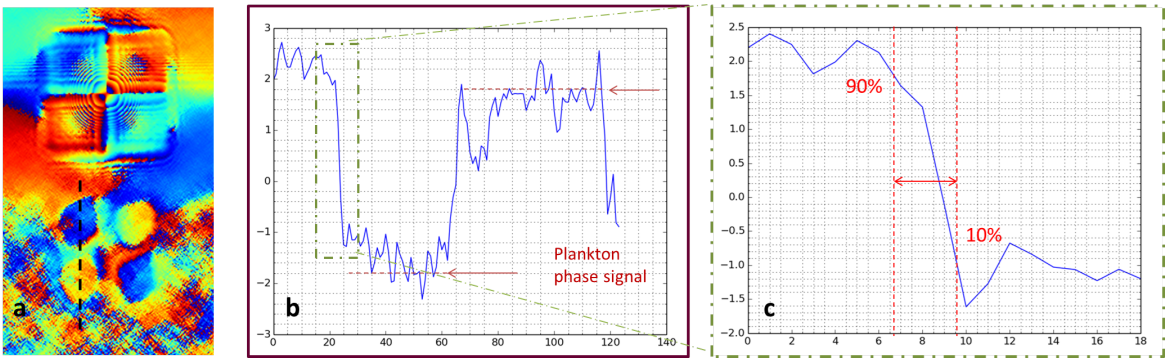

Figure 4.25: (a) Raw phase reconstruction of four coccolithophorids, (b) line plot along black dashed line, (c) inset of dashed region in (b) showing the knife-edge resolution.

the phase of the sample substrate and reference substrate respectively, and $\Delta\phi$ is the measured shift in phase between the sample reconstruction and the surrounding. At 8 keV energy, the measured phase shift at the first reconstruction corresponds to $\Delta\phi_1 = 4.15 = 1.01 + \pi$ rad and $\Delta\phi_2 = 1.45$ rad. With $\phi_{s1} + \phi_{s2} = 0.24$ rad, $\phi_{obj} = \Delta\phi_1 + (\phi_{s1} + \phi_{s2}) = 1.01 + 0.24 = 1.25$ rad, and $\phi_{obj} = \Delta\phi_2 - (\phi_{s1} + \phi_{s2}) = 1.42 - 0.24 = 1.21$ rad. We find that the two values of ϕ_{obj} calculated for the two phase reconstructions in Figure 4.25(a) are in high agreement with one another within a 3% error bar, which means that the holographic reconstructions provide reliable phase measurement results. The second plot in the figure displays a resolution measurement by a knife-edge profile showing the 90%-10% width to be 2.5 pixels or 169 nm with a pixel size of 67.7 nm.

Figure 4.26 shows reconstructions obtained from various measurements of two specimens of plankton platelets. From the collection of reconstructed images, we find that most specimens appear to be skewed or have a round shape with a point end. Some research on marine microplankton taxonomy [60, 61] has documented that the plankton platelets knowns as coccolithophorids can be found in different phases where the shape of the coccospheres changes according to the phase they are in. It is seen that the coccolithophorids appearing in our reconstructions resemble the holococcolith phase which have a characteristic of being flat and lack a surrounding radiating membrane as described in [60, 61]. Our plankton specialist has confirmed that the extracted sample contains an equal probability of holococcoliths and heterococcoliths. Yet, we believe that the skewed and pointy

edges are merely a result of the platelets being fragmented and broken due the sample being grinded during preparation. However, a most recent SEM image of a sample taken from the same capsule was produced by Elisabeth Read. As we see in Figure 4.27, even though the concentration of the sample is much higher than what we prepared for this experiment, the SEM image shows us the fragments of HOL phase coccolithophorids which agree with the shapes that we observed from the holographic imaging experiment. Marine micro-plankton samples are of high interest in oceanography, marine biology, and archaeology, particularly to understand the history of the earth. One interest is to study the distribution and concentration of trace elements deposited in calcified shells. Investigation of remineralisation, calcification and iodine deposits in the plankton helps to trace paleoceanographic conditions and gain insight into global climate changes that date back to millions of years.

As we have seen in Section 4.2.3, the quantitative analysis is most accurate when there is a clear understanding of the phase and absorption contributions of the reference and substrates, assuming minimal contribution from additional elements affecting the beam illumination such as the beamstop, slits, and windows. With our holographic diffraction x-ray imaging technique, we are able to use the extracted phase information (calculated in the previous paragraph) and the absorption maps to extract the electron density and determine the concentration of trace elements and calcification or remineralisation.

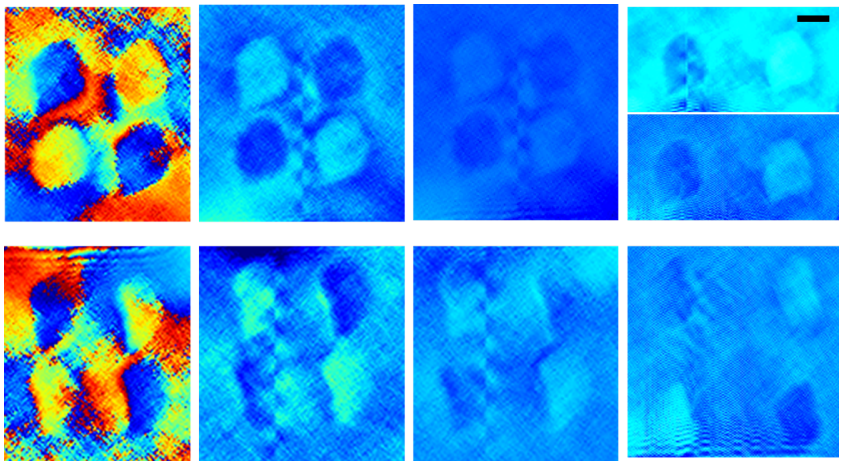

Figure 4.26: Selection of reconstructions of microplankton coccolithophorids using silicon pillar reference at 50 s, 100s, and 200s exposure. Scale bar = 2 μm.

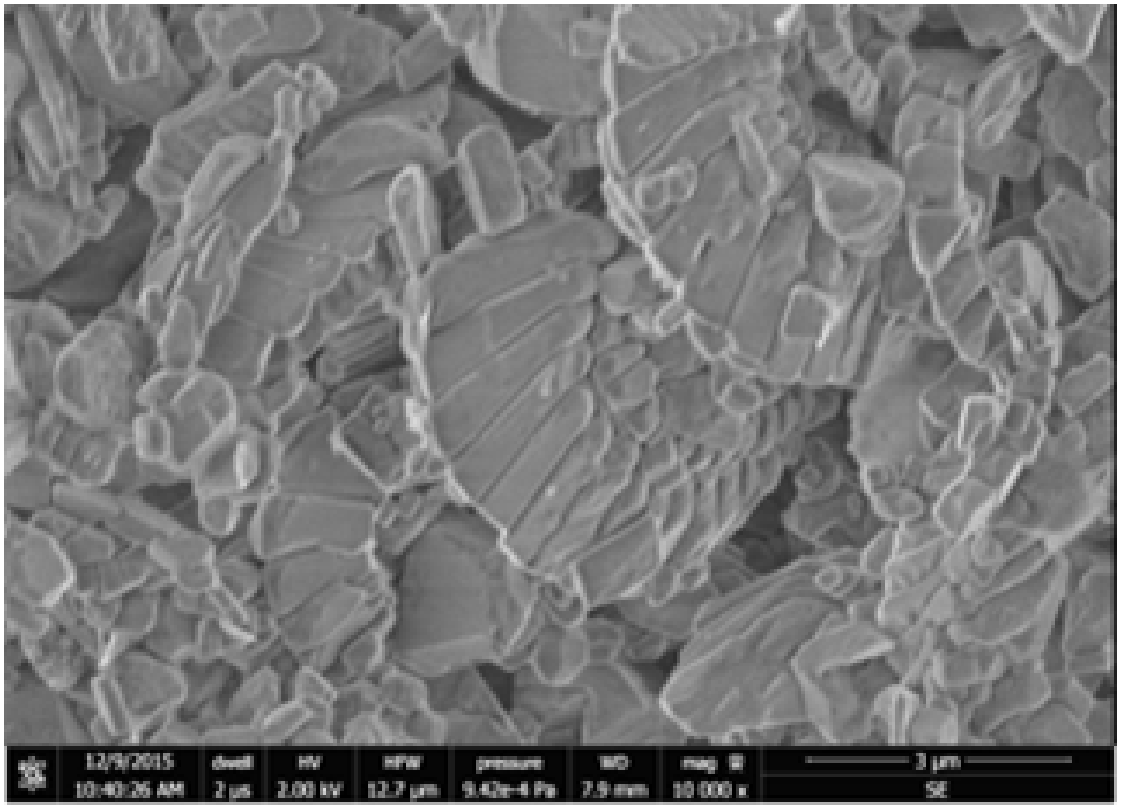

Figure 4.27: SEM image of similar membrane deposited with the plankton from the same sample but with higher concentration that our holographic data. Fragments of coccolithophorids of both the HET and HOL phase are abundant.

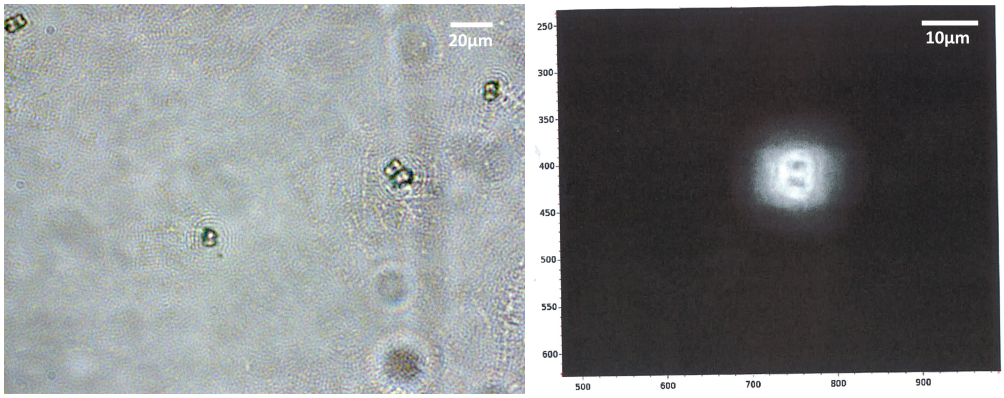

Figure 4.28: Optical micrograph (left) and near-field projection (right) of Radiodurans bacteria cell.

Deinococcus Radiodurans Bacteria

Cells of the Deinococcus Radiodurans bacteria wild-type strain were ordered from DSMZ [66] as a freeze-dried culture in a powder palette. A sample of bacteria was prepared from the freeze-dried palette at the laboratories of I13. A sample was hydrated and deposited on the flat surface of a 1 mm silicon nitride membrane and let to dry at 30° under ambient pressure. The bacteria sample was mounted into the holographic setup with the ALD wireframe references which were previously tested in Section 4.1.2. We scan through the sample using an alignment microscope that provides magnified projections of the sample in the near-field. We perform a scan similar to STXM of the entire sample membrane to obtain a map of all the specimens on the membrane. We inspect the specimens using the alignment microscope and select specimens (Figure 4.28(right)) that have suitable sizes for the imaging technique by correlating with the optical microscope images (Figure 4.28(left)) obtained before the x-ray experiment. The specimens were typically selected not to be in the smaller size range (5 μm) to suit the holographic experimental conditions. For this reason, without cross-validating with another imaging technique, we can not be sure where what we image is a single cell or a tetrad of bacterial cells.

With a documented electron density of $\rho = 1.35 g/cm^3$ [71], this sample qualifies as a very weakly scattering sample with a transmission 99.8% and a maximum phase 0.1π for x-ray imaging at 9 keV. Contrary to the plankton sample which is

mainly composed of $CaCO_3$ and contributes a sizeable phase shift, the chemical composition of the bacterial cell is assumed to be similar to H50C30N9O10S1 which exhibits the same characteristics as light hydrocarbons with high energy x-rays. Therefore with far-field coherent diffraction imaging, we expect to find difficulty with obtaining image reconstructions with sufficient contrast.

The reconstructed sample areas obtained by holographic diffraction imaging using the iridium wireframe reference and exposing three different bacteria specimens are shown in Figure 4.29, as the background-corrected normalised phase of the reconstructions using the both the real-space and Fourier-space differentiation procedure. To the untrained eye, it seems that there is no reconstruction of the bacteria at the locations above and below the reference square. However, by examining the collection of reconstructions we find that some products in the image are constant and some are not. The constant products in the image are the reference autocorrelation and its near-field propagation fringes, vertical and horizontal fine modulations due to detector gaps, and weak circular low-frequency fringes resulting the high intensity zero-order peak, the beamstop cut-off, and from specks and contributions from the substrate. We find that the aforementioned effects are almost equally present in all the six reconstructions displayed. However, there are some changes among the reconstructions particularly in the area shown in a red square above the reference square autocorrelation (which is where we expect the object reconstructions to be in-focus). By examining these areas, we find some weak outline of structures that appear as thin blobs. Yet, the contrast level is very low, but in some reconstructions we are able to distinguish the sample, owing to the edge-enhancement capability of the imaging system, and we in fact see the fairly sharp outline of the bacterial cell with low contrast as seen in Figure 4.29(b-c). In addition, in Figure 4.29(b) and (e), we can distinguish two copies of 2 horizontally extended bean-shaped structures which appeared to be vertically attached where the two on the right have a positive intensity and the two on the left have a negative intensity, which is an expected alternation due to the holographic method as previously seen with the test-samples. The other two reconstructions due to the other two corners may be either overlapping with the reference autocorrelation or simply outside the FOV since the bacterial cell might be larger than 6 μm. In

other cases such as Figure 4.29(c,d), it appears as if the bean-shaped structure is rather shrivelled and deflated, and this may be due to the fact that the bacteria on this membrane were not cultivated in a nutrient medium and were not active cells but merely rehydrated in water from a frozen palette.

The signal arising from the bacteria reconstructions is plotted in Figure 4.30 comparing the signal strength to the background and to the reference autocorrelation signal. As we already know, the sample signal is very low, and has a magnitude of 10% above the background signal, as in the highlighted dashed square of the plot in Figure 4.30(b). Unfortunately, we are not able to characterise the sample information or gain knowledge any further than what we have already observed. In order to obtain better reconstructions, it is beneficial to lower the x-ray energies down to around 6 keV (or lower) where it has been successfully implemented with ptychographic experiments at PSI with the same type of sample. Apart from decreasing the energy, it would be suitable to prepare a reference with a thickness that provides higher contrast, i.e a phase-shift of exactly π for the case of a bare square pillar structure, or a thicker ALD coating of Iridium to provide higher absorption contrast and a π phase-shift to provide high phase contrast. This method is also fully extended to soft x-ray imaging where one can perform the same experimental holographic imaging method but with fabricated references of much less thickness and hence a possibly higher edge/nanolayer sharpness. Such a bacteria sample would potentially be a good candidate for successful soft x-ray imaging of biomolecules. A cut-out magnified selection of reconstructions is shown in Figure 4.31 and 4.32 where the voluminous bean-shaped cell structures are more clearly visible in the bottom row as well the thinner shrivelled cells in the top row. Another possibility to enhance the sample reconstruction signal would be the coat the substrate including the deposited bacteria with a nanolayer of a heavy metal by e-beam evaporation, sputtering, or ALD, or even to deposit gold nanoparticles by e-beam evaporation to increase the sample contrast and aid in distinguishing samples from the background and irrelevent particles.

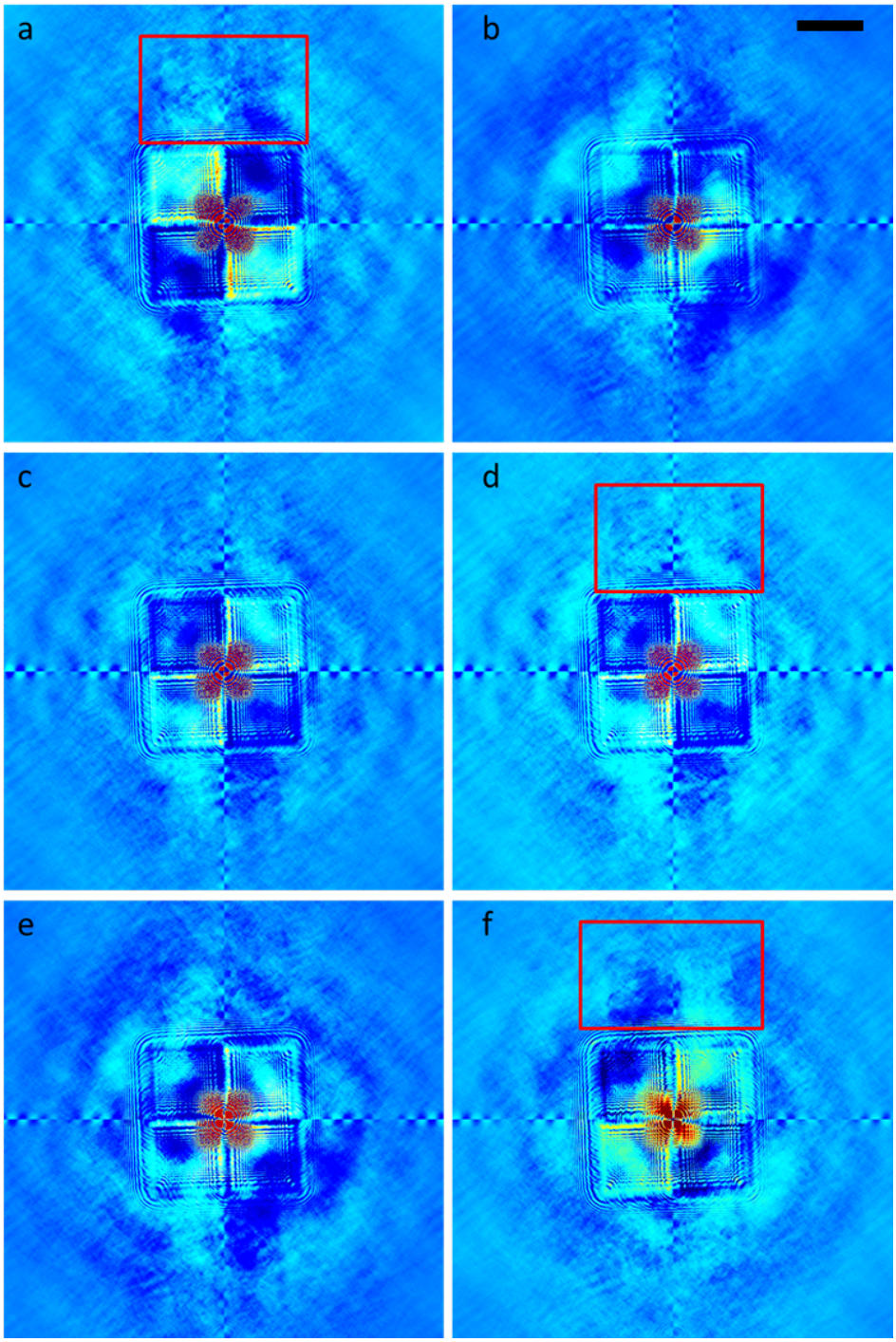

Figure 4.29: Selection of background-filtered reconstructions of the 3 different Radiodurans bacterial cells with the wireframe reference from 500 sec exposure. The upper regions (red box) are where the bacteria images are expected. Scale bar: 5 μm.

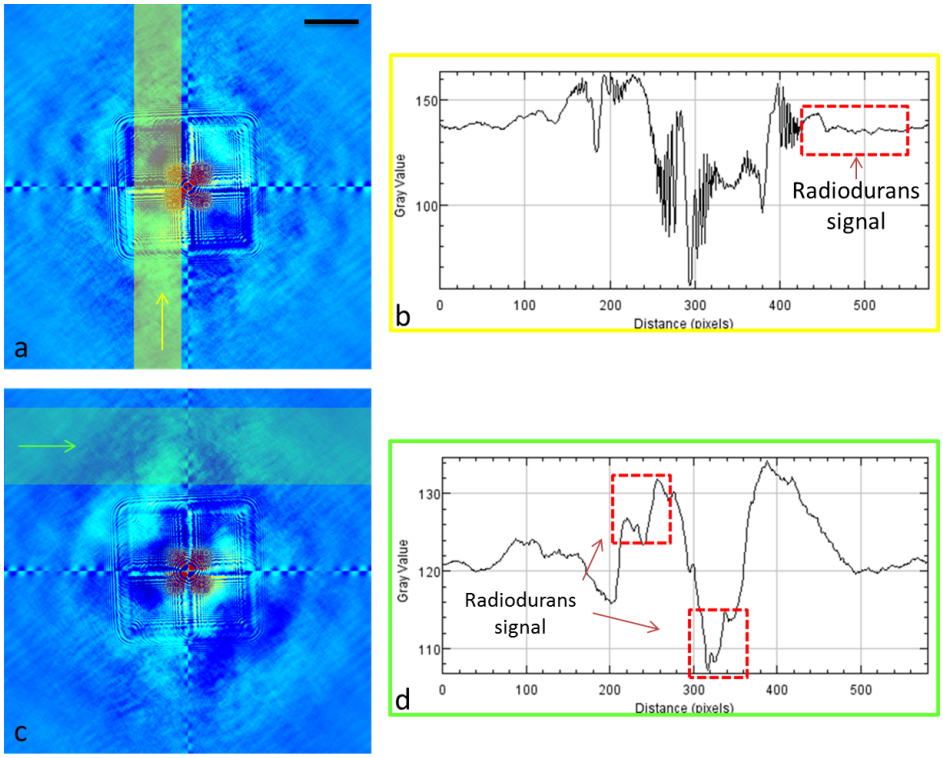

Figure 4.30: (a,c) background-corrected reconstructions of Radiodurans sample with Ir/Si reference. (b) profile plot through summed vertical yellow region showing the signal level of the bacteria compared to the reference signal, and (d) that of the horizontal green area comparing with the background signal. Scale bar: 5 μm.

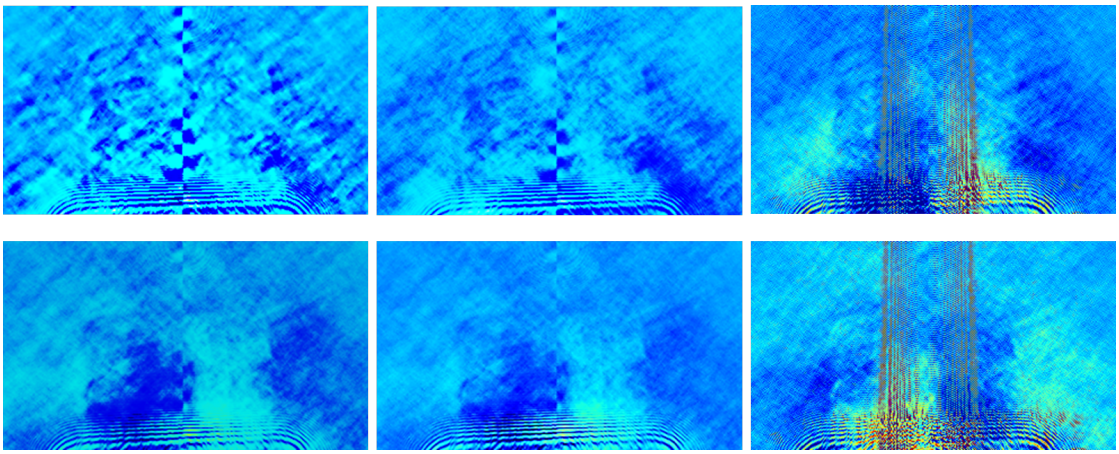

Figure 4.31: Selection of magnified crop-outs showing the reconstruction of the bacteria cells where the bean-shaped structures are visible. (top) shows thin shrivelled structure. (bottom) shows more voluminous structure.

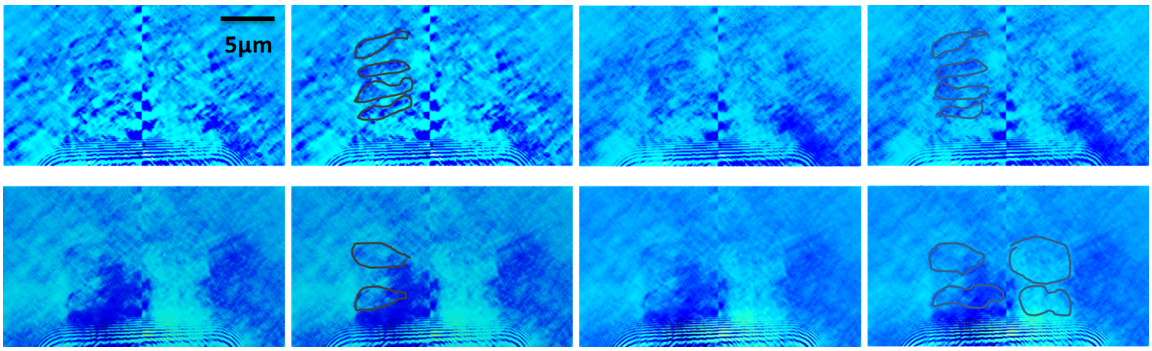

Figure 4.32: Highlighted outline of the bacterial cells.

4.4 Discussion

We have performed holographic experiments and simulations using phase-shifting extended references and successfully obtained image reconstructions of absorption and phase using both strongly and weakly scattering test-samples. In the previous section, we discussed the successful results of applying this holographic imaging method to biological samples. Here we give a comparison of reconstructions between the square-shaped reference and the wireframe structure, specifically in regards to resolution and contrast, and we will discuss image averaging and post-processing refinement to improve statistics. We will introduce further computational and experimental methods that have prospect to enhance image quality. We will finally conclude the chapter with the outlook and further applications.

4.4.1 Resolution

The two structures generating the reference waves in the previously discussed experiments deliver different resolution due to their structural differences. We conclude that the image error provided by square-shaped references has low sensitivity to the sharpness of edges compared to a pinhole or a slit reference. This is discussed in Chapter 2 and in more detail by Guizar who concluded that with the square reference, the error does not change much beyond a certain edge sharpness; whereas the pinhole and slit references shows an exponential dependence on the reference sharpness. For example, a small pinhole reference delivers high resolution but low SNR, and vice versa, whereas with a square reference the SNR stays relatively constant for increasing corner sharpness. This proves to be beneficial since it makes the technique less sensitive to noise, it is more robust to lower incident flux, and it eases much of the structural and geometrical requirements of the square reference in comparison to the pinhole/slit reference. Therefore, as we have seen with experiments in Section 4.1.1 performed at 8 keV with 50 sec exposure time and low photon count of 3.3 $\times 10^7$ as well as with a fairly modest reference edge-sharpness, we are still able to obtain sample reconstructions with sufficient SNR and a resolution of 130 nm (shown in Figure 4.33 (a)).

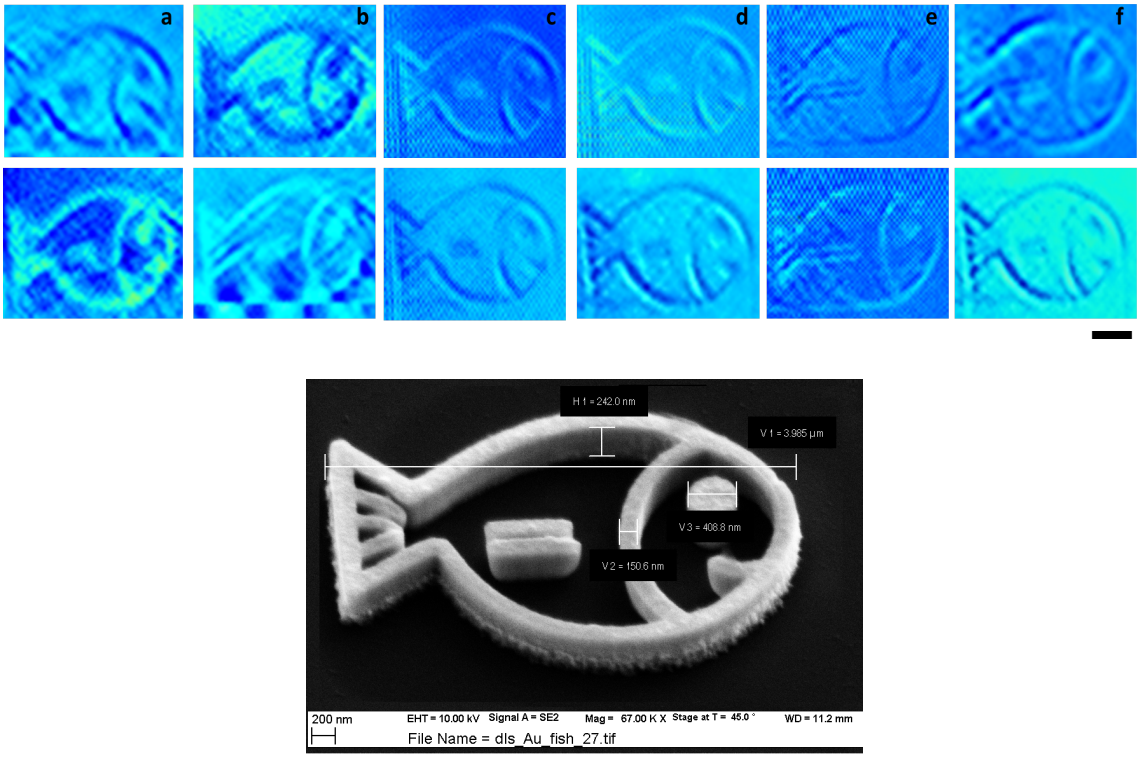

Figure 4.33: Background-corrected reconstructions of the gold fish sample with varying exposure, energy, and for the Gxy and DF-filter methods for full-area Si pillar: (a)50s 8kev, (b)100s 9kev. Ir/Si wireframe reference: (c) 200s, (d)300s Gxy, (e)300s DF-filter, (f)500s (bottom is twin image of top), Scale bar: 1 μm; compared to the SEM image.

By increasing the incident flux and the exposure time (up to a certain threshold), we are able to see an improvement in the resolution at 90 nm. By using a ultra-sharp reference fabricated using atomic layer deposition structured in the shape of a wireframe of compound materials, the resolution is finally refined to the absolute maximum allowed by the experimental parameters, i.e to the maximum angle limited by the detector size equal to 61 nm.

Table 4.4 shows the values of the resolution corresponding to the highest order detected fringes given by $\rho_{p,q}$ and the values of the reconstructed image resolution calculated by a 90%-10% knife edge test of the reconstructions of the gold fish test sample. Moreover, Figure 4.33 shows the evolution of the sample reconstructions with the silicon pillar reference and the Ir/Si nano-wireframe throughout an increase of photon flux. We find a clear improvement in resolution with the wireframe

reference where we resolve the tail and fin with details of sub-100 nm. With the increased exposure time and by applying the reconstruction procedure using the differential Fourier operator, we are able to resolve the gap between the two horizontal fins (Figure 4.33(e)) which has a maximum width size of 50 nm. The SNR also improves with the Ir/Si wireframe reference (Figure 4.33(c,d)) compared to the silicon pillar (Figure 4.33(a,b))and reaches a steady level at around 2.45×10^9 detected photons above which the reconstructions suffer more artefacts and noise resulting from the non-linear dynamics of the detector over a certain threshold.

Furthermore, we observe the difference between the contrast mechanisms involved with the two types of references. Reconstructions obtained with the iridium wireframe reference show a clear differential contrast around the sample edges compared to the reconstructions obtained with the silicon pillar that show a constant contrast. The top and bottom row of sample images (in Figure 4.33(a) to (f)) are two complex conjugate reconstructions located at two virtual reference corners. The complex conjugate images obtained with the silicon pillar have opposite intensities, and those obtained with the wireframe have opposite directions of differntial contrast (opposite diagonal directions of the phase gradient). By comparing the holographic reconstructions to the SEM image shown in Figure 4.33(bottom), it is evident that the reconstructions are highly comparable and unveil all of the sample details with good resolution.

Ref. Structure	**Ref. Material**	$\mathbf{E}_{photon}$	$\mathbf{N}_{total}$	$\rho_{p,q}$	$\rho_{x,y}$
square pillar	9 μm Si	8 keV	3.3 $\times10^7$ ph	102 nm	130 nm
square pillar	9 μm Si	9 keV	1.17 $\times10^9$ ph	75 nm	90 nm
wireframe	3.9 μm Ir/Si	9 keV	2.45×10^9 ph	61 nm	61 nm
wireframe	3.9 μm Ir/Si	9 keV	9.73×10^9 ph	61 nm	$\leq$ 61 nm *

Table 4.4: Measured resolution $\rho_{p,q}$ from q_{max}, and $\rho_{x,y}$ from image reconstructions with different reference types at varying photon energy and flux.

4.4.2 Image Averaging

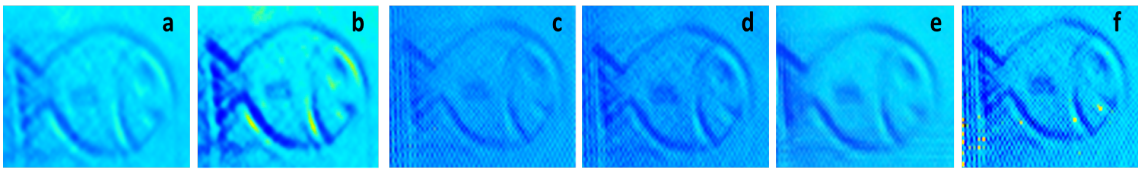

Figure 4.34: Comparison of (a) original reconstruction at high exposure with (b) sum of 5 reconstructions; (c) original, (d) sum of 5, (e) averaged over 5 and denoised using a smoothing function, (f) image sharpening filter.

The square-shaped reference (albeit a pillar or wireframe structure) produces four reconstructions at the locations of the four virtual corners, as well as their complex conjugates centro-symmetrically from the reference. This aspect counts as an advantage allowing us to have a more extensive visualization of the sample, compared to a single point reference, in addition to enhancing the success rate of obtaining a distinguishable reconstruction. Other than that, it also allows us to average the four reconstructions and potentially increase the SNR and differentiate artefacts from actual sample detail. In addition, another advantage of our holographic setup for increasing sample statistics is the fact that the sample plane and reference plane are physically separated. In other words, the sample being mounted in an unconfined manner allows us to shift the sample laterally and longitudinally.

By laterally shifting the sample and keeping the reference fixed, we change the offset distance between the center of the reconstructions and the reference autocorrelation and hence we obtain several datasets with multiple positions of the sample in the beam. This proves beneficial when the illumination beam is not completely uniform, which means that we would illuminate the sample at different positions and recover information that may otherwise be obstructed or poorly illuminated. Furthermore, reconstructions obtained at several sample positions with fixed and known step sizes can then be combined to produce an averaged reconstruction. All this being done while keeping the reference at a fixed position in the center of the beam

signifies that the combined data all have the same reference wave characteristics. More importantly, it proves beneficial again compared to a fixed-plane setup where shifting the sample for better illuminating also entails shifting the reference with it and hence potentially poorly illuminating the reference as a result.

Throughout our experiments, we have taken advantage of our unconfined geometrical setup and have performed measurements with multiple shifted sample positions which has drastically increased our success statistics compared to a fixed plane scenario. This has also enabled us to obtain live reconstructions for certain positions to cross-validate the setup and then alter the parameters as needed. This also creates an advantage compared to a fixed-plane scenario where one can only simulate or predict the experimental result before fabricating the sample. But once the sample is finalised and fabricated, if the experimental data prove it not to be well-designed, then one needs to perform a new fabrication and repeat the experiment, which is time consuming. In addition, when having the sample fixed on the same substrate as the reference, one would need to deposit or fabricate same good-quality sample specimens in the vicinity of every fabricated reference. Since sample specimens are generally not so homogeneously distributed in size, shape, and quality (especially biological samples), this means that there is a high chance that a good sample is present next to a poor reference. On the other hand, using our unconfined setup, we are able to locate the reference of best quality and scan through the samples of interest. Consequently, we can collect holographic data of a large set of samples distributed densely on one membrane or even on different membranes while keeping the best-chosen reference at a fixed position.

Therefore, the potential of this holographic unconfined setup is well beyond what has already been accomplished in our experiments and demonstrates high advantage especially for imaging radiation-sensitive and biological samples, as well as samples that require collection of a large number of datasets. Figure 4.34 shows an example of a reconstruction obtained using the iridium wireframe reference (Figure 4.34(a) and (c). Figure 4.34(b) and (d) show the sum of reconstructions from five shifted datasets of Figure 4.34(a) and (c) respectively; Figure 4.34(e) shows the mean of the 5 datasets with a denoise filter applied, and Figure 4.34(f) shows

the summed reconstructions (d) with a sharpening filter applied. The summed reconstructions, even of only five datasets, shows a distinguishable increase in SNR and contrast and filters out the irrelevant artefacts. Due to lack of a large number of shifted datasets, we have only been able to obtain a certain extent of averaged data. Recording further datasets will ofcourse provide better statistics. The averaged reconstruction with an applied denoise filter smoothes out the sharp edges but removes noise as well as contributions of the repeating overlapping reconstructions from the reference corrugations. Sharpening the summed reconstructions provides a higher contrast and better resolution but also increases the background noise into high-frequency perturbations.

4.4.3 Contrast

The experimental and simulated results illustrate that the contrast is independent of the total surface area of the reference, specifically for the case of a square reference. Given the same material used for the wireframe reference or the square reference, the contrast of the absorption image with the full-area reference would be the same as that of the sample edges with the wireframe reference . Therefore we must point out that using a phase-shifting wireframe reference does not provide image samples with increased signal, it merely serves as an edge-enhancement method that also provides differential phase contrast and provides bulk information. We must distinguish the difference between contrast enhancement of the bulk and edge-contrast enhancement. While the wireframe reference does provide edge enhancement, the contrast of the bulk is not necessarily enhanced, depending on the sample properties.

Furthermore, the symmetry of the square (or parallelogram) structure leads to the SNR being is independent of the reference surface area [47]. Another special feature of this type of reference is that the amplitude strength of the wireframe reference signal would be the same as that of the full-square reference, since the derivative reduces the square reference to 2 sets of vertical and horizontal wires as well. The dependence of the error and the resolution on the reference length for the parallelogram shape is discussed in length in the thesis of M. Guizar who calculated

the expected image squared-error for different types of extended references and concludes that the paralellogram reference is the most robust to noise and is independent of the length L of the reference. While the contrast is independent of the reference size, it is dependent on the complex transmissivity of the object and the reference. When introducing a reference composed of two structures of different material, the phase contrast and absorption contrast change as a function of the x-ray properties of the two materials i.e the ratios of βs an δs; and the individual phase shifts accumulate to form a phase gradient.

With all this in mind, it important to note that the virtue of a holographic method that utilises a reference of compound structures with phase-shifting properties lies mostly in the experimental application with hard x-rays in addition to sample fabrication. Indeed one can easily suggest to use a dense material such as iridium with a phase shift of π and ultra-sharp edges placed on a highly transmissive substrate and profess to obtain extreme contrast and resolution. But the fact of the matter is that the fabrication of such a structure for imaging with hard x-ray energies is virtually impossible and is hindered by not one but many challenges. On the other hand, the fabrication of thick yet almost atomically sharp structures of light material such as HSQ, SiO2, and silicon is very well routinely achievable by nanofabrication lithographic techniques. The highly sharp pillars of silicon introduce a reference signal with a π phase shift but barely introduce any absorption, which is where the advantage of the iridium wireframe setup lies. In addition, it is well known to lithographic experts that it is easier to produce an atomically sharp or ultra-high resolution structure from a thin material, than producing ultra-sharp or high-resolution thick and bulky, since the more the material the higher the error. That is why with atomic layer deposition, one can create a stable high-resolution nanolayer of a heavy-metal dense material by depositing atomic layers one upon the other in very high precision. This nanolayer of a π phase shift and considerable absorption is coated onto a sharp silicon pillar in a straightforward fashion. Therefore, the advantage of all this is that we create an outlet from the difficulties of fabrication and maintain a high-performance holographic reference structure that contributes sufficient phase and absorption contrast, high resolution, edge enhancement, as well as differential phase contrast.

Additional Methods

We find interest in exploiting the mathematical properties of various reference structures to open new horizons in holographic imaging with phase-shifting extended references. As we have seen with a reference of non-standard geometrical shape with structural layers, we are able to obtain a holographic reference that functions differently than the FTH and HERALDO setups. It provides new levels of phase contrast and absorption contrast by the virtue of differential point-source references while overcoming the noise-resolution coupled relation associated with the FTH method. It is important to mention that the nature of a differential reference allows us to tackle the reconstruction procedure in an alternative way. In contrast to applying the directional differentiation to the wireframe reference and obtaining derivated delta peaks, it is also sensible to apply a directional integrating operator that upgrades the differential reference to a full-area reference and transforms the corner derivated delta peaks consisting of a positive and negative double-peak into full single peaks. This has been applied by M. Guizar using a "cross-wire reference" which is similar to the wireframe reference in the sense that it applies with an integration operator. In such a way, all contributions to differential contrast and to edge-enhancement would be eliminated, and the reconstruction signal reduces to that of the bulk of the sample.

By changing the experimental parameters, i.e detector size, propagation distance, detector pixel size, and the photon wavelength, as well as improving the fabrication quality of the reference structure, it is possible to push the resolution limit further by an order of magnitude, realistically to a low nanometre scale. Yet, there are further methods to improve the resolution and the statistics of the reconstructions. By combining the holographic imaging results with an iterative input-output or a shrink-wrap algorithm, one can enhance the resolution beyond the reference resolution. The method relies on using the initial holographic reconstruction is used to provide a first guess of the phase and the apriori knowledge of the sample transmissivity serves as a mask for the iterative loop. It has been documented that such a method provides satisfying results and enhances the resolution as long as the oversampling condition is satisfied and the sample-reference

area is sufficiently isolated. Nevertheless, similar to non-scanning iterative methods with coherent diffraction imaging, the convergence towards a unique unambiguous solution not always guaranteed.

Furthermore, other holographic methods promise an improved SNR and resolution beyond the reference limit by deconvolution with the transmission function of the reference [72, 73, 74]. This method requires fully characterising the reference and obtaining spatially-resolved images of the reference generally using an alternative imaging technique such as SEM or TEM. Similarly, some other methods rely on a holographic reconstruction of the extended reference structure using another reference such as a pinhole to characterise the reference before employing it with a sample. The transmissivity of the extended reference recovered by the prior experiment is then plugged into the deconvolution algorithm. A recent study published in 2014, that alleviates the need for a specific geometry of reference structures and claims that any structure may be used, relies on empoying an apriori well-resolved image of the reference structure using a microscopical method. In some cases it appears such a method lacks self-sufficiency as the resolution of the holographic system would then depend on that of the reference-characterising microscope. In other words, the higher the resolution of the microscopical image of the reference, the higher the resolution of the sample resulting from the holographic reconstruction using that reference. In such a case, one wonders that if an object can be imaged with high spatial resolution using an alternative method then it would be redundant to apply the highly resolved image to refine a holographic image. However, it could seem beneficial if the holographic image provides additional information about the sample (other than two-dimendional spatial information which the electron microscope provides), such as 3d-images, quantitative analysis (electron density and index of refraction etc..) and time-resolved dynamic processes, which has not been fully achieved using the deconvolution method yet.

Ptychography [75, 76] has been a prominent iterative scanning method that delivers a stable statistics of converging unambiguous and well-resolved images of the of samples using a variety of radiation. Nevertheless, being a scanning method, it may be hindered when imaging radiation-sensitive samples. The holographic

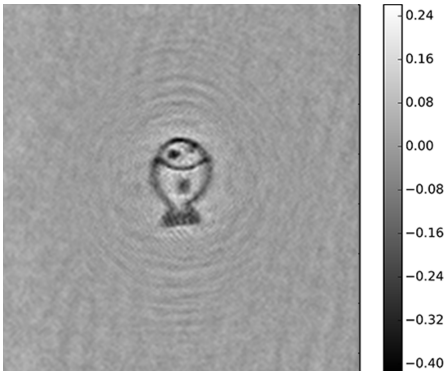

Figure 4.35: Ptychographic reconstruction of the gold fish test sample in Log amplitude.

methods using phase-shifting extended references dicussed in this thesis provide direct retrieval of the complex transmissivity by single shot exposure of the sample. As previously mentioned, it has proven that the resolution delivered by holographic imaging with prepared references is no longer limited by the edge resolution of the reference structure if the latter is be well-characterised using an alternative method. Since ptychographic and holographic experiments with hard x-rays are designed as very similar setups, it is possible to combine the two methods in one experimental session to obtain a superior result. Other than combining the two for the sake of correlative results, it is reasonable to ptychographically image the reference structure to obtain the two-dimensional transmission function of the reference with high-spatial resolution and low noise, and use that information as a holographic mask to the reference at the same photon energy and experimental parameters. This allows us to eliminate errors and undesired products in the reconstructions that result of cross-correlations with imperfections, specks, or any artifacts irrelevent to the reference structure.

To that end, we performed an initial ptychographic measurement [46, 16] using the same experimental setup and parameters as the holographic measurements taken place at I13, DLS, with a photon energy of 9 keV, a propagation distance of 14.5m, and a photon-counting detector 55 μm pixel size and 515×515 pixels. The only alteration of the setup was to utilise a high-efficiency Fresnel zone plate to form a converging beam with a 150 nm focal spot. We perform ptychographic spiral scans of the reference structures as well as the samples which were used with

the holographic experiments and obtain reconstructions of the imaged objects by iterative ptychography algorithms performed by Aaron Parsons.

Figure 4.35 shows ptychographic reconstruction of the phase of the gold fish test-sample and the gold cube test-sample, where it is evident that the resolution obtained is quite comparable to those obtained with the holographic reconstructions. Figure 4.36 shows ptychographic phase and amplitude reconstructions respectively of the $6\mu m$ and $4\mu m$ bare silicon cube, and the $6\mu m$ wireframe reference composed of a 3.9 μm-thick silicon pillar and a 10 nm iridium nanolayer. In Figure 4.36(top), the bumps along the edges of the $6\mu m$ silicon square are visible and validate our reference characterisation where we concluded that the repeating overlapping reconstructions arise due to these bumps. In addition, the amplitude reconstruction of the $6\mu m$ reference shows the shadow of another square reference at the four sides of the reconstruction area. This also justifies the appearance of additional out-of-focus reconstructions in the holographic data using the 6 μm pillar and our reasoning where we attributed the four out-of-focus corner reconstructions to a partially illuminated neighbouring reference square. In comparison, the iridium wireframe edge in Figure 4.36(bottom) appears sharper than that of the silicon pillar which correlates with the higher resolution holographic recontructions obtained with that reference. The 10nm-thick iridium edge is however barely visible in the phase reconstruction in Figure 4.36(bottom right), but we notice a fine line at the lower side of the square with a dark signal corresponding to a phase of -2.5 rad. In order to be able to use the ptychographic reconstructions as a mask for the holographic procedure and gain full advantage of joining the two techniques, one needs to obtain results of somewhat higher resolution and free of artefacts. Nevertheless, we find that our holographic results, conclusions, and quantitative measurements are in agreement with the ptychographic data, hence it serves well to apply both methods to correlate the results.

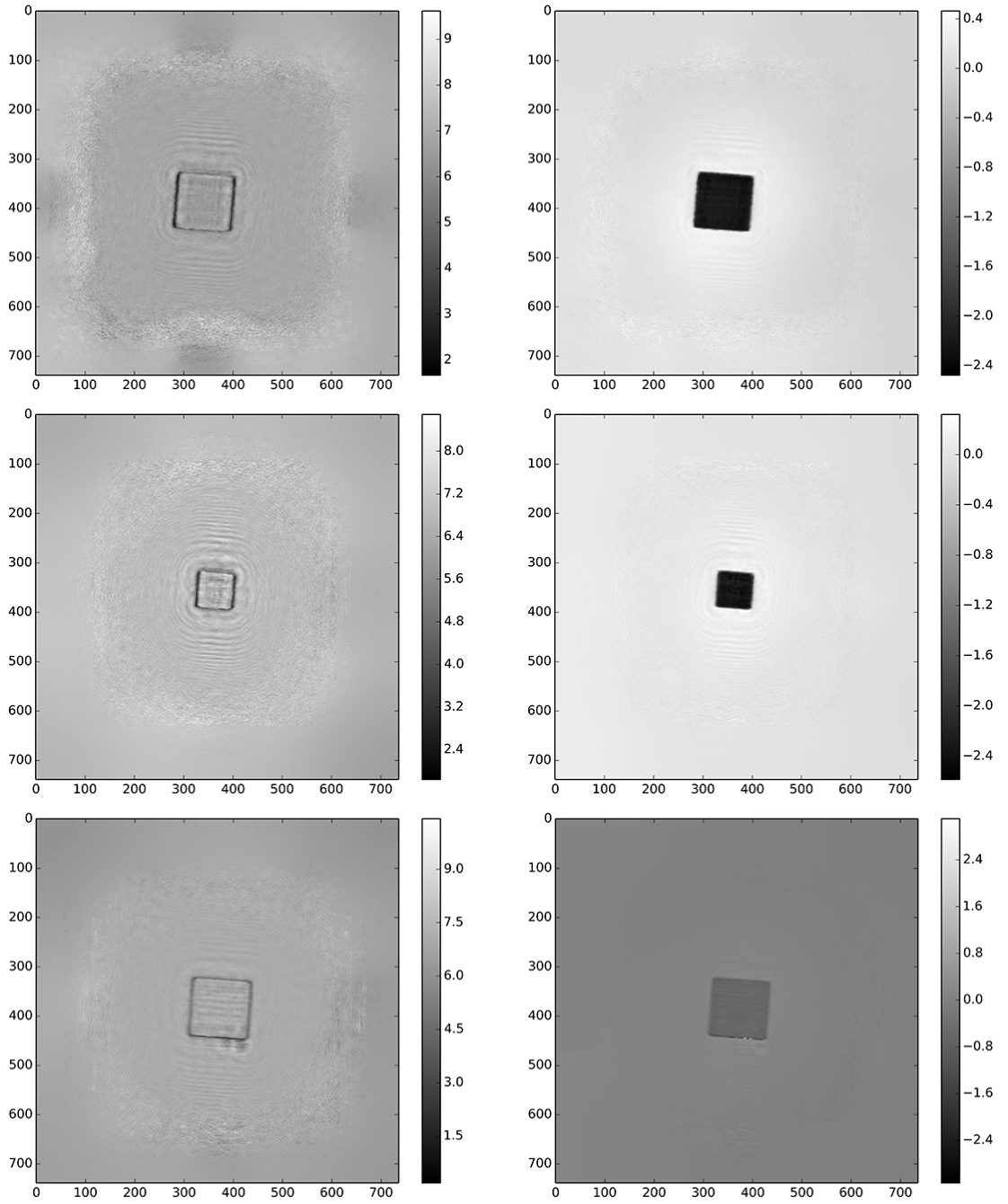

Figure 4.36: Ptychographic amplitude (left) and phase (right) reconstructions of the reference structures (top) 6 μm silicon pillar, (middle) 4 μm silicon pillar, (bottom) 5 μm Ir/Si nano-wireframe showing a sharper edge.

4.4.4 Conclusion

We have established a holographic imaging method that relies on phase-shifting extended references prepared by nano-fabrication and benefits from an unconfined sample geometry. At hard x-ray energies, we overcome the technical difficulties associated with preparing holographic references in an absorbing mask by using especially fabricated silicon pillars with sharp edges as well as high-resolution wireframe reference by atomic layer deposition prepared by Jeroen Bosgra at Paul Scherrer Institute. We have essentially upgraded the potential of holographic imaging with hard x-rays, by designing these reference with specific dimensions and characteristics that produce a large phase shift instead of being an absorbing reference on a transmissive substrate, or a transmissive reference on an absorbing substrate, and we have established that such a method potentially delivers twice the contrast in comparison to the latter.

Furthermore, by physically decoupling the reference from the sample in z, we create new degrees of freedom that allow us to scan through a multitude of samples with keeping the reference fix, to collect 3-dimensional data by tomographic measurements, and to ease many of the experimental setbacks and fabrication difficulties associated with having a single sample on the same membrane as the reference. In addition, the unconfined sample geometry creates a much needed flexibility during data acquisition where the sample can be shifted in x and y at a fixed reference position and with a fixed illumination beam, causing a large improvement in the statistics of sample reconstructions. Thirdly, this unconfined geometry facilitates imaging of sensitive samples and specimens of biological nature. The reason is that by having the two stages physically decoupled, we are able to record individual holographic diffraction shots of the reference structure alone, the sample alone, and the beam passing through only the substrates. By recording the individual shots, we obtain individual autocorrelations of the holographic components and hence can use them to perform background subtraction, data correction, and reference characterisation. This means that instead of exposing the sample by twice the exposure time to enhance its signal statistics with respect to the background,

the reference, or the substrates, we can merely subtract the reference/substrate autocorrelation contributions from the holographic reconstruction and allow the sample images to appear with higher contrast than otherwise expected.

Furthermore, the development of the wireframe reference fabricated by depositing a nano-layer of iridium by atomic layer deposition has opened the doors to holographic imaging with differential contrast and edge enhancement. We have demonstrated, through the analysis of simulations and experimental results using a wireframe extended reference with phase-shifting and absorbing properties, that despite the nanoscale- width of the wireframe, the reconstructions of samples are produced with high contrast and SNR in addition to resolution equivalent to the smallest possible spatial width given by the experimental setup, i.e the real-space pixel size of 61 nm. The resolution-contrast trade-off associated with Fourier transform holography using a single (or multiple) pinhole as a point-source reference maintains that the smaller the pinhole, the higher the resolution but the lower the contrast. Contrary to that, we overcome this issue by demonstrating that the wireframe reference being a few nanometer wide in a direction perpendicular to the incoming beam but also being a few microns deep in the parallel direction to the beam, results in a high reference signal strength and in reconstructions of high contrast as well as resolution at its maximum limit.

Consequently, we studied the characteristics of the wireframe reference that produce differential phase contrast and edge contrast enhancement in the absorption images, and have explained the mathematical reasoning that leads to the arisal of double point-source peaks of opposite polarity at the locations of the reference corners, or in other words what can be viewed as the derivative of the delta function. Although this can be treated by performing an integral operator in the reconstruction procedure, we have shown that if the reference parameters are chosen correctly, the directional differentiation produces reconstructions with contrast of the bulk of the sample in addition to edge-enhanced contrast for the absorption images and differential phase contrast for the phase images.

We have provided methods to directly extract quantitative sample information from the obtained reconstructions such as the phase shift of the sample

material and the absorption, given sufficient theoretical knowledge of the sample and reference substrates, and the phase and absorption of the reference structure, and assuming a uniform flat illumination beam. We have calculated the phase values of our test-samples and compared them to the theoretical values and have found a high agreement between the two. Results of data averaging and post-processing refinement was discussed and it was shown that the contrast and statistics maybe be largely enhanced by summing up many reconstructions produced from shifted sample positions.

We have demonstrated that such a holographic method using phase-shifting references in an unconfined sample geometry is applicable to imaging biological samples and weakly scattering samples. We have obtained reconstructions of weakly scattering samples with a resolution of 105 nm, where the sample was 590nm-thick silicon dioxide, coated with 10 nm of iridium at 9 keV photon energy contributing 99.7% transmission and 0.05π phase shift. We have also implemented the technique with marine microplankton samples, specifically to image the "platelets" or coccolithophorids constituting the plankton, mainly composed of CaCO3. This experiment was implemented with a silicon pillar reference of modest edge sharpness. Nevertheless we successfully produced reconstructions of a variety of coccolithophorids with high contrast and a resolution of 169 nm, where we were able to distinguish structural details about the coccolithophorids, such as a certain skewness in the shape as well as pointy corners, that can potentially aid to understand the phases of the plankton formation.

Moreover, the method was applied with a biological sample of Deinococcus Radiodurans bacteria, which is a bacteria strain whose cells consist of 4 quadrants shaped into two bean-like cells. The expected absorption and phase shift contribution of these samples was close to null at 9 keV. However, using the wireframe reference, we were able to obtain some outline information of the bacterial cells that shows bean-shaped structures in one case, and shriveled structures in another, which appear to be due to the lack of nutrient medium on the substrate or dehydration; a result of the sample preparation. The signal strength of the bacteria reconstructions shows a level of almost 10% above the background level which is

still very low. But this proves that by adjusting the photon energy to 6 keV or lower, one can obtain an improved sample signal strength and stronger scattering to potentially obtain images with pixel-size-limited resolution as the test-sample measurements illustrate.

Compared to CDI methods and scanning methods, this holographic technique provides a reconstruction of the complex transmissivity of the sample from a single recorded shot with detected number of photons as low as 1×10^7, and it does not involve any iterative numerical procedure to obtain the reconstructions. The data can be further refined using an iterative mask, but in its basic form, the method does not need the additional processing. The total procedure from experimental to numerical is in fact straight-forward and not time-consuming. It is important to invest some time into creating a uniform homogeneous flat beam with high incident flux. Once this is done, the experimental procedure simply involves illuminating the sample positioned within a correct offset with respect to the reference (in x,y and z) and the data acquisition involves recording a single holographic diffraction pattern at a photon-counting detector located in the far-field at a sufficient exposure time of 50 - 500 sec (depending on the incident flux), so as to accumulate a minimum of 10^7 total photons per shot at the detector. Apart from the beam formation, the experimental procedure from aligning to data acquisition takes a few hours.

The numerical processing of the reconstructions take a few seconds per data set, and by understanding the experimental parameters, one can calculate where and how the sample reconstruction is expected to appear. And by examining the first live reconstructions, one immediately obtains sufficiently revealing information about the sample to adjust the experimental parameters and flux / exposure time, and finally apply the necessary numerical adjustments to refine the result.

Therefore, in comparison to iterative methods, the reconstruction procedure is obtained within seconds, providing initial information about the sample; or if all the parameters are well-set, it could provide a well-resolved unambiguous image immediately. In comparison to scanning methods, this being a single shot measurement means that the expense in time and effort is largely reduced. In addition, the method can be extended to 3-dimensional imaging: by rotating the

sample while keeping the reference fixed, we obtain reconstructions at all rotation angles that can be combined into a tomographic image. These attributes, i.e being a single-shot method that non-iteratively produces immediate three-dimensional sample reconstructions [77, 78, 79], present an advantage over CDI and scanning methods, specifically for imaging with x-ray free electron lasers of sensitive samples by "the diffract and destroy method" [17, 22] as well as time-resolved dynamic processes [80, 52].

5 Experimental Results: HDXI using Fresnel Zone-Plates

In the previous chapter, we demonstrated the result of using phase-shifting extended references as a square or wireframe structure to obtain sample reconstructions by applying an inverse Fourier transform and a directional differential filter. By applying the derivative in the two directions of the square sides, we reduce the extended structure to a point-source. Similarly, the Fresnel zone-plate (FZP) [4] has x-ray refractive properties that converges the incident light with high-efficiency into a focal point with a diameter equal to the width of the outermost zone width. Hence, the focal point of the FZP can be viewed as a point-source in regards to holographic imaging. FZPs may be used in different holographic setups to produce sample images for a variety of applications. For example, it can provide a point-source reference wave coaxially illuminating the object in an inline holography setup resulting in magnified holographic images with a resolution limited by the numerical aperture. As another example, while the FZP also functions as an x-ray lens, the positive and negative order focal spots of the FZP may be used to produce a holographic image and as well as a real image in a single setup [81]. Third, the focal spot produced by the convergence of the first order diffracted waves of the FZP can be used in a FTH setup to serve as an alternative to a pinhole reference providing much higher reference flux [82, 83, 84]. In the aforementioned examples, the size of the focal spot provides the resolution limit of the imaging system, which is a function of the outermost zone-width. The resulting image contrast is a function of the FZP area and efficiency.

In the standard FTH scheme, a milled pinhole serves as the point-source reference that ideally respresents a delta-function whose cross-correlation with the object provides two complex-conjugate images of the sample. The pinhole reference scenario suffers a drawback where the resolution and contrast are inversely proportional with respect to the size of the pinhole. This can be overcome by utilising a high-efficiency high-resolution zoneplate (FZP) producing a fine focal spot and maintaining a high transmitted flux. A high-efficiency FZP is one that is manufactured in such a way that the zones represent a high filling area of the total area. A high-resolution FZP is one with a fine outermost zone whose width is comparable to the desired resolution limit. In this chapter, we will discuss experimental results obtained with Fresnel zone-plates in a Fourier transform holography scheme. We have tested FTH experiments using FZPs with high energy x-rays in two different scenarios: a holographic reference created by a partition of a highly efficient large-area zone-plate with 150 nm outer-zone width; and a holographic reference created by multiple microscale zoneplates with 70 nm outer-zone width. We maintain the sample in an unconfined geometrical setup in both scenarios that each portray individual benefits in regards to sample preparation requirements, field-of-view, experimental flexibility and general applicability.

5.1 Off-axis FT-Holography using partial FZPs

Fresnel zone-plates used for imaging at hard x-ray wavelengths normally have a diameter of 100 μm - 500 μm to produce a large numerical aperture, high-efficiency, and to mimic the performance of an optical lens with the highest possible intensity collimated into the first order focus.

We aim to use the high-efficiency 400 μm FZP as a point-source reference for a FTH imaging setup. At 9.7 keV with a 14.5 m propagation distance and a 55 μm pixel size, the illuminated sample area must be a maximum of 17 μm to maintain the oversampling condition. This restriction means that the 400 μm FZP and the sample can not be placed side-by-side in the same plane because the total illuminated sample area will be larger than 400 μm and hence will not be oversampled. Bringing the sample laterally closer to overlap the FZP area will break the FTH setup and result in a different imaging mechanism. Yet, another problem arises here, which has to do with the focal length of large-area FZPs at hard x-ray wavelengths. For example, a 400 μm FZP at 9.7 keV results in a first-order focal length of 0.47 meters. By placing the sample in-plane with the FZP, the inverse Fourier transform of the recorded diffraction pattern reconstructs the sample area at the FZP plane. In order to obtain the successful FTH result, i.e the cross-correlation of the focal point with the object wave, the reconstructed IFFT area must be then propagated to the focal plane by 0.47 meters. Such a long propagation distance means that we are no longer in the near-field limit and therefore the method fails. To be able to successfully apply a near-field propagator to bring the sample into the focal plane, the distance between the sample and focus must not exceed the order of 1 cm. Therefore, we must separate the sample from the FZP along the z-axis, and ideally place it in the vicinity of the focal spot.

It is also important to note that with such large-area FZPs, the intensity of higher order positive and negative waves diffracted by the FZP is not negligable. Hence it is necessary that the sample is not illuminated by the higher orders waves and that the object wave does not interferes with the higher order FZP waves. For a successful FTH experiment, we must maintain that the object wave is a result of

the illumination of an isolated zero-padded sample by the incident coherent parallel beam. Another condition is to maintain that the object wave only interferes with the off-axis reference wave as a high-NA diverging spherical wave.

To satisfy the oversampling condition, we must maintain that the lateral offset distance between the reference point-source (i.e the focal point in this case) and the sample is within the oversampled area of 17 μm. Another important condition is to coherently illuminate both the sample and reference areas to obtain the full interference of the reference wave and sample wave. This means that the lateral distance between the sample and reference must not excede the lateral spatial coherence length.

We conclude that to be able to use the high-efficiency high-NA large-area FZP as a holographic reference source, the geometrical setup of the sample and the FZP must be specifically arranged to satisfy all the conditions. Given all the requirements, the solution would be to separate the sample from the FZP along the z-axis by the focal length and to laterally offset the sample from the focal spot by a maximum of 17 μm, all the while employing an order-sorting aperture (OSA) and central stop (CS) to deflect and block all the higher order waves.

Yet, with the sample being placed at a z-distance close to the focal plane, we must maintain the parallel-beam illumination of the sample without exposing the sample to the diffracted waves of the FZP. This is done by offsetting the lateral position of the central stop thus allowing the zero-order direct beam to emerge from the FZP with a sufficiently large beam diameter and illuminate the sample. The zero-order direct beam serves as the parallel-beam illumination of the sample. Offsetting the central stop by -y perturbs the axiosymmetric deflection of the negative order waves of the FZP and causes them to deflect less in -y and more in +y, and inversely for the positive orders. Due to this effect, we must then laterally offset the OSA again by -y , to successfully block all the unwanted FZP diffracted orders while allowing the positive first order and the direct zero order beams to pass through. The setup is illustrated in the schematic in Figure 5.1.

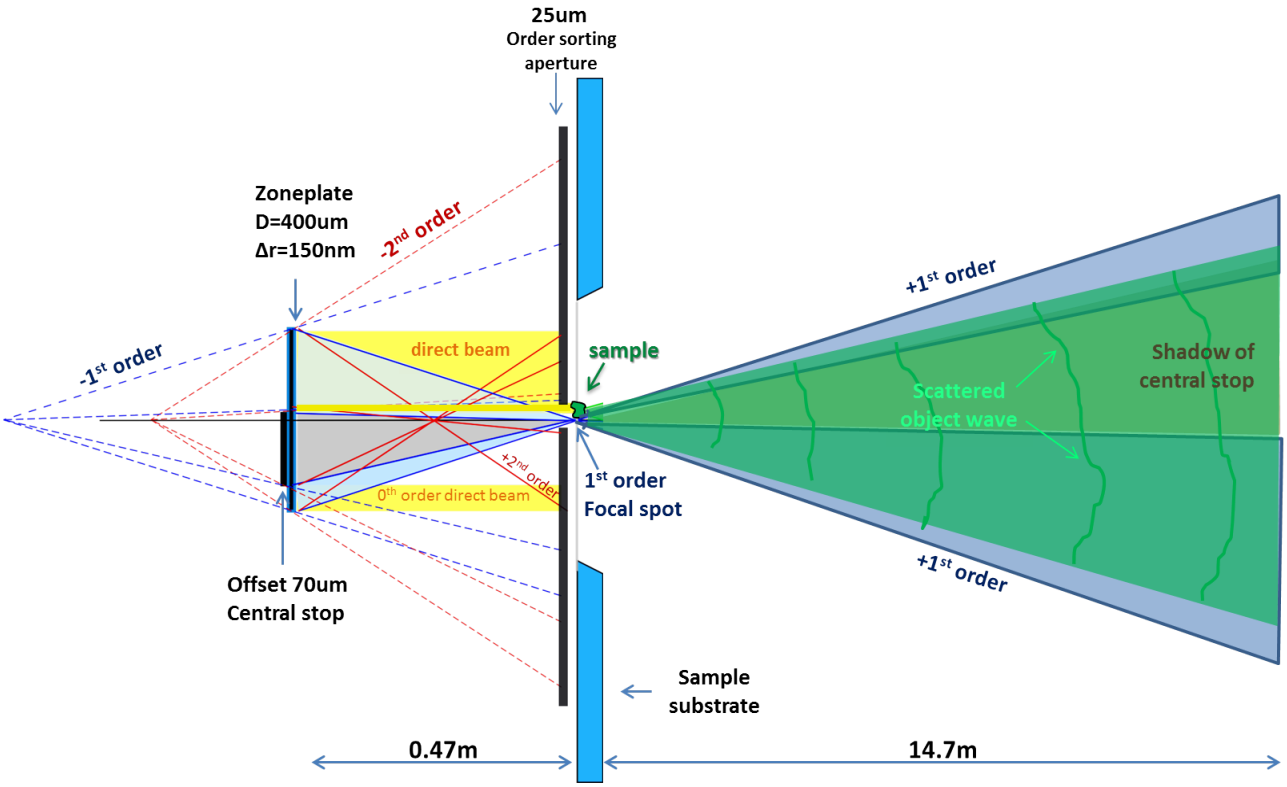

Figure 5.1: Schematic of the experimental setup.

5.1.1 Experimental Setup

The FZP with 400 μm diameter and 150 nm outer-zone width is aligned into the incident coherent x-ray beam which is shaped using beam-forming upstream slits, monochromatised at 9.7 keV, and focused into the experimental hutch using complex refractive lenses. The FZP is fabricated as a stacking structure so as to ensure high efficiency and focus a high fraction of the incident light into the first focal order. At 0.47 m downstream from the FZP, the test-sample is mounted on a piezo stage with xyz translation. At a distance of around 100 μm upstream the sample, an order-sorting aperture of 25 μm diameter is placed concentric with the FZP. Due to the slight misalignment of FZP zone stacks, the FZP does not only generate odd diffractive orders as in the ideal theoretical case, but also generates even orders. This means that the choice of OSA positioning should be decided also based on the ray tracing of even diffractive orders.

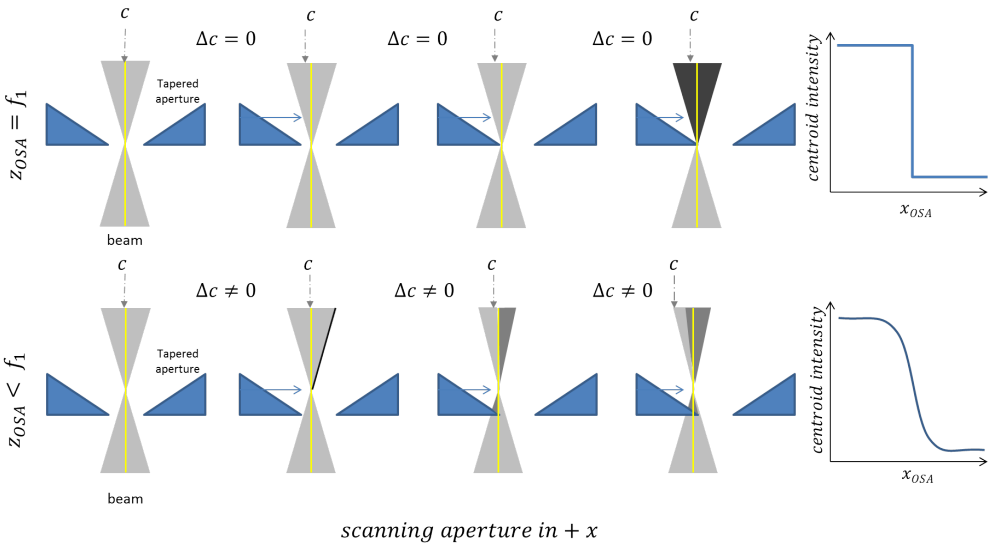

Figure 5.2: Schematic of alignment procedure for detecting the position of the focal spot.(top) row is the case where z is aligned to z_f, (bottom) is the case where z is not aligned to z_f.

Tracking the Focal Spot

The sharp tapered edges of the OSA apertures are used to test the xyz position of the first order focal spot and verify the alignment procedures. With the central stop placed very close to and centered with the FZP and with the sample not inserted in the beam, we perform an edge scan of the OSA along the z-direction to determine the z coordinate of the focal spot. As illustrated in Figure 5.2, when the OSA edge is aligned with z_{f1}, the first order beam is not perturbed as the OSA is scanned in x and there is no change in the projected cone intensity until the OSA edge hits the focal spot where the intensity quickly drops to zero and we observe dark field imaging as the projected cone becomes dark and the contrast flips. On the other hand, when the OSA edge is not aligned with the focal plane and the OSA is scanned across the cone in x, small shifts in x result in a perturbation in the first order beam and changes arise in the projected cone intensity due to the beam size being larger than at the focal plane. when the edge hits the cone is gradual as the beam size is large.

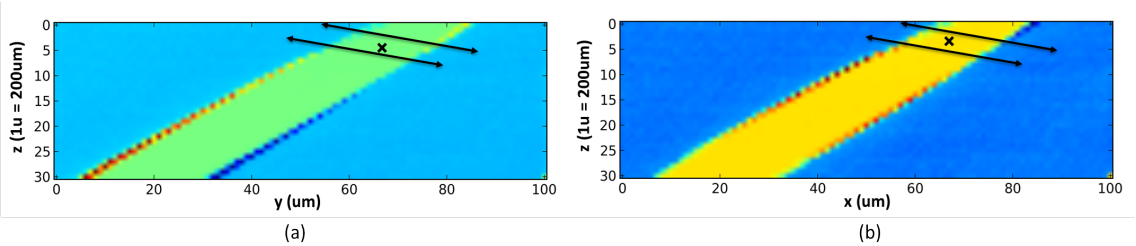

Figure 5.3: Focal tracking: two plots of the change in centre-of-mass as a function of the x-shift and y-shift. The region highlighted by the double line is the focal region.

Plotting the centre of mass of the cone projection as a function of the x-y positions of the OSA at every z-position results in a step function that is sharpest at z_{f1} and smoother and more gradual at $z \neq z_{f1}$. Furthermore, as we scan the OSA edge in x and y, we find a zero or minimal total shift Δc in the center of mass at z_{f1} for every Δx, while at $z \neq z_{f1}$ the total shift Δc is non-zero. To determine z_{f1} more accurately, we plot Δc for every z as a function of x_{OSA} and y_{OSA}, which results in the two plots in Figure 5.3 (a) and (b) respectively. We find the regions highlighted by the two lines to correspond to the estimated z_{f1} spot which is where Δc is minimal. The change in pixel color denote a change in Δc on a single axis, so we find the ordinate value along which the color-coded beam consists of a constant value, which is around $z = 6u$. The distance between the FZP and OSA is 473 mm for the OSA piezo coordinate of z = 0. Using the value extracted from the plot, given that the $z = 0u$ in the plot corresponds to the intitial z position of -6 mm, we find that the focal plane is at -4.8 mm, which corresponds to a distance of 468.2 mm from the FZP. With the theoretical value z_{f1} being 468 mm and the depth of focus being 350 μm, we find that the experimentally calculated focal length of 468.2 mm is in good agreement with the theoretical value. Hence we accurately determine z_{f1} in order to position all the elements correctly to satisfy the holographic conditions.

We fix z_{OSA} at z_{f1} and perform a test to determine x_{f1} and y_{f1} with respect to the OSA. At z_{f1}, when the OSA is aligned to x_{f1} and y_{f1}, we observe a bright circular projection of the first-order FZP cone with the dark projection of the centered central stop blocking the beam (as shown in Figure 5.4(a)). However, when the OSA is scanned along the x-axis, we observe a fast decrease in intensity and a sudden transition between bright-field imaging and dark-field imaging.

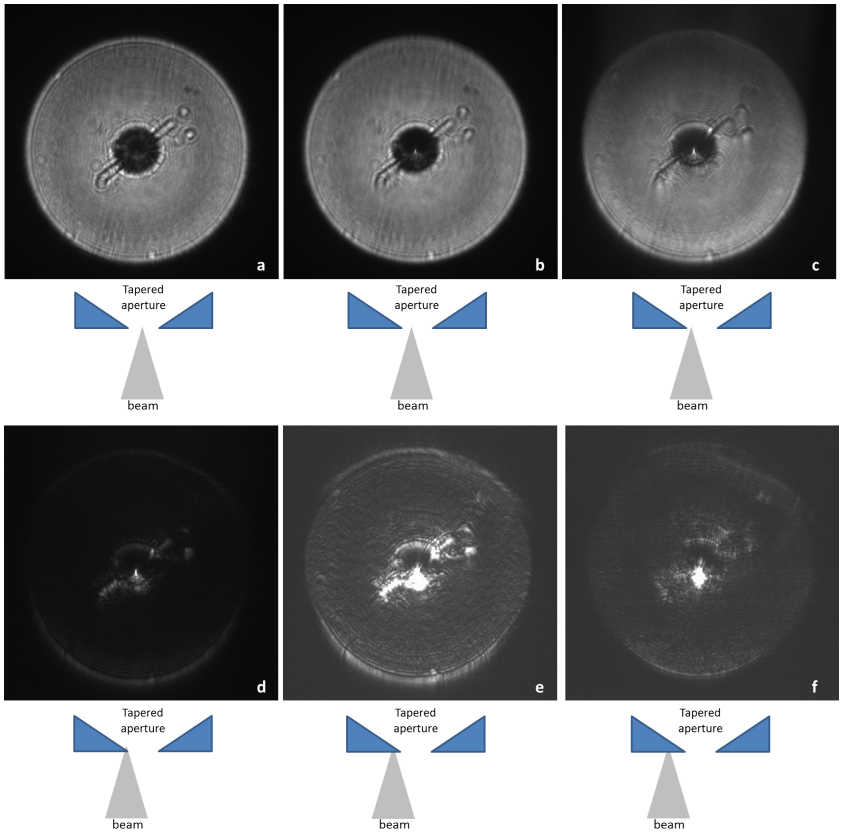

Figure 5.4: Transforming the signal of the projection from bright-field to dark-field as the focal spot is clipped by the tapered edge.

When the tip of the tapered edge cuts the focal spot (Figure 5.4(d)), the intensity is at its minimum and the contrast changes to differential phase contrast due to the OSA edge being tapered and the transition in transmission not being binary. This can also be viewed as a filter of the fourier spectrum of the focal spot which results in dark-field contrast. As the OSA is scanned further and the beam *sees* the tapered edge, we observe differential phase contrast with a higher intensity (Figure 5.4(e)) than at the tip of the edge. As the scanning continues, it reaches a point where the edge is too thick to transmit or cause a phase shift and the intensity drops back to zero again (Figure 5.4(f)). By calculating Δx and Δy between the maximum intensity projection and the dark-field projection, we obtain x_{f1} and y_{f1} with respect to the OSA edge. Consequently, we also estimate the radius of the OSA to be 12 μm, which agrees with the preliminary value of 12.5 μm.

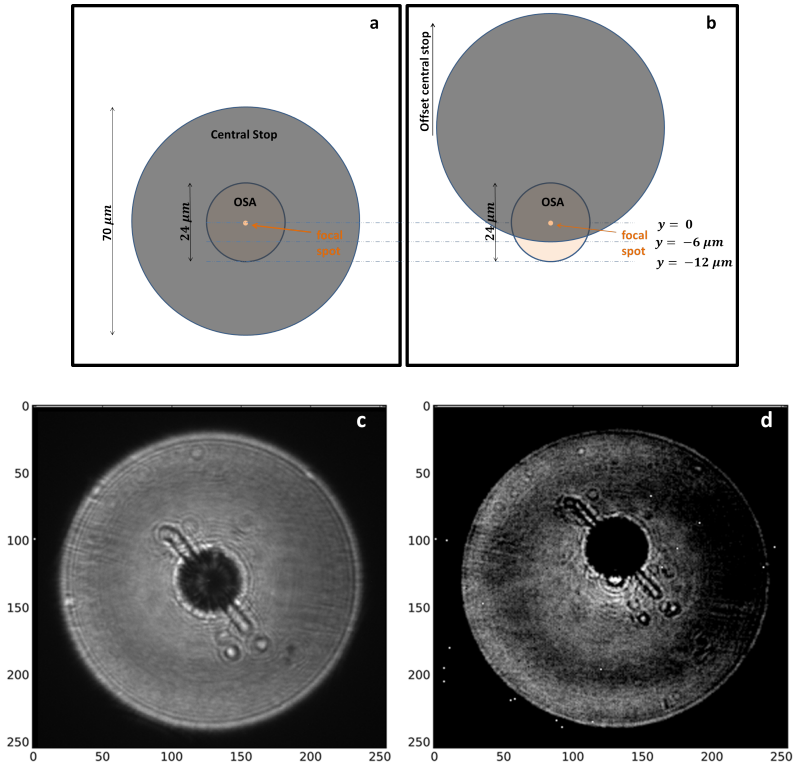

Figure 5.5: Offseting the central stop to allow the direct beam through and form a crescent-shaped illumination area.

Offsetting the Central Stop

After determining the coordinates of the first order focal spot, we are able to arrange all the relevant elements to apply to the FTH experimental design. The central stop that is placed a few mm away from the zoneplate is offset in the y direction by 35 μm from the center in order to allow the zero-order direct beam to pass through to illuminate the sample. Consequently, the OSA is also offset in the y-direction so as to block the higher and negative orders while maintaining that the focal spot does not interfere with the OSA edge. The projection of the offset central stop and the OSA results in a crescent-shaped sample area with the vertical width of 6 μm. The center of the sample area is separated by 12 μm from the focal point (reference source) which satisfies the oversampling condition.

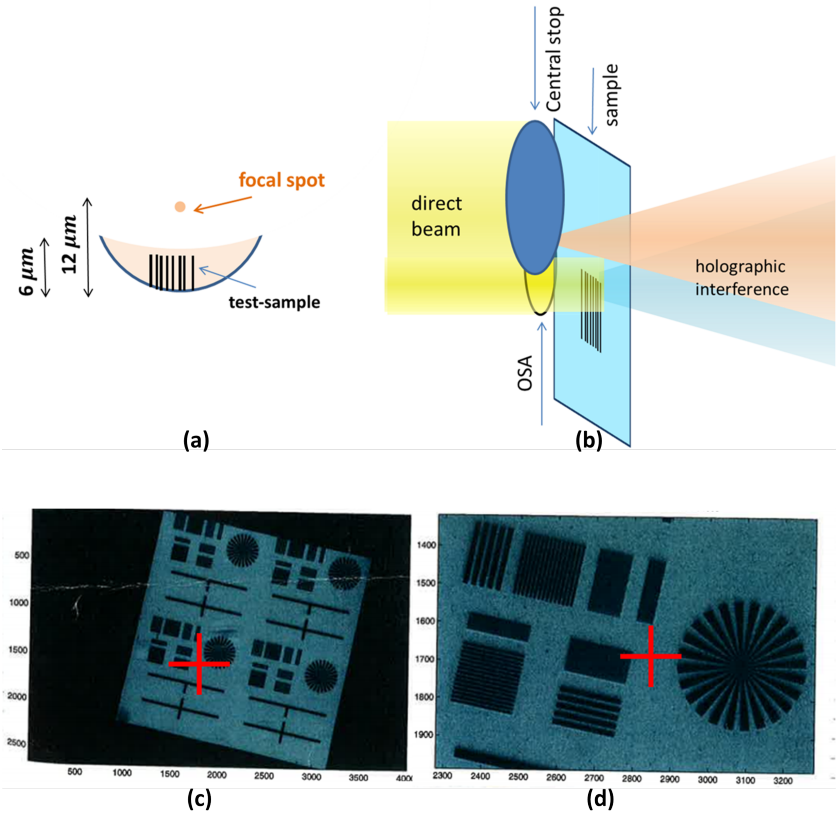

Figure 5.6: (top) Alignment of the central stop and OSA to form a crescent-shaped beam exposing the sample. (bottom) FOV of the test-sample. red cross signifies the region of interest.

Sample Alignment

After constructing required the illumination area and aligning the focal spot to satisfy the holographic separation conditions and the oversampling condition, we align the test-sample into the direct beam. The test-sample substrate is mounted on a piezo stage and positioned at the z distance of the first order focal spot. The OSA is slightly shifted upstream in z and shifted in x-y to the appropriate position to block all undesired higher orders and to allow the installation of the sample at the focal plane. We use an available test-sample that consists of a Siemens star and sets of repeating gold bars of varying periodicity and width. Since we know that the lateral distance between the illumination crescent area and the focal spot

is 12 μm, we locate a test-sample on the substrate which is isolate by a diameter of at least 24 μm so as to not interfere with the neighbouring structures. The isolation of the sample and the transparency of the substrate is critical to allow the first-order diverging reference wave to propagate from the focal spot and pass through the substrate unperturbed. Hence we select two sets gold bars to image as a 0.5 μm thick gold test-sample: a) horizontal gold bars of 0.5 μm width, 0.5 μm periodicity and 10 μm length; and b) horizontal gold bars of 1 μm width, 1 μm periodicity, and 10 μm length; which proves to be a strongly scattering sample producing rectangular diffraction modulations.

5.1.2 Data Acquisition Procedure

By scanning the sample through the crescent aperture, we obtain interference patterns of the sample wave and the first-order reference wave recorded in the far-field with a photon-counting detector located at 14.7m downstream. the propagation of the first order cone from the FZP appears as a bright disc filling half the area of the 515 pixel detector (as in Figure 5.7(a)). The projection of the misaligned central stop appears as a small dark disk vertically offset to the center of the bright disc. When the sample is inserted in the path of the direct beam, the scattering signal of the sample is observed as rectangular interference fringes within the bright disc. This signifies the interference between the positive order reference wave and the object wave. While the scanned sample does not perturb the first-order cone, we obtain data that is reconstructable as an FTH method. When the sample is scanned further in y, it cuts through the first-order cone emerging from the focal point and additional artifacts occur where the periodic gold bars act as a diffraction grating themselves and split the reference wave into higher order diffracted waves. The effect of the gold bars acting as a diffraction grating with respect to the first-order cone is shown in the Figure 5.7(a), (b), and (c) as the grating becomes completely overlapping with the focal wave. Figures 5.7(d) through (i) show how the diffraction fringes and the contrast changes as the sampled is scanned through the crescent aperture from top to bottom until it begins to interfere with the focal wave and splits the cone projection.

The reconstruction of the recorded diffraction patterns proves most effective when the OSA and central stop positions are also scanned. To that end, we record datasets for every test-sample position with 2 loops of scanned variables. At every sample position, we shift the OSA position and the central stop by 7 μm in steps of 1 μm. Thus, we obtain a two large datasets with and without exposing the sample,

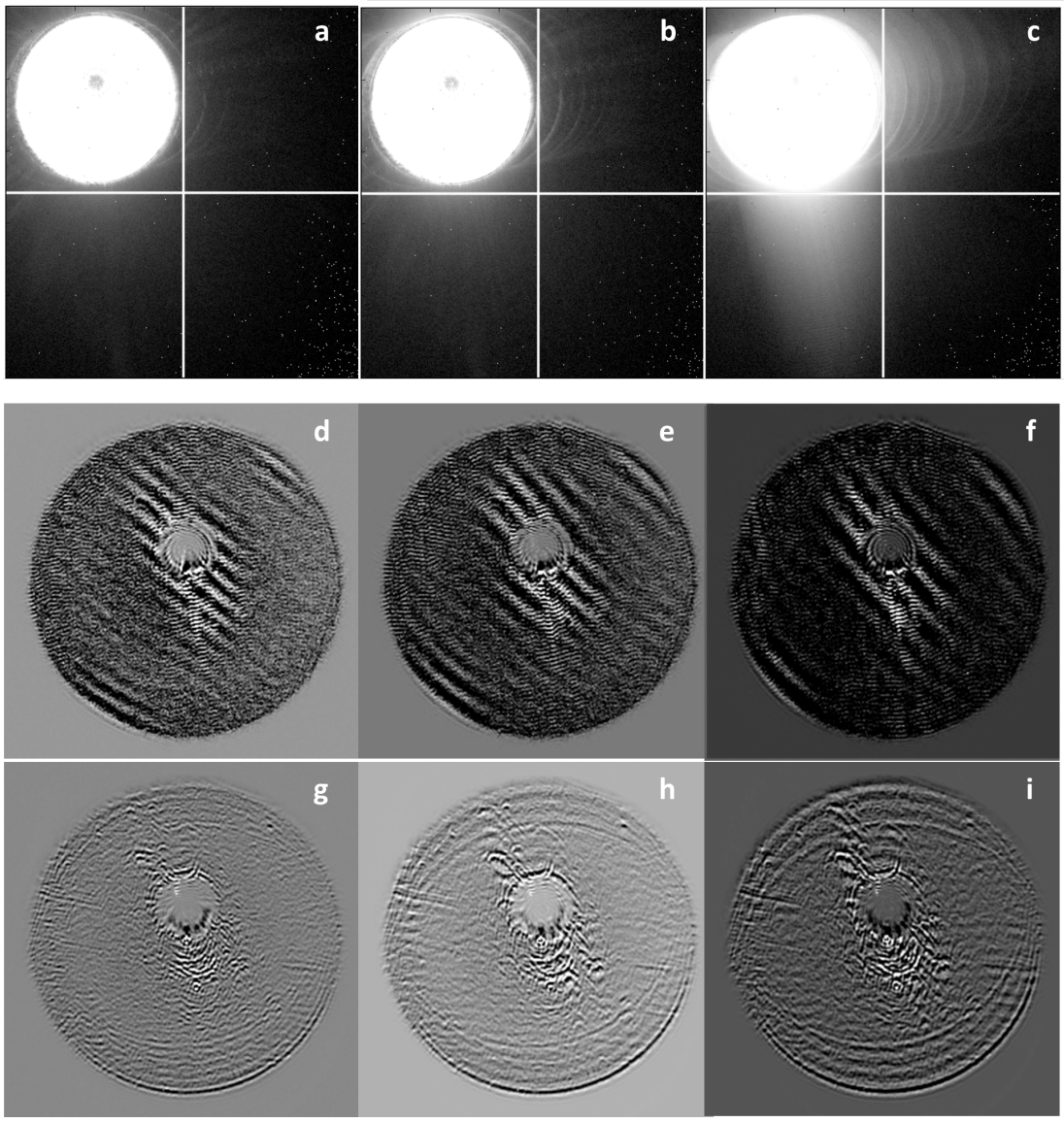

Figure 5.7: (a,b,c) diffraction patterns as the gold bars are scanned through the beam and clip the focal spot. (d to i) intensity of the diffraction patterns within the cone where (i) showed grating diffraction of the cone itself.

constituting a nested loop of 3 scannables: the shifted sample, the shifted OSA, and the shifted central stop. The reconstruction procedure involves taking the IFFT of the recorded diffraction pattern, subtracting by the background pattern, without applying a near-field propagator as the sample plane is placed within the range of the focal depth.

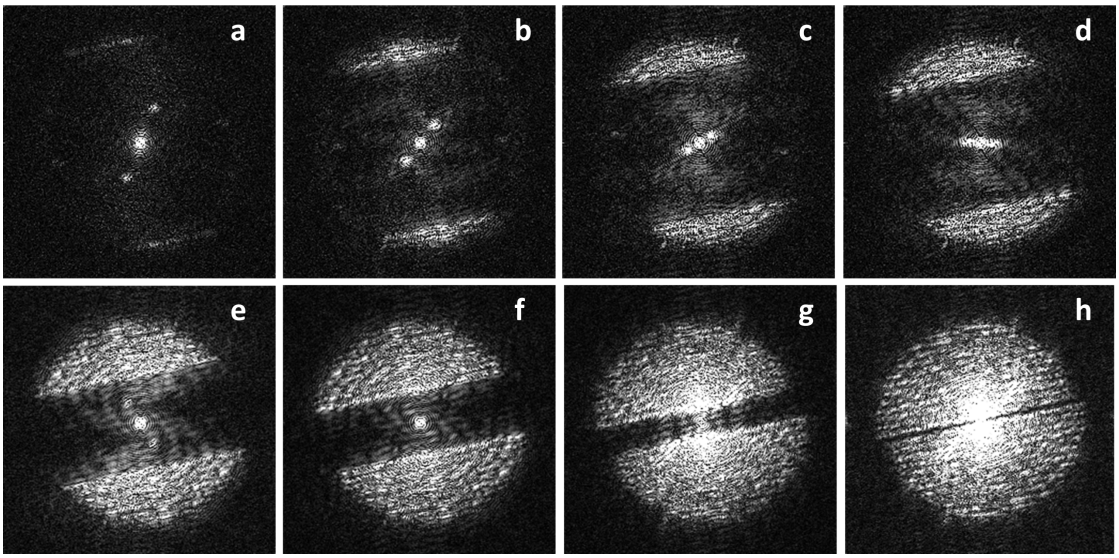

Figure 5.8: Reconstructed field of view as the sample is scanned (horizontal gold bars of 0.5 μm periodicity).

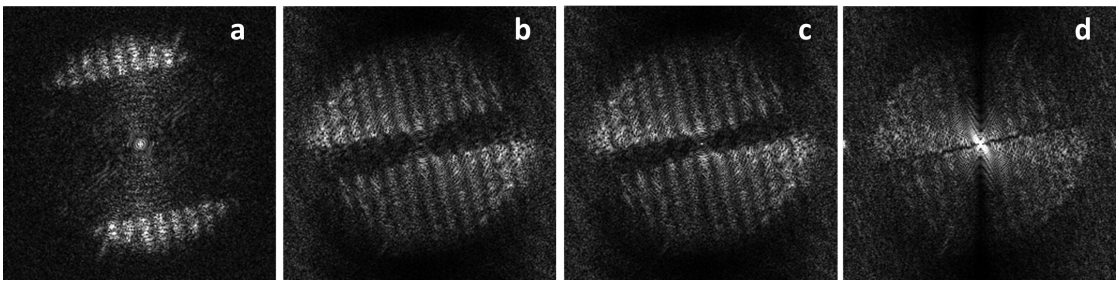

Figure 5.9: Reconstructed field of view as the sample is scanned (vertical gold bars of 1 μm periodicity).

5.1.3 Results and Discussion

By subtracting the background reconstruction, we successfully remove the contributions of the aperture edge and the signal due to diffraction of the crescent edges. This way we also successfully remove the constant background signal in the reconstructed area due to the zero-order peak in the diffraction pattern. Hence, the signal of the sample cross-correlation with the focal point is not overpowered by the background signal and appears with higher contrast than what would have been obtained without background-subtraction. The result of applying the background subtraction to the computed reconstructions is shown in Figure 5.8 and 5.9 where two samples were used: a set of horizontal gold bars with 0.5 μm width and 0.5 μm bar separation, and a set of vertical gold bars with 1 μm width and 1 μm separation. The figures show the reconstructions as the sample is being shifted from top to bottom until it interferes with the reference wave. The reconstructions constitute of a bright spot in the center, which corresponds to the autocorrelation of the reference, i.e the autocorrelation of the first-order focal spot. The autocorrelation of the test-sample exists in the center of the reconstructions but it is extremely faint in Figure 5.8(a,b) due to the weakness of its amplitude strength compared to the reference signal autocorrelation. The sample autocorrelation should consist of the autocorrelation of the crescent aperture in addition to the autocorrelation of the horizontal bars. Since we apply the background substraction, the autocorrelation of the crescent aperture is efficiently removed. In Figure 5.8(d) to (f), the sample autocorrelation somewhat intensifies, due to the larger exposure area of the sample and the existence of more scattering material, which strengthens the sample scattering signal.

The cross-correlation of the gold bars sample with the focal point results in two complex conjugate reconstructions of the gold bars shaped by the OSA aperture. By performing the previously discussed nested scans of the central stop and OSA, we efficiently recover all the spacial extent of the sample; we are not restricted by the crescent-shape aperture and hence the generated reconstructions is not crescent-shaped but only limited to the total diameter of the aperture. For that reason, the sample gold bars in Figure 5.8 and 5.9 fill up the 25 μm aperture and

are not obstructed as they shift downwards. Another conclusion that we draw by observing the reconstructions is that the cross-correlation between the sample and the reference yields much higher intensity than the sample autocorrelation. This is due to the fact that the reference signal strength is very high, and once cross-correlated with the sample function it amplifies the latter with it. This is why the reference autocorrelation and the reference-sample cross-correlation (in the reconstructions in Figures 5.8 and Figure 5.9) both have high contrast compared to the sample autocorrelation and are the two prominent components of the reconstruction.

Under ideal circumstances, the FZP focuses the first-order cone into a focal spot with a lower limit diameter of 150 nm which represents the reference point-source. This in turn serves as the resolution limit of the holographic system. In addition, the resolution is limited by the spatial extent of interference between the reference wave and the scattered object wave. The projection of the first-order cone only fills up almost half of the detector area (equivalent to 255×255 px^2). With $z = 14.7m$, $E = 9.7keV$, and a pixel size of $55\mu m$, the effective object-space pixel size is 134 nm. The spatial extent of the reference cone leads to a maximum attainable theoretical resolution of 150nm. If the reference cone fills up the entire detector at 515×515 px^2, the resolution limit reaches up to 66 nm. Yet, this is only true if the scattering angle of the sample is high enough to extend over that area. In other words, the image resolution is not only limited by the size of the reference focal spot but by the angular extent of interference between the reference cone and the sample. To improve the results, one could setup the experiment such that the diameter of the projected reference cone fills up the entire detector, by changing the propagation distance or by changing the diameter of the zoneplate. Furthermore, the recorded data corresponds to 100 cumulative shots of 1 sec exposure, which amounts to a total exposure of a 100 sec. The exposure time and incident flux could be safely increased by five times in order to detect higher scattering angles.

With all these factors in mind, and given that the object-space pixel size is 134 nm and that the sample exposure could be further increased, the reconstructed images of the gold bars yield of resolution of 550 nm as measured with the 90%-10%

knide edge test in Figure 5.10(b). The calculated visibility from the normalised background-subtracted reconstructions (in Figure 5.10(b1)) leads to an average transmission value of 72.9%, where the theoretical value of $1\mu m$-thick gold at 9.7 keV is 78.4%; and that of the $0.5\mu m$-thick gold in Figure 5.10(c1) gives an average transmission value of 83.7% where the theoretical value is 88.6%. Both experimental values differ from the theoretical values by around 5%. Apart from measurement errors, this difference can be attributed to the absorption of the sample substrate and the absorption of the silicon wafer substrate that underlies the zoneplate.

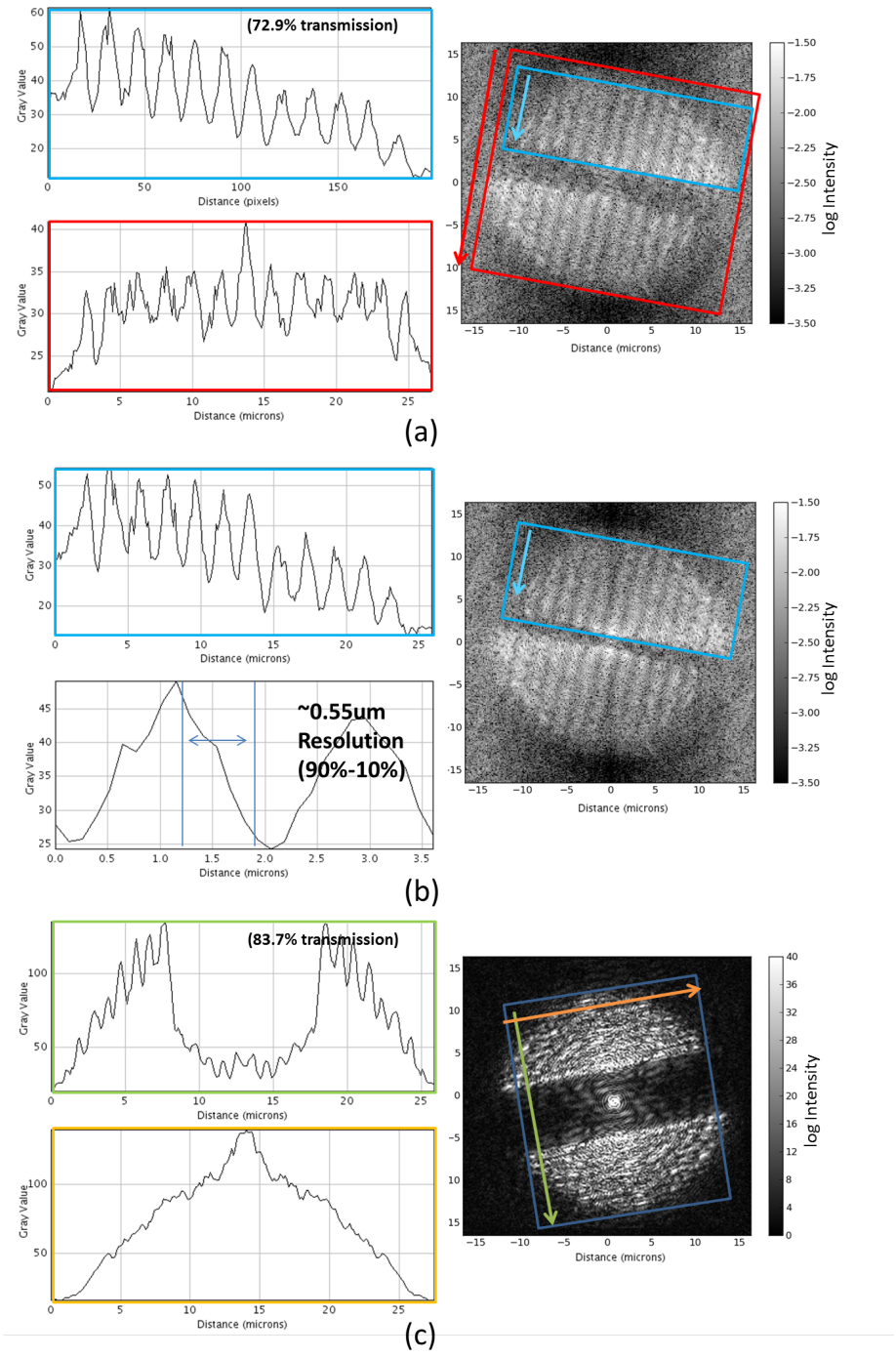

Figure 5.10: analysis of visibility and knife-edge resolution of reconstructions of gold bar test-samples reconstructions: (a) vertical bars 1 μm thick, (b) same, (c) horizontal bars 0.5 μm thick.

5.1.4 Conclusion

Using the first-order focal wave of a large-area FZP as the reference source in a Fourier transform holography setup has proved to generate sample reconstructions with high contrast. Even though the setup was designed such that the illumination area was limited to the offset between the OSA and the central stop, we have shown that by scanning the two components for every shifted sample position we are able to recover the full extent of the sample area without being limited to illumination crescent shape.

In our experimental setup, we have only taken up a fraction of the detector area, which has limited the maximum attainable resolution. Yet, we conclude that the resolution can be further increased by allowing the reference cone to cover the full detector area. In case of a setup and a FZP that generates a much larger projected cone diameter, it would be beneficial to use a larger detector array. This means that apart from the reference-point resolution limit, the method can be further pushed to the detector limit. In our experimental results specifically, however, given the object-space pixel size of 134 nm and the low exposure time, we have been able to produce sample reconstructions with a 550 nm resolution, which can be further improved by increasing the reference cone diameter and increasing the exposure time.

The success of the experimental procedure depends on the intricate alignment of the offsetting and order sorting elements as well as the accurate tracking of the focal spot. Although this is routinely acheivable with a bit of hard work, it is a tedious procedure that requires a lot of apriori calculations to track the FZP diffraction orders. Such a method is useful to image extended samples with high contrast. Another important benefit is that it does not require high technical expertise in FZP fabrication or sample preparation, compared to the silicon reference pillars required to have sharp edges. It has the advantage of employing an off-the-rack zoneplate, available to most x-ray imaging labs, that is typically used for x-ray microscopy to quickly and efficiently return immediate feedback about the sample by a single computational step. Nowadays, it is feasible to manufacture FZPs with high-efficiency at hard x-ray wavelengths with outer-zone widths of less than 70

nm. This means that using a finer-width FZP potentially increases the holographic resolution limited by 2. With this factor in mind, in addition to the previously discussed prospect of having full coverage of the detector area, this holographic method has the potential of reaching the single-pixel resolution limit.

Nevertheless, we have implemented an alternative method that uses multiple small micro-FZPs with fine outer-zone widths to serve as holographic references. The micro-scale area of the FZPs would lead to a millemeter range focal length which allows us to position the sample close to the focal plane without having to offset any of the components and to remain within the near-field limit when propagating from the FZP plane to the focal plane. This leads to the facilitation of the overall experimental procedure compared to the large-area FZP method. In the following section, we will discuss the setup, procedure, and results of using multiple high-resolution micro-FZPs for Fourier transform holography.

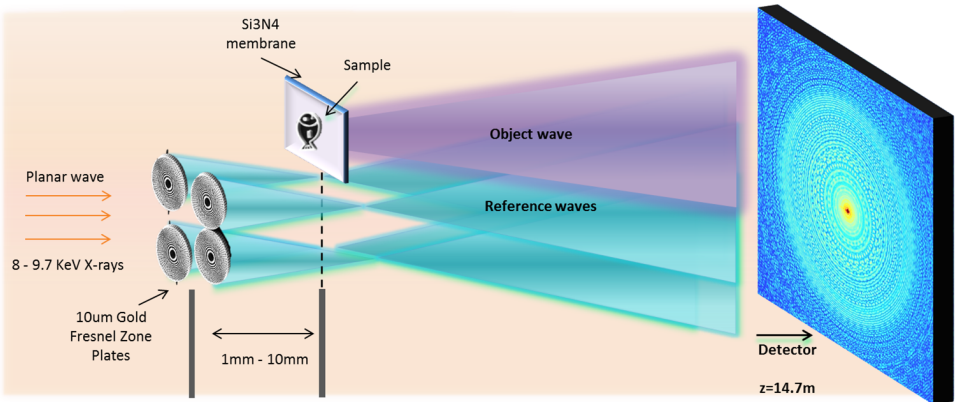

Figure 5.11: Schematic of experimental setup.

.

5.2 Fourier-Transform Holography with Micro-ZPs

In this section we will discuss results obtained by arranging a FTH setup at hard x-ray energies using microscale high-efficiency Fresnel zone-plates (FZP) [5, 56] with fine outerzone width. The micro-FZPs prove to provide a strong holographic reference signal [84?] with high resolving power and are particularly useful for facilitating the experimental procedure and sample positioning. In the following, the procedure and setup will be described, the phase and amplitude reconstructions will be shown and compared and the method will be assessed for further applications.

5.2.1 Setup

A homogeneous flat incident beam of x-ray photons at an energy of 9 keV is formed using sets of beam forming slits, passing through a quadruple crystal monochromator and complex refractive lenses to arrive at the sample stage that is 137 m from the x-ray synchrotron source of DLS, hence having the characteristic of high spatial coherence. The zoneplate specimen used during the tests consists of four FZPs positioned a few micron apart, with the lateral separation between them designed to satisfy holographic separation conditions for a sample placed in the center of the four. The FZPs were fabricated using e-beam lithography by J. Bosgra at PSI, which at 9 keV with a diameter of 10 μm each and an outermost

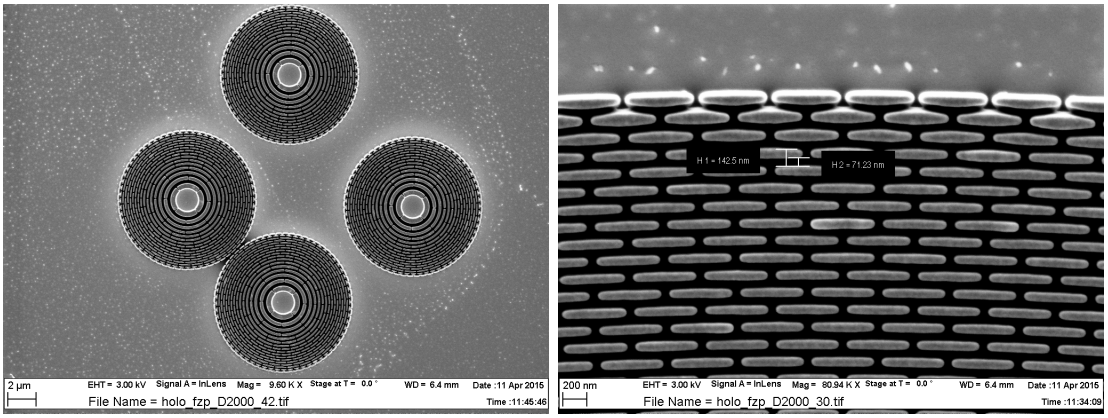

Figure 5.12: SEM images of the fabricated FZPs showing the outerzone width of 71nm.

zone-width of 70 nm (shown in Figure 5.12(b)) gives a focal length of 5 mm, a depth of focus of 71 μm and a numerical aperture of 0.98 $\times 10^{-3}$. With the zone height of 1.4 μm gold and 36 zones distributed across 10 μm in a blazed stacking, we obtain a high-effiency FZP. This means that theoretically 8% of the incident light is transmitted through the first order diffracted wave of the FZP, and the flux of the higher orders decreases by $1/n^2$ where n is the diffractive order.

The FZPs are aligned in the beam which is then clipped to cover only the FZPs and not impinge any neighbouring structures lest to create stray diffraction artifacts. Downstream from the FZPs, the sample is mounted on a separate stage equipped with translation and rotation piezos and is first positioned at z$\leq 1mm$ and then at z = 10 mm away from the FZPs while being centered in x and y to the center of the four FZPs. The interference between the four reference waves generated from the FZPs and the object wave generated by the scattering of the parallel incident beam off the sample is recorded as a far-field diffraction pattern at a photon-counting detector located 14.7 m from the sample, with N$\times$ N $= 515 \times 515 px^2$ and a 55 μm pixel size. We record single-shot diffraction patterns at an exposure time of 200 sec to 320 sec with a total detected number of photons of 2.54 $\times 10^9$ per shot. To compensate for missing information in the gaps and dead pixels of the detector array (as in Figure 5.13(a)), we record four separate shots at four shifted detector positions and create a patched up array as in Figure 5.13(b).

5.2.2 Results and Discussion

We have not used a central stop to block the zero-order beam and deflect the negative-order diffracted waves nor have we used an order-sorting aperture (OSA) to block the positive higher orders. The reason is that we do not expect the negative and higher order waves to have a crucial influence on the holographic reconstructions since their intensity relative to the first order wave is rather small. The more relevant reason is that the reconstructions due to their respective focal spots would be highly out-of-focus. With the sample positioned at z = 10 mm from the FZPs, and with the focal lengths $f_1 = 5$ mm, $f_3 = f_1/3$, and $f_5 = f_1/5$, the reconstructions due to the 1st, 3rd, and 5th order focal points come into focus at -5 mm, -8.3 mm, -9 mm away from the sample respectively. Yet, the reconstructions due to the 3rd and 5th order at -8.3 mm and -9 mm have an intensity signal proportional to 1/9 and 1/25 of that of the first order respectively. Hence we expect the satisfactory performance of the setup without using an OSA, the lack of which also enables flexibility of sample positioning. If we had a single FZP in the beam with no OSA, only a single first order diffracted wave passes through, and we would see in the near-field the first-order cone with a diameter corresponding to the geometrical projection of the zone-plate diameter at the specific z distance. In the far-field however with a single FZP one would obtain an Airy disc-like pattern. On the other hand, with four FZPs illuminated without the OSA, the interference between the diffracted cones of the four FZPs is obtained as shown in the recorded diffraction pattern in Figure 5.13. We observe the contribution of the diffracted waves modulated by the zone structures (shown in Figure 5.12(a)) and overlapping with the weak scattering signal of the sample.

By applying an inverse Fourier transform (IFFT) to the recorded diffraction pattern, we reconstruct the total autocorrelation of all contributing components at the z-position of the FZP. Since the first order focus is located at +5 mm from the FZP position, and the negative first order at -5 mm from the FZP, with the sample at +10 mm from the FZP, applying the IFFT will not show the reconstructions of the sample. In order to obtain the cross-correlation of the first-order focal point with the sample function, we need to propagate the IFFT of the diffraction pattern by

the focal distance to arrive at the focal spot location. Therefore the reconstruction procedure involved in this experiment is of two simple steps: an inverse FFT and a near-field propagation by $\pm f_1$ to obtain the cross-correlations. By near-field propagation of the IFFT by +5 mm, we arrive at the position of the positive first-order focal spot and obtain the cross-correlation $t(x,y) * f_1(x,y) = t(x,y)$; and by propagating by −5 mm, we arrive at the negative first-order focal spot and obtain the cross-correlation $f_1(x,y) * t(x,y) = t*(x,y)$ as the complex-conjugate of $t(x,y)$.

We must also note that the sample is not positioned at a distance equal to f_1 from the FZP but it is at around +4 mm further downstream from $+f_1$. This means that when we perform the near-field propagation by $\pm f_1$, we do not obtain the reconstruction of the sample function as it is in the sample plane, but we obtain magnified image of the sample convoluted with a curvature corresponding to that of the wave diverging from the focal spot to the position of the sample. The reconstruction at $\pm f_1$ will be in-focus because it is will the focal points are located but it will correspond to the projection of the sample function at the focal points since the sample is not coplanar with the focus. If we consider $z_{f_1} = 0$, the sample almost at $z_{sample} = +5$ mm, and $z_{zp} = -5$ mm, from the calculation of geometric optics the approximate magnification of the sample reconstruction after applying the near-field propagation is M = 2.

Figure 5.13(c) shows the amplitude autocorrelation resulting of the IFFT. It represents the autocorrelation of the four FZP structures which appears as intense concentric rings, in addition to the contributions of the sample which are still out-of-focus here and not visible. Moreover, we find sharp spots at what represents the respective centers of the FZPs and their centro-symmetric positions, i.e a total of 8 sharp spots. This arises due to the cross-correlation of one FZP with the one another. The four FZPs being almost identically designed and fabricated means that the cross-correlation of two is analogous to the autocorrelation of one. The autocorrelation by definition is the fourier transform of the squared intensity of a diffraction pattern or Fourier spectrum. Bearing this in mind and recalling that the structure function of a FZP represents that of an Airy disc or the Fourier transform

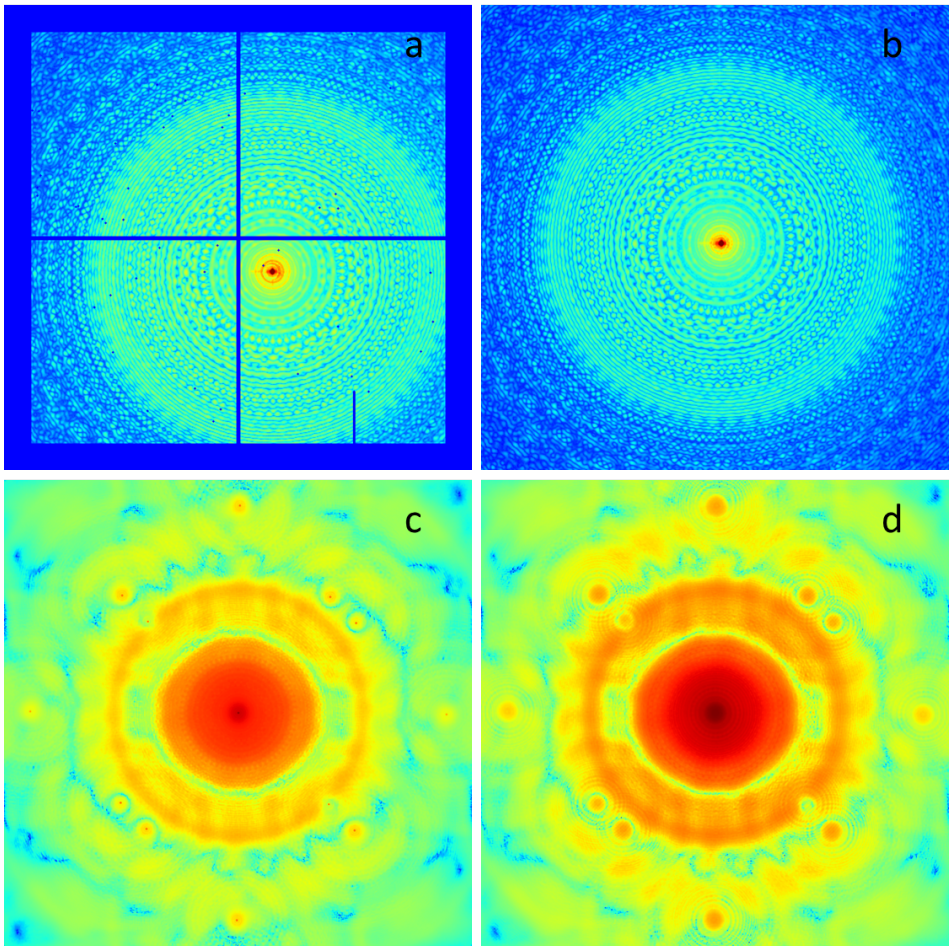

Figure 5.13: (a) diffraction pattern without exposing the sample, (b) corrected diffraction pattern of the zoneplate and the sample exposed. (c) IFFT of (b) without background subtraction, (c) near-field propagated IFFT.

of a point-source, we conclude that the autocorrelation of the FZP reduces to the point-source function, which is why the IFFT in Figure 5.13(a) shows sharp in-focus points. We do not assume that these are reconstructions of the focal spots at the focal planes because the IFFT reconstructs the area at the FZP plane and not at the plane of focus. The reconstructions of the 8 point-sources (which can also be considered to represent what the focal spots should look like in the focal plane) are seen in Figure 5.13(c). The near-field propagation by 5 mm of the reconstructed field of view (Figure 5.13(c)) obtained by the IFFT is seen in Figure 5.13(d).

The reconstruction of the gold fish test-sample is not visible in the propagated reconstructed area in Figure 5.13(d). This is due to the strong reference signal overpowering the sample signal, albeit from the reference autocorrelation or from the sum of higher-order reference contributions. Yet, with our flexible setup and our sample being physically unconfined from the zoneplates, we are able to record separate diffraction patterns of the FZPs without exposing the sample to perform background subtraction and retrieve the sample reconstructions.

To that end, we recorded separate datasets with the sample out of view at the same exposure time and incident flux. This data reconstructs the autocorrelation of the four FZPs including the contributions from the higher order waves, the beam profile, and the substrate contributions. Yet, we only recorded single shots at a single detector position without performing the four shifts to patch up the data and correct for the detector gaps. This means that the background dataset does not have the same total flux and exposure as the datasets that include the sample. This effect will result in the background subtraction procedure being not completely effective. The normalised IFFT of the background diffraction pattern is subtracted from that with the sample exposed, which should theoretically cancel out the contribution due to the reference autocorrelation, the cross-correlation with the beam imperfections, and the cross-correlation with the substrate. The result of performing the background subtraction in object-space is shown in Figure 5.14 which shows the amplitude and phase of the near-field propagated area by $+5$ mm and -5 mm i.e the two complex-conjugate reconstructions at $+f_1$ and $-f_1$.

The final reconstructions of the test-sample are shown in Figure 5.14(e,f) which represent the cross-correlation of the sample function with the focal spots of the four micro-FZPs overlapped with what remains unfiltered of the background contribution of the direct beam and the reference waves of all orders and their respective cross- and auto-correlations. The test-sample gold fish image is magnified and convoluted with the wave curvature of the reference at the sample position. Despite the overlapping contributions due to the incomplete background subtraction, we are able to distinguish the details of the sample both in amplitude and phase. The sample image itself does not contain errors within its detail and neglecting the quasi-constant overlapping background signal, we find that the sample outline

appears sharp and well-resolved. The eye, mouth, fins, and corners of the tail are all visible and resolvable.

5.2.3 Conclusion

From this, we conclude that the 70 nm focal spots serving as a point-source reference do have the potential for producing high-resolution reconstructions of the sample with high contrast, as long as an efficient background correction is performed. This can be better achieved by using an OSA to filter out all the positive higher order contributions and a central stop near the FZP to deflect the negative orders. In addition, it should prove beneficial to record the background diffraction shots with the sample out of view with the exact same parameters as the holographic data, such as the incident flux, the exposure time, as well as the size of the final data array, i.e shifting the detector to obtain a final patched up array with parameters identical to the holographic array.

If the magnified image convoluted with the wave curvature proves to be problematic, it is also very straightforwardly remedied by moving the z-position of the sample to be coincident with that of the first order focal spot. This will help to avoid any signal loss due to propagation. To get the most out of the sample scattering signal and to avoid the exposure of the sample with insufficient incident flux, it is also useful to place the sample closest to the FZP in z, hence allowing the initial direct collimated beam to illuminate the sample with maximum flux.

In summary, with proper experimental procedures, applying holographic imaging using high efficiency micro-ZPs of a diameter as small as 10 μm and fine outer-zone widths of 70 nm proves to hold high potential to provide sample reconstructions by single Fourier transform. Normally with high energy X-rays, standard sizes for Fresnel zone-plates that deliver an intense converging beam are at least 100 μm. Nevertheless, we have proved that a FZP as small as 10 μm can efficiently serve as a high-resolution holographic reference that still delivers a strong reference signal. In fact the reference signal produced by the micro-FZP is still intense so as to overpower the sample scattering signal, which leads to requiring

background subtraction. With a potential to fabricate high-efficiency micro-FZPs with outer-zone width as fine as 20 nm [86], FTH using micro-FZPs as reference sources can produce even higher-resolution sample images up to 14 nm (70% of the outer-zone width).

We find such a holographic method using micro-FZPs to be applicable to samples with different scattering properties. Evidently, with more weakly-scattering samples or low-absorption samples, the efficiency of the background subtraction procedure becomes more crucial; whereas with more strongly scattering samples and thicker absorbing samples, the sample's signal strength will become sufficient to balance out the reference signal and not be overpowered by it.

It is important to note that the holographic mechanism of the point-source reference produced by the FZP is similar but unequal to that of the standard pinhole reference used in standard FTH. The reason is that the incident flux impinging on the surface area of the pinhole dictates the reference signal strength, whereas with the zoneplate, the incident beam illuminates a large 10 μm reference zoneplate area which collimates the beam with high-efficiency into a focal spot of much higher intensity than that of a pinhole. This is why FTH using micro-FZPs proves to be more advantageous over standard pinhole FTH. With micro-FZP references, the resolution-contrast inverse relation that stands with pinhole FTH is no longer valid, as the resolution is limited by the outer-zone width and the contrast is limited by the total area of illumination and the efficiency of the zone-plate. Whereas with the pinhole reference, the size of the pinhole governs both the resolution and the contrast with inverse proportionality.

With soft x-rays the choice of reference is more flexible since fabrication requirements are less stringent. However, for application with hard x-rays, this method proves advantageous since it is virtually impossible to fabricate a point-source reference of nanoscale size while maintaining sufficient absorption/phase contrast in the longitudinal direction with respect to the mask. With the unconfined sample setup, we have additional flexibility to position the sample as needed and scan through multiple samples to obtain instantaneous reconstructions. All these advantages, in addition to fast and easy data processing and potential for further

improvement, demonstrate that FTH using high-resolution micro-FZPs stands as a noteworthy imaging technique for hard x-rays that produces both phase and absorption images of the sample from single-shot exposure.

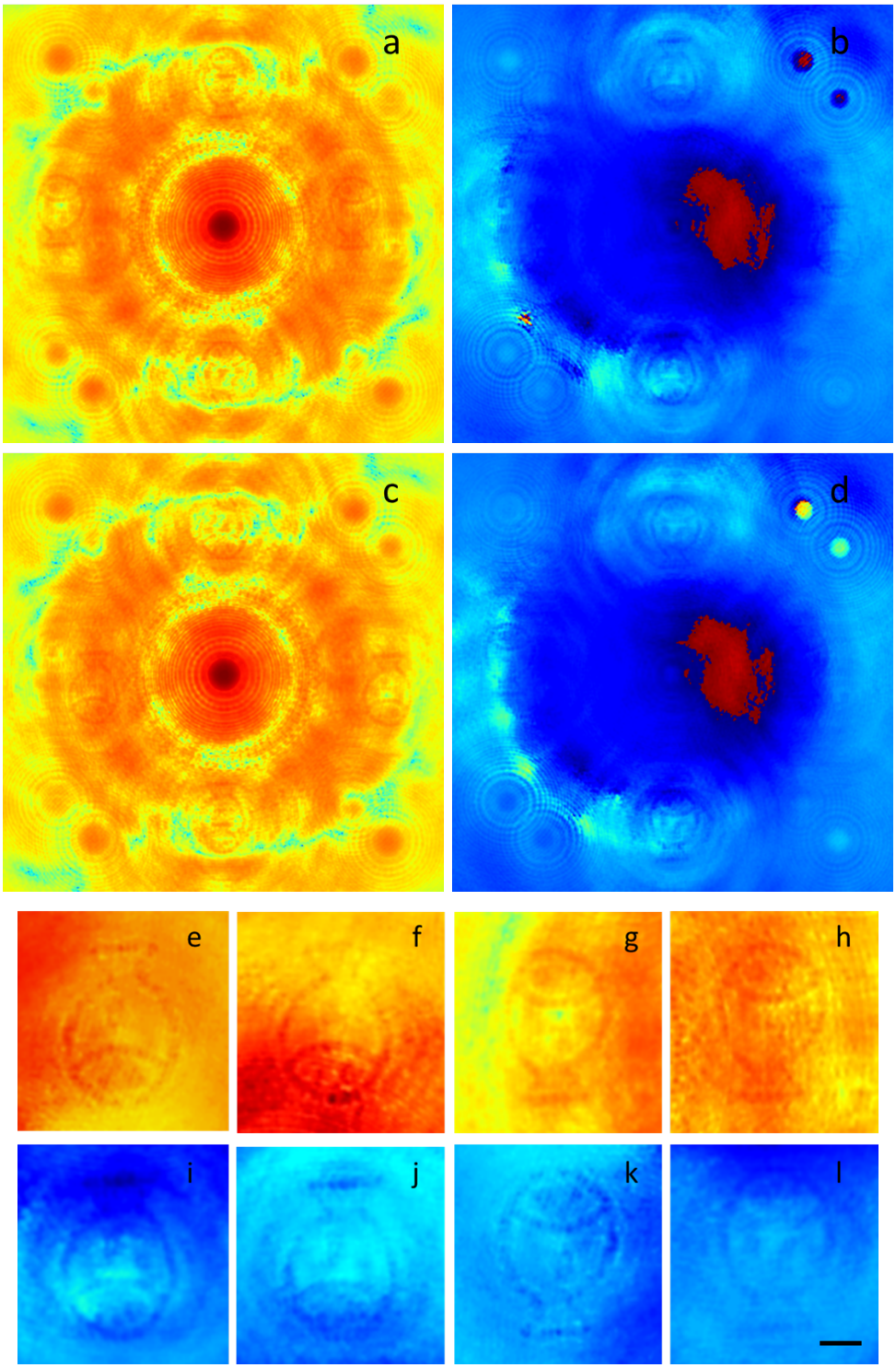

Figure 5.14: (a,b) amplitude and phase reconstructions obtained by background subtraction and propagated to $+\Delta z$. (c,d) same, propagated to -Δz. (e-l) selection of magnified gold fish reconstructions in amplitude and phase of the twin images. Scale bar: 1 μm.

6 Conclusion

We have showed a variety of holographic imaging methods that involve a single computational step to reconstruct phase and amplitude of the imaged specimens. Using high-efficiency high-resolution zoneplates holds prospect as the development in lithography and nano-fabrication is ever advancing. FZP- Fourier transform holography provides intense references beams to image thick samples with high resolution and low noise. We have implemented micron sized FZPs as holographic references and had them decoupled from the sample frame, contrary to the mainstream work in FTH with FZPs. So far, it has been rare to achieve high resolution within a flexible sample geometry when it comes to FTH with FZPs at hard x-ray wavelengths. Yet, we have provided methods that prove that flexibility and resolution can come hand in hand.

We have successfully developed single-shot diffraction imaging using phase-shifting holographic reference and produced reconstructions by a direct non-iterative numerical calculation. We innovated a novel holographic reference fabricated by atomic layer deposition and serving as a compound wireframe structure of heavy and light material. The reference structed produced by ALD results in sample reconstructions of a resolution reaching the detector limit at 61nm. Despite it being a nanolayer, it maintains high reference signal strength and leads to amplified image contrast. In addition, it results in noise-robust imaging and portrays edge-enhancement and differential contrast due to the nature of the wireframe. We

have applied the method to a variety of samples and proved that is applicable to weakly and strongly scattering samples as well as low absorption and weak phase objects. We extended the method to imaging of biological samples and obtained reconstructions with high contrast and resolution in the upper limit of 100nm. Furthermore, we implemented a setup which physically decouples the sample plane from the reference plane allowing to manipulate the field of view, shift and rotate the sample, and scan through a multitude of samples while maintaining constant experimental conditions and maintaining a fixed sample plane. The setup also allows us to perform data refinement by subtracting the background and reference contributions from the reconstructed area, hence removing artifacts and enhancing the sample signal. Quite importantly, the flexible setup also eases many of the fabrication requirements and technical constraints that would otherwise limit the method. Holography using extended references has been mainly implemented using soft x-rays, optical light, and EUV radiation, with a lag with hard x-rays due to the difficult fabrication challenges. We have hereby presented methods for coherent holographic diffraction imaging with hard x-rays that provide high resolution and contrast by single-shot exposure, non-iterative numerical processing, and an unconfined sample geometry. With all these advantages in addition to further advancement in nano-fabrication, the specially designed holographic reference structures that we have showed holds potential for refining to sub-nm resolution and offers great applicability to single-shot femtosecond 3-dimensional imaging using x-ray free-electron-lasers.

Declaration of Authorship

I, Mirna Saliba, declare that this thesis titled, Non-iterative Holographic Diffraction Imaging using Phase-Shifting References by Single-Shot Exposure with High Energy Coherent X-rays, and the work presented in it are my own. I confirm that:

- This work was done wholly or mainly while in candidature in collaboration with Diamond Light Source UK for a research degree at the University of Zurich, Switzerland .
- Where any part of this thesis has previously been submitted for a degree or any other qualification at the University or the Synchrotron Facility or any other institution, this has been clearly stated.
- Where I have consulted the published work of others, this is always clearly attributed.
- Where I have quoted from the work of others, the source is always given. With the exception of such quotations, this thesis is entirely my own work.
- I have acknowledged all main sources of help.
- Where the thesis is based on work done by myself jointly with others, I have made clear exactly what was done by others and what I have contributed myself.

Signed: Date:

Bibliography

[1] J. M. Kenney, J. Kirz, H. Rarback, R. Feder, D. Sayre, and M. Howells. Scanning soft-x-ray microscopy with a fresnel zoneplate at the national synchrotron light-source. *Proceedings of the Society of Photo-Optical Instrumentation Engineers*, 447, 158-163 (1984).

[2] J. M. Kenney, J. Kirz, H. Rarback, M. R. Howells, P. Chang, P. J. Coane, R. Feder, P. J. Houzego, D. P. Kern, and D. Sayre. Soft-x-ray microscopy at the nsls. *Nuclear Instruments & Methods in Physics Research Section a-Accelerators Spectrometers Detectors and Associated Equipment*, 222(1-2), 37 (1984).

[3] J. Vila-Comamala, A. Diaz, M. Guizar-Sicairos, A. Mantion, C. M. Kewish, A. Menzel, O. Bunk, and C. David. Characterization of high-resolution diffractive x-ray optics by ptychographic coherent diffractive imaging. *Opt. Express*, 19(22) (2011).

[4] J. Vila-Comamala, M. Wojcik, A. Diaz, M. Guizar-Sicairos, C. M. Kewish, S. Wang, and C. David. Angular spectrum simulation of x-ray focusing by fresnel zone plates. *Journal of synchrotron radiation*, 20(Pt 3), 397-404 (2013).

[5] S. Gorelick, J. Vila-Comamala, V. A. Guzenko, R. Barrett, M. Salomé, and C. David. High-efficiency fresnel zone plates for hard x-rays by 100 kev e-beam lithography and electroplating. *Journal of synchrotron radiation*, 18(3), 442-446 (2011).

[6] B. Janssens. Aberration-corrected tem. *Imaging & Microscopy*, 9(2), 42-43 (2007).

[7] J. C. Spence. Lensless imaging: a workshop on "new approaches to the phase problem for non-periodic objects". *Ultramicroscopy*, 90 (2001).

[8] S. Marchesini, H. N. Chapman, S. P. Hau-Riege, R. A. London, A. Szoke, H. He, M. R. Howells, H. Padmore, R. Rosen, J. C. H. Spence, and U. Weierstall. Coherent x-ray

diffractive imaging: applications and limitations. *Optics Express*, 11(19), 2344-2353 (2003).

[9] H. N. Chapman and K. A. Nugent. Coherent lensless x-ray imaging. *Nature Photonics*, 4(12), 833-839 (2010).

[10] J. C. H. Spence, U. Weierstall, and M. Howells. Phase recovery and lensless imaging by iterative methods in optical, x-ray and electron diffraction. *Philosophical Transactions of the Royal Society of London Series a-Mathematical Physical and Engineering Sciences*, 360(1794), 875-895 (2002).

[11] R. H. T. Bates. On phase problems I. *Optik*, 51(161), 223 (1978).

[12] H. He, S. Marchesini, M. Howells, U. Weierstall, G. Hembree, and J. C. H. Spence. Experimental lensless soft x-ray imaging using iterative algorithms: phase diffuse scattering. *Acta Cryst* A59, 143-152 (2003).

[13] J. Miao. The oversampling phasing method. *Acta Cryst* D56, 1312-1315 (2000).

[14] P. Thibault, M. Dierolf, A. Menzel, O. Bunk, C. David, and Franz Pfeiffer. High-resolution scanning x-ray diffraction microscopy. *Science*, 321(5887), 379-382 (2008).

[15] P. Thibault, V. Elser, C. Jacobsen, D. Shapiro, and D. Sayre. Reconstruction of a yeast cell from x-ray diffraction data. *Acta Cryst* A62, 248-261 (2006).

[16] J.M. Rodenburg. Ptychography and related diffractive imaging methods. *Advances in Imaging and Electron Physics*, 150, 87-184 (2008).

[17] J. Spence. X-ray imaging: Ultrafast diffract-and-destroy movies. *Nature Photonics*, 2(7), 390-391 (2008).

[18] H. N. Chapman *et al.*. Femtosecond diffractive imaging with a soft-X-ray free-electron laser. Nat. Phys. 2, 839-843 (2006).

[19] R. Neutze, R. Wouts, D. van der Spoel, E. Weckert and J. Hajdu. Potential for biomolecular imaging with femtosecond X-ray pulses. Nature, 406, 752-757 (2000).

[20] C. M. Günther, B. Pfau, R. Mitzner, B. Siemer, S. Roling, H. Zacharias, O. Kutz, I. Rudolph, D. Schondelmaier, R. Treusch, and S. Eisebitt. Sequential femtosecond x-ray imaging. *Nature Photonics*, 5(2), 99-102 (2011).

[21] M. M. Seibert *et al.*, Single mimivirus particles intercepted and imaged with an x-ray laser, Nature 470, 78-81 (2011).

[22] H. N. Chapman, P. Fromme, A. Barty, T. A. White, R. A. Kirian, A. Aquila, M. S. Hunter, J. Schulz, D. P. DePonte, U. Weierstall *et al.* Femtosecond x-ray protein nanocrystallography. *Nature*, 470(7332), 73-77 (2011).

[23] H. N. Chapman, A. Barty, S. Marchesini, A. Noy, S. R. Hau-Riege, C. Cui, M. R. Howells, R. Rosen, H. He, J. C. H. Spence, U. Weierstall, T. Beetz, C. Jacobsen, and D. Shapiro. High-resolution ab initio three-dimensional x-ray diffraction microscopy. *Journal of the Optical Society of America a-Optics Image Science and Vision*, 23(5), 1179-1200 (2006).

[24] M. Howells, M. Iarocci, and J. Kirz. Experiments in x-ray holographic microscopy using synchrotron radiation. *J Opt Soc Am A*, 3(12), 2171, 1986.

[25] Dennis Gabor et al. A new microscopic principle. *Nature*, 161(4098), 777-778, 1948.

[26] Dionys Gabor. Microscopy by reconstructed wave-fronts. In *Proceedings of the Royal Society of London A: Mathematical, Physical and Engineering Sciences*, 197, 454-487 (1949).

[27] L. Rong, F. Pan, W. Xiao, Y. Li, and F. Wang. Twin image elimination from two in-line holograms via phase retrieval. *Chinese Optics Letters*, 10(6), 060902-60904 (2012).

[28] I. McNulty, J. Kirz, C. Jacobsen, E. Anderson, and M. Howells. Soft x-ray microscopy using fourier transform holography. *Nuclear Instruments & Methods in Physics Research Section a-Accelerators Spectrometers Detectors and Associated Equipment*, 291 (1990).

[29] M. R. Howells, B. Calef, C. J. Jacobsen, J. H. Spence, and W. Yun. *A modern approach to x-ray holography*, volume 507 of *Aip Conference Proceedings*. (2000).

[30] S Eisebitt, J Lüning, WF Schlotter, M Lörgen, O Hellwig, W Eberhardt, and J Stöhr. Lensless imaging of magnetic nanostructures by x-ray spectro-holography. *Nature*, 432(7019), 885-888 (2004).

[31] W. F. Schlotter, R. Rick, K. Chen, A. Scherz, J. Stöhr, J. Lüning, S. Eisebitt, Ch Günther, W. Eberhardt, O. Hellwig, and I. McNulty. Multiple reference fourier

transform holography with soft x rays. *Applied Physics Letters*, 89(16), 163112 (2006).

[32] S. Marchesini, S. Boutet, A. E. Sakdinawat, M. J. Bogan, S. Bajt, A. Barty, H. N. Chapman, M. Frank, S. P. Hau-Riege, A. Szöke, C. Cui, D. A. Shapiro, M. R. Howells, J. C. H. Spence, J. W. Shaevitz, J. Y. Lee, J. Hajdu, and M. M. Seibert. Massively parallel x-ray holography. *Nature Photonics*, 2(9), 560-563 (2008).

[33] S. Marchesini, H. He, H. N. Chapman, S. P. Hau-Riege, A. Noy, M. R. Howells, U. Weierstall, and J. C. H. Spence. X-ray image reconstruction from a diffraction pattern alone. *Phys. Rev. B*, 68(14) (2003).

[34] H. He, S. Marchesini, M. Howells, U. Weierstall, H. Chapman, S. Hau-Riege, A. Noy, and J. C. H. Spence. Inversion of x-ray diffuse scattering to images using prepared objects. *Phys. Rev. B*, 67 (2003).

[35] H. He, U. Weierstall, J. C. H. Spence, M. Howells, H. A. Padmore, S. Marchesini, and H. N. Chapman. Use of extended and prepared reference objects in experimental fourier transform x-ray holography. *Applied Physics Letters*, 85(13), 2454 (2004).

[36] Manuel Guizar-Sicairos and James R. Fienup. Holography with extended reference by autocorrelation linear differential operation. *Opt. Express*, 15(26), (2007).

[37] D. Zhu *et al.*, High-resolution x-ray lensless imaging by differential holographic encoding, Phys. Rev. Lett. 105, 043902 (2010).

[38] Manuel Guizar Sicairos. Holographic x-ray image reconstruction through the application of differential and integral operators. *Optics Letters*, 35(7) (2010).

[39] B. Enders, K. Giewekemeyer, T. Kurz, S. Podorov, and T. Salditt. Non-iterative coherent diffractive imaging using a phase-shifting reference frame. *New Journal of Physics*, 11(8) (2009).

[40] S. G. Podorov, K. M. Pavlov, and D. M. Paganin. A non-iterative reconstruction method for direct and unambiguous coherent diffractive imaging. *Opt. Express*, 15(16), 9954-9962 (2007).

[41] O. K. Ersoy, *Diffraction, Fourier optics and imaging.* John Wiley & Sons, (2006).

[42] Joseph W Goodman. *Introduction to Fourier optics.* Roberts and Company Publishers (2005).

[43] D. Attwood, *Soft x-rays and extreme ultraviolet radiation: principles and applications*, Cambridge University Press (1999).

[44] P. Thibault, Algorithmic Methods in Diffraction Microscopy, PhD Thesis, Cornell University, (2007).

[45] K. K. Sharma, *Optics: Principles and Applications* p.406, Academic Press, (2006).

[46] P. Thibault, M. Dierolf, O. Bunk, A. Menzel, and F. Pfeiffer. Probe retrieval in ptychographic coherent diffractive imaging. *Ultramicroscopy*, 109(4), 338-343 (2009).

[47] M. Guizar-Sicairos. Methods for coherent lensless imaging and x-ray wavefront measurement, PhD Thesis, Rochester University, (2010).

[48] B. Enders. Single-step inversion for coherent diffraction imaging - a generalization to fourier transform holography, Diplomarbeit, Georg-August-Universität zu Göttingen, (2009).

[49] E. E. Fenimore. Coded aperture imaging: predicted performance of uniformly redundant arrays. *Applied Optics*, 17(22), 1978.

[50] L.M. Stadler, C. Gutt, T. Autenrieth, O. Leupold, S. Rehbein, Y. Chushkin, G. Grubel, Hard X Ray Holographic Diffraction Imaging. *Phys. Rev. Lett.* 100, (2008).

[51] H. Iwamoto and N. Yagi, Hard X-ray Fourier transform holography from an array of oriented referenced objects. *J. Synch. Rad.* 18(4), 564-8, (2011).

[52] D. Gauthier, M. Guizar-Sicairos, X. Ge, W. Boutu, B. Carré, J. R. Fienup, and H. Merdji. Single-shot femtosecond x-ray holography using extended references. *Phys. Rev. Lett.*, 105(9) (2010).

[53] C. Rau, T. Weitkamp, A. Snigirev, C.G. Schroer, J. Tummler, B. Lengeler. Recent developments in hard X-ray tomography. *Nuclear Instruments & Methods in Physics Research Section a-Accelerators Spectrometers Detectors and Associated Equipment*, 467, 929-931, (2001).

[54] C. Rau, U.H. Wagner, A. Peach, I.K. Robinson, B. Singh, G. Wilkin, C. Jones. The Diamond Beamline I13L for Imaging and Coherence, *AIP Conference Proceedings*, 1234, 121-125 (2010).

[55] F.A. Vittoria, P.C. Diemoz, M. Endrizzi, L. De Caro, U.H. Wagner, C. Rau, I.K.

Robinson, A. Olivo. Phase retrieval through a one-dimensional ptychographic engine, *Opt Express*, 22(14), 17281-17291 (2014).

[56] K. Jefimovs, J. Vila-Comamala, T. Pilvi, J. Raabe, M. Ritala, C. David. Zone-doubling technique to produce ultrahigh-resolution x-ray optics, *Phys. Rev. Lett.*, 99(26), 264801 (2007).

[57] SEM images taken by Jeroen Bosgra at the Laboratory for Micro- and Nanotechnology, Paul Scherrer Institut, Switzerland.

[58] S. Redfern, E. Read, O. Branson, H. Elderfield, T. Tyliszczak, C. Rau, A. Bodey. X-ray imaging and 3D recontruction of chemical alteration in plankton shells - a key indicator of past climate, *Bruker microCT User Meeting* (2015).

[59] S. Woelfl , M. Mages, S. Mercado, L. Villalobos, M. Óvári, F. Encina. Determination of trace elements in planktonic microcrustaceans using total reflection X-ray fluorescence (TXRF): First results from two Chilean lakes, *Analytical and Bioanalytical Chemistry*, 378(4), 1088-1094 (2004).

[60] J. Young, M. Geisen, L. Cros, A. Kleijne, C. Sprengel, I. Probert, J. Ostergaard. A Guide to extant coccolithophore taxonomy. *Journal of Nanoplankton Research*, Special Issue 1 (2003).

[61] B.R. Heimdal. Modern Coccolithophorids. Identifying Marine Phytoplankton. Academic Press, San Diego. p. 731–831 (1997)

[62] D. Dooling, NASA Science News, Meet Conan the Bacterium: Humble microbe could become "The Accidental (Space) Tourist" (1999) www.science.nasa.gov/science-news/science-at-nasa/1999/ast14dec99_1/

[63] S.E. DeWeerdt, The World's Toughest Bacterium: Deinococcus radiodurans may be a tool for cleaning up toxic waste and more, Genome Network News, (2002) www.genomenewsnetwork.org/articles/07_02/deinococcus.shtml

[64] K.S. Makarova, L. Aravind, YI Wolf. Genome of the Extremely Radiation-Resistant Bacterium Deinococcus radiodurans Viewed from the Perspective of Comparative Genomics. *Microbiology and Molecular Biology Reviews.* 65(1), 44-79 (2001).

[65] V. Mattimore and J. R. Battista. Radioresistance of Deinococcus radiodurans: Functions Necessary To Survive Ionizing Radiation Are Also Necessary To Survive Prolonged Desiccation, *Journal of Bacteriology*, 178(3), 633–637 (1996).

[66] Leibniz-Institut DSMZ - Deutsche Sammlung von Mikroorganismen und Zellkulturen GmbH. www.dsmz.de/catalogues/details/culture/dsm-20539.html

[67] R. Plackett, I. Horswell, E. N. Gimenez, J. Marchal, D. Omar and N. Tartoni. Merlin: a fast versatile readout system for Medipix3, *Journal of Instrumentation*, 8 (2013).

[68] V. Kohn, I. Snigireva, and A. Snigirev. Direct Measurement of Transverse Coherence Length of Hard X Rays from Interference Fringes, *Phys. Rev. Lett.*, 85, 2745 (2000).

[69] N. Tartoni, G. Dennis, P. Gibbons, E. Gimenez, I. Horswell, J. Marchal, U. Pedersen, Z. Pesic, R. Plackett, C. Rau, R. Somayaji, J. Spiers, J. Thompson, B. Willis, C. Angelsen, P. Booker, S. Burge, J. Lipp, T. Nicholls, S. Taghavi, M. Thorpe. Excalibur: A three million pixels photon counting area detector for coherent diffraction imaging based on the Medipix3 ASIC. *Nuclear Science Symposium and Medical Imaging Conference (NSS/MIC)*, IEEE, Anaheim, CA, 530-533 (2012).

[70] Excalibur Detector Development, Detector Group, Diamond Light Source Ltd. www.diamond.ac.uk/Science/Research/Detector/Excalibur.html

[71] R.N. Wilke, M. Priebe, M. Bartels, K. Giewekemeyer, A. Diaz, P. Karvinen, and T. Salditt. Hard X-ray imaging of bacterial cells: Nano-diffraction and ptychographic reconstruction. *Opt. Express*, 20(17), 19232-54 (2012).

[72] A. V. Martin and L. J. Allen. Direct retrieval of a complex wave from its diffraction pattern. *Optics Communications*, 281(20), 5114-5121 (2008).

[73] A. V. Martin, A. I. Bishop, D. M. Paganin, and L. J. Allen. Practical implementation of a direct method for coherent diffractive imaging. *Ultramicroscopy*, 111(7), 777-81 (2011).

[74] A. V. Martin, A. J. D'Alfonso, F. Wang, R. Bean, F. Capotondi, R. A. Kirian, E. Pedersoli, L. Raimondi, F. Stellato, C. H. Yoon, and H. N. Chapman. X-ray holography with a customizable reference. *Nat Commun*, 5, 4661 (2014).

[75] A. Menzel, P. Thibault, M. Dierolf, C. M. Kewish, O. Bunk, C. David, W. Leitenberger, and F. Pfeiffer. *Advances in Ptychographical Coherent Diffractive Imaging*, volume 7076 of *Proceedings of the Society of Photo-Optical Instrumentation Engineers (Spie)*. 2008.

[76] P. Thibault, M. Guizar-Sicairos, and A. Menzel. Coherent imaging at the diffraction limit. *Journal of synchrotron radiation*, 21(Pt 5), 1011-8 (2014).

[77] T. Gorniak, R. Heine, A. P. Mancuso, F. Staier, C. Christophis, M. E. Pettitt, A. Sakdinawat, R. Treusch, N. Guerassimova, J. Feldhaus, C. Gutt, G. Grübel, S. Eisebitt, A. Beyer, A. Gölzhäuser, E. Weckert, M. Grunze, I. A. Vartanyants, and A. Rosenhahn. X-ray holographic microscopy with zone plates applied to biological samples in the water window using 3rd harmonic radiation from the free-electron laser flash. *Opt. Express*, 19(2) (2011).

[78] M. Bartels, M. Priebe, R. N. Wilke, S. P. Kruger, K. Giewekemeyer, S. Kalbfleisch, C. Olendrowitz, M. Sprung and T. Salditt. Low-dose three-dimensional hard x-ray imaging of bacterial cells, *Optical Nanoscopy* 1(1), 10 (2012).

[79] F. Buttner, M. Schneider, C. M. Gunther, C. A. Vaz, B. Lagel, D. Berger, S. Selve, M. Klaui, and S. Eisebitt. Automatable sample fabrication process for pump-probe x-ray holographic imaging. *Opt Express*, 21(25), 30563-72 (2013).

[80] E. B. Malm, N. C. Monserud, P. W. Wachulak, C. Brown, W. Chao, E. Anderson, H. Xu, C. P. Hains, G. Balakrishnan, C. S. Menoni, J. J. Rocca, and M. C. Marconi. Time Resolved Holography Scheme Using a Table Top Soft X-Ray Laser, volume 147 of *Springer Proceedings in Physics*. Springer-Verlag Berlin, Berlin (2014).

[81] W. Leitenberger, T. Weitkamp, M. Drakopoulos, I. Snigireva, A. Snigirev. Microscopic imaging and holography with hard X-rays using Fresnel zone-plates. *Optics Communications* , 180(4-6), 233-238 (2000).

[82] W. Leitenberger and A. Snigirev. Fourier Transform Holography with Coherent Hard X-rays, *Proc of VI Int Conf X-ray Microscopy*, 507, 497 (2000).

[83] W. Leitenberger and A. Snigirev. Microscopic imaging with high energy x-rays by Fourier transform holography. *Journal of Applied Physics*, 90 (2), 538-544 (2001).

[84] M. Nishikino, H. Yamatani, K. Nagashima, and T. Kawachi. Development of Soft X-ray Fourier Transform Holography with Fresnel Zone Plate, *X-ray Lasers*, 130, 427 (2008).

[85] J. Geilhufe, B. Pfau, M. Schneider, F. Büttner, C. M. Günther, S. Werner, S. Schaffert, E. Guehrs, S. Frömmel, M. Kläui, and S. Eisebitt , *Nat. Commun.* 5, 3008 (2014).

[86] S.-R. Wu, Y. Hwu, and G. Margaritondo, Hard-X-ray Zone Plates: Recent Progress. *Materials* 5(12), 1752-1773 (2012).